

# MITTEILUNGEN

aus dem Institut für Geophysik und Meteorologie  
der Universität zu Köln

Herausgeber: M. Kerschgens, F. M. Neubauer, M. Pätzold, P. Speth B. Tezkan

---

Heft 162

Heiko Backes

**Titan's Interaction  
with the  
Saturnian Magnetospheric Plasma**

KÖLN 2005



---

Titan's Interaction  
with the  
Saturnian Magnetospheric Plasma

---

INAUGURAL-DISSERTATION  
ZUR  
ERLANGUNG DES DOKTORGRADES  
DER MATHEMATISCH-NATURWISSENSCHAFTLICHEN FAKULTÄT  
DER UNIVERSITÄT ZU KÖLN

VORGELEGT VON  
**HEIKO BACKES**  
AUS WADERN

KÖLN 2004

Berichterstatter: Prof. Dr. F. M. Neubauer  
Prof. Dr. M. K. Dougherty  
Prof. Dr. B. Tezkan

Tag der mündlichen Prüfung: 2.12.2004

## Abstract

An advanced 3D model for Titan's interaction with the Saturnian magnetospheric plasma has been developed. The ideal magnetohydrodynamic (MHD) equations have been extended in order to account for the effects of Titan's dense neutral atmosphere on the plasma interaction. The ion-neutral friction plays a key role in the deceleration of the magnetospheric plasma. The ionosphere is created from the neutral atmosphere by applying a 3D radiation model for the solar EUV radiation. Impact ionization rates by photoelectrons are calculated effectively. In order to include the process of impact ionization by magnetospheric electrons we have developed a time dependent flux tube model which accounts for flux tube motion through the atmosphere and electron heat conduction along the magnetic field lines. On Titan's nightside magnetospheric electron impact ionization is the only source for ion production. Thus, we obtain a 3D ionosphere that depends on the Saturnian local time (SLT) and the subsolar latitude (SSL). As a reference for the incident magnetospheric plasma the parameters derived from Voyager 1 measurements are used. The model is applied to three different cases that match the situations at the Cassini flybys TA, T5, and T34 at Titan.

The results cover two fields, the ionosphere and the global plasma interaction. In the first part the resulting ionospheric properties are discussed. The peak electron density on the dayside is about an order of magnitude lower than on the nightside. The behavior of certain ionospheric regions and layers as a function of the angle to the ram direction and SLT are examined in the upstream hemisphere. The model produces a magnetic ionopause layer that separates the upper magnetized from the lower non- or weakly magnetized ionosphere. Its altitude varies between 500 km on the nightside and 1000 km on the dayside. We derive an empirical expression for the magnetic field magnitude at the magnetic barrier peak. Two different mechanisms for the generation of the magnetic barrier are discussed.

The global plasma interaction is explained in terms of MHD waves. The super-Alfvénic flow produces Alfvén tubes. The primary interaction region, where the effect of the neutral gas on the plasma is above 1%, has a radius of 2.3 Titan radii. The major part of the magnetospheric plasma flows around a domain that consists of the primary interaction region and the volume where the nominal northern and southern Alfvén tubes intersect each other in the tail. The deflected flow from the two flanks converges at about 4.5 Titan radii downstream from Titan's center. Plasma pick-up occurs basically at the flanks of Titan's atmosphere. In the tail region the increased plasma density is distributed along the magnetic field by a pressure gradient. We derive a total loss rate of 30 g/s independent of SLT.

The plasma interaction generates an electric current system. The currents in the primary interaction region are split into their diamagnetic, inertial, and atmospheric contributions. The magnetic ionopause layer is associated with atmospheric currents. The upper boundary of the magnetic barrier corresponds to diamagnetic currents. Inertial currents appear in regions of plasma pick-up and accelerate the newly-created plasma. The currents in the primary interaction region are connected to the currents in the Alfvén tubes. The net current along one half Alfvén tube is about  $3 \times 10^4$  A.

For a comparison with the data from the first close Titan encounter of Cassini, we present the results from the model for TA along the trajectory. Our model predicts an inbound and outbound crossing of the magnetic ionopause layer.



## Zusammenfassung

Diese Arbeit beschäftigt sich mit der Plasmawechselwirkung des Saturnmondes Titan mit dem ihn umströmenden magnetosphärischen Plasma. Er ist der größte der Saturnmonde und nach Jupiters Ganymede der größte Satellit unseres Sonnensystems. Nicht zuletzt eine dichte Stickstoffatmosphäre - ähnlich der Erde, nur viel kälter - machen ihn zu einem interessanten Forschungsobjekt.

Die Cassini Raumsonde umkreist vom Juli 2004 an 4 Jahre lang Saturn, fliegt dabei über 40 mal zum Teil sehr dicht an Titan vorbei und untersucht dabei unter anderem die Eigenschaften von Titan und seiner Plasmaumgebung. Angetrieben durch die einmalige Gelegenheit, experimentelle Daten aus in-situ Messungen mit theoretischen Modellen vergleichen und dadurch die Modelle weiterentwickeln zu können, entstand die Idee zu dieser Arbeit.

Die bisherigen Erkenntnisse über die Plasmawechselwirkung von Titan stützen sich in erster Linie auf den Vorbeiflug der Voyager 1 Raumsonde im Jahr 1980. Durch die Analyse der Daten konnten *Neubauer et al.* [1984] eine obere Grenze für ein inneres Dipolmoment bestimmen. Demnach ist die Magnetfeldstärke an der Oberfläche von Titan kleiner als 4 nT, kleiner als das Magnetfeld von Saturn an der Position von Titan.

In Bezug auf seine Plasmawechselwirkung reiht sich Titan damit ein in die Reihe der nicht-magnetischen Körper mit ausgeprägter Atmosphäre. Weitere Spezies dieser Gattung sind Venus, Mars und Kometen wie z.B. Halley. Im Vergleich zu diesen hat Titan einige Besonderheiten: (1) Das anströmende magnetosphärische Plasma, das Voyager 1 antraf, konnte durch eine sub-sonische und super-Alfénische Machzahl charakterisiert werden. Eine Plasmawechselwirkung mit einem Plasma mit diesen Eigenschaften wurde bisher noch nirgendwo sonst angetroffen. (2) Die Ausdehnung der Atmosphäre hat die gleiche Größenordnung wie der Satellitenradius, anders als bei Mars und Venus, bei denen die Atmosphäre den festen Körper um nur wenige Prozent vergrößert. Die neutrale Koma von Kometen ist noch weiter ausgedehnt. Allerdings spielt dort die Neutralgasgeschwindigkeit eine wichtige Rolle bei der Plasmawechselwirkung, während sie bei Titan annähernd vernachlässigbar ist. (3) Die Wechselwirkung wird wesentlich durch die Ionosphäreigenschaften bestimmt. Die lokale Beschaffenheit der Ionosphäre hängt vom Winkel zur Sonne als Erzeuger ab. Zusätzlich wird die Wechselwirkung von der Richtung des anströmenden Plasmas, bei Titan das (fast) korotierende magnetosphärische Plasma von Saturn, geprägt. Damit ändern sich die Eigenschaften der dem anströmenden Plasma zugewandten Ionosphäre innerhalb eines Titantages. Venus, Mars und Kometen wechselwirken mit dem Sonnenwind, Plasma und Ionisationsquelle kommen aus der gleichen Richtung. (4) Titan umkreist Saturn in einem Abstand nahe am nominellen Magnetopausenabstand. In Zeiten von hohem dynamischem Sonnenwinddruck wird die Magnetopause näher an Saturn gedrückt, und Titan kann für eine gewisse Zeit die Saturnmagnetosphäre verlassen und mit dem "Magnetosheath" Plasma oder sogar mit dem Sonnenwind vor der Bugstoßwelle wechselwirken. Diese Plasmen unterscheiden sich wesentlich vom Magnetosphärenplasma. Dieser Fall wird in unserem Modell nicht berücksichtigt.

Bei der Wahl eines geeigneten Modells für die Beschreibung der Wechselwirkung von Titan mit dem Magnetosphärenplasma fiel unsere Entscheidung darauf, einen Magnetohydro-

dynamischen (MHD) Ansatz zu wählen, obwohl es offensichtliche Gründe gibt, die dagegen sprechen. So sind die Gyroradien der Ionen im anströmenden Plasma in der gleichen Größenordnung wie der Satellitenradius. Damit spielen Gyroeffekt bei Titan sicherlich eine Rolle. Außerdem gibt es einen Bereich, in dem der Hall-Effekt sich bemerkbar macht. Das ist in dem Bereich der Atmosphäre, in dem die Gyration der Ionen durch Stöße mit dem Neutralgas verhindert wird, aber die Elektronen weiterhin um die magnetischen Feldlinien gyrieren. Beide Effekte werden in der MHD unterdrückt.

Dass wir uns dennoch für die MHD entschieden haben, hat im wesentlichen zwei Gründe: (1) Die ausgedehnte, dichte Atmosphäre von Titan beeinflusst entscheidend die Plasmawechselwirkung durch Plasmaproduktion und Stöße zwischen Neutralteilchen und Plasma. (2) Die Wechselwirkung hat entscheidende dreidimensionale Eigenschaften. Ein Modell in weniger als drei räumlichen Dimensionen hat daher eine nur sehr beschränkte Aussagekraft. Die Methode der MHD ermöglicht es, beidem Rechnung zu tragen, wobei der erste Grund dazu führte, eine Fluid-Beschreibung zu wählen, weil es dort im Gegensatz zu kinetischen oder Hybridmodellen möglich ist, Neutralgasstöße zu behandeln. Der zweite Grund veranlasste uns dazu, die Anzahl der Fluide auf eins zu reduzieren, um das Problem mit hoher Gitterauflösung in drei Dimensionen numerisch, d.h. mit nicht zu großen Rechenzeiten, traktabel zu machen. Nach unserem Wissen gibt es zur Zeit keine Methode, die Ionen-Neutralgasstöße und kinetische Effekte mit zufriedenstellender Auflösung in einem Modell vereint.

Die Plasmawechselwirkung von Titan wird bestimmt durch drei Komponenten: das einströmende magnetosphärische Plasma, die Neutralatmosphäre und die Ionosphäre. Einen möglichen Einfluss des festen Körpers auf die Wechselwirkung haben wir vernachlässigt, obwohl Induktionseffekte die Wechselwirkung beeinflussen können wie bei den Jupitermonden Europa und Callisto [Neubauer, 1999]. Für das anströmende Magnetosphärenplasma haben wir die Eigenschaften gewählt, die Voyager 1 bei seinem Vorbeiflug gemessen hatte [Neubauer, 1980], wobei die Eigenschaften auf eine Plasmaspezies reduziert wurden. Energie (kinetische, thermische, magnetische) und Impuls sind identisch mit den gemessenen Werten.

Für die Neutralgasverteilung in unserem Modell nehmen wir die beiden dominierenden Spezies des Neutralgasmodells von Keller *et al.* [1992] (eine Weiterentwicklung des Modells von Yung *et al.* [1984]; Yung [1987]): molekularer Stickstoff und Methan. Es hat sich herausgestellt, dass das Exosphären gas  $H_2$  für die Wechselwirkung in erster Ordnung vernachlässigbar ist.

Ein entscheidender Vorteil unseres Modells gegenüber anderen Modellen ist unser Ionosphärenmodell. Die Ionosphäre wird innerhalb des Modells aus dem Neutralgas in drei Dimensionen erzeugt. Bei Titan sind die hauptsächlichsten Ionisationsprozesse Photoionisation durch die solare EUV Strahlung, Ionisation durch Photoelektronen und Ionisation durch magnetosphärische Elektronen [Keller *et al.*, 1992]. Die beiden ersten Quellen kommen aus Richtung der Sonne und sind deshalb auf der Nachtseite nicht vorhanden.

Für die Berechnung der Photoionisationsrate benutzen wir das Strahlungsmodell von Richards *et al.* [1994], das die solare EUV Strahlung in 37 Wellenlängenbereiche unterteilt, die getrennt voneinander mit einem Proxi für die Sonnenaktivität skaliert werden. Die Strahlung wird entlang der Sonnen-Titan Linie durch die Neutralatmosphäre absorbiert und ionisiert

dabei die Atmosphäre. So erhalten wir eine dreidimensionale Verteilung von Photoionisationsraten. Der Effekt der Photoelektronen wird effektiv berücksichtigt.

Die größte Herausforderung für unser Modell bestand darin, die Ionisation der magnetosphärischen Elektronen zu berechnen. Die Elektronen gyrieren um die magnetischen Feldlinien, sind damit an das Magnetfeld gebunden, können sich aber entlang des Magnetfeldes frei bewegen und damit Energie entlang des Magnetfeldes verteilen. Um dem gerecht zu werden, haben wir ein Flussröhrenmodell entwickelt, das es erlaubt, die Bewegung der Elektronen mit dem Magnetfeld und die Wärmeleitung der Elektronen entlang des Magnetfeldes zu simulieren und dadurch die Ionisationsrate durch Stöße mit magnetosphärischen Elektronen zu berechnen. Die Bewegung der Flussröhren ist dabei ein wichtiger Parameter, der in keinem Modell für die Elektronen bei Titan bisher berücksichtigt wird. Unser Modell ist nach unserem Wissen das erste, das in der Lage ist, dreidimensionale Stoßionisationsraten bei Titan zu berechnen.

Wir haben unser Modell auf drei verschiedene Bedingungen (Winkel, Anströmrichtung, Sonnenrichtung) angewandt, die den erwarteten Situationen während der Cassini Vorbeiflüge TA, T5 und T34 an Titan entsprechen. TA ist ausgewählt worden, weil es mit einem Abstand von 1200 km der erste nahe Vorbeiflug an Titan ist und damit die erste Gelegenheit bietet, Modellergebnisse mit realen Daten zu vergleichen. Bei T5 strömt das Plasma ungefähr die Nachtseite und bei T34 ungefähr die Tagseite an - das sind die beiden Situationen, in denen die Anströmionosphäre am unterschiedlichsten ist.

Die Ergebnisse umfassen zwei Bereiche: die Ionosphäre und die globale elektromagnetische Wechselwirkung. Im Ionosphären teil haben wir die Ionisationsraten und die resultierenden Ionosphären dichten mit anderen Modellergebnissen verglichen. Die Übereinstimmung mit den Ergebnissen des eindimensionalen Modells von *Keller et al.* [1992] sind sehr gut, obwohl unser Modell sehr vereinfacht ist im Vergleich zum Modell von *Keller et al.* [1992], das viele Ionen- und Neutralgasspezies und deren chemische Reaktionen beinhaltet. Allerdings zeigt sich, dass die Plasmadichten in der oberen Atmosphäre von unserem Modell niedriger sind als die im Wechselwirkungsmodell von *Keller et al.* [1994b]. Das liegt am anströmenden Plasma, welches das obere Ionosphärenplasma wegspült [*Ip*, 1990].

Der Vergleich der Stoßionisationsraten mit dem 1D Modell von *Gan et al.* [1992] auf der angeströmten Nachtseite zeigt auch sehr gute Übereinstimmungen. Auf der Tagseite sind unsere Ergebnisse sehr unterschiedlich: In unserem Modell werden die magnetosphärischen Elektronen zusammen mit dem Magnetfeld von der Photoionosphäre daran gehindert, in die Atmosphäre einzudringen und dort zu ionisieren. Die Berücksichtigung der Flussröhrendynamik ist ein großer Vorteil unseres Modells gegenüber anderen. In der Ionosphäre in unserem Modell ist die Plasmadichte am Ionosphärenpeak auf der Nachtseite etwa eine Größenordnung niedriger als auf der Tagseite. Die Peakionosphären dichten in der Morgen- und Abendatmosphäre stimmen mit den aus den Voyager 1 Messungen abgeleiteten überein [*Bird et al.*, 1997].

Die Plasmawechselwirkung führt dazu, dass der obere Teil der Ionosphäre magnetisiert und der untere fast magnetfeldfrei ist. Die Grenzschicht zwischen beiden Regionen bezeichnen wir als magnetische Ionopause. Wir diskutieren die Abhängigkeit der Lage der magnetischen

Ionopause von der Lokalzeit und der Lage bezüglich des anströmenden Plasmas. Die Höhe variiert zwischen 500 und 1200 km und ist maximal auf der Tagseite und minimal auf der angeströmten Nachtseite.

Beim Übergang vom magnetosphärischen Plasma zum Ionosphärenplasma zeigt das Druckprofil einen charakteristischen Verlauf. Das Magnetosphärenplasma ist dominiert vom thermischen Druck, in der magnetischen Barriere dominiert der magnetische Druck, und der Reibungsdruck (eigentlich die Reibungskraft) balanciert den magnetischen Druck in der magnetischen Ionopause. Wir zeigen, dass Plasmadivergenz entlang vom Magnetfeld verantwortlich ist für die Magnetfelderhöhung in der magnetischen Barriere und nur zu einem kleinen Teil die Reibung mit dem Neutralgas.

Wir zeigen, dass sich der magnetische Druck am Peak der magnetischen Barriere in der Äquatorebene durch eine Cosinusquadrat-Funktion des Winkels zur Anströmachse beschreiben lässt. Danach ist der magnetische Druck beim Winkel Null nahezu gleich dem Gesamtdruck des anströmenden Plasmas. Zu den Flanken hin bleibt ein Viertel konstant und Dreiviertel variieren mit dem Cosinusquadrat des Winkels. Entlang einer Magnetfeldlinie durch die magnetische Barriere nimmt die magnetische Feldstärke linear mit zunehmendem Abstand zur Äquatorebene ab. Aus unseren Modellergebnissen leiten wir eine empirische Funktion für die magnetische Feldstärke im Barrierenpeak auf der Anströmseite ab.

Im Ergebnisteil, der die globale Wechselwirkung beschreibt, zeigen wir, dass sich die globale Plasmawechselwirkung durch die drei MHD Wellen beschreiben lässt. Bei einem subsonischen super-Alfvénischen Plasma breitet sich die schnelle Welle in alle Richtungen (auch stromaufwärts) aus, und langsame und Alfvénwellen propagieren entlang der Alfvéncharakteristiken. Es zeigt sich, dass es sinnvoll ist, die Plasmawechselwirkung in drei Bereiche einzuteilen: Erstens den Hauptwechselwirkungsbereich, der dadurch definiert ist, dass außerhalb davon der Einfluss des Neutralgases auf das Plasma vernachlässigbar ist und deshalb die idealen MHD-Gleichungen gelten. Die Größe dieses Bereiches ist ein Maß für die Größe des Hindernisses, das Titan für das anströmende Plasma darstellt. Wir berechnen den Radius der Region zu 2,3 Titanradien. Den zweiten Bereich stellt der durch Alfvén und langsame MHD-Welle geprägte Bereich dar, in dem das Magnetfeld einen bestimmten Winkel zum Hintergrundfeld einnimmt. Die Geschwindigkeit in diesem Bereich ist auf wenige Prozent der Geschwindigkeit des anströmenden Plasmas reduziert. Der dritte Bereich ist die Region im nahen Schweif, in der sich nördlicher und südlicher Alfvénflügel überlagern. Dieser Bereich begrenzt den Bereich, durch den das massebeladene Plasma strömt und in dem die Plasmageschwindigkeit reduziert ist.

Wir zeigen, dass sich die Geschwindigkeits- und Magnetfeldprofile in Anströmrichtung und außerhalb der Hauptwechselwirkungsregion durch das Abklingen der Amplitude der schnellen MHD-Welle im bewegten Plasma beschreiben lässt. Das Plasma, das das Haupthindernis und die Alfvénflügel umströmt, fließt unmittelbar hinter dem Überlagerungsbereich der Alfvénflügel zusammen und sorgt dort für eine Magnetfelderhöhung. Wir interpretieren die Erhöhung als ähnlichen Mechanismus, der auch zur Erhöhung des Magnetfeldes in der magnetischen Barriere führt.

Titan dient für die Saturnmagnetosphäre auch als Plasmaquelle [Eviatar et al., 1982]. Wir

erhalten eine Verlustrate von 30 g/s. Das Plasma im Schweif ist nahe bei Titan auf die Äquatorebene konzentriert. Weiter hinten im Schweif verteilt sich das Plasma entlang des Magnetfeldes, beschleunigt durch einen magnetischen Druckgradienten parallel zu  $\vec{B}$ . Senkrecht zu  $\vec{B}$  wird der Druckgradient balanciert durch einen Gradienten im dynamischen Druck.

Wir interpretieren das elektrische Stromsystem, das die Wechselwirkung im Plasma erzeugt, indem wir die Ströme in den drei Bereichen diskutieren. Die Ströme in den Alfvénflügeln lassen sich in einen Anteil parallel und einen Anteil senkrecht zur Alfvéncharakteristik unterteilen. Die Berechnung der Divergenz aus den Modellergebnissen zeigt, dass beide Ströme im näheren Umfeld von Titan getrennt von einander Divergenz gleich Null erfüllen, wie es bei den idealen Alfvénflügeln im sub-Alfvénischen Plasma der Fall ist [Neubauer, 1980]. Die Ströme in der Hauptwechselwirkungsregion lassen sich in einen diamagnetischen, einen Trägheits- und einen atmosphärischen Anteil aufspalten. Den oberen Rand der magnetischen Barriere bilden diamagnetische Ströme und im unteren Rand, der magnetischen Ionopause, fließen atmosphärische Ströme. Trägheitsströme sind eng mit der Massebeladung verknüpft und beschleunigen das neu aufgenommene Plasma. Wir diskutieren, wie sich die Ströme durch den Überlagerungsbereich der Alfvénflügel fortsetzen.

Am Ende der Arbeit werden die Ergebnisse des TA Modells entlang der Vorbeiflugstrajektorie von Cassini detailliert analysiert. Cassini fliegt durch die nördliche Schweifregion und wird dabei in die Ionosphäre eintauchen und nach unseren Modellvorhersagen zweimal die magnetische Ionopause durchqueren. Das Magnetometerexperiment an Bord von Cassini wird die magnetische Ionopausendurchgänge als Änderungen der Magnetfeldstärke um den Faktor drei innerhalb von zwei Minuten wahrnehmen.

Doch selbst wenn die Daten, die Cassini bei Titan messen wird, wesentlich von den Ergebnissen unseres Modells abweichen - und dieser Fall ist der wahrscheinlichste -, so behandelt unser Modell doch auch grundsätzliche Fragen im Hinblick auf eine super-Alfvénische Wechselwirkung, und der Vergleich der gemessenen Daten mit den modellierten wird in jedem Fall neue Erkenntnisse bringen.



---

# Contents

---

<b>1</b>	<b>Introduction</b>	<b>1</b>
<b>2</b>	<b>Titan in the pre-Cassini era</b>	<b>5</b>
2.1	Titan . . . . .	5
2.2	Titan at the Voyager 1 encounter . . . . .	7
2.3	Comparison of Venus and Titan . . . . .	11
2.4	Comparison with the plasma interaction of comets . . . . .	15
<b>3</b>	<b>Posing the problem</b>	<b>17</b>
<b>4</b>	<b>Model description</b>	<b>21</b>
4.1	MHD model . . . . .	21
4.2	Model of the neutral atmosphere . . . . .	28
4.3	Solar radiation model . . . . .	29
4.4	Flux tube model . . . . .	31
4.4.1	Geometry of the flux tube model . . . . .	31
4.4.2	Continuity equation of magnetospheric electrons . . . . .	33
4.4.3	Temperature equation of magnetospheric electrons . . . . .	33
4.4.3.1	Adiabatic heating and elastic energy transfer . . . . .	35
4.4.3.2	Inelastic cooling and impact ionization rates . . . . .	35

4.4.3.3	Heat conduction . . . . .	36
4.4.4	The flux tube model and energy conservation . . . . .	37
4.4.5	Other sources for ionization . . . . .	38
4.5	Model summary and initial conditions . . . . .	39
<b>5</b>	<b>Results</b>	<b>43</b>
5.1	Model situations . . . . .	43
5.1.1	TA . . . . .	44
5.1.2	T5 . . . . .	45
5.1.3	T34 . . . . .	46
5.2	Ionosphere . . . . .	46
5.2.1	Plasma production rates . . . . .	47
5.2.2	Ionospheric plasma temperature . . . . .	55
5.2.3	Pressure profiles along the ram direction . . . . .	59
5.2.4	Magnetization of the ionosphere . . . . .	62
5.2.5	Layers and plasma regions . . . . .	73
5.3	Collision frequencies and magnetic diffusion . . . . .	84
5.4	Magnetic pile-up . . . . .	88
5.5	Global plasma interaction . . . . .	91
5.5.1	Electric currents . . . . .	91
5.5.1.1	Currents in the sub-Alfvénic case . . . . .	91
5.5.1.2	The super-Alfvénic interaction . . . . .	93
5.5.1.3	Currents in the Alfvén tube . . . . .	95
5.5.1.4	Currents in the primary interaction region . . . . .	99
5.5.1.5	Currents in the nominal intersection region . . . . .	103
5.5.1.6	Summary of current system . . . . .	106
5.5.1.7	Typical values for currents at Titan . . . . .	106
5.5.2	Global plasma flow and magnetic field geometry . . . . .	107
5.5.2.1	Upstream magnetic field and velocity profile . . . . .	107
5.5.2.2	Magnetic field and velocity profile at the flanks . . . . .	112
5.5.2.3	Plasma flow around the Alfvén tubes . . . . .	114

---

5.5.2.4	Tail region . . . . .	114
5.5.2.5	Summary of plasma flow and magnetic field . . . . .	116
5.5.3	Plasma pick-up . . . . .	119
5.5.4	Temperature of magnetospheric electrons . . . . .	132
5.6	Comparison with other models . . . . .	139
5.7	The first close flyby of Cassini at Titan - TA . . . . .	145
<b>6</b>	<b>Summary</b>	<b>155</b>
<b>A</b>	<b>Calculations</b>	<b>159</b>
A.1	Decay of fast mode . . . . .	159
A.2	The thermal conductivity of supra-thermal electrons . . . . .	160
	<b>Bibliography</b>	<b>165</b>



---

## INTRODUCTION

---

On the 15th of October in 1997 the Cassini space craft has been launched to start its nearly seven years lasting journey to the Saturnian system. The major science objectives of the space mission are Saturn with its rings, *Titan*, the icy satellites, and the Saturnian magnetosphere (listed in that order on the official Cassini web page). With its dense neutral atmosphere Titan is a unique object in the solar system. In more than forty close flybys Cassini will make a special effort to explore that interesting physical system. Apart from many state-of-the-art physical instruments Cassini also carries the Huygens probe which will descend through Titan's nitrogen atmosphere, driven only by its gravitation, and collect a lot of atmospheric and - if it survives the landing procedure - surface data.

From the point of view of plasma physics Titan is also very special. It represents the class of non-magnetic body with substantial atmosphere interacting with a streaming magnetized plasma like Venus, Mars, or comets. But Titan is unique with respect to its plasma interaction in several issues: (1) It interacts with the Saturnian magnetospheric plasma which was found to be sub-sonic and super-Alfvénic during the Voyager 1 encounter, plasma properties which have so far not been encountered anywhere else in the solar system. (2) The upstream side of Titan depends on the Saturnian local time at Titan, i.e. the upstream side can be dayside, nightside, or in-between. At objects that interact with the solar wind, the plasma always streams towards the dayside. (3) During times of high solar wind pressure the magnetopause layer of Saturn's magnetosphere is pushed towards Saturn, and Titan can be outside of the magnetosphere and interact with the magnetosheath plasma or even with the pre-shock solar wind [Wolf and Neubauer, 1982; Schardt *et al.*, 1984]. Thus, Titan's plasma interaction can have many faces.

Motivated by the Cassini Mission that would provide us a unique chance to explore the interesting plasma environment of Titan, we started at the beginning of 2000 - Cassini had just reached the astroid belt - to develop a model for Titan's plasma interaction with the magneto-

spheric plasma in preparation for Cassini's arrival. The first step was to choose an appropriate method. Titan's plasma interaction is very complex and involves many scales and there is no method that is able to cover the whole interaction process. Although it is known, since the Voyager 1 encounter in 1980, that the gyroradius of ions in the incident magnetospheric plasma is of the order of Titan's radius, we decided to use a fluid (magnetohydrodynamic (MHD)) approach for our model. Other methods that can account for single particle effects like hybrid or kinetic models are not able to account for the influence of a neutral gas on the plasma. Moreover, a fluid approach only accounts for the lowest frequencies in the plasma and cuts off processes like the Hall effect for example.

However, despite the constraints of MHD models we have chosen this approach basically because of three reasons. (1) There is no approach that is able to combine all the processes that are involved in the interaction. (2) The plasma interaction problem is a 3D problem and the 2D and 1D approximations cut-off important details. MHD models in 3D can be run with a sufficient high spatial grid resolution. (3) The dense extended neutral atmosphere of Titan plays a principal role in the plasma interaction.

The kernel of our model consists of ZEUS 3D [Stone and Norman, 1992a] - an ideal time-dependent single-fluid MHD code. We have extended the equations in order to account for the influence of the neutral atmosphere on the plasma. The consistent treatment of the neutral gas affects all equations. The neutral atmosphere in our model consists of methane and molecular nitrogen which are known to be the major constituents of the atmosphere.

An important participant in the plasma interaction is the ionosphere which is created from the neutral atmosphere by basically three processes: photoionization, ionization by photoelectrons, and ionization by magnetospheric electrons. A detailed 3D solar radiation model is applied to the neutral atmosphere to obtain a 3D photo-ionosphere. Ionization due to photoelectrons is included effectively. The first two processes originate from the Sun and are therefore absent on Titan's nightside. Impact ionization by magnetospheric electrons is a quite complex process since it involves the energy of the magnetospheric electrons and the geometry of the magnetic field. Therefore this production rate depends on the plasma interaction and the plasma interaction depends on the ionospheric properties i.e. the production rate. We have developed a flux tube model that calculates the time-dependent ionization rates from magnetospheric electrons and the electron heat conduction along the magnetic field lines within the MHD model.

This is so far the only model that consistently includes the neutral gas effect on the plasma and produces a realistic 3D ionosphere within the model. Thereby it is able to produce features like a magnetic ionopause, a layer that separates the upper magnetized from the lower unmagnetized ionosphere. Additionally, the local time dependence of the interaction can be observed. The results presented here are from the application of our model to three different situations corresponding to the Cassini flybys TA, T5, and T34 at Titan.

In the meantime Cassini has reached the Saturnian system. The Saturn orbit insertion was successful and the first close Titan flyby with a closest approach altitude of 1200 km is near. Time to complete this work and await the first data from the Cassini magnetometer experiment (MAG) to (hopefully!) validate our results.

We have organized this work in the following way: In the following Chapter the characteristics of Titan especially with respect to the plasma interaction are briefly summarized. A discussion of the Voyager 1 results makes the major part of the Chapter. Moreover, Titan is compared to Venus and its plasma interaction. In Chapter 3 we concretize the situation that should be mapped by our model. The model itself is introduced in Chapter 4. We explain how the main building-blocks of the plasma interaction are represented in our model. After the description of the three model cases (TA, T5, and T34), the results Chapter (Chapter 5) consists basically of two major parts: an ionospheric part and a global plasma interaction part. In the ionospheric part the production rates and ionospheric densities are shown. The pressure profiles along the ram direction are discussed. The ionosphere is divided into different regions with certain plasma conditions. The dependence of these regions on Saturnian local time and distance from the sub-ram point is examined. The Section about collision frequencies and magnetic diffusion which actually belongs to the ionosphere is presented in a new Section because it contains fundamental information. It is followed by a short Section about the magnetic pile-up. In this rather theoretical Section we distinguish between two different processes that can lead to magnetic pile-up. The global plasma interaction is presented in terms of the created electric current system and in terms of the plasma flow and the magnetic field geometry that is set up by the interaction. Additionally, we discuss plasma pick-up and the temperature of the magnetospheric electrons.

In Section 5.6 we discuss other models of the plasma interaction of Titan and compare some of our results with them (if possible). At the end of the results Chapter we present the results from our simulation along the Cassini trajectory at TA. We discuss in detail the different regions Cassini will pass during its first close Titan flyby.



---

## TITAN IN THE PRE-CASSINI ERA

---

### 2.1 Titan

Titan, the largest Saturnian satellite and after Jupiter's satellite Ganymede the second largest satellite in the solar system, was discovered in 1655 by the Dutch astronomer Christiaan Huygens. It took more than 200 years until *Comas Sola* [1908] visually observed a limb darkening, the first report of Titan's atmosphere. In 1944 Gerald Kuiper observed spectral signatures implying the existence of methane at Titan which proved the presence of an atmosphere [Kuiper, 1944]. The origin of the atmosphere is not known until today [Owen, 1982]. The existence of an atmosphere caused a lot of scientists to draw their attention to Titan.

The milestone in Titan science and the source for nearly all that is known about Titan today were the Voyager missions launched in 1977. Especially, the close Titan flyby of Voyager 1 in 1980 with a closest approach altitude of 4394 km to the surface provided scientists with a huge amount of scientific information. Table 2.1 shows the main characteristics of Titan in comparison to the Earth's. Its dense nitrogen atmosphere is similar to the Earth's but much colder (94 K) with a surface pressure of 1.5 bar. This makes Titan a useful object to study the development of the Earth's atmosphere before oxygen became abundant. For atmospheric scientists Titan is in any way interesting. Nitrogen, hydrogen, and carbon react with each other in various chemical reactions creating a "zoo" of chemical compounds. That is why Titan's atmosphere is sometimes called a chemical factory. The distance of Titan to the Sun is about 10 times larger than the Earth's distance which implies that the solar radiation which drives a lot of processes is 100 times less intense at Titan than at Earth.

The camera on board of Voyager 2 showed Titan enveloped by a dense aerosol layer preventing the observer from catching a glimpse of the surface. Therefore, surface structures were

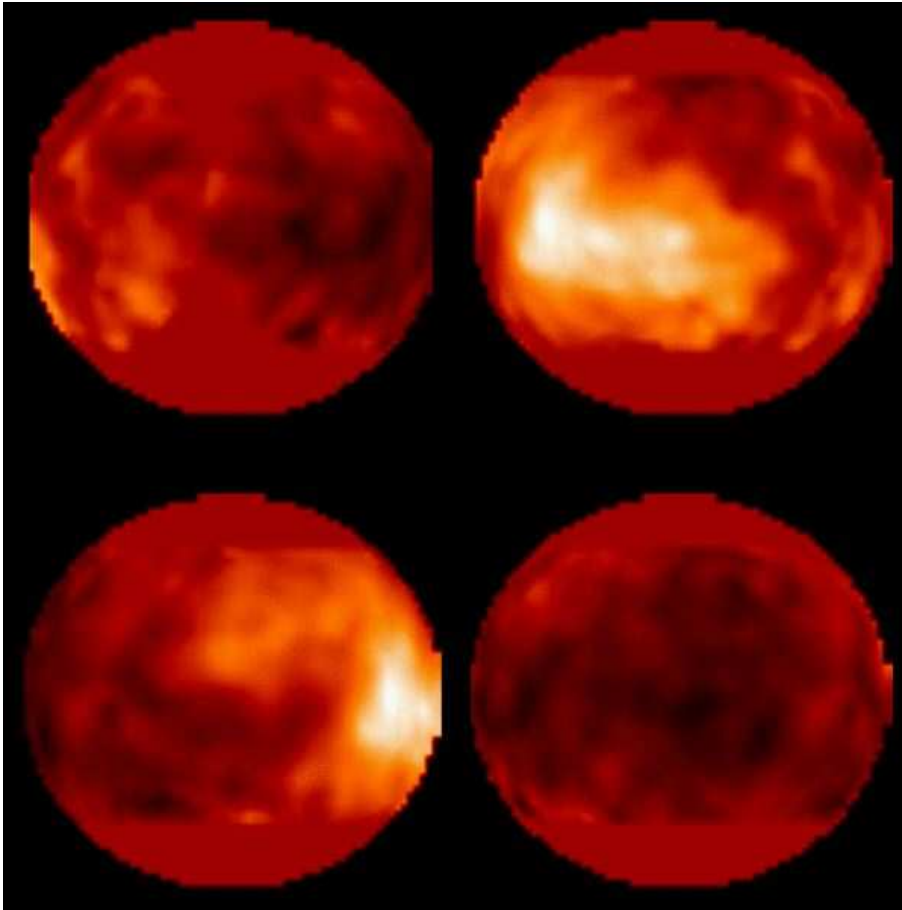


**Figure 2.1:** First image of the surface of Titan in the near infrared taken with HST [Smith *et al.*, 1996] during one Titan day. Shown are the Saturnian flank (upper left) the leading hemisphere (upper right), the anti-Saturnian flank (lower left), and the trailing hemisphere (lower right) with respect to Titan's orbital motion.

invisible until recently. There were speculations about a global  $\sim 1$  km deep ethane ocean covering Titan [Lunine *et al.*, 1983]. In 1994 the Hubble Space Telescope succeeded for the first time in taking pictures from the surface in the near infrared [Smith *et al.*, 1996]. The observational campaign took 1 Titan day (16 Earth days) and shows surface structures all around the satellite except for the poles where the optical depth is too high (see Figure 2.1). Although it is not clear up to now what surface features cause the structures that are recognizable in the pictures, the existence of a global ocean was disproved.

Since the Hubble observation there have been several observational campaigns from telescopes on Earth that have become possible due to the development of techniques like adaptive optics or speckle imaging. In speckle images from the Keck telescope the surface of Titan was visible as light and dark (low reflectivity) areas. The dark regions could possibly correspond to a liquid ethane oceans Gibbard *et al.* [1999]. Another highlight was the detection of methane clouds with the Keck telescope and with the Gemini telescope [Brown *et al.*, 2002; Roe *et al.*, 2002].

Returning to the subject of this work, the interaction of Titan with the surrounding Saturnian magnetospheric plasma, brings us back in time to the days of Voyager, i.e. to the 1980's. Up

	Titan	Earth
Radius	2575 km	6378 km
Mean orbital radius	$1.23 \times 10^6 \text{ km} = 20.3R_S$	
Surface gravitation	$1.35 \text{ ms}^{-2}$	$9.81 \text{ ms}^{-2}$
Surface pressure	1.5 bar	1 bar
Neutral atmosphere	$> 97\% \text{ N}_2$	$> 78\% \text{ N}_2$
Mean surface temperature	94 K	288 K
Rotational period	15.95 days	1 day
Orbital period	15.95 days	
Seasonal period	29.46 years	1 year
Distance from Sun	9.45 AU	1 AU

**Table 2.1:** Titan characteristics after Voyager 1 encounter.

to now, i.e. in the pre-Cassini era, Voyager 1 provided the only in-situ measurements at Titan.

## 2.2 Titan at the Voyager 1 encounter

The up-to-date (pre Cassini/Huygens) knowledge about Titan and its plasma environment is based on the close encounter of Voyager 1 on 12 November 1980. The flyby geometry is shown in Figure 2.2. It was a flyby through the wake of Titan with respect to the streaming plasma with a closest approach altitude of 4394 km ( $=1.7$  Titan radii ( $R_T$ )). The encounter occurred during a time of nearly solar maximum activity at equinox conditions and at 13:30 Saturnian local time (SLT, for definition see Figure 5.1). The plasma flow around Titan was determined by several in-situ measurements performed by the magnetometer, plasma science, plasma wave, planetary radio astronomy, and low energy charged particles experiments, and by the remote ultraviolet spectrometer experiment. The observed signatures of Titan's interaction with the Saturnian magnetospheric plasma are summarized in *Neubauer et al.* [1984].

One of the questions that could be answered for the most part from the Voyager data and that is essential for the plasma interaction is the question of an internal magnetic field at Titan. *Neubauer* [1978] derived a maximum global magnetic field of  $\sim 100$  nT at Titan's equator from density and size of the satellite and from cosmochemical considerations that put constraints on the internal composition of Titan. From the information contained in the Voyager 1 data *Neubauer et al.* [1984] were able to improve the estimates about an internal magnetic field. They derived an upper bound of 4.1 nT at the equator. Since this is even lower than the Saturnian magnetic field at Titan's orbit ( $\sim 5$  nT) one can say that with respect to the plasma interaction Titan does not possess a noticeable internal magnetic field.

If an obstacle in a streaming plasma possesses a substantial magnetic field like for example the Earth in the solar wind, the real obstacle consists of the magnetic field. If no magnetic field is present the next candidate for the interaction with the streaming plasma is the upper atmosphere and especially the ionosphere. The next information Voyager 1 provided us with is the composition of the upper atmosphere. The ultraviolet spectrometer (UVS) on board

Magnetic field magnitude	5 nT
Direction	~ perpendicular to orbital plane
Mean plasma flow speed	120 kms <sup>-1</sup>
Proton number density	0.1cm <sup>-3</sup>
N <sub>+</sub> number density	0.2cm <sup>-3</sup>
Electron temperature	200 eV
Proton temperature	210 eV
N <sub>+</sub> temperature	2.9 keV
Electron number density	0.3cm <sup>-3</sup>
Mass density	2.9 amucm <sup>-3</sup>
Thermal pressure	1.1 × 10 <sup>-10</sup> Pa
Plasma beta $\beta = p/(B^2/(2\mu_0))$	11.1
Alfvén speed	64 kms <sup>-1</sup>
Sound speed ( $\gamma = 2$ )	210 kms <sup>-1</sup>
Fast magnetoacoustic speed	220 kms <sup>-1</sup>
Alfvén Mach number	1.9
Sonic Mach number	0.57
Fast Mach number	0.55

**Table 2.2:** Properties of the incident plasma during the Voyager 1 encounter taken from Neubauer *et al.* [1984].

performed a solar occultation experiment during the flyby which measured the differential absorption of sunlight as a function of altitude and wavelength in the atmosphere [Broadfoot *et al.*, 1981; Smith *et al.*, 1982]. One of the results of the analyses was that nitrogen (N<sub>2</sub>) is the most abundant species followed by methane. Lindal *et al.* [1983] derived a tropospheric volume mixing ratio of at least 97% for nitrogen. The temperature at an altitude of 3840 km at the terminators was extracted from the data by Smith *et al.* [1982] to be  $186 \pm 20$  K. Friedson and Yung [1984] have calculated diurnal exospheric temperature variations of  $\sim 30$  K. Since then various models for the neutral atmosphere have been developed [Hunten *et al.*, 1984; Yung *et al.*, 1984; Strobel, 1985; Atreya, 1986; Yung, 1987; Yelle *et al.*, 1997]. In this work we use model of Yung *et al.* [1984]; Yung [1987] that has been improved by Keller *et al.* [1992]. There are newer and improved atmospheric models of Titan [Toublanc *et al.*, 1995; Lara *et al.*, 1996; Yelle *et al.*, 1997]. But we have decided to use the model of Keller *et al.* [1992] to make a comparison with the ionospheric model of Keller *et al.* [1992] easier.

Voyager 1 also provided information about the ionosphere of Titan. Lindal *et al.* [1983] derived upper bounds for the ionospheric peak electron density of 3000 cm<sup>-3</sup> at the evening terminator and 5000 cm<sup>-3</sup> at the morning terminator from the occultation data. In a reanalysis of the data Bird *et al.* [1997] found a peak electron density of  $2400 \pm 1100$  cm<sup>-3</sup> at an altitude of  $1180 \pm 150$  km at the evening terminator.

The signatures of Titan's plasma interaction with the Saturnian magnetospheric plasma in the plasma data [Hartle *et al.*, 1982; Gurnett *et al.*, 1982] and in the magnetic field data [Ness *et al.*, 1982] showed interesting features. From a synthesis of the data [Neubauer *et al.*, 1984]

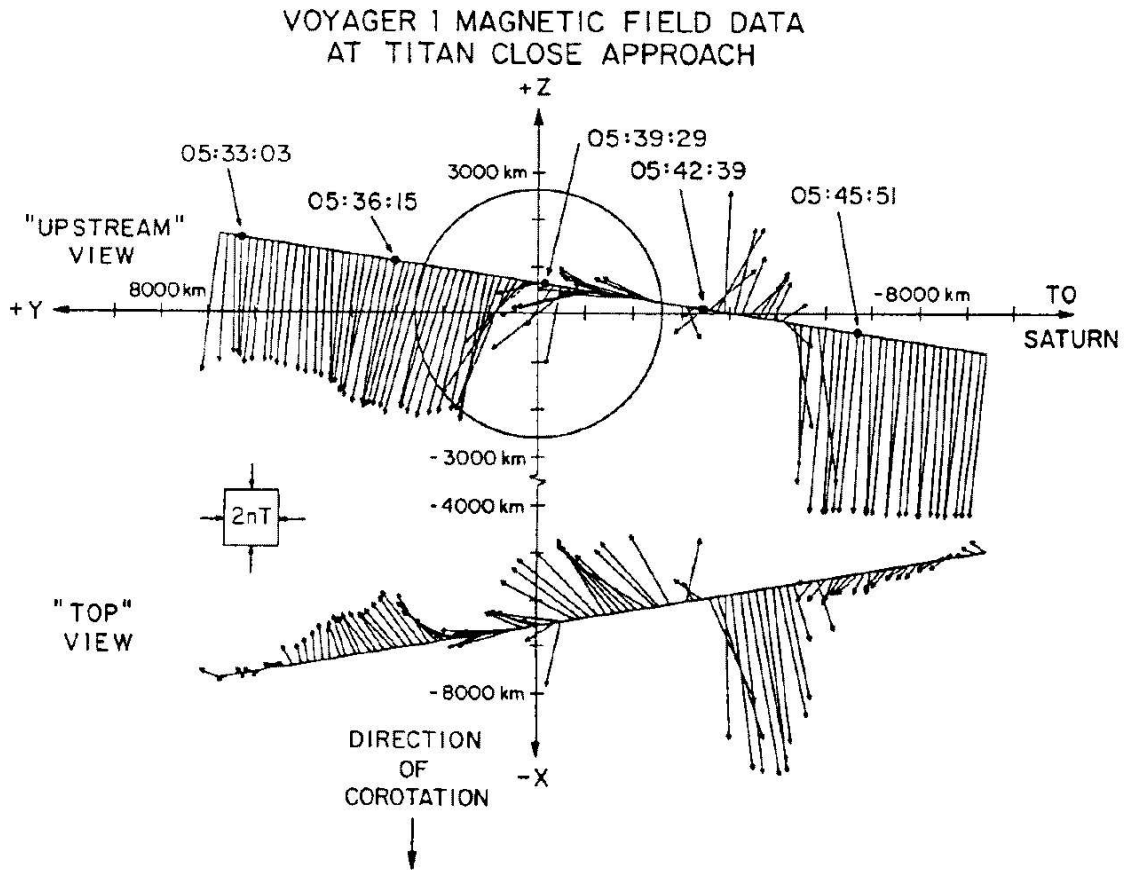


**Figure 2.2:** Projections of magnetic field vectors on  $yz$  and  $xz$  plane along the Voyager 1 flyby trajectory (taken from Ness et al. [1982]). Note that the coordinate system is different to that used in this work.

derived magnetic field and plasma properties of the incident plasma given in Table 2.2. Thereafter, the Alfvénic and sonic Mach numbers of the incident plasma during the time of the Voyager 1 encounter were  $M_A = 1.9$  and  $M_s = 0.57$ . As Neubauer et al. [1984] pointed out the combination of a super-Alfvénic and sub-sonic Mach number is so far unique compared to other observed plasma environments. They also mention that the Voyager 1 measurement is only a snapshot of the plasma properties. The magnetospheric plasma in the outer Saturnian magnetosphere is known to be highly variable [Wolf and Neubauer, 1982]. Since the Mach numbers are near 1 the plasma at Titan's orbit can be named trans-sonic and trans-Alfvénic. Fig. 2.2 shows the projection of the Voyager 1 flyby trajectory in two planes. Along the trajectory the magnetic field vectors measured by the magnetometer instrument on board are plotted. In the upper projection the observer looks towards the streaming plasma. The wake appears as a significant deviation of the magnetic field vectors from the  $-z$ -direction. The neutral sheet crossing becomes obvious in the second projection where the observer looks along the nominal magnetic field in  $-z$ -direction. Before crossing the neutral sheet the magnetic field vectors point towards Titan and afterwards they point away from the satellite which is consistent with the expected draping of magnetic field lines around the obstacle [Alfvén, 1957] except that the draping is somewhat stronger than expected for the derived upstream plasma conditions. The angular offset of the wake with respect to the nominal corotation

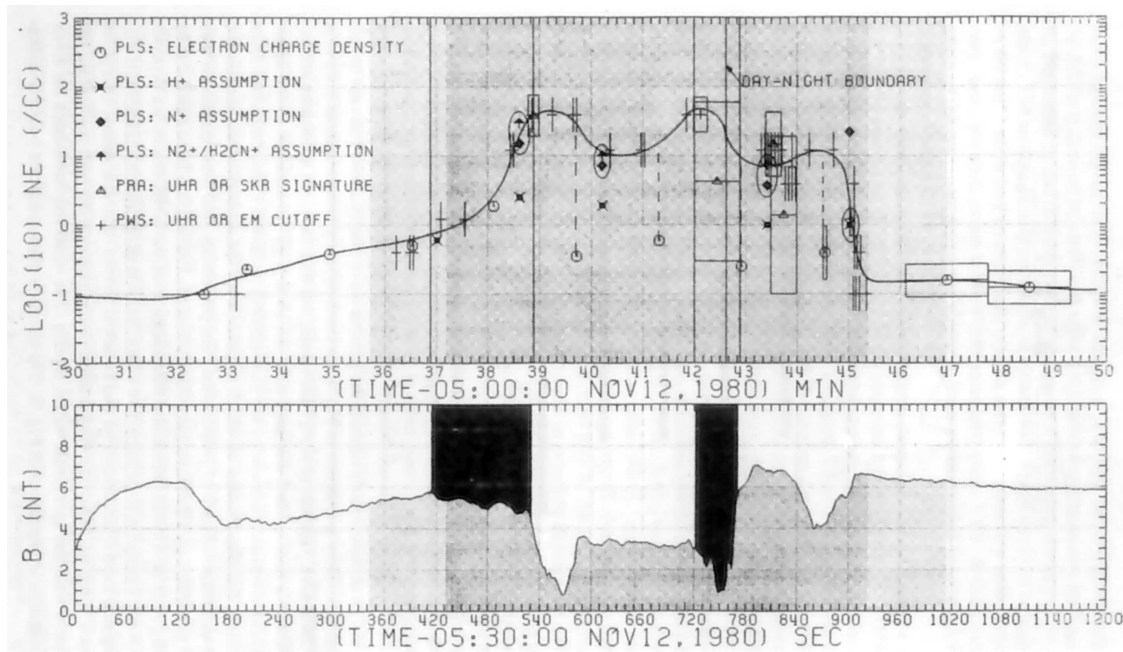


**Figure 2.3:** Electron and ion densities (top) and magnetic field magnitude along the Voyager 1 trajectory (taken from Neubauer *et al.* [1984]). Four tail lobe picture from Voyager 1 magnetic field observations (taken from Ness *et al.* [1982]).

direction (in  $-x$  direction in the coordinate system used by Ness *et al.* [1982]) is principally due to a deviation of the plasma flow direction from the corotational direction of  $20^\circ$  [Hartle *et al.*, 1982] which may be caused by a motion of the magnetopause during that time. From symmetry considerations in the magnetic field data Kivelson and Russel [1983] obtained a deviation of  $27^\circ$  from the nominal direction. The difference of the two angles may be caused by the plasma interaction.

In Figure 2.2 ion and electron number densities and the magnetic field magnitude is plotted along the trajectory. The enveloping electron density was derived from the plasma wave experiment. Thereafter, the maximum electron density in the wake is  $\sim 60 \text{ cm}^{-3}$ , two orders of magnitude higher than the background electron density. The electron density has three maxima which coincide with minima in the magnetic field magnitude. Along the inbound trajectory is a smooth gradient in the electron density while at the outbound wake boundary the density decreases to the background density with a steep gradient.

The asymmetry in the magnetic field magnitude has led Ness *et al.* [1982] to draw a four lobe picture of the tail. The enhanced magnetic field then corresponds to magnetic field lines that are connected with the nightside atmosphere of Titan. This interpretation implies that Voyager 1's crossing of the current sheet occurred simultaneous with the crossing of the day-night boundary (see Figure 2.2).

Summarized, the pre Cassini picture of Titan's interaction with the Saturnian magnetospheric plasma is the following: A non-magnetic body with a substantial atmosphere and ionosphere interacts with a trans-sonic and trans-Alfvénic plasma. The frozen-in Saturnian magnetic field drapes around the obstacle. But the basic interaction will be determined by the com-

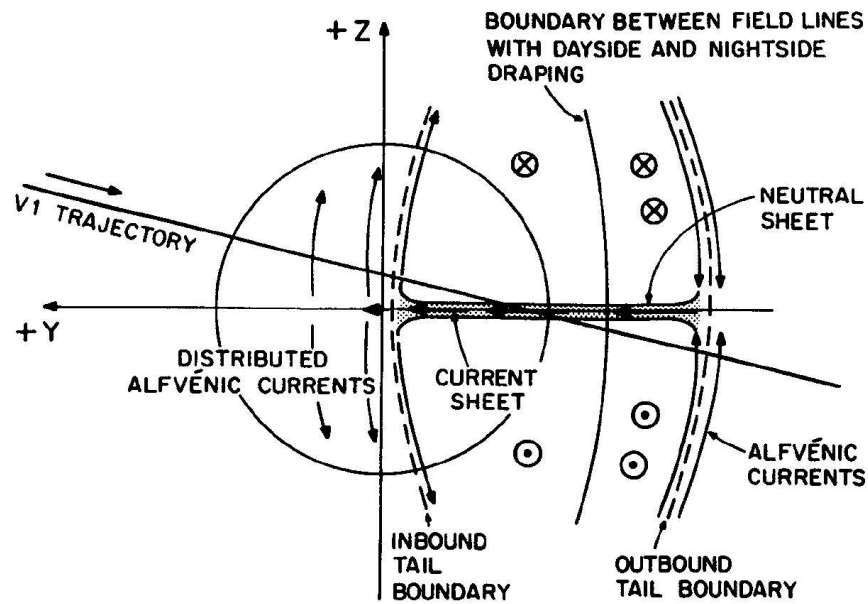


**Figure 2.4:** Four tail lobe picture from Voyager 1 magnetic field observations (taken from Ness et al. [1982]).

plicated system formed by the solid body, the neutral atmosphere and ionosphere, and the magnetospheric plasma which is not yet fully understood. The Cassini/Huygens mission will bring light into that peculiar system that Voyager only allowed us to catch a glimpse of and will be a further milestone in the exploration of Titan.

## 2.3 Comparison of Venus and Titan

As Titan, Venus represents a non-magnetic body placed in a streaming magnetized plasma which is in the case of Venus the solar wind. Since the early 1960s many space missions starting with Mariner 2 have encountered Venus and made a lot of measurements. Especially the Pioneer Venus Orbiter that orbited Venus beginning in 1978 for more than a decade provided scientists with a huge amount of data and is responsible for today's understanding of this system. In this section the main characteristics of Venus' interaction with the solar wind are summarized and compared with the situation at Titan.

Table 2.3 shows the main characteristics of Venus in comparison to Titan. A remarkable difference between Titan and Venus is the atmospheric extension compared to the radius of the solid body. A good measure for the atmospheric extension is the altitude of the exobase. At Titan the altitude of the exobase is 60% of the satellite's radius, at Venus it's only a few percent. The exobase serves as a good measure for the obstacle size for the plasma. Thus, the obstacle that Titan represents for the streaming plasma is significantly larger than the solid body.

The electron density at the ionospheric peak at Venus is about two orders of magnitude higher than at Titan [Brace et al., 1983] due to the smaller distance to the Sun and the higher in-

	Venus	Titan
Radius	6052 km	2575 km
Surface gravitation	8.87 ms <sup>2</sup>	1.35 ms <sup>2</sup>
Surface pressure	90 bar	1.5 bar
Mean surface temperature	735 K	94 K
Ionospheric peak altitude	~ 140 km	~ 1100 km
Ionospheric peak density $n_e$	~ 10 <sup>5</sup> cm <sup>-3</sup>	~ 5 × 10 <sup>3</sup> cm <sup>-3</sup>
Neutral density at ionospheric peak	~ 10 <sup>8</sup> cm <sup>-3</sup>	~ 10 <sup>9</sup> cm <sup>-3</sup>
Neutral atmosphere	CO <sub>2</sub> (95%)	N <sub>2</sub> (> 97%)
Exobase altitude	180 km (= 0.03 $R_V$ )	1600 km (= 0.6 $R_T$ )
Distance from Sun	0.72 AU	9.45 AU

**Table 2.3:** Characteristics of Venus and Titan.

tensity of EUV radiation as the main source of ionization while the neutral gas density at the ionospheric peak is even higher at Titan than at Venus [von Zahn *et al.*, 1983] (see Table 2.3).

Table 2.4 compares typical properties of the solar wind plasma measured at Venus with the plasma at Titan during the Voyager 1 encounter. At Venus the solar wind is super-sonic and super-Alfvénic which leads to the formation of a bow-shock in front of the obstacle. At Titan the magnetospheric plasma is sub-sonic and no bow shock is apparent. Apart from that, the upstream plasma at Venus is dominated by the dynamic pressure  $\rho v^2$  while the magnetospheric plasma at Titan is dominated by the thermal pressure.

Additionally to the solar wind plasma at Venus typical properties of the postshock plasma are given in Table 2.4. The shock transition changes the upstream plasma parameters in such a way that the properties of the post-shock solar wind plasma come very close to the properties of the incident plasma at Titan. The shocked plasma is sub-sonic and sub-Alfvénic, but both Mach numbers are close to 1. The dominant pressure is the thermal pressure and the plasma  $\beta$  is clearly above 1 as at Titan. The plasma parameter that effectively determine the interaction are those of the postshock plasma rather than those of the preshock plasma. Thus, the incident plasma is basically very similar at Titan and at Venus.

Although in principal the bow shock changes the solar plasma parameters to become similar to the magnetospheric plasma at Titan, the gyroradius of a newly created ion is reduced by more than one order of magnitude and thereby becomes different from that parameter at Titan. A new ion created from a neutral atom which is slow compared to the plasma bulk velocity, moves in the plasma rest frame with the plasma bulk velocity. In the solar wind this leads to a gyro motion with a radius of the scale of the planet's radius ( $r_g = mv/eB \approx 6000$  km). The increase of the magnetic field magnitude and the decrease of the plasma bulk velocity lead to the reduction of the gyroradius. Hence, at Venus the effect due to the finite gyroradius of the ions is low while at Titan it will be noticeable.

As the shocked plasma approaches the obstacle, the thermal pressure is converted into magnetic pressure in the so-called magnetic pile-up region or magnetic barrier and there is a transition from a high- $\beta$  to a low- $\beta$  plasma [Russell and Hoppe, 1983]. At the boundary be-

	SW at Venus	post-shock SW at V.	Titan
Velocity	400 kms <sup>-1</sup>	100 kms <sup>-1</sup>	120 kms <sup>-1</sup>
Density	18 cm <sup>-3</sup>	72 cm <sup>-3</sup>	0.1 cm <sup>-3</sup>
Magnetic field	11 nT	44 nT	5 nT
Average angle of $\vec{B}$ and $\vec{v}$	40°	-	90°
Dynamic pressure $\rho v^2$	$5 \times 10^{-9}$ Pa	$10^{-9}$ Pa	$10^{-11}$ Pa
Thermal pressure	$7 \times 10^{-11}$ Pa	$4 \times 10^{-9}$ Pa	$10^{-10}$ Pa
Sonic Mach number $M_s$	6.6	0.45	0.7
Alfvénic Mach number $M_A$	6.1	0.9	1.2
Fast magnetosonic Mach number	4.7	0.4	0.6
Plasma $\beta$	1.5	5	10
Gyroradius of new ion	6040 km = $1.0R_V$	380 km = $0.06R_V$	3500 km = $1.4R_T$

**Table 2.4:** Comparison of plasma properties at Venus and at Titan. For the calculation of the gyroradius  $O^+$  has been used at Venus and  $O^+$  and  $N^+$  at Titan.

tween the shocked solar wind plasma and the ionosphere nearly all of the pressure has been converted into magnetic pressure. The processes that cause the pressure conversion are discussed in Section 5.4. The region between the ionosphere and the bow shock is sometimes called magnetosheath in analogy to the region behind the bow shock at the interaction of the solar wind with a magnetic body (like at Earth). Sometimes this region is called ionosheath in order to emphasize that the obstacle consists of an ionosphere and not a magnetosphere and that the boundary layer is the ionopause and not the magnetopause.

The interaction of the solar wind with Venus strongly depends on the incident solar wind dynamic pressure. The ionosphere of Venus was found to have basically two states [Luhmann *et al.*, 1980]: a magnetized state and an unmagnetized state. The unmagnetized state corresponds to low solar wind dynamic pressure. The thermal ionospheric plasma pressure in that case balances the solar wind pressure (which has been transformed into magnetic pressure in the magnetic barrier) and a thin ionopause layer forms. Inside of this layer the electron density drops by two orders of magnitude at the same time magnetic field increases with altitude. Apart from small scale magnetic structures the ionosphere is free of magnetic field. The shielding is achieved by electric currents flowing inside of the magnetic ionopause.

When solar wind pressure is high the ionosphere is in a magnetized state. The ionopause layer is broader and at lower altitudes. The maximum thermal pressure of the ionosphere is not sufficient to balance the solar wind pressure. The magnetic field is pushed deep into the atmosphere until the collisions with the neutral gas and local photoionization rates are sufficient to prevent the magnetic field from reaching lower altitudes [Mahajan *et al.*, 1989; Cravens and Shinagawa, 1991]. The magnetic structure in the ionosphere is determined by plasma convection and magnetic diffusion [Cravens *et al.*, 1984].

The flow of the ionosheath plasma with the frozen-in magnetic field around the Venus ionosphere causes the magnetic field lines to drape around the body [Alfvén, 1957]. Downstream of Venus the magnetic field in the wake region is more or less in radial direction. The magnetic field configuration around Venus is illustrated in Figure 2.5 taken from Saunders and

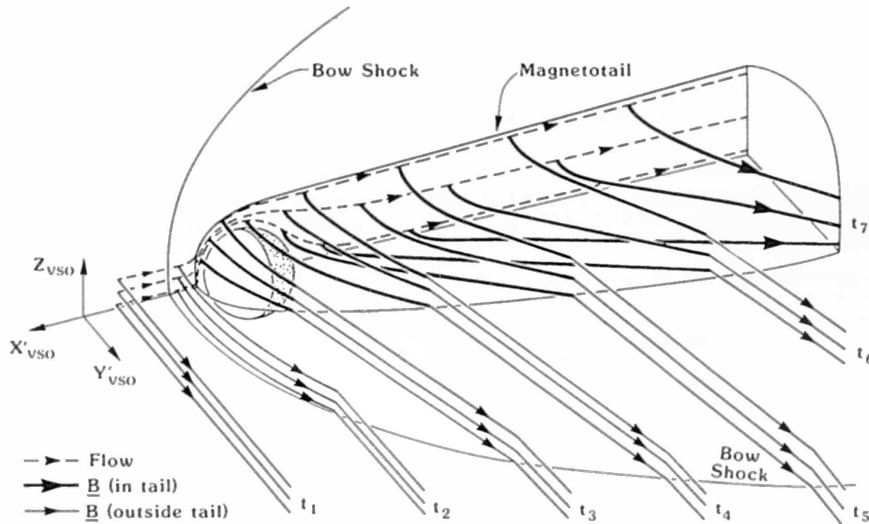


**Figure 2.5:** Flow and magnetic field configuration around Venus (taken from Saunders and Russell [1986]).

Russell [1986].

As the upstream magnetization of the ionosphere, the downstream ionosphere also depends on the incident solar wind pressure and has basically two states. At low solar wind pressure there are low magnitude variable magnetic fields in the downstream ionosphere and in-between are regions with a large steady radially directed magnetic field. The regions with the large magnetic field are called magnetic holes since inside of them the plasma density is depleted [Brace *et al.*, 1982; 1983]. Figure 2.6 shows a drawing the configuration of the Venus ionosphere as a result of the Pioneer Venus Orbiter mission.

At Titan the thermal pressure of the ionosphere is too low to balance the incident plasma pressure which is comparable to the situation at Venus during times of high solar wind dynamic pressure. Thus, the magnetization of the ionosphere should be similar to that of Venus in the magnetized state, i.e. the neutral gas should play a role in the pressure balance. The magnetic field line draping around the obstacle and the wake magnetic field for the most part depend on the properties of the incident plasma which are comparable at Venus and Titan. Indeed, Voyager 1 found strong draping signatures in Titan's wake. But the observed draping at Titan is stronger than at Venus and the transition to the non-draped region is abrupt compared to Venus where the transition is rather smooth. In principal the plasma interactions of Venus and Titan are similar [Kivelson and Russell, 1983].

At the end of this Section we want to point out the main differences between Titan and Venus: (1) The atmosphere is more extended at Titan (as mentioned above) which gives the obstacle a more cometary (see next Section) character. (2) The gyroradius of newly created ions is of the order of Titan's radius which will cause asymmetric ion pick-up. (3) The direction of the streaming plasma is independent of the direction of the major source for ionospheric production (solar EUV). Thus, the upstream side at Titan can be dayside, nightside, or in-between. This effect is assumed to be the cause for the asymmetries in the

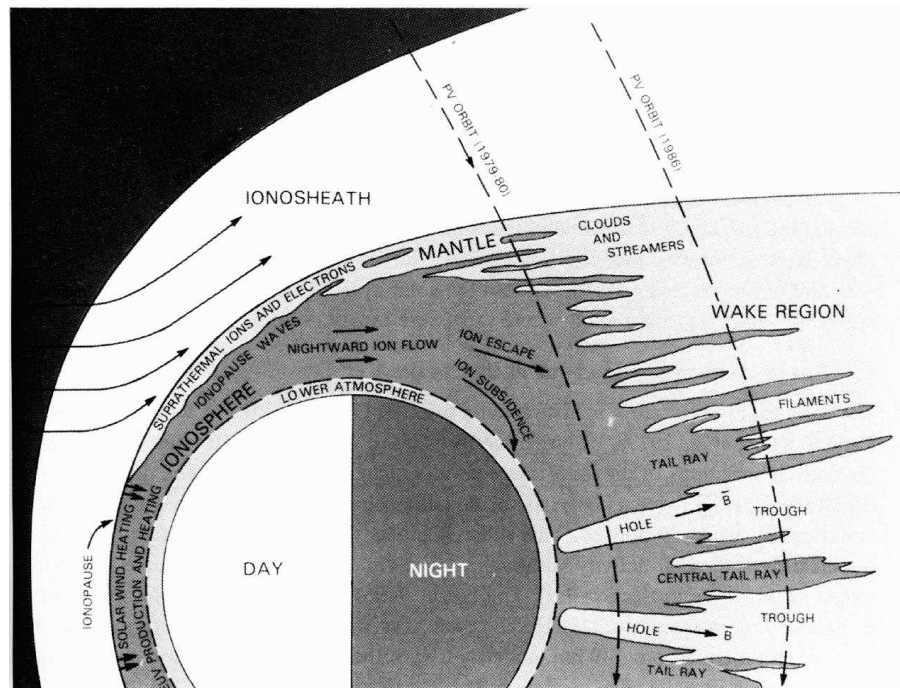


**Figure 2.6:** Global configuration of the Venus ionosphere from PVO data. The altitude scale is expanded by a factor of two relative to the planet (taken from Brace and Kliore [1991]).

wake magnetic field during the Voyager 1 encounter [Ness *et al.*, 1982; Neubauer *et al.*, 1984]. (4) During times of high solar wind pressure and Saturnian local times around noon at Titan, the magnetopause can be pushed towards Saturn and Titan can interact with the magnetosheath solar wind or even with the incident solar wind which means an abrupt change of the incident plasma properties [Wolf and Neubauer, 1982; Schardt *et al.*, 1984].

Another planet that belongs to the class of non-magnetic bodies (apart from the crustal magnetic fields) interacting with a streaming plasma is Mars. Comparisons of Mars and Venus have shown that their plasma interactions are comparable [Shinagawa and Cravens, 1989; Vaisberg *et al.*, 1990]. Due to the larger amount of data and therefore to the better understanding of the Venusian system we have restricted our comparison to Venus.

## 2.4 Comparison with the plasma interaction of comets

Due to many space missions to the comets Halley, Giacobini-Zinner, and Grigg-Skjellerup the cometary plasma environment when their distance to the Sun is near 1 AU is quite well observed. Especially the Giotto mission to Halley which proved the existence of the predicted [Biermann *et al.*, 1967] diamagnetic cavity around the cometary nucleus [Neubauer, 1986; 1988] made large contributions to our picture of the cometary plasma interaction region.

One difference between a planetary and cometary plasma interaction consists in the different scales for both. As discussed in the last section the extension of the atmosphere relative to the solid body at Venus is very low. A typical length scale for the global Venus plasma

interaction is the planetary radius. A comet consists basically of ice and dust. Close to the Sun ( $\sim 1$  AU), the impact of solar radiation causes the ice to sublimate and by that produce neutral gas which, accelerated by the pressure gradient to the ambient environment, moves radially away from the nucleus. This cometary atmosphere is called coma and the typical extension of the coma is an order of magnitude larger than the extension of the solid nucleus.

Apart from the atmospheric scale we have already mentioned a second difference between planets and comets: While typical velocities in a planetary neutral atmosphere are slow compared to the typical flow velocity of the incident plasma and have usually no favored direction, the neutral gas in a cometary coma streams radially away from the nucleus. In models for the plasma interaction of planetary bodies (like in this model) the neutral gas velocity is usually set to zero while it plays a crucial role in the plasma interaction of comets [*Schmidt et al.*, 1988].

Comparing Titan to Venus we have seen that the extension of Titan's atmosphere is comparable to the scale of the solid body which gives Titan a more cometary character in that respect. An obstacle that is determined by the neutral atmosphere is called a "soft" obstacle. But apart from this similarity Titan's plasma interaction should rather be classified as planetary than as cometary.

---

## POSING THE PROBLEM

---

Before we turn over to the description of the model and to the results we briefly want to define the situation to which the model is applied.

Figure 3.1 displays a schematical map of Titan's orbit around Saturn. Like the Earth, Saturn has an internal magnetic field which represents an obstacle for the streaming solar wind plasma. In the bow shock the supersonic solar wind becomes subsonic and then streams in the magnetosheath around the Saturnian magnetosphere. The layer between the magnetosphere and the magnetosheath solar wind plasma is the magnetopause.

As the name indicates, the region inside of the magnetosphere is controlled by the Saturnian magnetic field. The Saturnian magnetic field can be approximated by a dipole that is nearly aligned with the axis of planetary rotation [Smith *et al.*, 1980; Acuña and Ness, 1980]. Recently, Giampieri and Dougherty [2004] have found a significant dipole tilt of  $0.17^\circ$  from the analyses of Pioneer 11, Voyager 1 and Voyager 2 data. Besides Saturn there are several other objects inside of the magnetosphere, like the ring particles, the icy satellites, and last but not least Titan with its atmosphere. All that objects including Saturn itself serve as a source for molecules and atoms that are distributed inside of the magnetosphere. Part of the molecules and atoms are ionized by the solar radiation or by collisional processes [Richardson, 1998] and as charged particles they gyrate around the Saturnian magnetic field lines. Titan is supposed to be the second most important source of plasma (after Saturn) in Saturn's magnetosphere [Blanc *et al.*, 2002].

Saturn rotates with a period of 10.7 hours and so does the neutral atmosphere and, accelerated by friction with the neutral atmosphere, the ionosphere. Together with planet and atmosphere the internal magnetic field rotates. The rotation is transported to all the plasma along a magnetic field line from the northern hemisphere to the southern hemisphere by Alfvén waves (or field aligned currents) [Hill, 1979] so that the whole magnetosphere corotates. If plasma

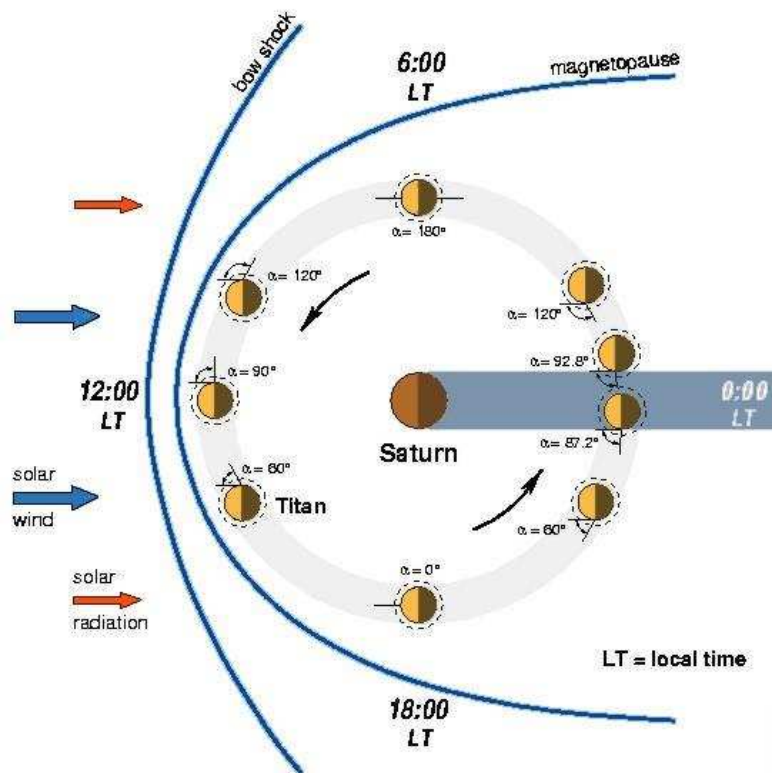


**Figure 3.1:** Titan's orbit around Saturn in the equatorial plane

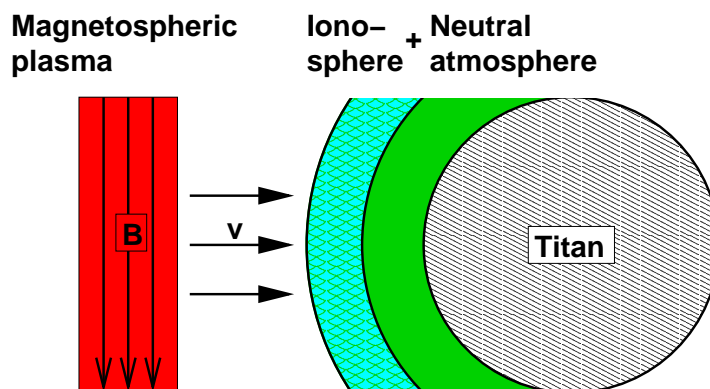


**Figure 3.2:** Schematic illustration of the components of the plasma interaction at Titan: magnetospheric plasma, ionosphere, neutral atmosphere, and solid body.

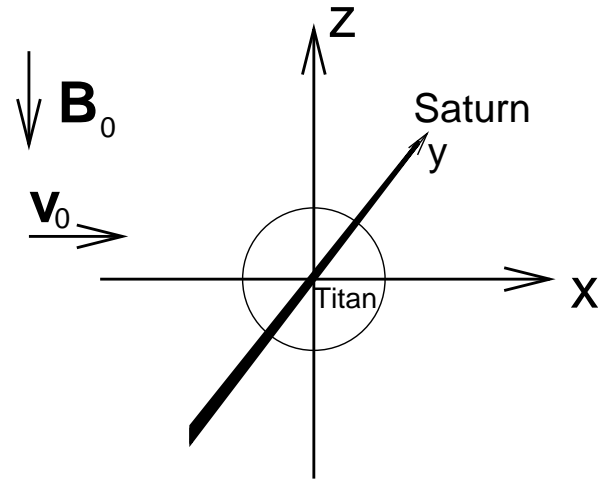


**Figure 3.3:** *Coordinate system for in this model*

is added inside of the magnetosphere it generates a current system that effectively transports momentum from the ionosphere to the location of the newly created plasma and thereby accelerates the plasma until it reaches corotational speed.

In the inner magnetosphere this is exactly correct. The energy required to achieve corotation increases with increasing distance to the planet. Thus, plasma sources in the outer magnetosphere decelerate the plasma so that the velocity is below the corotation speed. However, from a global point of view one can say that the plasma inside of a magnetosphere corotates or at least sub-corotates [Eviatar and Richardson, 1986].

Titan encircles Saturn with an orbital radius of  $20.3 R_S$  once in 15.95 days in the same direction as Saturn rotates. The plasma that inhabits the magnetosphere at the orbital distance of Titan only needed 10.7 hours if it were perfectly corotating. Although at the position of Titan the magnetospheric plasma velocity is below the corotation velocity [McNutt Jr. *et al.*, 1979], the magnetospheric plasma is still faster than the orbital velocity of Titan. Thus, the magnetized plasma streams around Titan and the satellite represents an obstacle for the plasma. The just described situation generates the plasma interaction that we want to describe with our model.

The actors in that interaction are the magnetospheric plasma on the one hand and Titan with its neutral atmosphere and ionosphere on the other hand (see Figure 3.2). We have developed our model in the Titan centered coordinate system that is displayed in Figure 3.3. The incident plasma flows along the  $x$ -axis, the Saturnian magnetic field at the position of Titan points towards the  $-z$ -direction, and the  $y$ -axis completes the right-handed system and points towards Saturn. The coordinate system for the flux tube model (see Section 4.4) moves with the plasma. It is also illustrated in Figure 3.3.



---

## MODEL DESCRIPTION

---

### 4.1 MHD model

We have chosen a fluid approach to model the plasma interaction of Titan with the ambient magnetospheric plasma. Before we derive our model equations we will briefly summarize the steps from the single particle to a fluid description and discuss the applicability of a fluid model to the case of Titan. A detailed derivation of the procedure describe here can be found e.g. in *Boyd and Sanderson* [1969].

A plasma consists of a huge number of ions and electrons. Here, we are not interested in knowing the exact motion of a single particle but want to know how the bulk plasma behaves. The starting point for such a treatment is the characterization of the plasma species by its distribution function. The evolution of the distribution function for a species  $s$  is determined by the Boltzmann equation (e.g. *Schunk and Nagy* [2000])

$$\frac{\partial f_s}{\partial t} + \vec{v}_s \cdot \vec{\nabla} f_s + \vec{a}_s \cdot \vec{\nabla}_v f_s = \frac{\delta f_s}{\delta t}. \quad (4.1)$$

On time scales that are large compared to the collision time of the particles within one plasma species, the velocity distribution of that species is given by a drifting Maxwellian.

Multiplying the Boltzmann equation with powers of the velocity and integrating it over velocity space, the fluid equations are obtained. The set of equations derived with that procedure is infinite in number because the equation for the moment of order  $n$  involves the next higher order. In the case of ideal MHD the system of equations is closed by assuming adiabatic conditions ( $p \sim \rho^\gamma$ ). Additional conditions have to be fulfilled by the plasma in order to ensure the validity of the fluid approach.

Time and length scales: A typical length scale for a single particle in a magnetic field is its

gyro radius ( $r_g$ ) and a typical time scale is its gyro period ( $1/\omega_g$ ). The validity of the fluid description requires:

$$\tau \gg \frac{1}{\omega_g} = \frac{m}{eB} \quad (4.2)$$

and

$$L \gg r_g = \frac{v_{th}}{\omega_g} = \sqrt{\frac{2kT}{m}} \frac{m}{eB} = \sqrt{\frac{2mkT}{e^2 B^2}} \quad (4.3)$$

where  $L$  and  $\tau$  are length and time scale for the fluid problem. For the right hand side of the inequalities the plasma species has to be taken that maximizes the value. For the application to Titan we take the values of the magnetospheric plasma measured by Voyager 1 (Table 2.2). In Eq. (4.2) the species with the largest mass is N, the magnetic field is  $B = 5$  nT leading to a time of  $1/\omega_g = 29$  s. A typical time scale for the global plasma interaction of Titan is the time it takes the plasma to move a typical length, which is one Titan radius  $R_T = 2575$  km. With the velocity of 120 km/s measured by Voyager 1 this leads to a time of  $\tau = 21.4$  s, which is of the same order of magnitude as the gyro period. To calculate the length scale we use nitrogen at a temperature of  $kT = 2.9$  keV in Eq. (4.3), leading to  $r_g = 5800$  km, which is even larger than  $L = R_T$ , the typical length scale for the fluid.

If the conditions above (Eq. (4.2), Eq. (4.3)) are fulfilled, single particle effects do not play any role and the plasma completely behaves as a fluid. If they are not fulfilled, additionally (to the fluid behavior) single particle effects play a role. Even in the case of Titan where the conditions are clearly not fulfilled, the fluid description is a valid approach that describes important features of the plasma. But one has to keep in mind that this is not the end of the story and that single particle effects certainly play a role at Titan.

The fluid description has some advantages. The low number of equations compared to kinetic models enables one to use a higher spatial resolution. Apart from that, there is no kinetic model that includes ion-neutral collisions. At Titan ion-neutral collisions play a crucial role below an altitude of 1000 km [Ip, 1990] which is the altitude of the ionospheric peak. Therefore, e.g. the magnetization of the ionosphere cannot be described by kinetic models. However, with increasing computational power in the future, fluid and kinetic models should be coupled. In this work we show the fluid properties of Titan's plasma interaction and we are aware of the limits of such a description.

An additional assumption for the derivation of the ideal MHD equations [Boyd and Sander-son, 1969] is *quasi-neutrality*, which is justified when the length scale is much larger than the Debye length. The resulting ideal single fluid MHD equations are

$$\frac{\partial \rho}{\partial t} + \vec{\nabla} \cdot (\rho \vec{v}) = 0 \quad (4.4)$$

$$\rho \left( \frac{\partial \vec{v}}{\partial t} + \vec{v} \cdot \vec{\nabla} \vec{v} \right) = -\vec{\nabla} p + \frac{1}{\mu_0} (\vec{\nabla} \times \vec{B}) \times \vec{B} \quad (4.5)$$

$$\frac{\partial \vec{B}}{\partial t} = \vec{\nabla} \times (\vec{v} \times \vec{B}) \quad (4.6)$$

$$\frac{\partial e}{\partial t} + \vec{\nabla} \cdot (e \vec{v}) = -p \vec{\nabla} \cdot \vec{v} \quad (4.7)$$

The kernel of our model is Zeus 3D [Stone and Norman, 1992a;b], a code that solves the ideal

MHD equations for mass density (Eq. (4.4)), velocity (Eq. (4.5)), magnetic field (Eq. (4.6)), and internal energy (Eq. (4.7)). The variables are bulk variables that composed from the bulk variables of each plasma species. For a plasma consisting of one ion species and an electron species the bulk variables are given by

$$\rho = \rho_i + \rho_e \quad (4.8)$$

$$\vec{v} = \frac{\rho_i \vec{v}_i + \rho_e \vec{v}_e}{\rho_i + \rho_e} \quad (4.9)$$

$$e = \frac{3}{2}p = \frac{3}{2}(p_i + p_e). \quad (4.10)$$

For a detailed derivation of the ideal MHD equations from the electron and ion fluid equations see e.g. *Boyd and Sanderson [1969]*.

One of the striking properties of Titan is its dense neutral atmosphere. The interaction of the plasma with the neutral gas introduces additional terms to the ideal MHD equations. To derive these terms one has to insert the influence of the neutral gas into each of the equations for each fluid and combine them to obtain the single fluid representation of the extra terms. Qualitatively, the processes that are introduced by the neutral gas are: (1) production of plasma from the neutral gas and recombination, which gives contributions to all of the MHD equations; (2) collisions between plasma species and the neutral gas transfer momentum and energy; (3) collisions also lead to a finite electrical conductivity introducing a diffusion term into the magnetic induction equation.

We will now derive the single-fluid equations from the two-fluid equations for one ion and one electron species with the inserted effects of the neutral gas. The equations for one fluid of species  $s$ , which can be either electrons or ions, with the included terms are [*Schmidt et al., 1988; Cravens, 1997; Schunk and Nagy, 2000*]:

$$\frac{\partial \rho_s}{\partial t} + \vec{\nabla} \cdot (\rho_s \vec{v}_s) = m_s \frac{\delta n_s}{\delta t} \quad (4.11)$$

$$\rho \left( \frac{\partial \vec{v}_s}{\partial t} + \vec{v}_s \cdot \vec{\nabla} \vec{v}_s \right) = n_s q_s [\vec{E} \times \vec{B}] - \vec{\nabla} p_s + \frac{\delta M_s}{\delta t} \quad (4.12)$$

$$\begin{aligned} \frac{\partial e_s}{\partial t} + \vec{\nabla} \cdot (e_s \vec{v}_s) &= -p_s \vec{\nabla} \cdot \vec{v}_s - \frac{1}{2} m_s \vec{v}_s^2 \frac{\delta n}{\delta t} - \vec{v}_s \frac{\delta M_s}{\delta t} \\ &+ \frac{\delta E_s}{\delta t} \end{aligned} \quad (4.13)$$

with

$$\frac{\delta n_s}{\delta t} = m_s \left( \sum_{ns} P_{s,ns} - L_s \right) \quad (4.14)$$

$$\frac{\delta M_s}{\delta t} = -m_s \sum_{ns} (n_s \mathbf{v}_{s,ns} + P_{s,ns}) (\vec{v}_s - \vec{v}_{ns}) \quad (4.15)$$

$$\begin{aligned} \frac{\delta E_s}{\delta t} &= \sum_{ns} \mathbf{v}_{s,ns} \frac{\rho_s}{m_s + m_{ns}} (3k(T_{ns} - T_s) + m_{ns} (\vec{v}_s - \vec{v}_{ns})^2) \\ &+ \sum_{ns} r_s \left( \frac{1}{2} m_{ns} \vec{v}_{ns}^2 + \frac{3}{2} k T_{ns} \right) P_{s,ns} \\ &- \left( \frac{1}{2} m_s \vec{v}_s^2 + \frac{3}{2} k T_s \right) L_s. \end{aligned} \quad (4.16)$$

These are the the continuity equation (4.11), the momentum equation (4.12), and the equation for the internal energy (4.13) of plasma fluid  $s$ .  $\rho_s$  is the mass density,  $\vec{v}_s$  the velocity,  $e_s$  the internal energy,  $n_s$  the number density,  $q_s$  the elementary charge,  $\vec{E}$  the electric field,  $p_s = \frac{2}{3}e_s = n_s k T_s$  the pressure, and  $m_s$  the mass. The index  $ns$  labels the neutral species. The  $\delta$ -terms on the right hand side of the equations name the terms that originate from the neutral gas influence which are: ion and electron production and loss ( $\frac{\delta n_s}{\delta t}$ )<sup>1</sup>, change of momentum due to collisions and mass loading ( $\frac{\delta M_s}{\delta t}$ ), energy transfer with the neutral gas and change of energy due to plasma production and loss ( $\frac{\delta E_s}{\delta t}$ ). Note, that in the internal energy equation for the magnetospheric electrons additional heating and cooling terms appear corresponding to inelastic collisions with the neutral gas and heat conduction. We will come to that later on (see Eq. (4.45) and Eq. (4.46)).

In the model we assume a constant neutral gas temperature for each of the two neutral species,  $T_{ns} = 186$  K [Smith et al., 1982; Hanel et al., 1981].

The collision frequencies of the ions with the neutrals are independent of temperature [Banks and Kockarts, 1973a]

$$v_{i,ns} = 2.6 \times 10^{-9} n_{ns} \sqrt{\frac{\alpha_{0,ns}}{\mu_{A,ns}}} \text{ s}^{-1}. \quad (4.17)$$

$\alpha_{0,ns}$  is the polarizability of the neutral gas species  $ns$  in units of  $10^{-24} \text{ cm}^{-3}$  and  $\mu_{A,ns}$  is the reduced mass in amu. The values of the polarizability are taken from Banks and Kockarts [1973a] [1973]:  $\alpha_{0,N_2} = 1.76$  and  $\alpha_{0,CH_4} = 2.59$ .

The electron neutral collision frequencies depend on the electron temperature. We use the dependence given in the table in Keller et al. [1992].

The neutral gas density was kept constant below an altitude of 1000 km in the collision terms for numerical reasons. If the gradients in the coefficient for the magnetic diffusion (in Eq. 4.25) are too high the term becomes unstable. The results show that the plasma velocity has already dropped to zero above that altitude and therefore the pressure balance and the macroscopic structure of the interaction are not influenced by this approximation. But below 1000 km the transport of magnetic field by magnetic diffusion is artificially slowed.

Electron temperature and the plasma temperature are variables that do not explicitly appear in the ideal MHD equations. Therefore, temperature has to be defined as a function of the MHD variables. In our model we define a temperature by assuming that the mean temperature of ions and electrons is equal. The total pressure in an ideal gas is given by  $p = nk(T_i + T_e) = 2nkT$  with  $T = T_i = T_e$  and  $n = n_i = n_e$  (quasi-neutrality). Then the temperature can be written as a function of  $\rho$  and  $p = \frac{2}{3}e$

$$T = \frac{pm_i}{2k\rho}. \quad (4.18)$$

The loss rate  $L$  is given by

$$L = \alpha_D n^2 \quad (4.19)$$

with  $\alpha_D$  the dissociative recombination coefficient. Dissociative recombination is much faster than radiative recombination. If dissociative recombination is possible, the radiative recom-

<sup>1</sup>The loss rate is rather a result of the finite temperature than due to the influence of the neutral gas.

bination rate can be neglected. We assume for the loss process that the plasma only consists of  $N_2^+$ . In the regions where the loss of plasma is noticeable this is a reasonable assumption since it leads to the right ionospheric peak electron densities. The dissociative recombination coefficient is taken from *Banks and Kockarts [1973a]*:

$$\alpha_{D,N_2} = 3 \times 10^{-7} \left( \frac{300}{T_e} \right)^{1/3} \text{ cm}^3 \text{ s}^{-1}. \quad (4.20)$$

For the electron temperature  $T_e$  we use  $T_i = T_e = T$  and  $T$  is obtained from Eq. (4.18) The sources for the plasma production in Eq. (4.14) that we have included into the model are photoionization, ionization by photoelectrons, and electron impact ionization by magnetospheric electrons

$$P_{s,ns} = P_{s,ns,ph} + P_{s,ns,pe} + P_{s,ns,ms}. \quad (4.21)$$

They will be explained in detail in Section 4.3 and Section 4.4 (Eq (4.30), Eq (4.35), and Eq (4.49)).

The interaction with the neutral gas changes the plasma momentum (Eq. (4.15)) due to collisional momentum transfer and mass loading. When plasma is produced from a - compared to the plasma bulk velocity - slowly moving neutral gas, the plasma momentum remains nearly unchanged while the mass density is increased by the mass of the new ions. In order to conserve momentum, the bulk velocity decreases. The processes in Eq. (4.14) and Eq. (4.15) also give contributions to the internal energy of the plasma (Eq. (4.13)). Additionally, an energy transfer of thermal and kinetic energy between neutral gas and plasma takes place (Eq. (4.16)), and production and loss of plasma change the internal energy of the plasma. The factor  $r_s$  in the term for the increase of internal energy due to production is the fraction of the energy of original neutral gas that goes to the plasma species  $s$ . Ionization at least creates two plasma species, one ion and one electron, and the thermal energy has to be distributed between the two. Energy conservation requires  $r_i + r_e = 1$ .

In Eq. (4.14) to Eq. (4.16) we have not included collisions of electrons and ions. In the single-fluid model, electron-ion collisions cancel in the momentum equation because the transfer of momentum between ions and electrons does not change the total plasma momentum. In the energy equation they appear in the Joule heating terms. Due to the dense neutral atmosphere we neglect electron-ion collisions against ion-neutral and electron-neutral collisions as *Schmidt et al. [1988]* did in their model for the plasma interaction of Halley.

The single-fluid equations are derived from the multi-fluid equations by adding and subtracting the electron equations to and from the ion equations. For the terms that do not contain the influence of the neutral gas this procedure results in the ideal MHD equations ((4.4), (4.5), (4.6), (4.7)). For the derivation we assume that the plasma consists of one ion species and one electron species. Compared to the plasma velocity, the velocity of the neutral gas is negligible. In the following we set  $\vec{v}_n = 0$ . Adding the continuity equations (4.11) leads to:

$$\frac{\partial \rho}{\partial t} + \vec{\nabla} \cdot (\rho \vec{v}) = \sum_{ns} m_{ns} P_{ns} - m_i L \quad (4.22)$$

where  $ns$  labels the neutral species ( $N_2$  and  $CH_4$  in our model) and  $m_i$  is the ion mass in the plasma. Detailed ionospheric models [*Keller et al., 1992*] have shown that for the plasma

interaction the production of multiple charged ions can be neglected at Titan. In this case, the ion production rate is equal to the electron production rate  $P_{ns} = P_{i,ns} = P_{e,ns}$  and the production rate from the neutral species  $ns$  is given by

$$P_{ns} = P_{ns,ph} + P_{ns,pe} + P_{ns,ms} \quad (4.23)$$

with the photoionization rate  $P_{ns,ph}$  (Eq. (4.30)), the impact ionization by photoelectrons  $P_{ns,pe}$  (Eq. (4.35)), and by magnetospheric electrons  $P_{ns,ms}$  (Eq. (4.49)). Here, and in the rest of all the calculations, we have neglected terms of the order  $m_e/m_i$  compared to 1.

In the ideal MHD equations the ion mass does not appear explicitly. In our model with two neutral gas species, two sorts of ions are produced with  $m_{\text{CH}_4} = 16$  amu and  $m_{\text{N}_2} = 28$  amu. When plasma is produced in the model, the correct mass density is added to the plasma by treating the production for each neutral species separately. This ensures that the change of momentum and mass density due to plasma production is correct within the model. For the loss rate, the mass of the ion that recombines goes explicitly in the calculation of the mass density (Eq. (4.22)). Recombination and other processes that require explicitly the ion mass (e.g. for the calculation of the electron number density  $n = \rho/m_i$ ) affect only that regions (ionosphere) where 28 amu is a good approximation for the ion mass. Therefore, throughout the model we set  $m_i = 28$  amu. The average mass of the upstream magnetospheric plasma measured by Voyager 1 is  $m_{ms} = 9.7$  amu and the electron density is  $n = 0.3 \text{ cm}^{-3}$  [Hartle *et al.*, 1982; Neubauer *et al.*, 1984]. If we calculate the upstream electron density within our model we get  $n = \rho/m_i = 0.1 \text{ cm}^{-3}$ . Since in that regions the terms in the equations containing  $n$  are negligible, the validity of the model is not affected by this approximation.

The sum of the momentum equations (4.12) leads to the equation for the total plasma momentum:

$$\begin{aligned} \rho \left( \frac{\partial \vec{v}}{\partial t} + \vec{v} \cdot \nabla \vec{v} \right) &= -\vec{\nabla} p + \frac{1}{\mu_0} (\vec{\nabla} \times \vec{B}) \times \vec{B} - \sum_{ns} m_{ns} P_{ns} \vec{v} \\ &\quad - \sum_{ns} \left( \frac{m_e}{m_i} v_{e,ns} + v_{i,ns} \right) \rho \vec{v} \\ &\quad + \sum_{ns} (v_{e,ns} - v_{i,ns}) \frac{m_e}{e} \vec{j} \end{aligned} \quad (4.24)$$

Here appears the current density  $\vec{j}$  which is on the one hand given by the separate motion of positive and negative charges  $\vec{j} = e(n_i \vec{v}_i - n_e \vec{v}_e)$ . That is the reason why it appears in the single-fluid equations although it is absent in the multi-fluid equations. On the other hand the electric current is connected with the magnetic field via Ampère's law (the displacement currents can be neglected in our application since the fast magnetosonic velocity is much lower than the speed of light)  $\vec{j} = \frac{1}{\mu_0} \vec{\nabla} \times \vec{B}$ .  $\vec{j}$  does not increase the number of the variables that describe the single-fluid plasma.

The induction equation is obtained by subtracting the momentum equation of the electrons from the momentum equation of the ions.

$$\begin{aligned} \frac{\partial \vec{B}}{\partial t} &= \vec{\nabla} \times (\vec{v} \times \vec{B}) - \frac{m_e}{ne^2} \sum_{ns} (v_{e,ns} + \frac{m_e}{m_i} v_{i,ns}) \vec{j} \\ &\quad - \frac{m_e}{e} \sum_{ns} (v_{i,ns} - v_{e,ns}) \vec{v} - \frac{m_e}{n^2 e^2} L \vec{j}. \end{aligned} \quad (4.25)$$

The terms on the right hand side are motional field, magnetic diffusion, rotational induction, and a magnetic diffusion term due to the loss of plasma. In regions of low neutral gas densities the diffusion term is negligible and the magnetic field is frozen into the bulk plasma. When the neutral gas density is high enough for the magnetic diffusion to become noticeable or when the magnetic Reynolds number approaches the order of 1 or below, the magnetic field moves independently from the plasma. This is the case deep in the ionosphere below the ionospheric peak.

In this work we neglect the influence of the Hall term which introduces whistler waves to the model. The time scale of the whistler waves is in our case about two orders of magnitude lower than the time scale of sonic and Alfvén waves [Huba, 2003]. This would extend the simulation time by a factor of 100! The combination of Hall and advection term freezes the magnetic field (in the absence of magnetic diffusion) into the electron fluid in contrast to ideal MHD where the magnetic field is frozen into the bulk plasma. In the induction equation the Hall term has to compete with the convection term on the one hand and with the diffusion term on the other hand. In Section 5.3 we will discuss the region where the Hall term could possibly alter our results.

Summing the equations for the internal energy (Eq. (4.13), Eq. (4.16)) we obtain an equation for the total internal energy of the plasma.

$$\begin{aligned}
\frac{\partial e}{\partial t} + \vec{\nabla} \cdot (e\vec{v}) &= -p\vec{\nabla} \cdot \vec{v} + \frac{3}{2}nk \sum_{ns} v_{i,ns}(T_{ns} - T) \\
&+ \frac{3}{2} \sum_{ns} P_{ns}kT_{ns} - \frac{3}{2}LkT \\
&+ \sum_{ns} \left( \frac{P_{ns}}{n} + v_{i,ns} + \frac{m_e}{m_i} v_{e,ns} \right) \frac{1}{2}\rho\vec{v}^2 \\
&+ \sum_{ns} (v_{i,ns} - v_{e,ns}) \frac{m_e}{2e} \vec{v} \cdot \vec{j} \\
&+ \sum_{ns} \left( \frac{P_{ns}}{n} + \frac{m_e}{m_i} v_{i,ns} + v_{e,ns} \right) \vec{j}^2 + \frac{\delta E_{ms}}{\delta t} + \frac{\delta E_{pe}}{\delta t} \quad (4.26)
\end{aligned}$$

The terms on the right hand side are: adiabatic change of pressure, temperature coupling with the neutral gas, change of internal energy due to plasma production and loss, and Joule heating. Heat conduction and inelastic processes of magnetospheric electrons ( $\frac{\delta E_{ms}}{\delta t}$ , Eq. (4.54)) and the change of internal energy due to plasma heating by photoelectrons ( $\frac{\delta E_{pe}}{\delta t}$ , Eq. (4.36)) are also included. The temperature in the model is defined in Eq. (4.18). In the brackets of the Joule heating terms the production rate  $P_{ns}$  appears. When plasma is produced from neutral gas, there is an effective energy transfer from the kinetic to the thermal energy of the plasma, which can be mathematically treated in analogy to Joule heating.

The change of internal energy due to inelastic collisions and heat conduction of the magnetospheric electrons is explained in detail in the section about the flux tube model (Section 4.4).

## 4.2 Model of the neutral atmosphere

Titan's neutral atmosphere is a composition of a large number of neutral gas species, compounds of the atoms N, C, and H. Following the models of *Yung et al.* [1984]; *Yung* [1987] and *Keller et al.* [1992]<sup>2</sup>, which are based on measurements from Voyager 1, up to an altitude of 2500 km the main species are N<sub>2</sub> and CH<sub>4</sub>. Above 2500 km H<sub>2</sub> is the most abundant species. But the lower mass and the lower reaction cross sections (see e.g. *Schunk and Nagy* [2000]) compared to N<sub>2</sub> and CH<sub>4</sub> make it negligible for the plasma interaction. In this work we regard methane and molecular nitrogen as the only neutral species.

We assume a spherical symmetric atmosphere and neglect the dynamics of the neutral gas. This is reasonable since compared to the typical plasma velocities of  $\sim 100 \text{ kms}^{-1}$  the neutral velocities (wind speeds) of  $\sim 50 \text{ ms}^{-1}$  are negligible. The day to night temperature difference ( $\sim 20 \text{ K}$ ) is also negligible compared to the typical plasma energies of  $\sim 1 \text{ eV}$ . (Wind speeds and day to night temperature difference are taken from *Müller-Wodarg et al.* [2000]). As in *Keller et al.* [1992] the radial dependence of N<sub>2</sub> is determined by assuming hydrostatical conditions:

$$n(r) = n(r_1) \exp \left[ - \int_{r_1}^r \frac{dr'}{H(r')} \right] \quad (4.27)$$

with the scale height  $H(r) = \frac{kT(r)}{mg(r)}$  and  $g(r) = g(r_0)(r_0/r)^2$  with  $g(r_0) = 1.35 \text{ ms}^{-2}$  at the surface of Titan ( $r_0 = 2575 \text{ km}$ ). Taking two temperature regimes with constant temperature (165 K below 1265 km and 186 K above [*Smith et al.*, 1982; *Hanel et al.*, 1981]) and a given density  $n(h = 175 \text{ km}) = 4.18 \times 10^{16} \text{ cm}^{-3}$  [*Smith et al.*, 1982] the radial distribution of N<sub>2</sub> is given by the function ( $[r] = \text{km}$ ):

$$n_{\text{N}_2}(r) = \begin{cases} 4.18 \times 10^{16} \text{ cm}^{-3} \exp \left[ -1.83 \times 10^5 (1/2750 - 1/r) \right] & r < 3840 \text{ km} \\ 2.62 \times 10^8 \text{ cm}^{-3} \exp \left[ -1.62 \times 10^5 (1/3840 - 1/r) \right] & \text{else} \end{cases} \quad (4.28)$$

Up to the height of 925 km the mixing ratio of CH<sub>4</sub> and N<sub>2</sub> is constant (2%) [*Bertaux and Kockarts*, 1983; *Smith et al.*, 1982]. Above that height we solve the hydrostatic equation for CH<sub>4</sub> to derive the function for the radial distribution.

$$n_{\text{CH}_4}(r) = \begin{cases} 0.02 n_{\text{N}_2}(r) & r < 3500 \text{ km} \\ 5.48 \times 10^8 \text{ cm}^{-3} \exp \left[ -1.08 \times 10^5 (1/3500 - 1/r) \right] & 3500 \text{ km} \leq r < 3840 \text{ km} \\ 3.90 \times 10^7 \text{ cm}^{-3} \exp \left[ -9.26 \times 10^4 (1/3840 - 1/r) \right] & \text{else} \end{cases} \quad (4.29)$$

We neglect H<sub>2</sub> which is the most abundant species in Titan's exosphere above 2500 km. The contribution of H<sub>2</sub> to mass-loading by photoionization is very low due to its low rate coefficients [*Huebner*, 1985] and its low mass. The frictional force H<sub>2</sub> imposes to the plasma can be estimated by assuming a constant H<sub>2</sub> density of  $10^5 \text{ cm}^{-3}$ . If a plasma with a flow velocity of 120 km/s flows through this neutral cloud its flow velocity is reduced along a distance of  $R_T$  by  $\Delta v \approx 2575 \times 2 \times 10^{-9} \times 10^5 \text{ km/s} = 0.26 \text{ km/s}$ . Thus, H<sub>2</sub> is also negligible with respect to the frictional force and the neglect in the model is justified.

<sup>2</sup>Although there are newer models [*Fox*, 1997; *Yelle et al.*, 1997] we have decided to use the model of *Keller et al.* [1992] to make comparison with their detailed 1D model easier.

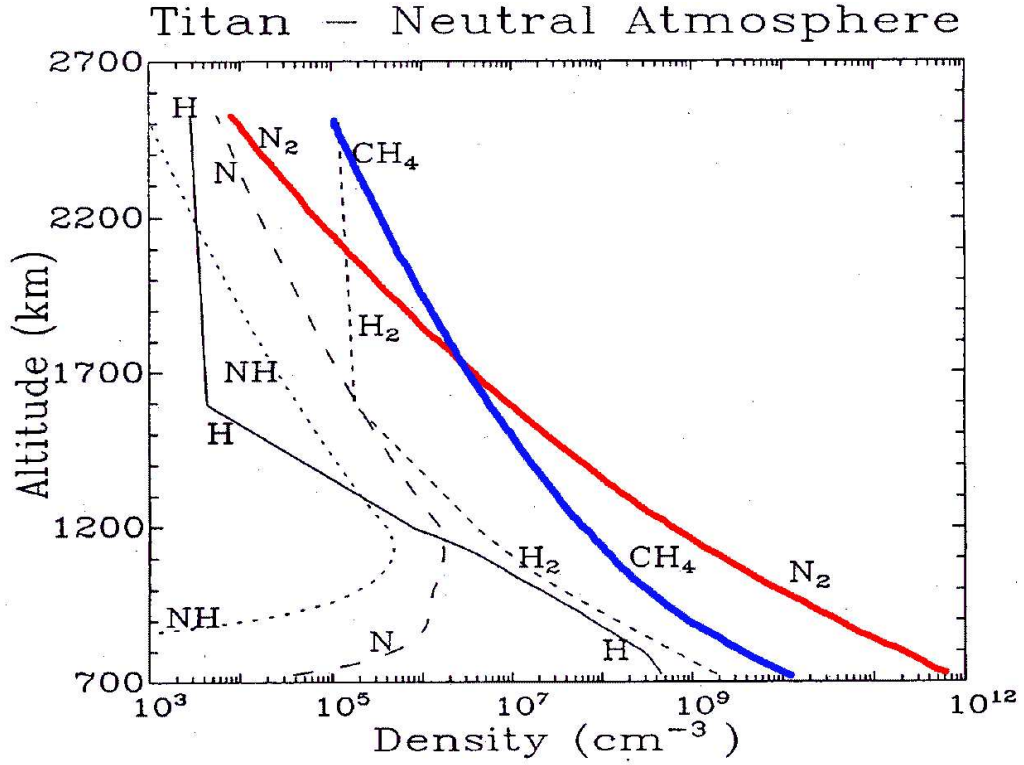


**Figure 4.1:** Neutral atmosphere taken from Keller et al. [1992] [1992]. The bold lines are the neutral densities used in this model.

The additional neutral gas density increases exponentially towards the surface of Titan. When the density is too high, the magnetic diffusion term in Eq. (4.25) becomes unstable. In order to conserve consistency in the model, the neutral gas density below 1000 km is set to the value at 1000 km for all terms in the model equations (Eq. (4.22,4.24,4.25,4.26)). The magnetic diffusion rate in the lower atmosphere is therefore too low in our model. The altitudes above 1000 km are not affected by the assumption. For the calculation of the production rates the full density profile down to the surface is applied.

### 4.3 Solar radiation model

In order to model the solar EUV flux we use the EUVAC *Richards et al.* [1994] model with the F74133 flux as reference flux for the solar activity. It consists of 37 bins for either wavelength intervals or discrete lines. With the absorption and ionization cross sections of the two neutral gas species  $N_2$  and  $CH_4$  *Schunk and Nagy* [2000] in the same bins we calculate the photoionization rates

$$P_{ns,ph}(\vec{r}) = n_{ns} \sum_i I(\vec{r}, \lambda_i) \sigma_{ion,ns}(\lambda_i) \quad (4.30)$$

where we sum over the wavelength bins. The solar flux for a given wavelength at position  $\vec{r}$  is calculated by integrating the incident flux along the ray path

$$I(\vec{r}, \lambda) = I_\infty \exp \left[ - \sum_{ns} \sigma_{abs,ns}(\lambda) \int_{\vec{r}}^{\infty} ds n_{ns}(s) \right]. \quad (4.31)$$

The process of photoionization transforms a neutral atom or molecule into an ion and an electron. Actually there are several ionization paths for a neutral atom or molecule leading to different final states. In Eq. (4.30) we use the total ionization cross section since in the frame of our model we are interested in rather the number of created ions and electrons than the exact atomic state of the ions.

If we subtract the energy that is needed for the ionization process from the total energy that is absorbed from the EUV by ionization the result is not zero. This rest energy is captured nearly completely by the newly created electron. This energy is distributed among the newly created ion and electron, photoelectron [Banks and Kockarts, 1973a]. The photoelectron interacts with the ions, electrons, and neutral particles and transports part of the energy into the magnetosphere. To calculate the exact energy contribution to the different channels is a complicated task and is beyond the scope of our model. A more exact treatment of photoelectrons can be found e.g. in Galand *et al.* [1999] and Gan *et al.* [1992]. We have developed a simplified model to account for the effects of the photoelectrons which we want to introduce in the following.

The total production rate of photoelectrons is given by Eq. (4.30). In order to calculate a secondary ionization rate by photoelectron impact we need to know the energy distribution of the photoelectrons. As the solar EUV radiation is divided into 37 bins in the model, we also divide the photoelectron energy into 37 bins. The production rate of photoelectrons in bin  $i$  is given by

$$P_{ns,ph,i}(\vec{r}) = n_{ns}I(\vec{r}, \lambda_i)\sigma_{ion,ns}(\lambda_i) \quad (4.32)$$

and the energy of the electrons in bin  $i$  is

$$E_{ns,i}(\vec{r}) = \frac{1}{P_{ns,ph,i}(\vec{r})} \left( n_{ns}I(\vec{r}, \lambda_i)\sigma_{ion,ns}(\lambda_i) \left( \frac{hc}{\lambda_i} - E_{ion,ns} \right) \right) \quad (4.33)$$

respectively. When we assume that the photoelectrons interaction cross sections with the neutral gas are much larger than the cross sections for the other processes we are able to calculate the secondary ionization rate of the photoelectrons

$$P_{ns,pe,i}(\vec{r}) = P_{ns,ph,i}(\vec{r}) \frac{\sigma_{ii,ns}(E_{ns,i})}{\sigma_{ii,ns}(E_{ns,i}) + \sigma_{ex,ns}(E_{ns,i})} \quad (4.34)$$

where  $\sigma_{ii,ns}$  is the electron impact ionization cross section  $\sigma_{ex,ns}(E_i)$  is the total excitation cross section for the neutral gas species  $ns$ . For  $N_2$  the considered processes are electronic excitations taken from Banks and Kockarts [1973a], vibrational and rotational excitations taken from Schunk and Nagy [2000], and ionization taken from the NIST database [Kim *et al.*, 1997]. The appropriate data for  $CH_4$  is taken from Gan and Cravens [1992]. We then get the total secondary production rate by summing over the energy levels

$$P_{ns,pe}(\vec{r}) = \sum_i P_{ns,ph,i}(\vec{r}) \frac{\sigma_{ii,ns}(E_{ns,i})}{\sigma_{ii,ns}(E_{ns,i}) + \sigma_{ex,ns}(E_{ns,i})}. \quad (4.35)$$

The second important contribution from the photoelectrons that we include in our model is the part of the energy that increases the total plasma pressure. In their one dimensional model with an emphasis on chemistry and energetics, Roboz and Nagy [1994] have calculated a peak

plasma heating rate by photoelectrons of  $\sim 30\text{eVcm}^{-3}\text{s}^{-1}$ . In a very crude approximation we assume that the fraction of photoelectron energy that heats the plasma is constant. The particular fraction  $\nu$  is then determined by limiting the peak heating rate to  $\sim 30\text{eVcm}^{-3}\text{s}^{-1}$

$$\frac{\delta E_{pe}}{\delta t}(\vec{r}) = \nu \sum_i \sum_{ns} n_{ns} I(\vec{r}, \lambda_i) \sigma_{ion,ns}(\lambda_i) \left( \frac{hc}{\lambda_i} - E_{ion,ns} \right). \quad (4.36)$$

The heating rate increases the total internal plasma energy (see Eq. (4.26)).

## 4.4 Flux tube model

In the frame of single-fluid MHD the electrons give contributions to the total plasma pressure but they do not appear explicitly in the model. In the true Titan environment the magnetospheric electrons serve as an energy source and as a source for plasma production by electron impact ionization of the neutral atmosphere. In order to account for these important contributions to the plasma interaction of Titan we developed a flux tube model running on top of the MHD model. In this section we explain the concept of this model.

Although the solar EUV radiation is the primary source of ionization and thereby above all other processes responsible for the formation of the ionosphere, at least on the nightside of Titan, where this source is absent, electron impact ionization plays a crucial role for the ionosphere. Plasma interaction depends on the properties of the ionosphere. Where the magnetic diffusion coefficient is low the magnetic field is transported by the electrons, or vice versa the electrons move together with the magnetic field. The electron impact ionization rate depends on the magnetic field geometry. But the magnetic field geometry by itself is a result of the MHD model and depends on the characteristics of the ionosphere and therefore on the ionization rates. Thus, the impact ionization rates of the magnetospheric electrons cannot be calculated a priori like the photoionization rates.

The motion of the electrons along the magnetic field transfers energy along the field line. If part of a field line is inside of the atmosphere this part is cooled down by the interaction with the neutral gas. Then the motion of the electrons along the field line transfers energy from the outer part of the field line (which is in the magnetosphere) into the atmosphere (ionosphere) (see Figure 4.2). This process can be interpreted as heat conduction from the warmer to the cooler parts of a flux tube.

The impact ionization rates and the energy transfer from the magnetosphere into the atmosphere are calculated in the frame of a flux tube (FL) model which is explained in detail in the following sections.

### 4.4.1 Geometry of the flux tube model

The flux tube model runs on a separate grid. At the beginning, when the simulation is started, the ZEUS-grid and the FL-grid are identical, except that the resolution of the FL-grid in  $y$  and  $z$  direction is twice that of the ZEUS-grid. At problem initialization, the magnetic field is set

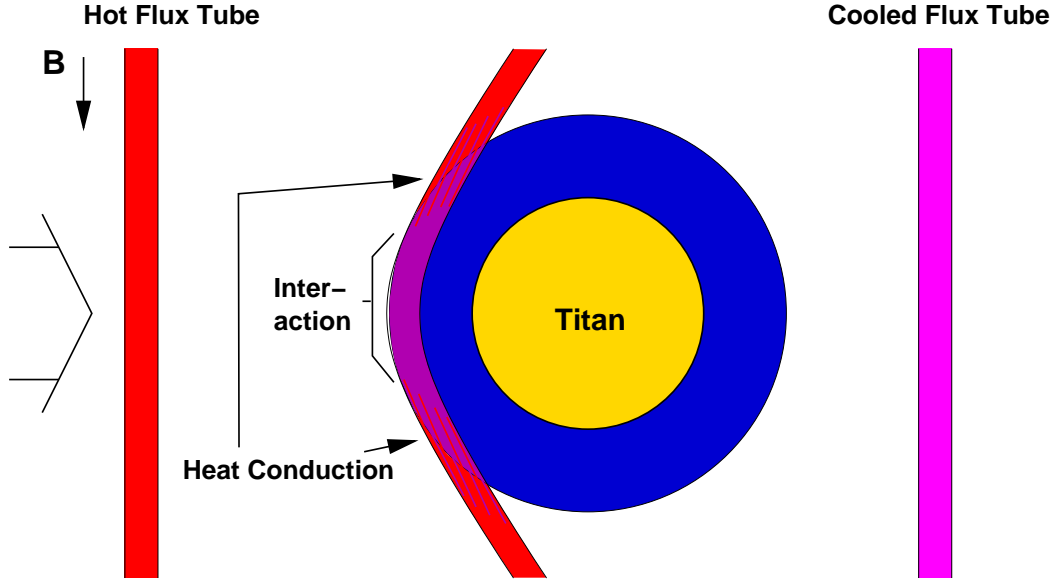


**Figure 4.2:** Schematical picture of a flux tube of magnetospheric electrons interacting with Titan's atmosphere.

to zero inside of a cylinder with the axis parallel to  $z$  and a radius of  $2.5R_T$  (see Section 4.5). In this region the FL-grid contains no grid points. To distinguish the coordinates of the two grids we label the coordinates and the indices of the coordinates in the FL-grid with the index  $fl$ . Then  $(i, j, k)$  labels a position in the ZEUS-grid and  $(i_{fl}, j_{fl}, k_{fl})$  labels a position in the FL-grid and

$$x_{fl} = x(i_{fl}, j_{fl}, k_{fl}) \quad (4.37)$$

$$y_{fl} = y(i_{fl}, j_{fl}, k_{fl}) \quad (4.38)$$

$$z_{fl} = z(i_{fl}, j_{fl}, k_{fl}). \quad (4.39)$$

All grid-points with the same  $i_{fl}$  and  $j_{fl}$  belong to the same flux tube and  $z_{fl}$  is parallel to the magnetic field at problem initialization. To ensure that the electrons belong always to the same flux tube, the FL-gridpoints moves with the plasma bulk velocity.

From timestep  $n$  to timestep  $n + 1$  the FL-grid moves as:

$$x_{fl}^{n+1} = x_{fl}^n + \Delta t v_x(x_{fl}^n, y_{fl}^n, z_{fl}^n) \quad (4.40)$$

$$y_{fl}^{n+1} = y_{fl}^n + \Delta t v_y(x_{fl}^n, y_{fl}^n, z_{fl}^n) \quad (4.41)$$

$$z_{fl}^{n+1} = z_{fl}^n + \Delta t v_z(x_{fl}^n, y_{fl}^n, z_{fl}^n) \quad (4.42)$$

where  $v_x, v_y, v_z$  are the velocities on the Zeus-grid interpolated to the position  $(x_{fl}, y_{fl}, z_{fl})$  on the FL-grid. Note, that after the first time step the FL-grid is not anymore regular because it follows the flow around the obstacle. We want to point out that because of the frozen-in magnetic field still all the points with the same  $i_{fl}$  and  $j_{fl}$  belong to the same flux tube. The chosen grid makes it quite easy to calculate processes along the magnetic field lines since the  $k_{fl}$  index is along the magnetic field line.

In regions where magnetic diffusion is noticeable and plasma and magnetic field move relative to each other the FL-grid points follow the plasma and not the magnetic field. The name

flux tube loses its legitimation in that region. But the temperature equation of the magnetospheric electrons (Eq. 4.46) is still valid in this case except for the heat conduction which is isotropic then. We will see that the flux tubes do not enter the regions below 1100 km where this situation occurs (see Section 5.3 and Section 5.5.4).

One remark about the flux tube motion: In reality, the flux tubes move with the electron velocity rather than the plasma bulk velocity, which is equivalent to including the Hall term into the induction equation (Eq. (4.25)). In this work the Hall term is neglected in the induction equation. In order to keep the FL-model consistent with that, the flux tubes are moved with the plasma bulk velocity,  $\vec{v}$ .

#### 4.4.2 Continuity equation of magnetospheric electrons

When electrons are produced from the neutral gas by electron impact they are much cooler than the producing magnetospheric electrons (ms-electrons) *Banks and Kockarts [1973a]*. The newly created cooler electrons are not involved in the ionization, excitation and heat conduction processes as the ms-electrons, because their temperature is too low. They form a different population of ionospheric electrons and their number is determined by the continuity equation (4.22). The number of ms-electrons is not changed by the ionization processes. The loss rate of ms-electrons is negligible due to their low density and their high temperature ( $L \sim T^{-1/3} n_{ms}^2$ ). Thus, the continuity equation of the ms-electrons contains no sources and sinks and is given by

$$\frac{\partial n_{ms}}{\partial t} + \vec{\nabla} \cdot (n_{ms} \vec{v}) = \frac{dn_{ms}}{dt} + n_{ms} \vec{\nabla} \cdot \vec{v}. \quad (4.43)$$

Although the total number of the ms-electrons is constant, the local number density is not constant. In the comoving frame of the FL-grid the number density changes due to the divergence of the flow (last term in Eq. (4.44)) which in our model is added as a source term.

Note that although the total number of the ms-electrons is constant, their ability to ionize is limited due to their finite amount of energy.

As discussed before, the motion of the ms-electrons with the plasma bulk velocity is consistent with the neglect of the Hall term in the induction equation. Further, it implies that the bulk velocity of the ionospheric electron species and the ms-electron species are equal which is achieved by the elastic energy transfer (see Eq. (4.46)) and by the electric field (both gyrate around the same magnetic field lines).

#### 4.4.3 Temperature equation of magnetospheric electrons

The magnetospheric electrons (ms-electrons) are described by a Maxwell distribution and are thereby determined by two parameters, the number density and the temperature. This is in accordance with the incident magnetospheric electron distribution measured by Voyager 1 *Hartle et al. [1982]*. Let us regard the magnetospheric electron density at a position  $\vec{r}$  moving along with the plasma bulk velocity and the frozen-in magnetic field. As it approaches Titan it comes into contact with the neutral atmosphere and the electrons start to exchange energy

with the neutral gas by exciting the neutral particles and ionizing them leading to a local cooling of the ms-electrons. The so established gradient in temperature of the ms-electrons causes heat conduction along the magnetic field lines (Figure 4.2). (The gyration of the electrons around the magnetic field lines prevents them from transferring energy perpendicular to the magnetic field (see discussion at the end of this section)). The local change of temperature of the ms-electrons by these processes also alters the total plasma pressure and is therefore included in Eq. (4.26).

The inelastic energy transfer from the neutral gas to the electrons can be neglected in the first place since the neutral gas temperature is at least two orders of magnitude lower than the electron temperature and the energy transfer takes primarily place from the more energetic to the less energetic fluid. This assumption becomes wrong when the electron temperature approaches the neutral gas temperature. As an approximation we use the neutral gas temperature as a lower bound for the electron temperature.

Apart from inelastic energy transfer and heat conduction, there are also elastic collisions of the ms-electrons with the neutral gas which are effectively already contained in the equation for the total plasma pressure (4.26). The elastic terms also have to appear in the equation for the temperature of the ms-electrons in order to calculate their temperature in the right way. Combining the continuity equation

$$\frac{\partial n_{ms}}{\partial t} + \vec{\nabla} \cdot (n_{ms} \vec{v}) = 0 \quad (4.44)$$

and the equation for the electron internal energy (Eq. (4.13) and Eq. (4.16) without production and loss)

$$\frac{\partial \frac{3}{2} n_{ms} k T_e}{\partial t} + \vec{\nabla} \cdot \left( \frac{3}{2} n_{ms} k T_e \vec{v} \right) = -n_{ms} k T_e \vec{\nabla} \cdot \vec{v} + R \quad (4.45)$$

we obtain an equation for the electron temperature:

$$\begin{aligned} \frac{3}{2} n_{ms} k \frac{dT_e}{dt} &= -n_{ms} k T_e \vec{\nabla} \cdot \vec{v} + HC \\ &\quad - \sum_{ns} (K_{ion,ns} + K_{ex,ns}) n_{ms} n_{ns} \\ &\quad + \sum_{ns} \nu_{e,ns} n_{ms} \frac{m_e}{m_{ns}} (3k(T_{ns} - T_e) + m_{ns} \vec{v}^2) \end{aligned} \quad (4.46)$$

where  $R$  in Eq. (4.45) is explicitly written in Eq. (4.46).  $K_{ex}$  and  $K_{ion}$  (Eq. (4.47)) are the coefficients for cooling due to excitation and ionization of the neutral gas and  $HC$  is the heat conduction term (Eq. (4.50)).  $\nu_{e,ns}$  is the elastic momentum transfer collision frequency of the ms-electrons with the neutral gas (see explanation after Eq. (4.17)). The terms on the right side of Eq. (4.46) are adiabatic heating, heat conduction, inelastic cooling, and elastic energy transfer with neutral gas. For the heat conduction we assume that it is confined to the magnetic field lines. There is no energy transfer within the magnetospheric electrons perpendicular to the magnetic field. As discussed in *Banks and Kockarts* [1973b] the heat conduction perpendicular to the magnetic field is a factor of  $\frac{1}{1+\Omega_e^2/\nu_e^2}$  lower than heat conduction parallel to the magnetic field.  $\nu_e$  is the collision frequency of the electrons with the neutral gas and  $\Omega_e$  the electron gyrofrequency. Our model is valid as long as the gyrofrequency is higher than the collision frequency. At high altitudes this is perfectly fulfilled since the neutral gas

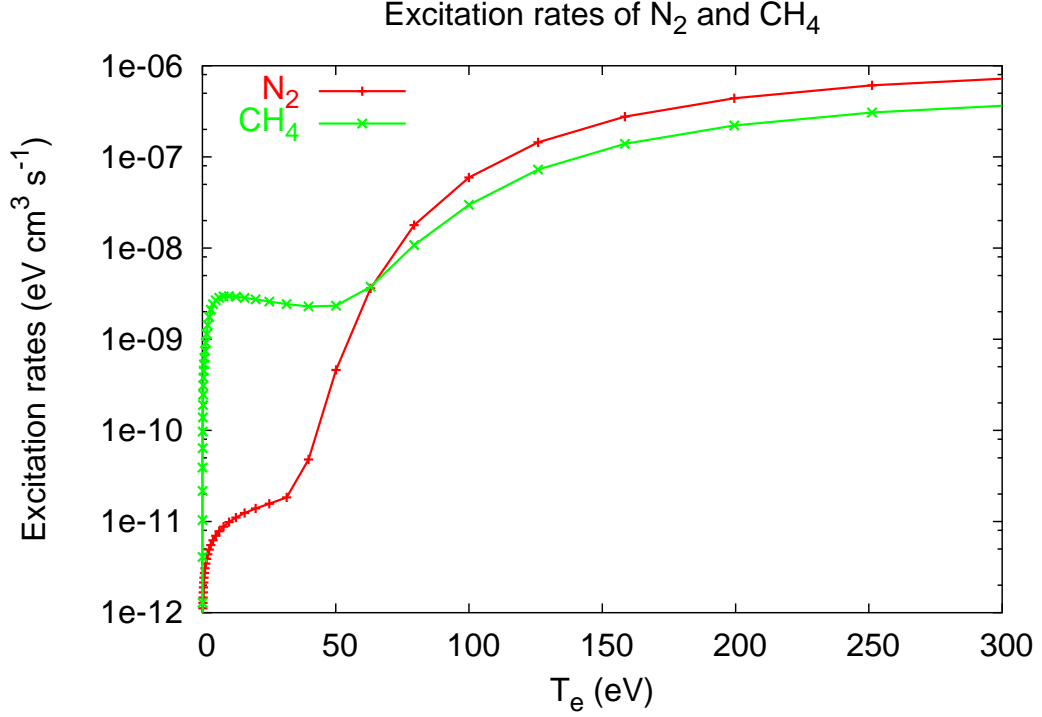


**Figure 4.3:** Total cooling rates due to excitation of  $N_2$  and  $CH_4$ . Ionization is not included.

density is low there. At an altitude of about 900 km both frequencies are in the same order of magnitude. But flux tubes are prevented from entering this region by collisions with the neutral gas and by ionospheric plasma (see Section 5.2.2). Thus, assuming heat conduction to occur solely along the magnetic field is a good approximation.

In the following we describe how the different processes are calculated in the model.

#### 4.4.3.1 Adiabatic heating and elastic energy transfer

The adiabatic heating is included simply as a source term by calculating the divergence of the velocity. The term for the elastic energy transfer in Eq. (4.45) is calculated in the same way as in the equation for the total plasma internal energy (Eq. (4.26)). The collision frequency as a function of temperature is taken from *Keller* [1992].

#### 4.4.3.2 Inelastic cooling and impact ionization rates

The cooling coefficients  $K_{ion}$  and  $K_{ex}$  contain the cooling due to excitation and ionization. They are calculated by integrating the given distribution function with the appropriate cross sections *Banks and Kockarts* [1973a].

$$K_{p,ns} = \int_0^{\infty} dE E_p f_E(E) \sigma_{p,ns}(E) v(E) \quad (4.47)$$

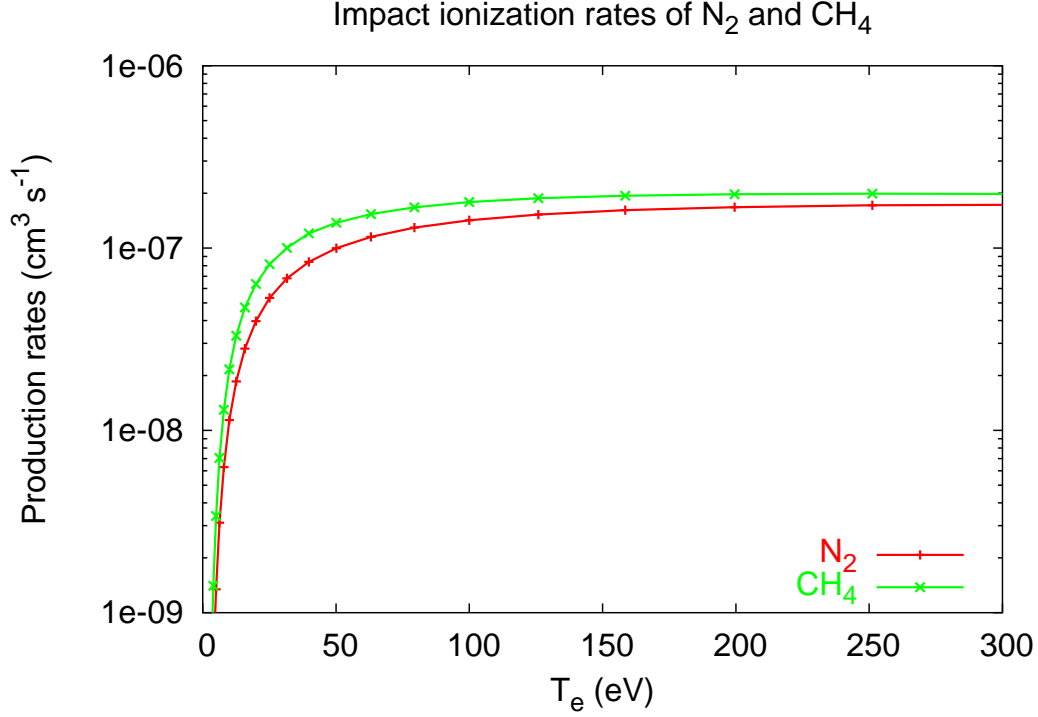


**Figure 4.4:** Electron impact ionization rates of  $N_2$  and  $CH_4$  as function of electron temperature

$p$  stands for ionization or the different excitation processes.  $f_E$  denotes the normalized distribution function in energy space

$$f_E(E) = \frac{2\sqrt{E}}{\pi} (kT_e)^{-1.5} \exp\left\{-\frac{E}{kT_e}\right\}. \quad (4.48)$$

The velocity at a given energy is  $v(E) = \sqrt{2E/m_e}$ . Figure 4.3 shows the solution of Eq. (4.47) as a function of electron temperature summed over all included excitation processes. For  $N_2$  the considered processes are electronic excitations taken from *Banks and Kockarts* [1973a], vibrational and rotational excitations taken from *Schunk and Nagy* [2000], and ionization taken from the *NIST* database [Kim et al., 1997]. The appropriate data for  $CH_4$  is taken from *Gan and Cravens* [1992].

With the temperature  $T_e$  from Eq. (4.47) and the density  $n_{ms}$  from Eq. (4.44) the impact ionization rate per volume by ms-electrons is given by

$$P_{ns,ms} = n_{ms}n_{ns} \int_{E_{ion}}^{\infty} dE f_E(E) \sigma_{ion,ns}(E) v(E). \quad (4.49)$$

Figure 4.4 shows the ionization rates of  $N_2$  and  $CH_4$  as a function of the electron temperature.

#### 4.4.3.3 Heat conduction

The heat conduction, the first term on the right side of Eq. (4.46), is assumed to occur solely along the magnetic field lines. Therefore we have chosen an appropriate grid geometry for

the flux tube model. As explained at the beginning of this chapter, the grid points of the flux tube model move with the plasma bulk velocity as does the magnetic field. That means, all the grid points that belong to the same field line at problem initialization do so for the rest of the simulation time. During simulation time the FL-grid loses its irregular character which introduces a metric factor into the heat conduction part of Eq. (4.46)

$$HC = -\vec{B} \cdot \vec{\nabla}(B^{-1}Q) \quad (4.50)$$

where the inverse magnetic field is a measure for the cross sectional area of a flux tube ( $\sim B^{-1}$ ).

The heat conduction vector  $\vec{Q} = (0, 0, Q)$  is proportional to the temperature gradient along  $\vec{B}$

$$Q = -\kappa \frac{\vec{B}}{B} \cdot \vec{\nabla} T_e \quad (4.51)$$

with the heat conduction coefficient

$$\kappa = \frac{7.7 \times 10^5 T_e^{2.5}}{1 + 3.22 \times 10^4 T_e^2 / n_{ms} (\sum_n \bar{\sigma}_{en} n_n + \frac{5}{4} \bar{\sigma}_{eeth} n_{eeth})} \left[ \frac{\text{eV}}{\text{cm s K}} \right]. \quad (4.52)$$

with  $\bar{\sigma}_{en}$  and  $\bar{\sigma}_{eeth}$  the Maxwellian average elastic momentum transfer cross sections for the interaction of ms-electrons with the neutral gas and the thermal electrons (for the derivation of Eq. (4.52) see section A.2). The advantage of the FL-grid is that the derivatives along  $\vec{B}$  can be easily represented in finite difference form

$$\vec{B} \cdot \vec{\nabla}(B^{-1}T_e) = B \frac{(B^{-1}T_e)|_{i_{fl}, j_{fl}, k_{fl}+1} - (B^{-1}T_e)|_{i_{fl}, j_{fl}, k_{fl}}}{|\vec{r}(i_{fl}, j_{fl}, k_{fl}+1) - \vec{r}(i_{fl}, j_{fl}, k_{fl})|} + O \quad (4.53)$$

with  $\vec{r}(i_{fl}, j_{fl}, k_{fl}) = (x_{fl}, y_{fl}, z_{fl})$  and  $O$  the error of the finite difference approximation.

For the heat conduction we assume that the plasma torus extends along  $\pm 100$  Titan radii along the magnetic field with a constant electron density. This agrees with the model of *Richardson* [1998] of the Saturnian magnetosphere (Figure 4.5). The torus serves as an energy reservoir and the heat conduction process couples Titan's ionosphere to this reservoir.

The coefficient for electronic heat conduction given in Eq. (4.52) varies over several orders of magnitude. This makes the numerical treatment of the heat conduction difficult. The higher the heat conduction coefficient the lower the time steps for the heat conduction process have to be chosen, i.e. the maximum heat conduction coefficient determines the time scale for the heat conduction.  $\kappa$  is highest outside of the interaction region where the denominator in Eq. (4.52) is equal to one. In that region  $\kappa$  is that high that it assures isothermal conditions. For the numerical treatment we have limited  $\kappa$  such that it still assures isothermal conditions outside of the interaction region on the time MHD time scale. The temperature in that region is anyway determined by the heat flux to the cooled region in the atmosphere and therefore by  $\kappa$  at the border of the cooled region. At this location  $\kappa$  is below our artificial limit. Thus, the heat conduction problem is treated correctly in our model.

#### 4.4.4 The flux tube model and energy conservation

The MHD model describes one effective plasma species which is characterized by 8 parameters,  $\rho, e, \vec{v}, \vec{B}$  (mass density, internal energy density, velocity and magnetic field vectors). The

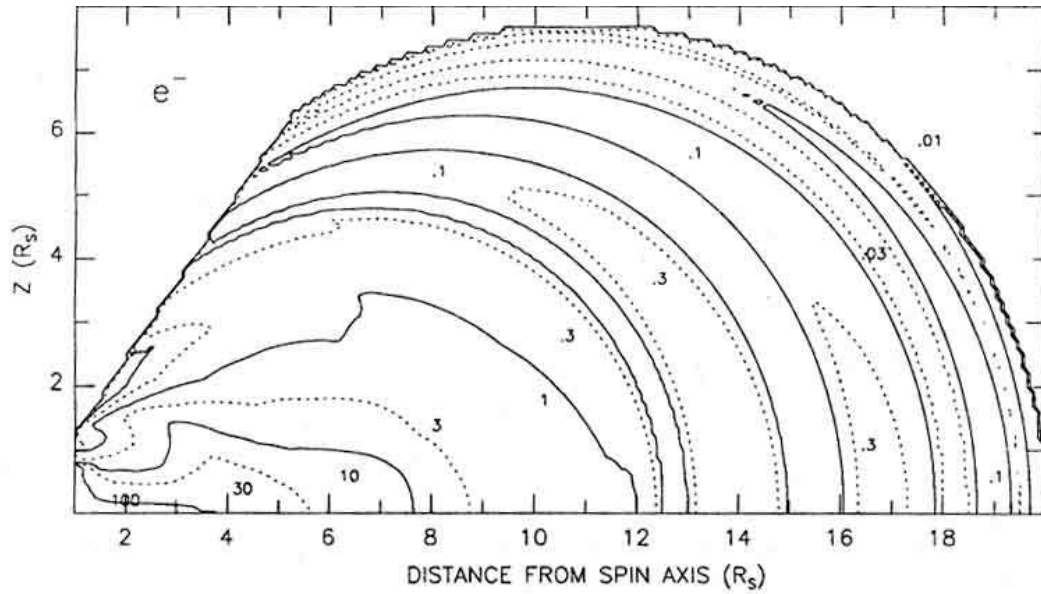


**Figure 4.5:** Electron density in the Saturnian magnetosphere in the plane perpendicular to Saturn's equatorial plane. Taken from Richardson [1998].

equation for the internal energy (4.26) describes the total plasma pressure of electrons and ions. The magnetospheric electrons are part of the total plasma and therefore give a contribution to the total pressure, but their energy equation ((4.45), (4.46)) is solved separately in the flux tube model. In this section we specify the extra contribution that the magnetospheric electrons give to the total plasma internal energy, i.e.  $\frac{\delta E_{ms}}{\delta t}$  in Eq. (4.26). Elastic collisions with the neutral gas and adiabatic change of internal energy of the magnetospheric electrons are effectively already contained in Eq. (4.26). Thus, the extra contributions of the magnetospheric electrons to the total internal energy are heat conduction ( $HC$ , Eq. (4.50)) and inelastic collisions

$$\frac{\delta E_{ms}}{\delta t} = HC - \sum_{ns} (K_{ion,ns} + K_{ex,ns}) n_{ms} n_{ns}. \quad (4.54)$$

#### 4.4.5 Other sources for ionization

Capone *et al.* [1976; 1980; 1981; 1983] and most recently Molina-Cuberos *et al.* [1999] have calculated the ionization rate by galactic cosmic radiation. In the upper-atmosphere ionization due to cosmic rays is negligible. But in the lower atmosphere ( $h < 400$  km) this effect produces a remarkable density of charged particles. Molina-Cuberos *et al.* [1999] obtain from their calculations a peak electron density of  $2000 \text{ cm}^{-3}$  at an altitude of  $h = 100$  km. The absolute value of the electron density is comparable to the ionospheric peak density [Ip, 1990; Keller *et al.*, 1992]. But in the low atmosphere the neutral gas density is several orders of magnitude higher than at the ionospheric peak. Therefore the plasma is completely determined by the neutral gas. But it may have an effect of the transport of magnetic field to the solid body and thereby on possible induction effects. However, in this model we neglect this low altitude ionosphere.

## 4.5 Model summary and initial conditions

The kernel of the model consists of Zeus3D (*Stone and Norman [1992a], Stone and Norman [1992b]*) which solves the time dependent ideal MHD equations in three dimensions. The extra terms that we have included into the model consider the effects of the neutral atmosphere on the plasma and are treated as source terms for the MHD equations. For the extra terms in the induction equation we use the semi-implicite Crank-Nicholson scheme [*Press, 1992*] to solve the magnetic diffusion equation. The model equations are the continuity equation (4.22), the momentum equation (4.24), the magnetic induction equation (4.25), and the equation for the internal energy (4.26).

The plasma production is due to photoionization and impact ionization by photo electrons and magnetospheric electrons. The photoionization rate is calculated at the beginning by integrating the solar EUV flux through the neutral atmosphere (see Section 4.2). The impact ionization by photoelectrons is calculated from the photoionization rate making simplifying assumptions (Section 4.3). In order to account for the energy transfer and impact ionization of the magnetospheric electrons we have developed a flux tube model which runs parallel to the MHD model (see Section 4.4). In the flux tubes the continuity equation (Eq. (4.44)) and the equation for the temperature (Eq. (4.45)) of the magnetospheric electrons are solved. For the heat conductions also the semi-implicite Crank-Nicholson scheme [*Press, 1992*] is used. Impact ionization rates and heating and cooling rates of the magnetospheric electrons are calculated and interpolated to the Zeus-grid.

In the used coordinate system the plasma streams along the  $x$ -axis, the background Saturnian magnetic field points in  $-z$ -direction, and the  $y$ -axis points towards Saturn and completes the right-handed system (see Figure 3.3). The center of Titan is in the origin of the coordinate system.

At  $t = 0$  the plasma velocity is constant ( $120 \text{ km s}^{-1}$ ) everywhere except for a sphere around Titan with a radius of  $3.5 R_T$ . In the shell from  $3.5 R_T$  to  $2.5 R_T$  the velocity decreases linearly and is zero inside the sphere with a radius of  $2.5 R_T$ . The magnetic field is constant ( $5 \text{ nT}$ ) and parallel to the  $-z$ -axis. In a cylinder parallel to the  $z$ -axis with a radius of  $2.5 R_T$  the magnetic field is set to zero at problem initialization and increases linearly in the cylindrical shell from  $2.5 R_T$  to  $3.5 R_T$ . We have chosen these initial conditions for the magnetic field in order to ensure that any magnetic field inside of Titan's atmosphere originates from the magnetospheric field, has been transported to that position, and is not a consequence of the initial conditions. Thermal pressure ( $1.1 \times 10^{-10} \text{ bar}$ ) and plasma mass density ( $2.9 \text{ amu cm}^{-3}$ ) are constant everywhere except for the ionospheric region.

For the initial ionosphere a spherical symmetric photo-ionosphere is created and then the continuity equation and the equation for the internal energy is solved for a time of 1/4 of a Titan day. On the nightside, the atmosphere at the location just before dawn has spend half a Titan day in darkness and near dusk the atmosphere has just entered darkness. Then, on average an atmospheric volume element on the nightside has spent 1/4 of a Titan day in darkness. Of course this is only true at equinoctium. For posing the initial conditions we neglect seasonal effects. Thus, the model starts with an ionosphere that is already cooler

than the background plasma and has a 3D structure with reasonable plasma densities on the nightside  $\sim 10 \text{ cm}^{-3}$ .

The Zeus-grid is divided into three regions with different spatial resolutions: a high resolution region  $[[ -2, 4], [ -2, 2], [ -2, 2]]$  (units in  $R_T$ ) with a grid size of 257 km, a medium resolution region in a shell (thickness  $2 R_T$ ) around the high resolution region with a grid size of 644 km, and a low resolution region with a grid size of 2575 km. The total grid volume is  $[[ -10, 15], [ -8, 8], [ -10, 10]]$ .

The initial FL-grid is identical with the Zeus-grid but with double resolution in the  $y$  and the  $z$  coordinate. The cylinder parallel to the  $z$ -axis with a radius of  $2.8 R_T$  contains no points in the FL-grid since  $B = 0$  in that region. For the heat conduction process the flux tubes are extended along  $z$ -axis from  $-100R_T$  to  $100R_T$  to account for the magnetospheric energy reservoir. In that region the heat conduction coefficient is very large and the outer parts of the flux tube are isothermal. The extended part of a flux tube has the same temperature as the grid point that connects the extended part with the standard grid. Thus, the procedure is: flux tubes are extended, heat conduction is calculated, extended parts are cut to calculate the other processes in the temperature equation.

The initial temperature of the magnetospheric electrons is 200 eV and the number density is  $0.3 \text{ cm}^{-3}$ . As the simulation starts, the FL-grid moves with the streaming plasma and from the inflow boundary new flux tubes enter the simulation box. When a plane of flux tubes enters the box another plane of flux tubes is deleted, which implies a finite lifetime of a flux tube in the model of  $\sim 50$  minutes. As the results show, this lifetime is sufficient for the flux tubes to pass the point in the ionosphere where impact ionization rate peaks. A longer lifetime would not change the production rates, but the flux tubes that enter the deep atmosphere would be more depleted of energy than they are in our model. The rate for the depletion decreases with time as the temperature gradient along the flux tubes decrease (typical for diffusion) and by that the heating rates of the ionosphere decrease. Additionally, in the lower ionosphere the collisions with the neutral gas completely determine the temperature. Thus, the chosen finite lifetime has neither an impact on the impact ionization rates nor on the ionospheric heating rates.

The solid body of Titan is simulated as a sphere with background plasma density. The internal energy is such that the radial pressure gradient on the surface is zero. The zero velocity inside of Titan is achieved by the high collision frequency of the plasma with the neutral atmosphere. Note that the model does not contain magnetic induction effects on the solid body which may be present at the real Titan.

The model has an explicit time dependence. The results presented here are at  $t = 54$  min after problem initialisation. A typical time scale is the time it takes the incident plasma to move one Titan radius, i.e.  $\tau = R_T/v_0$ . With the incident plasma parameters given above the time scale of the model is  $\tau = 21.46$  s. In that time unit the results presented are from  $t = 150\tau$ . At this time the model is stationary.

One of the specialities of the incident plasma is its sub-sonic character. In a subsonic (and sub-fast) plasma the fast MHD mode propagates towards the inflow boundary of the simulation box. The ZEUS model only allows basically two types of boundary conditions: inflow

	V1	This model
Magnetic field magnitude	5 nT	3.77 nT
Mean plasma flow speed	120 kms <sup>-1</sup>	113 kms <sup>-1</sup>
Mass density	2.9 amucm <sup>-3</sup>	2.24 amucm <sup>-3</sup>
Thermal pressure	$1.1 \times 10^{-10}$ Pa	$0.7 \times 10^{-10}$
Plasma beta $\beta = p/(B^2/(2\mu_0))$	11.1	12.4
Alfvén speed	64 kms <sup>-1</sup>	55 kms <sup>-1</sup>
Sound speed ( $\gamma = \frac{5}{3}$ )	191 kms <sup>-1</sup>	177
Fast magnetoacoustic speed	201 kms <sup>-1</sup>	185 kms <sup>-1</sup>
Alfvén Mach number	1.9	2.05
Sonic Mach number	0.57	0.64
Fast Mach number	0.55	0.61

**Table 4.1:** Incident plasma properties during the Voyager 1 encounter taken from Neubauer et al. [1984] and from this model. In this table  $\gamma = \frac{5}{3}$  is used while Neubauer et al. [1984] use  $\gamma = \frac{5}{3}$  (see Table 2.2)

(all variables on the boundary are set) outflow (none of the variables is set on the boundary). For a subsonic problem both types are not adequate. To reduce the problem we have chosen a quite large simulation box such that the amplitude of the fast mode that reaches the boundary is very low. But we observe an interesting effect: Due to the fast mode the value of all variables in the first grid cell differs from the value set on the boundary. Inside of the simulation box the (on the first cells) the values then are constant. Therefore the incident plasma parameters in our model differ by a small amount from the values during the Voyager 1 encounter. Table 4.1 compares the two sets of parameters. The basic plasma properties are equal.



---

## RESULTS

---

Since Cassini/Huygens has reached Saturn and the first near Titan flyby is close, we have the unique chance that the results from the model can be compared with real data measured at Titan. Therefore, it is reasonable to choose the parameters in the model such that they fit the situation that Cassini is expected to meet at Titan. In this sense the results of three cases are presented here corresponding to the expected conditions at Cassini flybys TA, T5, and T34. We have chosen TA because it represents the first close flyby and thereby the first chance to validate the model. At T5 the magnetospheric plasma nearly streams towards Titan's nightside and at T34 it nearly streams towards Titan's dayside, the two situations where the difference of the upstream ionospheric properties is largest.

In the next section we summarize the characteristics of the three cases and in the subsequent sections the results are compared.

### 5.1 Model situations

The expected solar activity state during the Cassini mission is near solar minimum *Schatten and Pesnell* [1993]. The proxy for the solar conditions in the EUVAC *Richards et al.* [1994] model for the solar EUV has been set appropriate for solar minimum conditions for all the three cases. During the Cassini encounter, Titan (and Saturn) is in late southern summer, i.e. the south pole is illuminated while the north pole is dark. The corresponding parameter in the model is the sub solar latitude (SSL) which is negative in all cases. The position of Titan with respect to Saturn and the solar position in the equatorial plane is determined by the Saturnian local time (SLT, see Figure 5.1). The angle between the Sun-Titan line and the plasma flow direction is determined by the two parameters SSL and SLT.

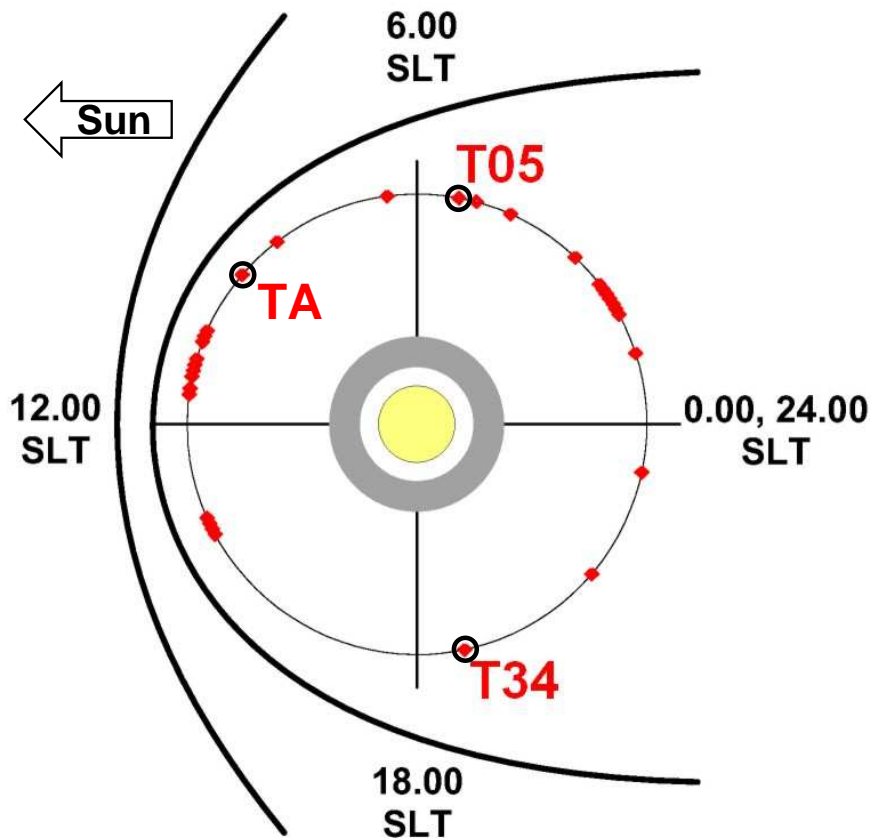


**Figure 5.1:** SLT at Titan at the Cassini flyby times (square dots). The black circles mark the three simulated cases.

### 5.1.1 TA

TA is a close flyby through the northern tail region with the nominal closest approach altitude of 1200 km. The upstream hemisphere corresponds to Titan's dawn side. The season at Titan is short after mid-summer. The trajectory and the characteristic parameters are displayed in Figure 5.2. Titan's position within the Saturnian magnetosphere is near the magnetopause (see Figure 5.1) indicating that there is a slight chance for Titan to be outside of the Saturnian magnetosphere [Siscoe, 1978; Schardt *et al.*, 1984]. But it is more probable that Titan is inside of the magnetosphere and that the results presented here are applicable. The angle between Sun-Titan line and plasma flow direction is  $70.8^\circ$  in this case.

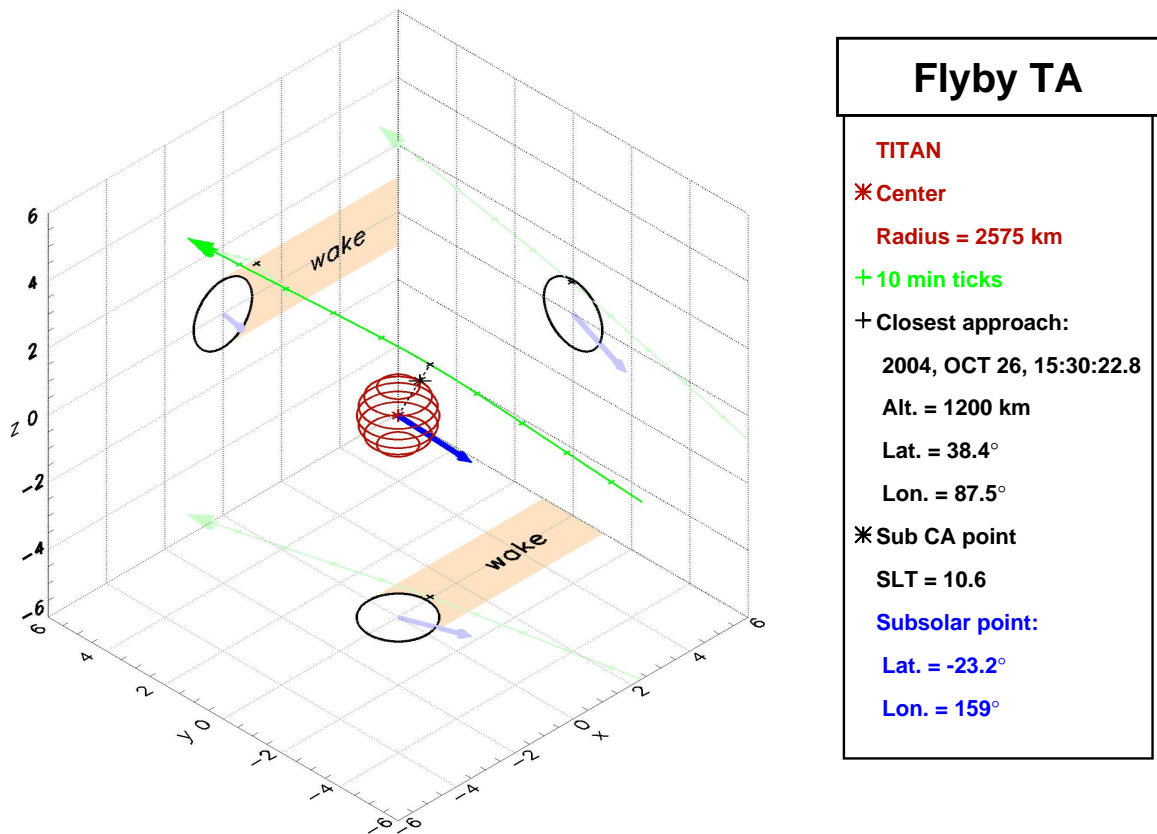


*Figure 5.2: Cassini trajectory at Titan flyby TA and characteristic parameters.*

### 5.1.2 T5

T5 nearly represents case in which the Saturnian magnetospheric plasma streams towards Titan's nightside. This is the situation where the magnetospheric electrons are essential for the upstream ionosphere. The nominal closest approach altitude is 950 km. The north polar flyby bares a good chance for the detection of a potential internal magnetic dipole. At T5 conditions, the probability for Titan being inside of the Saturnian magnetosphere is nearly 100%. The angle between Sun-Titan line and plasma flow direction is  $24.3^\circ$  in this case.

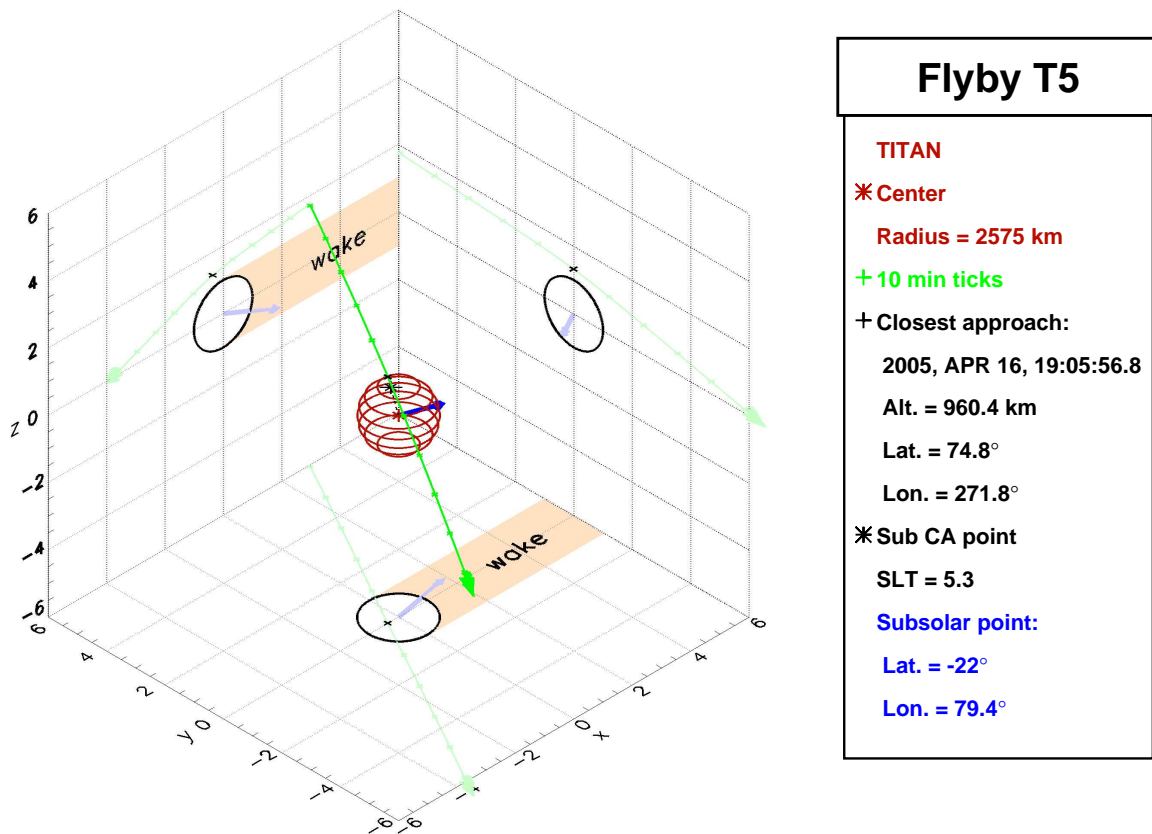


Figure 5.3: Cassini trajectory at Titan flyby T5 and characteristic parameters.

### 5.1.3 T34

At T34 the upstream hemisphere is identical with Titan's dayside. Thus, it represents the opposite case with respect to T5. Here, the plasma streams towards the dayside, i.e. the photoionosphere, and the magnetospheric electron have the deepest impact on the downstream side. The Cassini flyby trajectory is nearly exactly in the equatorial plane (see Figure 5.4). The closest approach altitude is 1301 km. T34 offers a good opportunity to observe the structure of the upstream magnetic pile-up region. At T34 the angle between Sun-Titan line and plasma flow direction is  $16.4^\circ$

## 5.2 Ionosphere

The real Titan ionosphere consists of a lot of chemical compounds and chemical reactions respond to changes in pressure, temperature, or energy input. It is beyond the scope of this work to reproduce the ionosphere in detail. This is done in 1D models by *Ip* [1990], *Keller et al.* [1992], *Mücke-Herzberg* [1998], and *Galand et al.* [1999]. In this model the response of the main ionospheric properties, which are electron density, thermal pressure, and magnetization, to the plasma interaction is examined. Ionospheric production rates from photoionization and impact ionization from photoelectrons and magnetospheric electrons (ms-electrons)

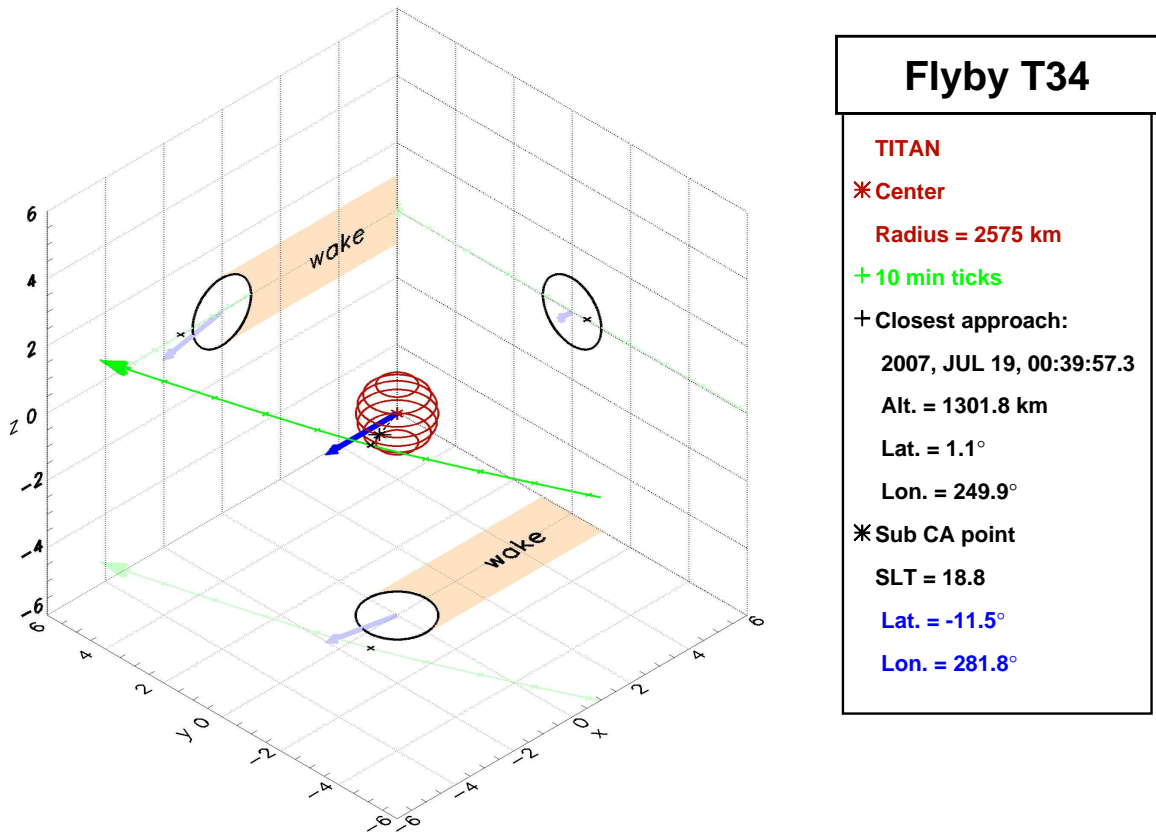


**Figure 5.4:** Cassini trajectory at Titan flyby T34 and characteristic parameters.

are calculated within the model. The ionization by ms-electrons depends on the magnetic field geometry and on the path a flux tube takes through the atmosphere. To account for these dependencies a flux tube model has been developed. To our knowledge, this is the first model that calculates impact ionization rates of ms-electrons at Titan in 3D. The resulting ionosphere is described in this section.

### 5.2.1 Plasma production rates

Plasma is produced by photoionization and by impact ionization from photoelectrons and magnetospheric electrons. In Figure 5.5 the electron production rates are plotted along the  $x$ -axis for the T34 case. In that case the negative  $x$ -axis is through the dayside ionosphere and the positive  $x$ -axis is through the nightside ionosphere. Additionally to the production rate the resulting ionospheric electron density ( $n_e$ ) is plotted. In contrast to early assumptions [Sittler Jr. *et al.*, 1983; Strobel and Shemansky, 1982; Bauer, 1985; 1987; McNutt Jr. and Richardson, 1988], on the dayside photoionization is by far the most important production process followed by the ionization by photoelectrons. Production by impact of ms-electrons takes only a small fraction of the total production rate in accordance with the models of Keller *et al.* [1992] and Gan *et al.* [1992]. Since the two leading processes are initiated by the solar EUV radiation, both of them are absent in the nightside ionosphere and the only plasma production is by ms-electrons. The peak rates on the dayside are  $P_{ph} = 22.3 \text{ cm}^{-3}\text{s}^{-1}$ ,

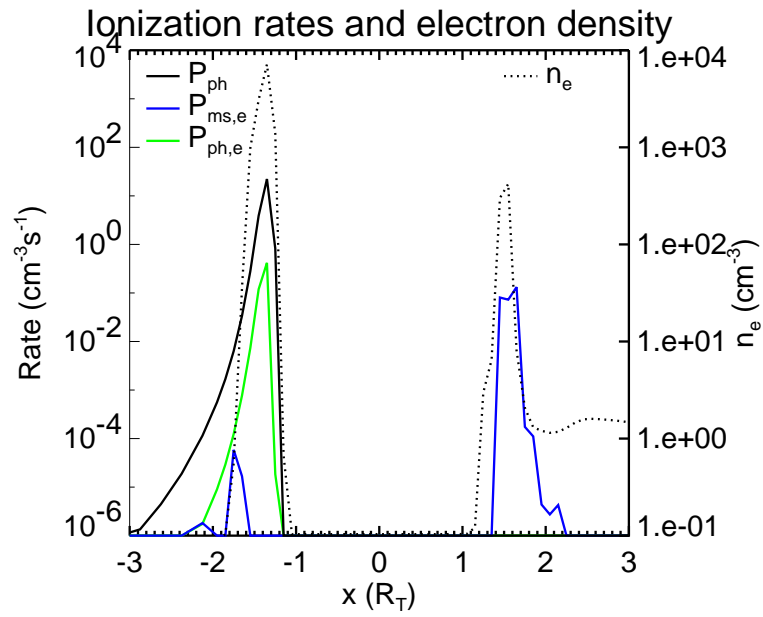


**Figure 5.5:** Production rates and electron density profile along the  $x$ -axis (upstream/downstream) for T34 conditions

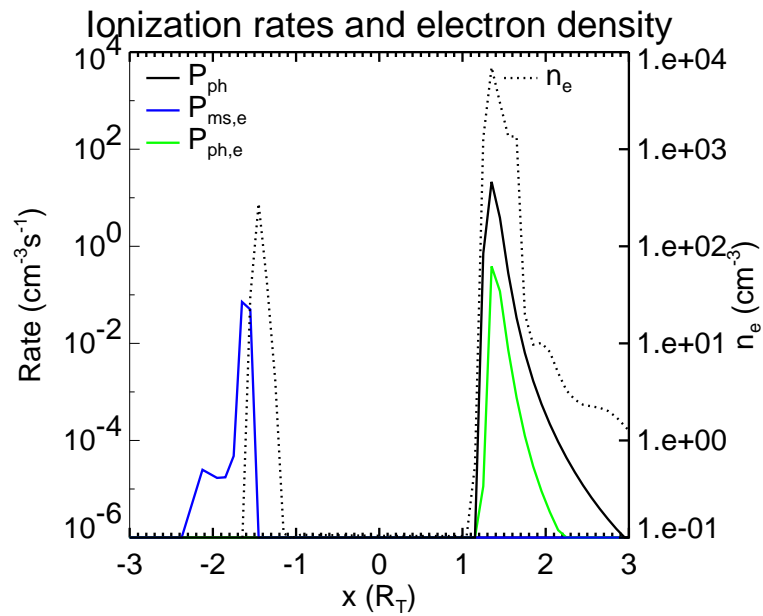


**Figure 5.6:** Production rates and electron density profile along the  $x$ -axis (upstream/downstream) for T5 conditions.

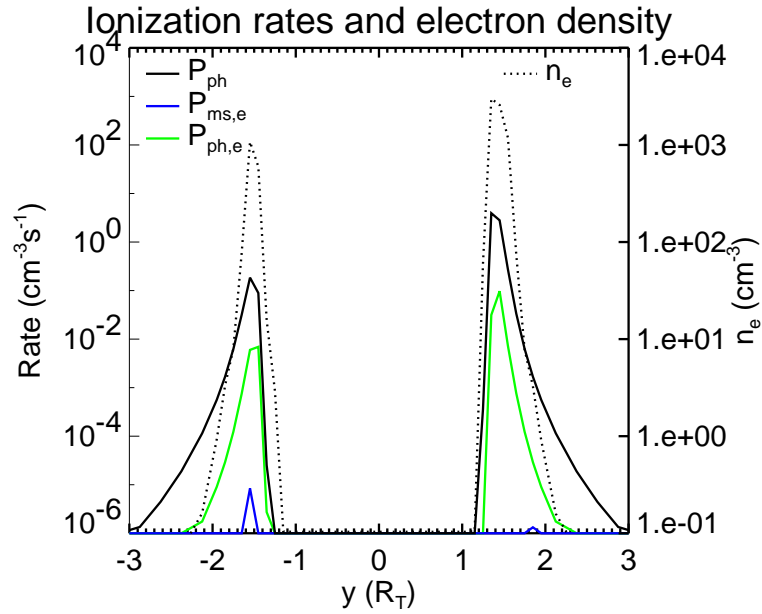


**Figure 5.7:** Production rates and electron density profile along the  $y$ -axis (flanks) for T34 conditions

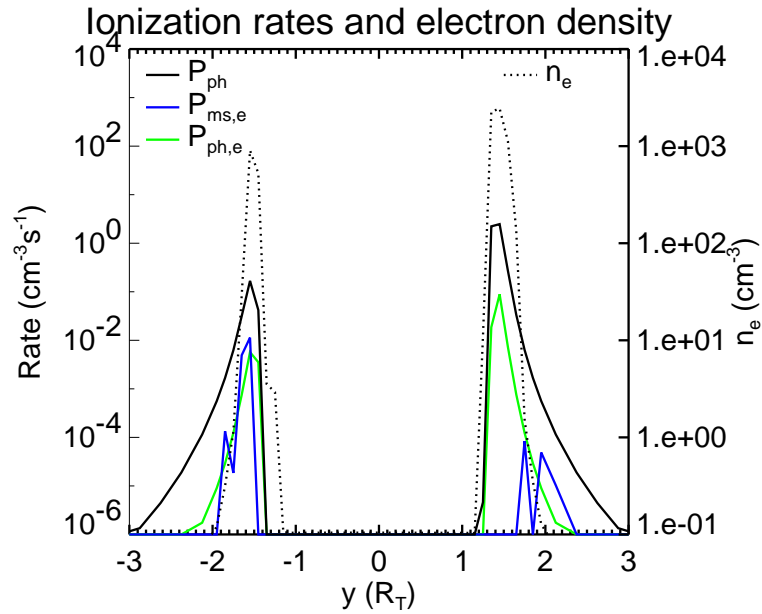


**Figure 5.8:** Production rates and electron density profile along the  $y$ -axis (flanks) for T5 conditions

$P_{pe} = 0.4 \text{ cm}^{-3}\text{s}^{-1}$ , and  $P_{ms} = 6 \times 10^{-5} \text{ cm}^{-3}\text{s}^{-1}$  with the resulting electron peak density of  $n_e = 7165 \text{ cm}^{-3}$  (with  $P_{ph}$  photoionization rate,  $P_{pe}$  ionization rate by photoelectrons, and  $P_{ms}$  the ionization rate by magnetospheric electrons). On the downstream nightside is  $P_{ph} = P_{pe} = 0$  and  $P_{ms} = 1.3 \text{ cm}^{-3}\text{s}^{-1}$  with a resulting peak electron density of  $n_e = 420 \text{ cm}^{-3}$ . The altitude of the dayside electron peak ( $h = 901 \text{ km}$ ) is lower than the nightside electron peak altitude ( $h = 1416 \text{ km}$ ).

The opposite case, where the dayside corresponds to the downstream side (positive  $x$ -axis)

and the nightside faces the upstream direction (negative  $x$ -axis) is at T5 conditions. Production rates and resulting electron densities along the  $x$ -axis are displayed in Figure 5.6. In this case the dayside peak rates are  $P_{ph} = 21.3 \text{ cm}^{-3}\text{s}^{-1}$  and  $P_{pe} = 0.4 \text{ cm}^{-3}\text{s}^{-1}$ . There is no plasma production from ms-electrons on the dayside. The reason for that is that on the downstream dayside the flux tubes with the ms-electrons are not able to enter the region with sufficiently high neutral gas density for the production. The resulting electron density peaks at  $n_e = 6997 \text{ cm}^{-3}$  at an altitude of  $h = 901 \text{ km}$ . The small differences in photo-production rate and peak density compared to the dayside of the T34 case arise from the fact that the angle between the Titan-Sun axis and the  $x$ -axis is larger in the T5 case (see Figures 5.4 and 5.3). On the upstream nightside ms-electrons are the only source for plasma production. The peak rate is  $P_{ms} = 0.07 \text{ cm}^{-3}\text{s}^{-1}$  at an altitude of  $h = 1674 \text{ km}$  leading to an electron peak density of  $n_e = 276 \text{ cm}^{-3}$  at an altitude of ( $h = 1158 \text{ km}$ ). The altitude of the peak electron density is lower than the altitude of the production rate because after the plasma is produced it is transported further down into the atmosphere.

Production rates and electron densities at the flanks are shown in Figure 5.7 for the T34 case and in Figure 5.8 for the T5 case. The flank plasma production is dominated by photoionization in both cases. Since the Titan-Sun direction is approximately along the  $x$ -axis the flanks correspond to the morning and evening terminator and thereby to the positions where the Voyager 1 radio occultation observations provided electron peak densities and altitudes. The analyses of the data by *Lindal et al.* [1983] gives upper bounds for the peak densities of  $3000 \text{ cm}^{-3}$  for the evening terminator (which was in Titan's tail region during the Voyager 1 flyby) and  $5000 \text{ cm}^{-3}$  for the morning terminator. In their reanalysis of the dual frequency Doppler data *Bird et al.* [1997] obtained an electron peak density of  $2400 \text{ cm}^{-3} \pm 1100 \text{ cm}^{-3}$  at an altitude of  $1180 \text{ km} \pm 150 \text{ km}$  for the evening terminator. We obtain at the Saturnian flank  $2998 \text{ cm}^{-3}$  at  $901 \text{ km}$  for T34 and  $2446 \text{ cm}^{-3}$  at  $1159 \text{ km}$  for T5, and at the anti-Saturnian flank  $1077 \text{ cm}^{-3}$  at  $1416 \text{ km}$  for T34 and  $905 \text{ cm}^{-3}$  at  $1416 \text{ km}$  for T5. Both, the model densities and altitudes, agree well with the observed values.

Production rates and electron densities along the  $z$ -axis, i.e. in the polar regions are displayed in Figure 5.9 for the T34 case and in Figure 5.10 for the T5 case. The negative  $z$ -axis is towards the south pole and the positive  $z$ -axis is towards the north pole. The sub solar latitude (SSL) is negative in both cases, i.e. the south pole is illuminated by the Sun leading to higher production rates and peak densities over the south pole. In order to get a better impression about what the ionospheric electron density looks like in 3D, the electron density is plotted in blue color contours in Figures 5.11, 5.12, 5.13 for T34 and Figures 5.14, 5.15, 5.16 for T5.

The ionospheric electron density from our model agrees well with the Voyager 1 measurements at the terminator and with the model of *Keller et al.* [1992]. They obtained a peak photoionization rate of  $17 \text{ cm}^{-3}\text{s}^{-1}$  at an altitude of  $1050 \text{ km}$  for a solar zenith angle of  $60^\circ$  while in this model the production rate at a solar zenith angle of  $70^\circ$  is  $7 \text{ cm}^{-3}\text{s}^{-1}$  at an altitude of  $901 \text{ km}$  which is less than one grid cell ( $275 \text{ km}$ ) difference. The peak production rate by ms-electron impact is  $\sim 0.1 \text{ cm}^{-3}\text{s}^{-1}$  (T5, nightside) which agrees well with the peak production rate obtained by *Gan et al.* [1992] in a two-stream model for upstream magnetic field geometry. The processes of the ms-electrons are treated by far more accurate in the model of *Gan et al.* [1992] than in this model. But in their model they do not account for

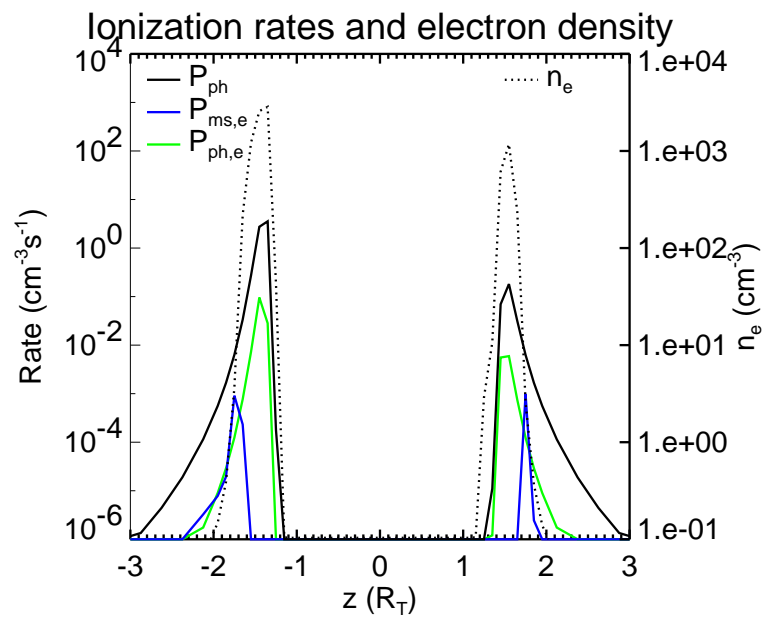
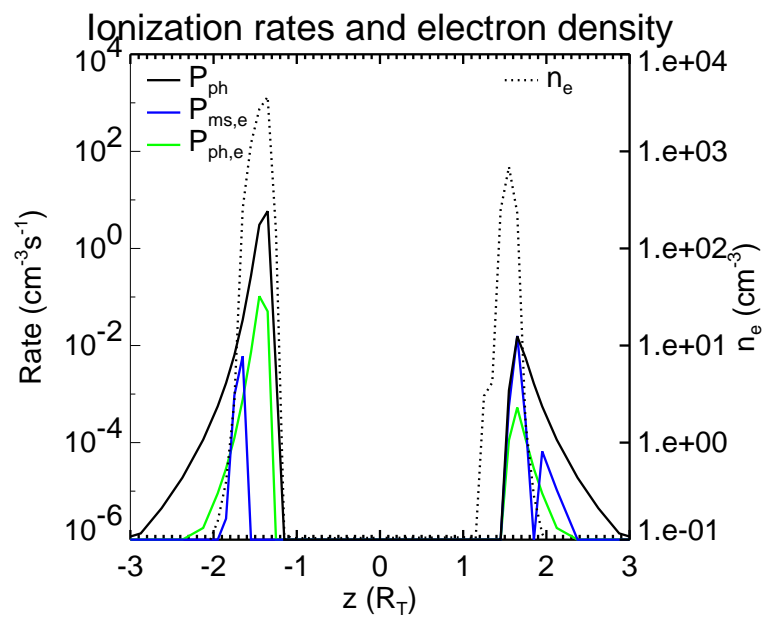


**Figure 5.9:** Production rates and electron density profile along the  $z$ -axis (polar) for T34 conditions



(a) T5

**Figure 5.10:** Production rates and electron density profile along the  $z$ -axis (polar) for T5 conditions

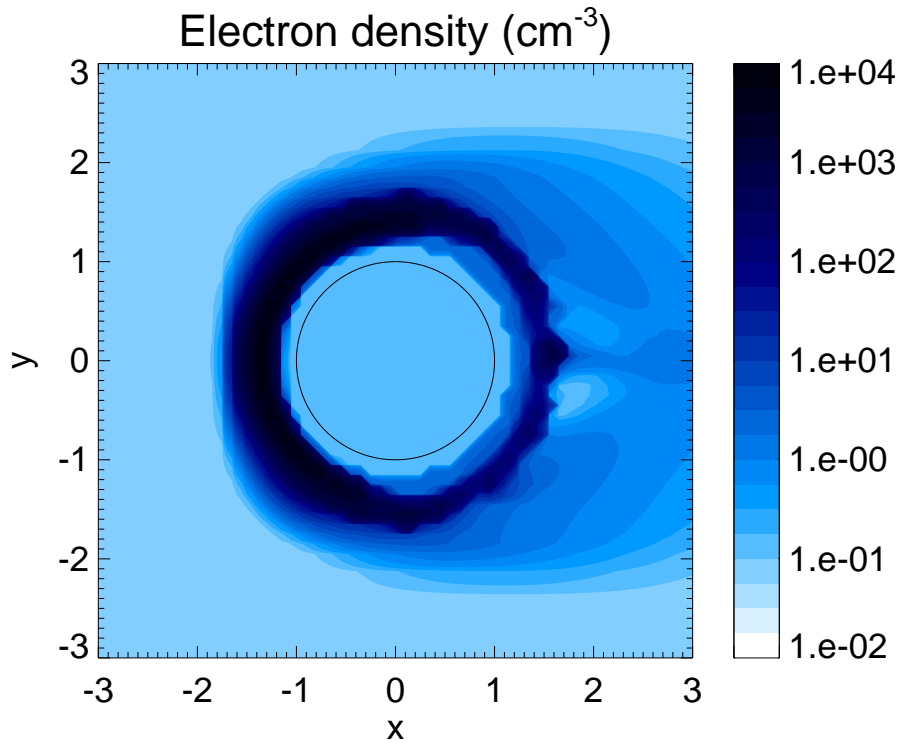


*Figure 5.11:* Electron number density on the  $xy$  plane at T34 conditions.

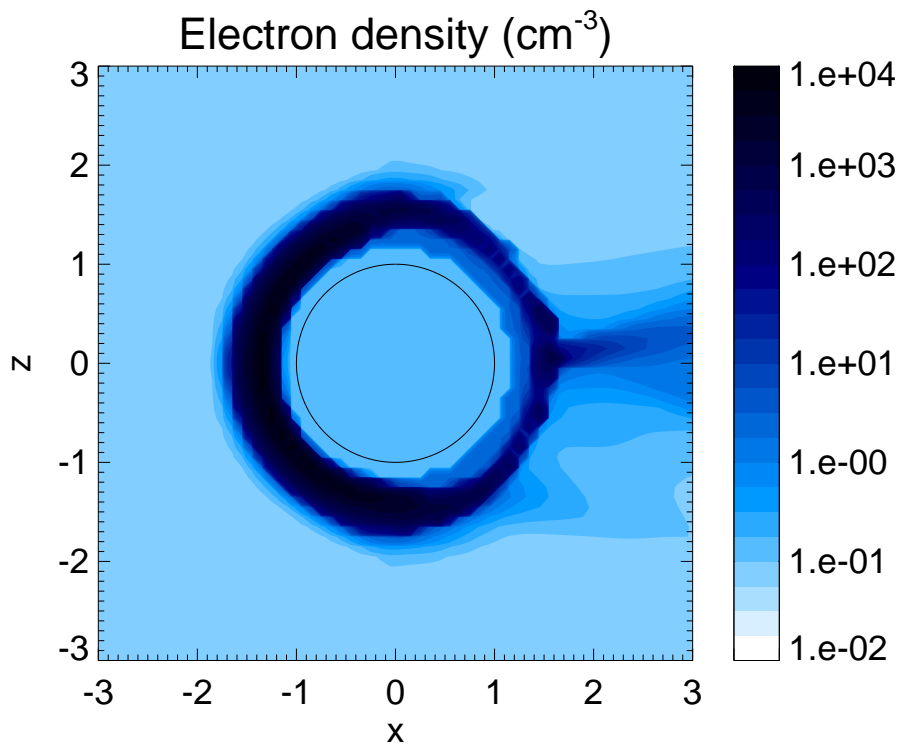


*Figure 5.12:* Electron number density on the  $xz$  plane at T34 conditions.

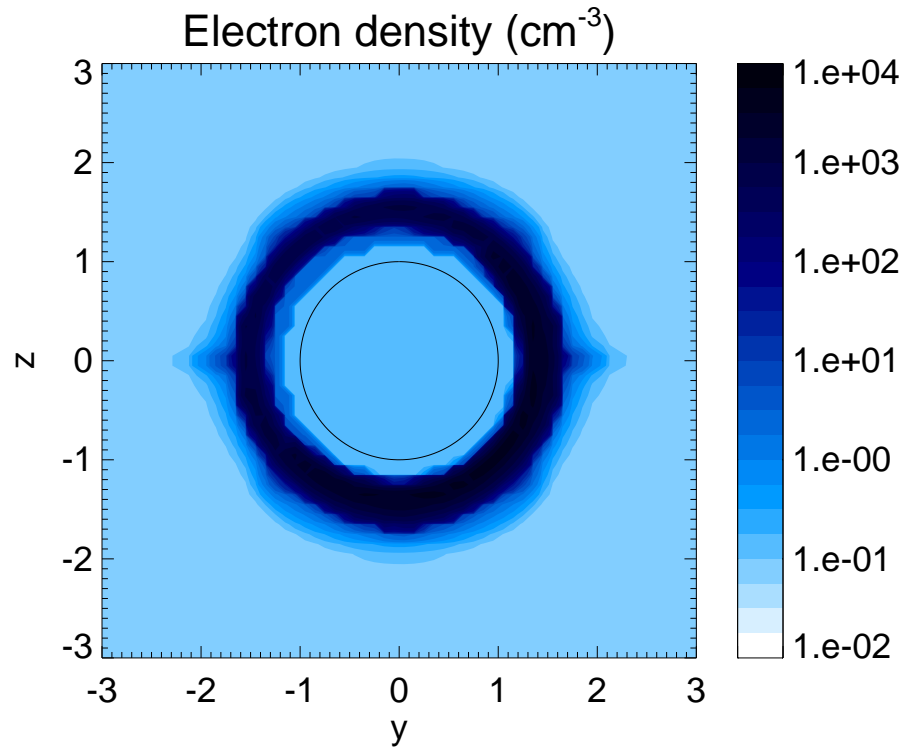


Figure 5.13: Electron number density on the  $yz$  plane at T34 conditions.

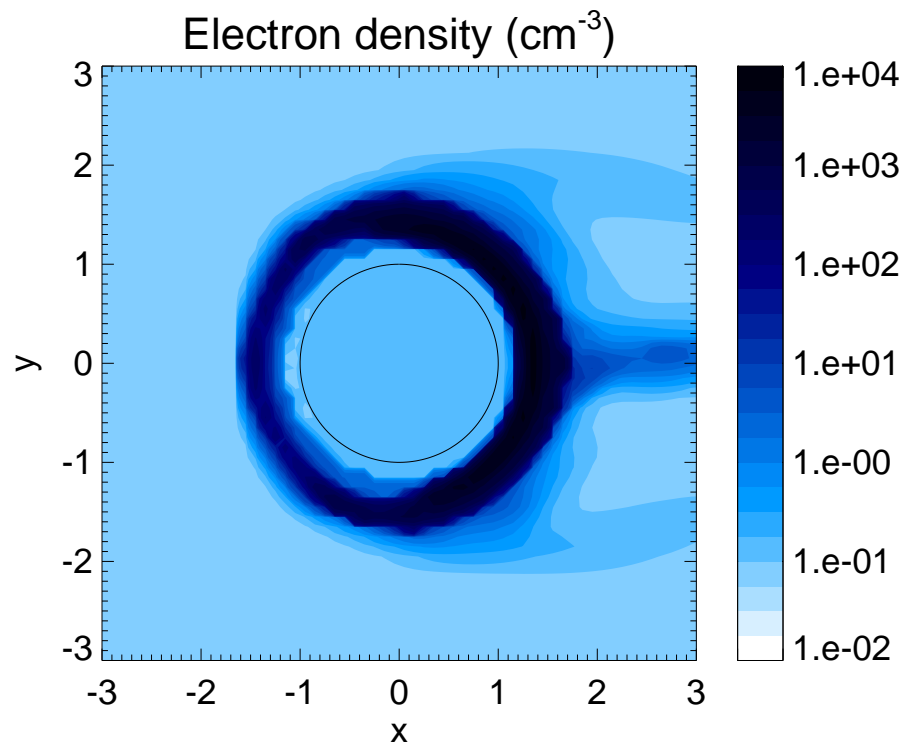
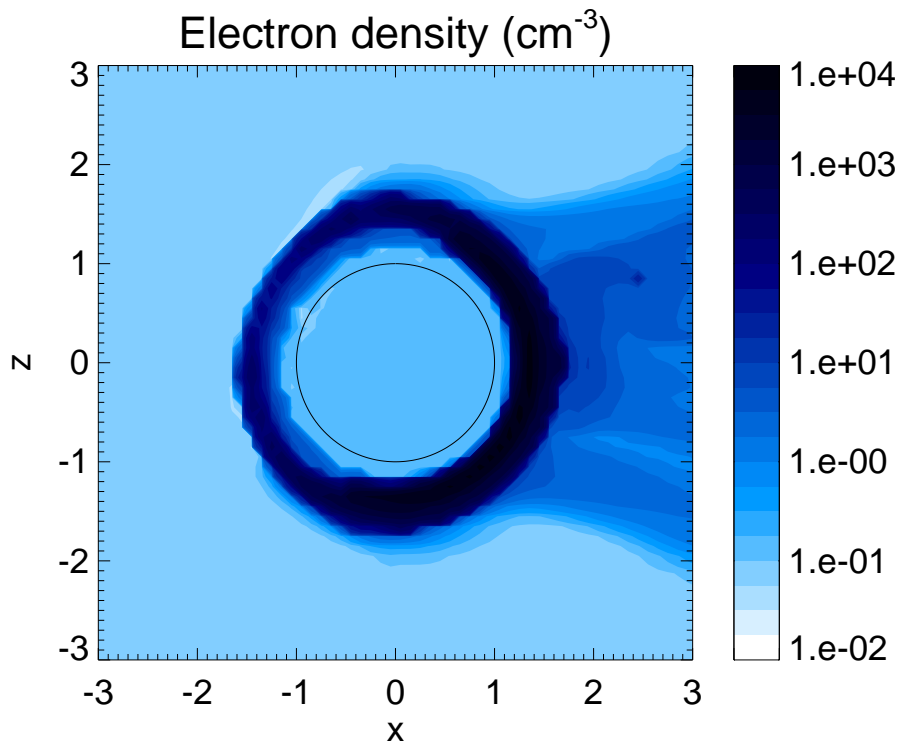
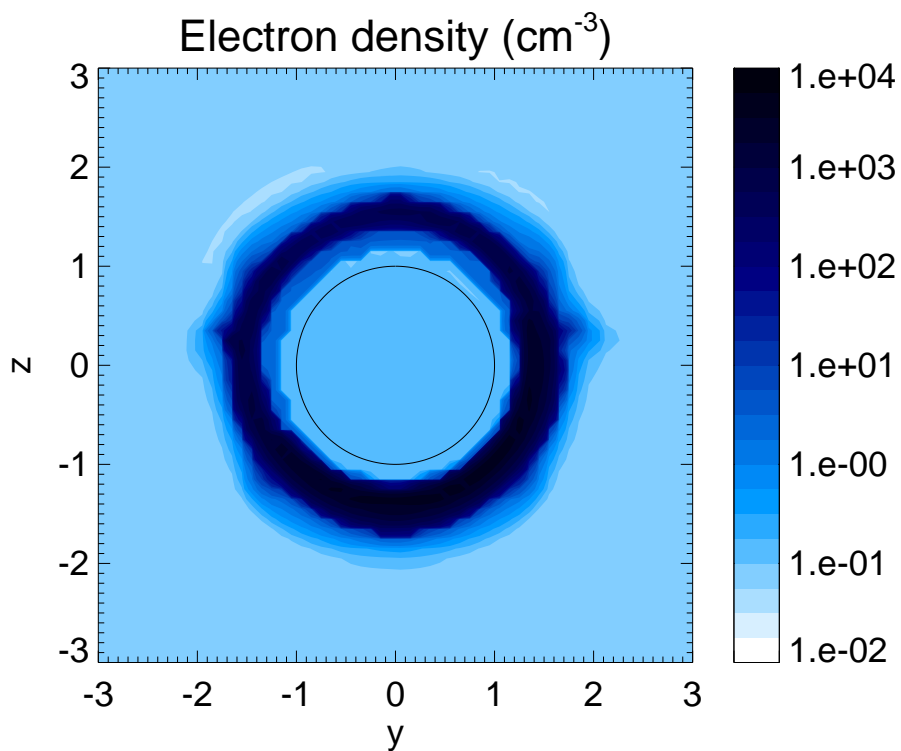


Figure 5.14: Electron number density on the  $xy$  plane at T5 conditions.



*Figure 5.15: Electron number density on the xz plane at T5 conditions.*



*Figure 5.16: Electron number density on the yz plane at T5 conditions.*

flux tube motion through the atmosphere and they assume a simple magnetic field geometry. Because of this, the production rate on the upstream dayside in our model is an order of magnitude lower than in their model. The flux tubes are prevented from entering that region by the photo-ionosphere.

*Galand et al.* [1999] have calculated the production rates for the nightside assuming the magnetic field to be perpendicular to satellite's surface with a multi-stream model. They obtain a peak ms-electron impact production rate of  $\sim 1 - 5 \text{ cm}^{-3}\text{s}^{-1}$  at an altitude of 600 km. The assumed magnetic field geometry is quite artificial. In our model the field is more or less perpendicular to the surface only on the downstream nightside (the region of the positive  $x$ -axis in the T34 case of our model (see Figure 5.5)). In this case we obtain a peak production rate of  $\sim 4 \text{ cm}^{-3}\text{s}^{-1}$  at an altitude of 1400 km, which is obvious different from the *Galand et al.* [1999] result. But like *Gan et al.* [1992] they do not take into account the motion of the flux tubes through the atmosphere which we claim to be important.

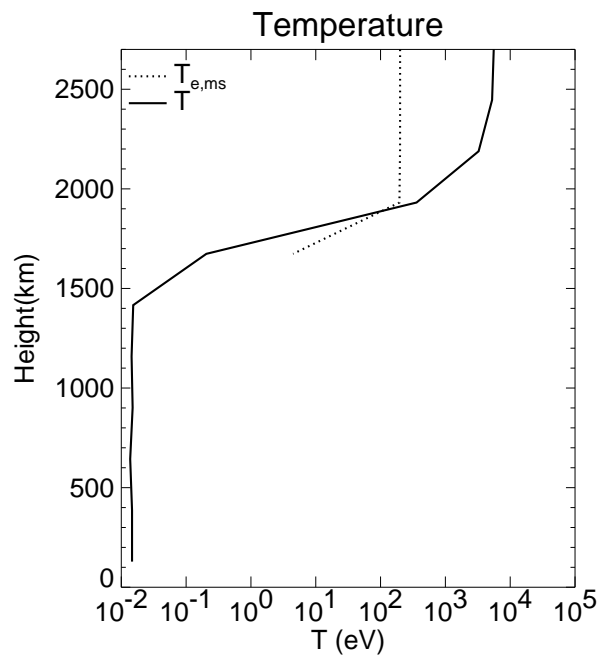
### 5.2.2 Ionospheric plasma temperature

In a single fluid ideal MHD model the temperature is not defined. We have defined an average temperature in Eq. (4.18) and additionally we solve the temperature equation for the ms-electrons (Eq. (4.46)). Note, that in Eq. (4.18) we assume a mass density of 28 amu for the whole simulation box. The mean ion mass in the incident magnetospheric plasma is about 10 amu (see Table 2.2). Thus, in our representation the temperature in the incident plasma is by about a factor of three too high. This has no consequences for the model results because terms in the equations (Eq. (4.22,4.24,4.25,4.26)) that explicitly contain the temperature only affect regions where the assumption of a mean ion mass of 28 amu is justified.

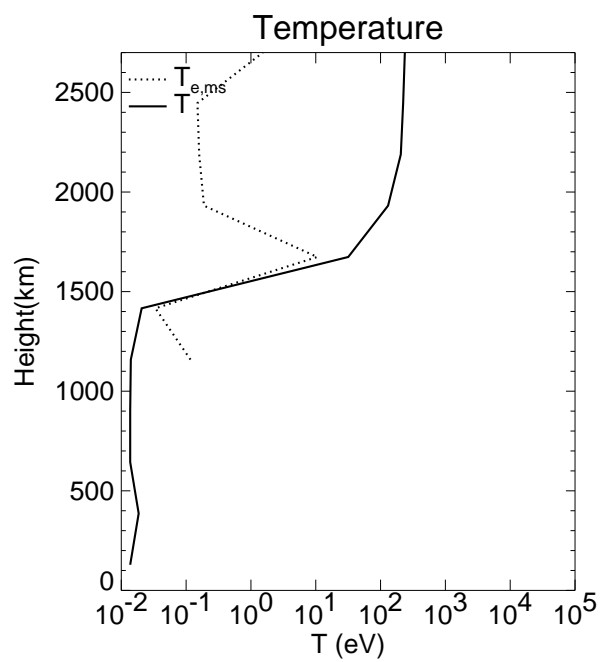
The two temperature profiles are plotted versus altitude in the upstream and downstream ionosphere for the T34 case (Figure 5.17) and the T5 case (Figure 5.18). The average temperature of the incident plasma is higher than the ms-electron temperature because of the higher temperature of  $\text{N}^+$  measured by Voyager 1 (see Table 2.2). Additionally it is artificially increased by a factor of three as mentioned above leading to an average temperature of  $T \approx 6000 \text{ eV}$  in the incident plasma.

On the upstream dayside of T34 (Figure 5.17a) the average plasma temperature ( $T$ ) decreases with decreasing altitude below 2500 km from the incident plasma temperature of  $\sim 6000 \text{ eV}$  to the atmospheric temperature of  $\sim 0.02 \text{ eV}$ . In the altitude range between 1900 km and 2500 km  $T$  decreases while the ms-electron temperature ( $T_{e,ms}$ ) remains constant. At that altitude photoionization produces cold plasma from the neutral atmosphere which leads to the decrease of  $T$ . But at that altitude the neutral gas density is too low to launch the cooling processes for the ms-electrons. This cooling sets in at 1900 km. Between 1900 km and 1600 km both temperatures decrease simultaneously. But still the decrease of  $T$  is larger than the decrease of  $T_{e,ms}$ . The difference is due to photoionization.

On the upstream nightside (Figure 5.18a) where not sufficient photons are present the decrease of  $T$  and  $T_{e,ms}$  sets in at the same altitude ( $\sim 1900 \text{ km}$ ).  $T_{e,ms}$  decreases due to ion production and elastic and inelastic collisions with the neutral gas. Note, that heating by heat

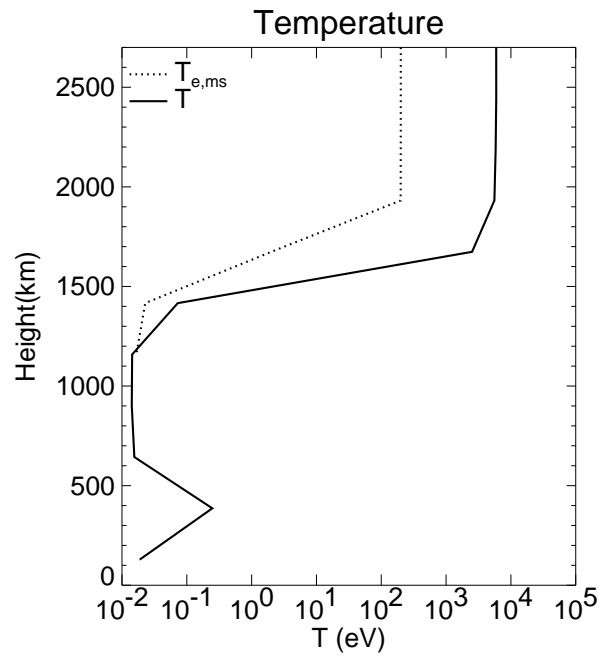


(a) upstream, dayside

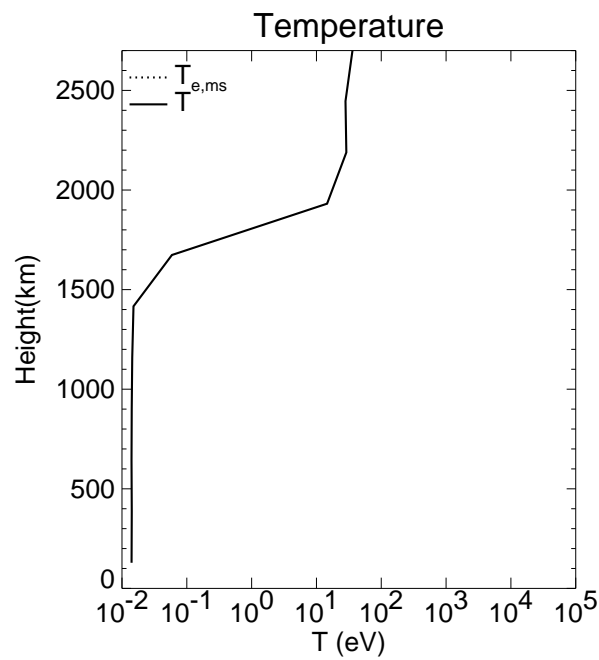


(b) downstream, nightside

**Figure 5.17:** Ionospheric temperature profiles of average plasma temperature ( $T$ ) and ms-electron temperature ( $T_{e,ms}$ ) at T34 conditions.



(a) upstream, nightside



(b) downstream, dayside

**Figure 5.18:** Ionospheric temperature profiles of average plasma temperature ( $T$ ) and ms-electron temperature ( $T_{e,ms}$ ) at T5 conditions.

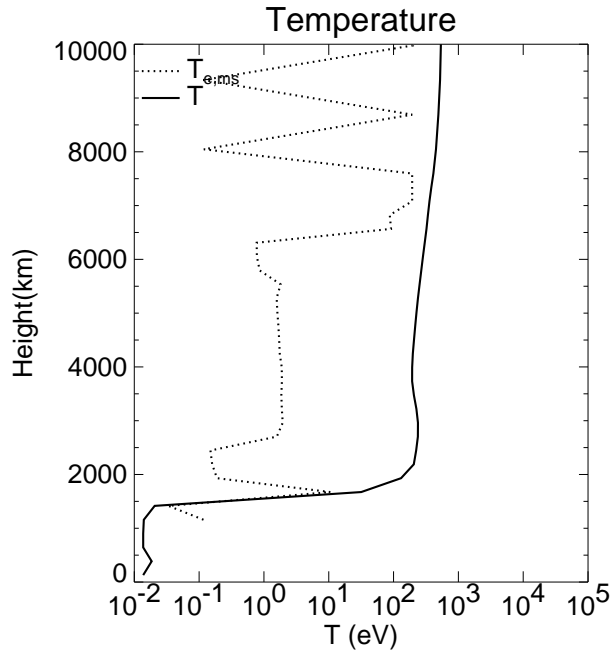


**Figure 5.19:** Ionospheric temperature profile of average plasma temperature ( $T$ ) and ms-electron temperature ( $T_{e,ms}$ ) on the downstream nightside (T34).

conduction along the field lines cannot lead to an increasing  $T_{e,ms}$  with decreasing altitude it can only change the slope of the decrease. At  $\sim 1200$  km both temperatures reach the low atmospheric temperature.

The ms-electrons do not reach all altitudes. They do not enter altitudes below 1600 km on the upstream dayside of T34 (Figure 5.17a) because of the high ionospheric plasma density produced by photoionization. At the upstream nightside of T5 (Figure 5.18a) and downstream nightside of T34 (Figure 5.17b) the ms-electrons reach down below an altitude of 1200 km. On the downstream dayside they even do not enter the plotted region below 2700 km because of the photo-ionosphere.

The peak of the average plasma temperature on the upstream nightside of T5 (Figure 5.18a) at  $\sim 400$  km is caused by Joule-heating, especially by the  $\vec{j}^2$ -term of the Joule heating (see Eq. 4.26). Two effects superpose each other at this altitude and produce the temperature peak: in this region the gradient of the magnetic field magnitude is large and thereby the electric currents are large ( $\vec{j} = \frac{1}{\mu_0} \vec{\nabla} \times \vec{B}$ ) and produce heat from the friction with the neutral gas (Joule-heating). Additionally, the ionospheric plasma density drops at this altitude (see Figure 5.24a). Thus, the produced heat is distributed among a small number of electrons and ions, which leads to a high plasma temperature. The temperature peak has no further effects on the dynamics in the model because at low atmospheric altitudes the neutral gas completely controls plasma dynamics.

The peak of  $T_{e,ms}$  on the downstream nightside (T34, Figure 5.17b) is an artefact of the model. In the tail region the grid of the flux tube model which moves with the plasma is stretched and the mapping of the temperature from the flux tube grid to the ZEUS-grid is quite inaccurate. But as Figure 5.19 indicates on average the ms-electrons are cooled below 6,000 km. Above

that altitude regions with hot flux tubes alternate with cool regions.

### 5.2.3 Pressure profiles along the ram direction

Along the ram direction (in the used coordinate system the  $x$ -axis) the plasma parameters change from the incident magnetospheric plasma to the ionospheric plasma. Both plasmas have different properties. In this section the transition from one to the other is examined on the basis of the pressure profiles along the ram direction for the dayside (T34) and the nightside (T5).

A plasma can be characterized e.g. by the sonic Mach number, the Alfvénic Mach number, and the plasma beta. The first is a measure for the relation between the plasma bulk velocity and the velocity of sound or in other words the relation between the dynamic pressure and the thermal pressure, the second gives the relation between dynamic pressure and the magnetic pressure, and the third is a measure for the relation between thermal and magnetic pressure. Thus, the plasma can be characterized by three types of pressure: the dynamic pressure, the thermal pressure, and the magnetic pressure. Regarding the equation for the plasma momentum (Eq. (4.24)), apart from the forces that correspond to the three pressure types, there are additional terms originating from the neutral gas: mass loading and friction. For the purpose of analyzing the plasma properties along the ram direction we rewrite the  $x$ -component of the stationary ( $\frac{\partial}{\partial t} = 0$ ) momentum equation (Eq. (4.24)) in the following way

$$\frac{\partial}{\partial x} \left( p_{th} + p_B + p'_B + p_{dyn} + p'_{dyn} + p'_{ml} + p'_{fric} \right) = 0. \quad (5.1)$$

The comparison of Eq. (5.1) with Eq. (4.24) gives the expressions for the pressures in Eq. (5.1).

Thermal pressure

$$p_{th} = p \quad (5.2)$$

Magnetic pressure

$$p_B = \frac{1}{2\mu_0} B^2 \quad (5.3)$$

Dynamic pressure

$$p_{dyn} = \rho v_x^2. \quad (5.4)$$

Additionally to the three types of pressure Eq. (5.1) contains pseudo-pressures which are:

Mass loading pressure

$$p'_{ml} = \int_{-\infty}^x dx m_i L v_x \quad (5.5)$$

Frictional pressure

$$p'_{fric} = \int_{-\infty}^x dx \nu \rho v_x \quad (5.6)$$

Magnetic pseudo pressure

$$p'_B = - \int_{-\infty}^x dx (\vec{B} \cdot \vec{\nabla}) B_x \quad (5.7)$$

Dynamic pseudo pressure

$$p'_{dyn} = \int_{-\infty}^x dx \left( \frac{\partial}{\partial y} \rho v_x v_y + \frac{\partial}{\partial z} \rho v_x v_z \right). \quad (5.8)$$

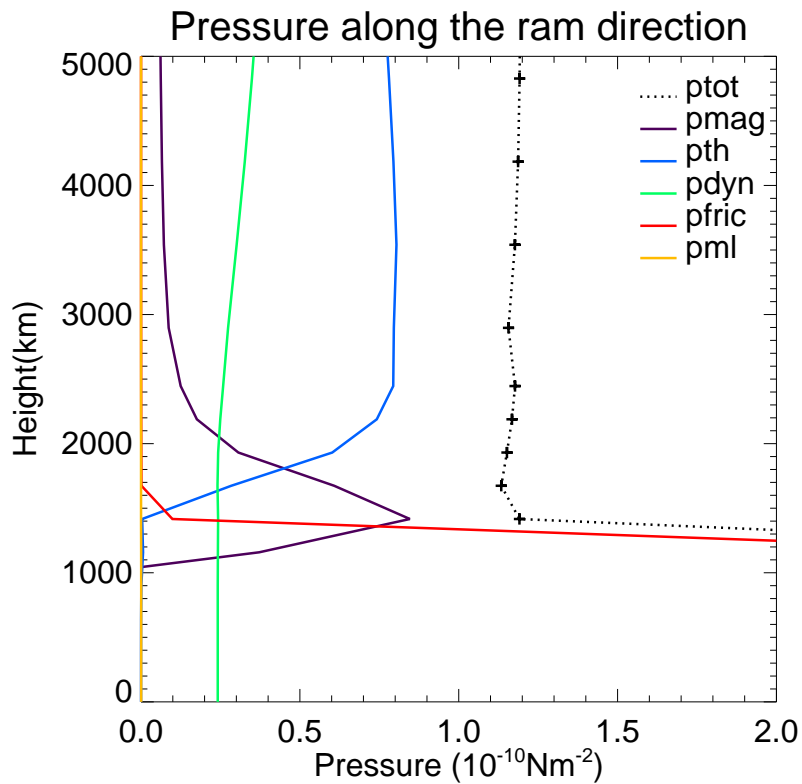
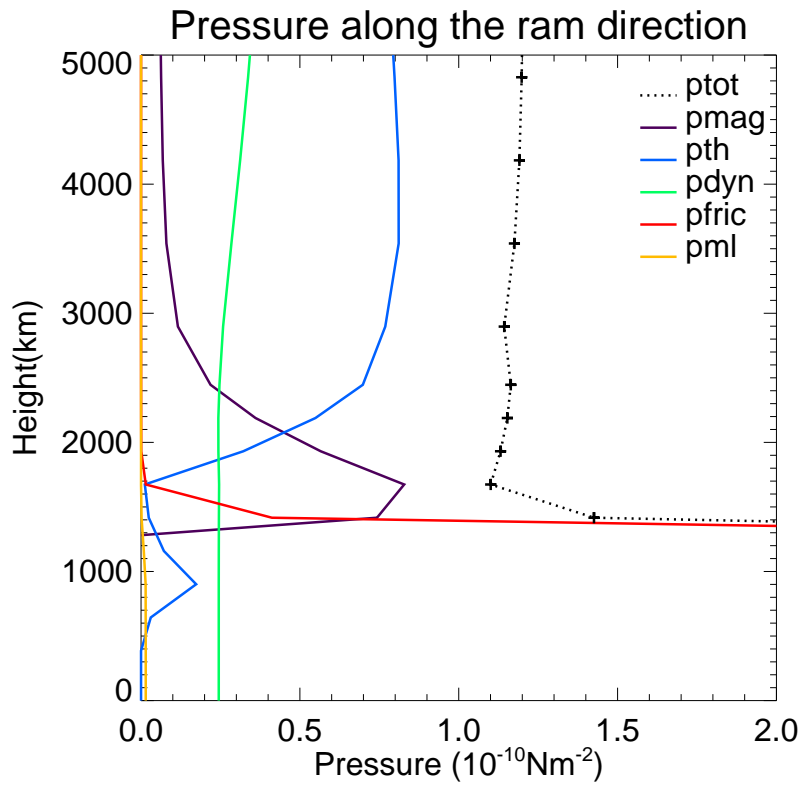


**Figure 5.20:** Pressure profiles along the ram (upstream) direction.

It has turned out that the last term in Eq. (4.24) which is proportional to  $\vec{j}$  is insignificant for the pressure balance and is left out here right from the beginning. In the expression for the frictional pressure  $\mathbf{v} = \sum_{ns} \left( \frac{m_e}{m_i} \mathbf{v}_{e,ns} + \mathbf{v}_{i,ns} \right)$ . In the incident plasma (noted symbolically as  $-\infty$ ) the integrands of the integral expressions are zero. To get the expression for the dynamic pressure and the dynamic pseudo pressure the continuity equation (Eq. (4.22)) has been involved, which leads to a drop out of the production rate  $P_{ns}$  and to the appearance of the loss rate  $L$  in the mass loading pressure term.

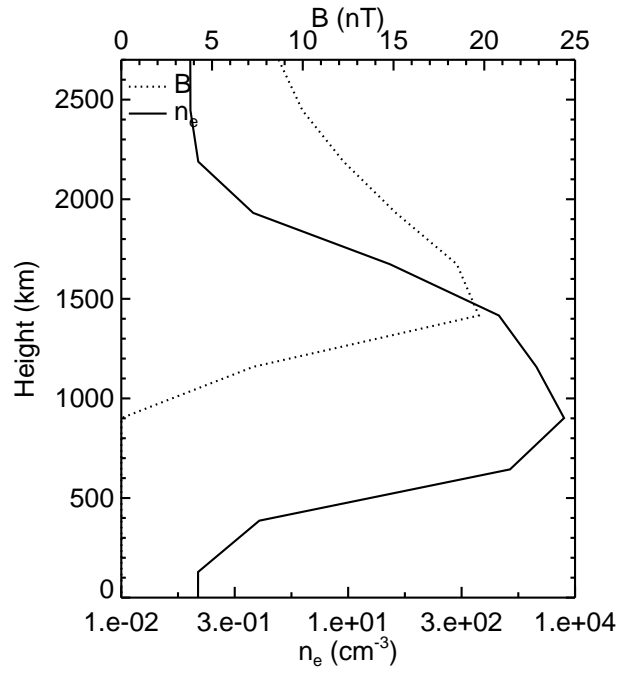
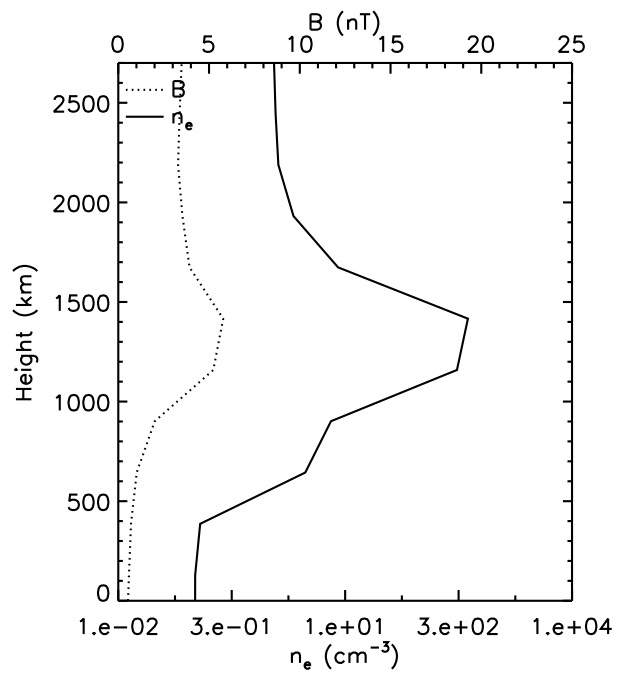
Figure 5.20a displays the pressure profiles along the dayside ram direction and Figure 5.20b along the nightside ram direction. In the plots  $pmag$  is the sum of the magnetic pressure (Eq. (5.3)) and pseudo pressure (Eq. (5.7)) and  $pdyn$  denotes the sum of dynamic pressure (Eq. (5.4)) and pseudo pressure (Eq. (5.8)). First thing to notice is that the structures for the night- and the dayside are quite the same, i.e. the basic features of the transition from magnetospheric to ionospheric plasma do not depend on Saturnian local time (SLT). The incident magnetospheric plasma is clearly dominated by the thermal pressure followed by dynamic and magnetic pressure ( $\beta \approx 10$ ). At lower altitudes the dynamic pressure decreases. The decrease is partly compensated by the dynamic pseudo pressure leading to a finite value of  $pdyn$  below 2000 km in Figure 5.20. The streaming of the plasma around the obstacle causes the magnetic field to pile-up in the so-called magnetic pile-up region or magnetic barrier. Conservation of the total pressure is achieved by a simultaneous decrease of thermal pressure. At an altitude of  $\sim 2000$  km magnetic and thermal pressure are equal  $\beta = 1$  and below that altitude the plasma is a low- $\beta$  plasma.

The dayside ionospheric thermal pressure is about an order of magnitude lower than the total incident plasma pressure, on the nightside it is even less. That means the ionosphere alone is not able to resist the incident magnetospheric plasma. This job is done by the neutral gas. At an altitude of 1400 km is a steep increase of frictional pressure. The frictional pressure by far exceeds the total pressure of the incident plasma. This does not violate the stationarity condition described in Eq. (5.1), which says that the total pressure is constant along the  $x$ -axis. One of the differences of the frictional pseudo pressure and a real pressure is that the frictional pressure only decelerates plasma but does not accelerate it<sup>1</sup>. Therefore, the gradient in the total pressure at 1400 km does not impose forces that change the profile. Mass-loading does not play any role in achieving pressure balance.

The described configuration of pressure along the ram direction suggests to divide the plasma into three types: (1) the incident magnetospheric plasma (high  $\beta$ , dominated by thermal pressure), (2) the magnetic barrier plasma (low  $\beta$ , dominated by magnetic pressure), and (3) the atmospheric plasma (controlled by collisions with the neutral gas). The three types of plasma are separated by two layers: the magnetospheric plasma is separated from the magnetic barrier plasma by a layer in which thermal pressure is converted into magnetic pressure. Inside of this layer there must be an altitude where  $\beta = 1$ . One could call this layer  $\beta 1$ -layer. between the magnetic barrier plasma and the atmospheric plasma the magnetic field drops to low values. We call the layer between the magnetized upper ionosphere and the non or weakly magnetized lower ionosphere magnetic ionopause (MIP).

---

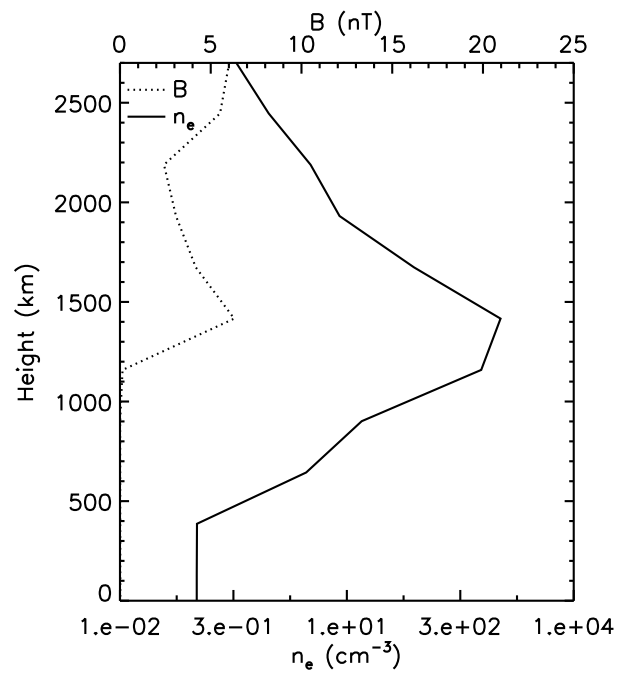
<sup>1</sup>The neutral gas velocity is assumed to be zero.

(a) upstream ( $-x$ -axis)(b) downstream ( $x$ -axis)

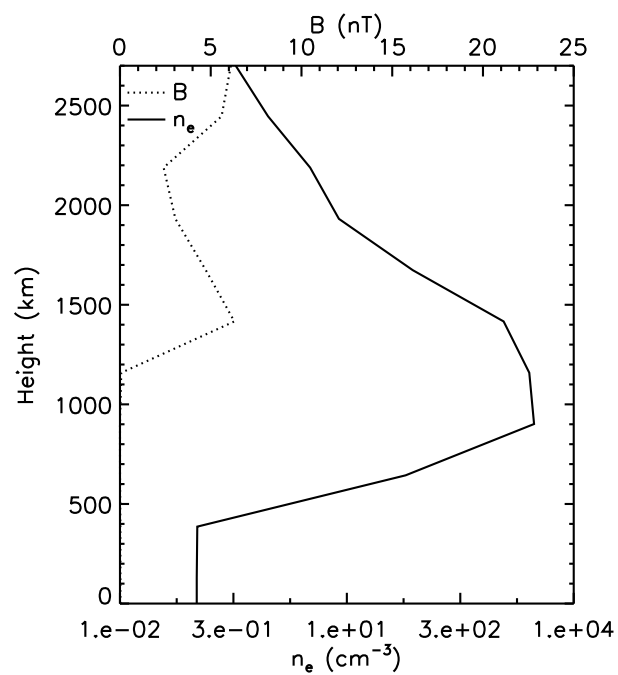
**Figure 5.21:** Magnetic field magnitude (dashed line and upper axis) and electron density at T34 conditions.

## 5.2.4 Magnetization of the ionosphere

Although the incident magnetospheric plasma is only weakly magnetized ( $\beta \sim 10$ ) the magnetic field plays an essential role in the plasma interaction with Titan's atmosphere. As dis-

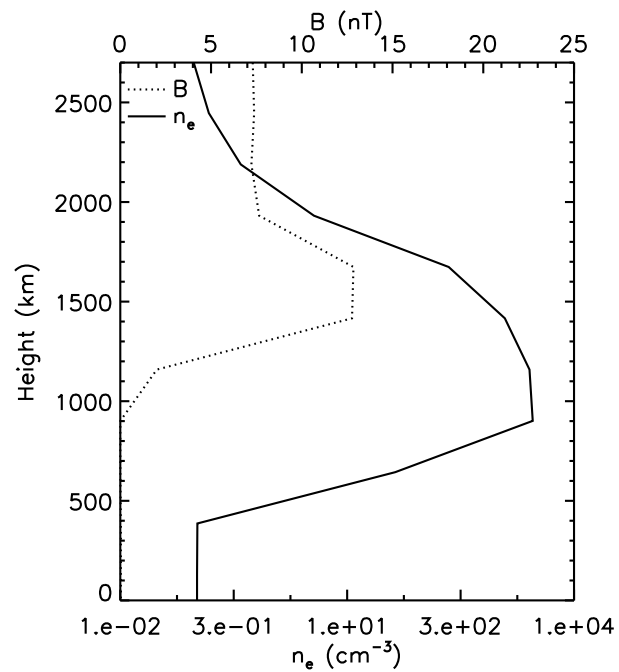


(a) Saturnian flank (y-axis)

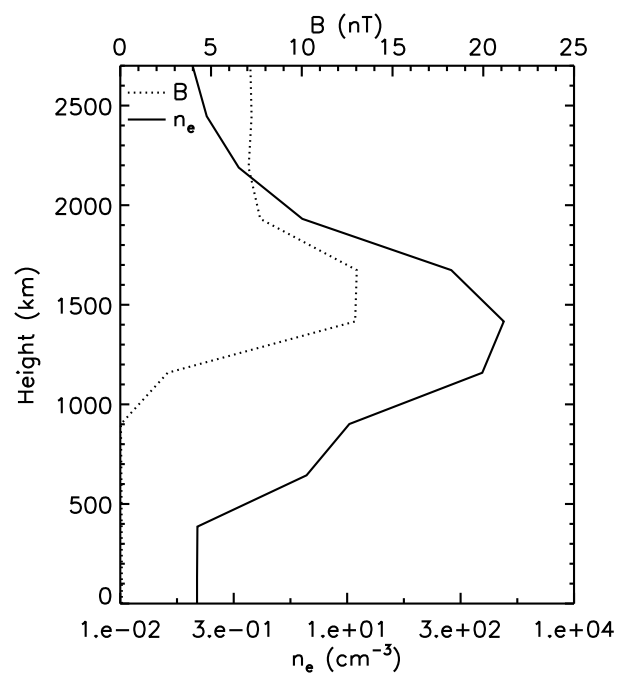


(b) anti-Saturnian flank (-y-axis)

**Figure 5.22:** Magnetic field magnitude (dashed line and upper axis) and electron density at T34 conditions.



(a) north pole (z-axis)

(b) south pole ( $-z$ -axis)

**Figure 5.23:** Magnetic field magnitude (dashed line and upper axis) and electron density at T34 conditions.

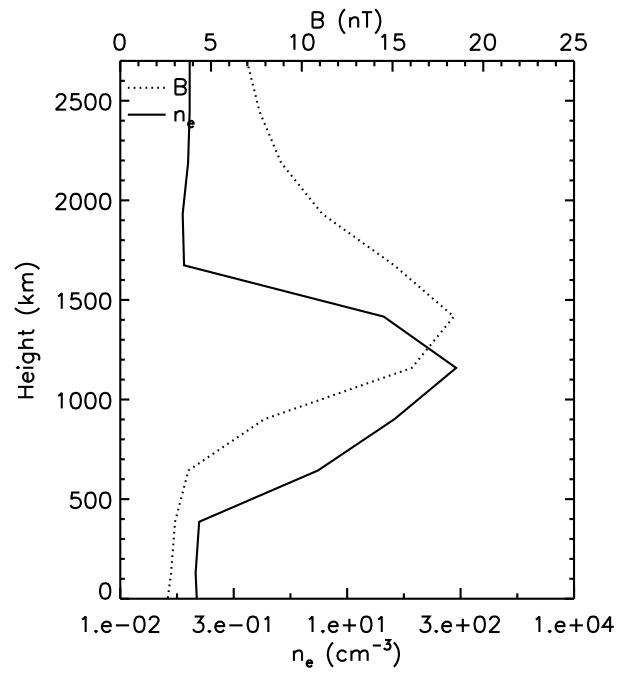
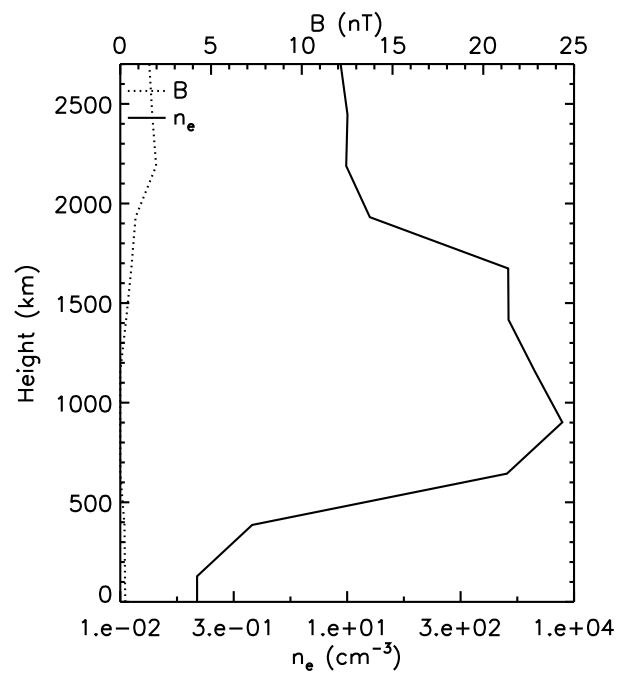
cussed in the last Section the plasma changes from magnetospheric high- $\beta$  plasma to a low- $\beta$  plasma in the magnetic barrier along the ram axis meaning that in this region the plasma is dominated by the magnetic pressure. In this section the magnetization of the ionosphere along the three axes of the coordinate system is examined and discussed for the T34 and the T5 case.

Magnetic field magnitude and electron density are plotted along the three axes for T34 conditions in Figure 5.21, 5.22, and 5.23 and for T5 conditions in Figure 5.24, 5.25, and 5.26. In the upstream dayside ionosphere (Figure 5.21a) the peak of the magnetic pile-up region is at an altitude of  $\sim 1500$  km which is above the ionospheric peak in electron density at  $\sim 900$  km. Below the peak of the magnetic barrier the magnetic field magnitude decreases linearly with altitude and becomes zero at  $\sim 900$  km. The ionosphere below the ionospheric peak is only weakly magnetized. As mentioned in the last section we call the layer that separates the magnetized upper from the non or low magnetized lower ionosphere, i.e. the sharp gradient in magnetic field magnitude, *magnetic ionopause* (MIP). The magnetic field magnitude at the peak of the magnetic barrier is determined by the total pressure of the upstream magnetospheric plasma (minus the residual dynamic pseudo pressure, see Figure 5.20a) since at this altitude nearly all the pressures have been converted into magnetic pressure. The resulting peak magnitude is  $\sim 20$  nT. Note that only part of the dynamic pressure is converted into magnetic pressure because of the divergence of the flow around the obstacle. The pressure corresponding to the flow divergence is the dynamic pseudo pressure (see Eq. 5.8) which is not negligible in the total pressure balance as Figure 5.20 indicates.

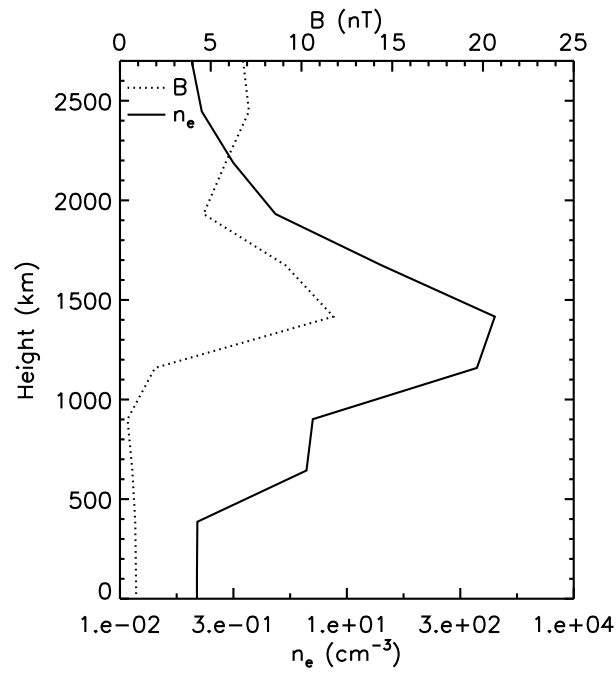
The structure of the magnetic field in the flank ionosphere is very similar on the Saturnian (Figure 5.22a) and the anti-Saturnian flank (Figure 5.22b) and due to the similar SLT conditions at the flanks of T34 and T5 (morning, evening), the basic shape of the magnetic field magnitude does not considerably differ. (Figure 5.25a,b). Above 2500 km the magnetic field magnitude is  $\sim 50$  % higher than the incident value due to a compression of the plasma at the flanks. Below 2500 km the magnitude decreases with altitude and reaches a minimum of  $\sim 2$  nT at  $\sim 1900$  km. Between  $\sim 1200$  km and  $\sim 1700$  km is the flank magnetic pile-up region with a peak magnitude of  $\sim 8$  nT at  $\sim 1400$  km.

The minimum in the magnetic field magnitude at the flanks at an altitude of  $\sim 1900$  km at T5 and  $\sim 2200$  km at T34 is a consequence of the topology of the magnetic field and is a 3D effect. In the 2D model of *Cravens et al.* [1998] appears no minimum at the flanks. The draped 3D magnetic field has to be such that  $\vec{\nabla} \cdot \vec{B} = 0$  is not violated which is in a 3D flow pattern much more complicated than in 2D. The accompanying (divergence zero) electric currents given by  $\vec{j} = \frac{1}{\mu_0} \vec{\nabla} \times \vec{B}$  are discussed in the Section 5.5.1.

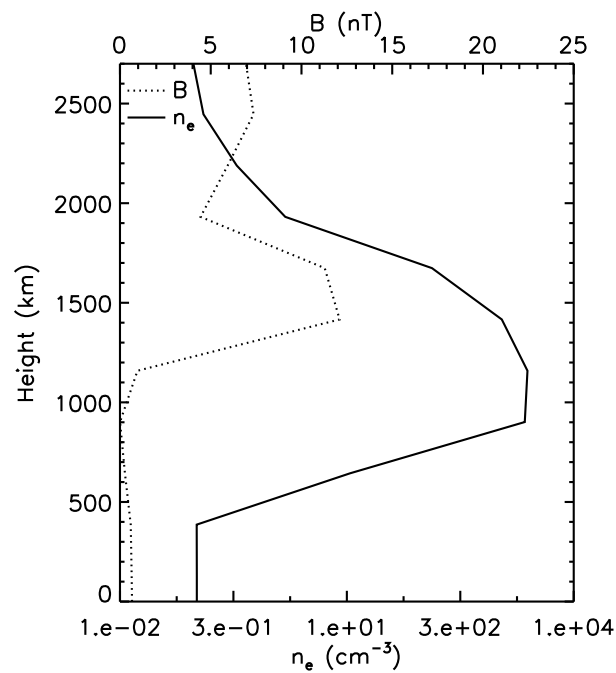
The structure of the magnetic field over the poles is also similar at T34 (Figure 5.23a,b) and T5 conditions (Figure 5.26a,b) and it basically does not differ from the upstream magnetic field profile but the gradient of the pile-up between  $\sim 1900$  km and  $\sim 1650$  km ( $\Delta z \approx 250$  km, one grid cell) is more sharp than in the upstream ionosphere and is accompanied by a steep gradient in the electron density. As Figure 5.27 indicates, the position of the steep gradient corresponds to the position where the plasma  $\beta$  equals one, i.e. to the transition from a high to a low- $\beta$  plasma. (Note, that the pressure in Figure 5.27 is the pressure along the  $z$ -axis. The pressures are defined in analogy to Eq. 5.2 to Eq. 5.8. The integrals are along the  $z$  coordinate

(a) upstream ( $-x$ -axis)(b) downstream ( $x$ -axis)

**Figure 5.24:** Magnetic field magnitude (dashed line and upper axis) and electron density at T5 conditions.

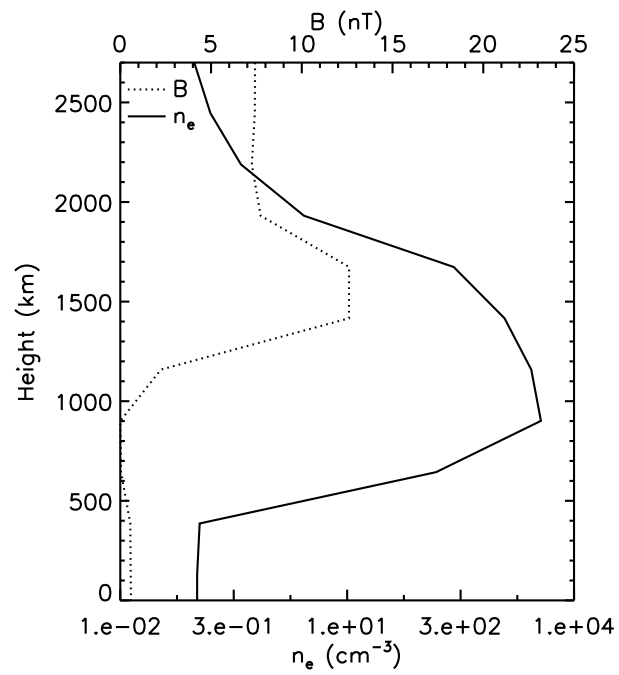
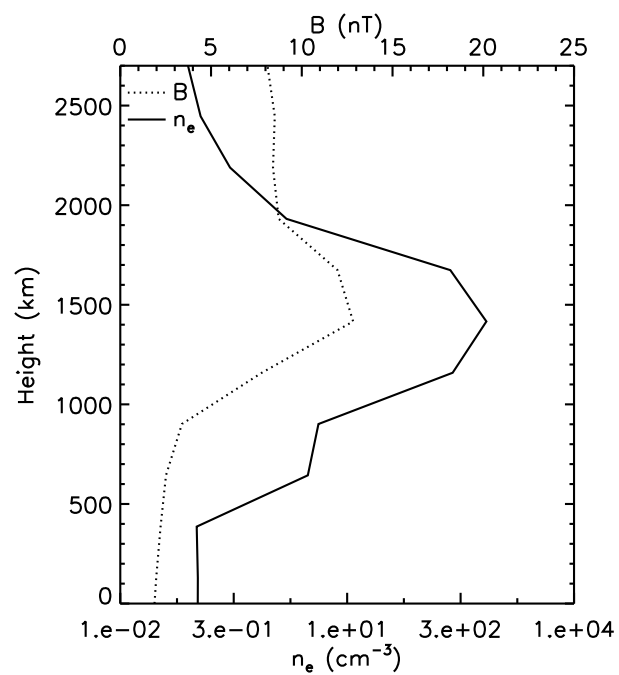


(a) Saturnian flank (y-axis)



(b) anti-Saturnian flank (-y-axis)

**Figure 5.25:** Magnetic field magnitude (dashed line and upper axis) and electron density at T5 conditions.

(a) north pole ( $z$ -axis)(b) south pole ( $-z$ -axis)

**Figure 5.26:** Magnetic field magnitude (dashed line and upper axis) and electron density at T5 conditions.

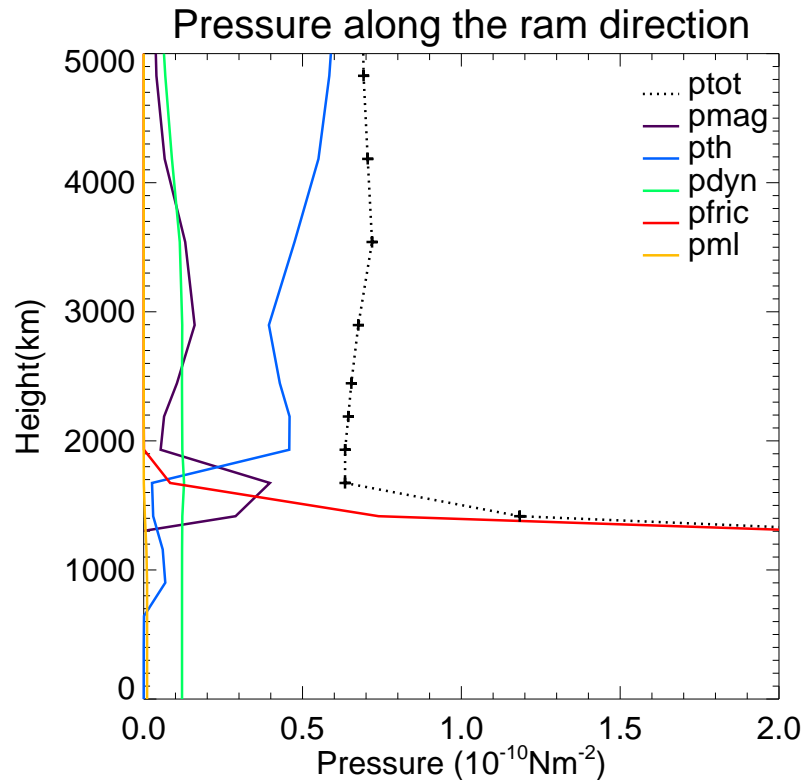


**Figure 5.27:** Pressure profiles over the south pole.

in that case.) In a sub-Alfvénic flow the magnetic field structure over the poles is determined by the Alfvén tubes.

The magnetic field magnitude and vectors in the  $xy$ ,  $xz$ , and  $yz$  plane are displayed in Figures 5.28, 5.29, 5.30 for the T34 case and in Figures 5.31, 5.32, 5.33 for the T5 case.

Figure 5.29 and Figure 5.32 show the draping of the magnetic field around the obstacle leading to a magnetic field direction in the tail region which is nearly perpendicular to the upstream magnetic field. It is obvious from the plots that there is always magnetic field diffusion towards the body of Titan from the nightside where the shielding ionospheric electron density is lower than on the dayside. The temporal varying magnetic fields can induce currents in presumably conducting layers in Titan's interior and the currents create a magnetic field that takes an influence on the plasma interaction. In this model we neglect possible induction effects of Titan's interior.

We want to draw the attention to another interesting result that is apparent in Figure 5.33. The projection of the draped magnetic field on the plane perpendicular to the plasma flow direction shows magnetic field vectors that are tangential to the surface of the obstacle as expected. The magnetic field that has been transported by diffusion shows a different behavior: the components in the mentioned plane point radially towards the center of the obstacle.

In summary the results for the magnetization of the ionosphere are: (1) The upper ionosphere is always magnetized. (2) The nightside ionosphere is nearly completely magnetized. (3) The higher the photoionization rate, the larger is the part of the lower ionosphere that is

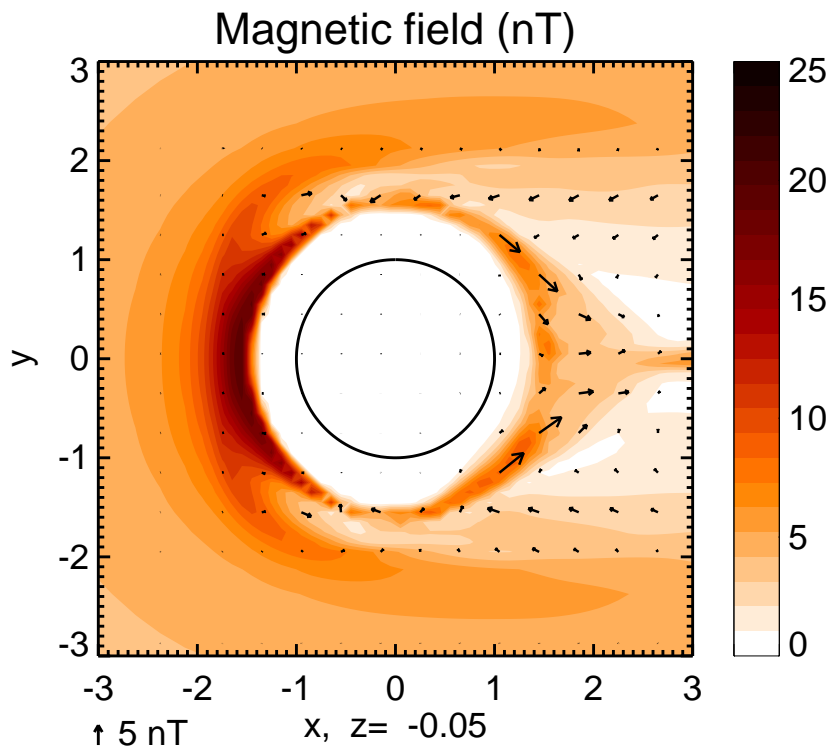


Figure 5.28: Magnetic field magnitude and vectors in the xy plane at T34 conditions.

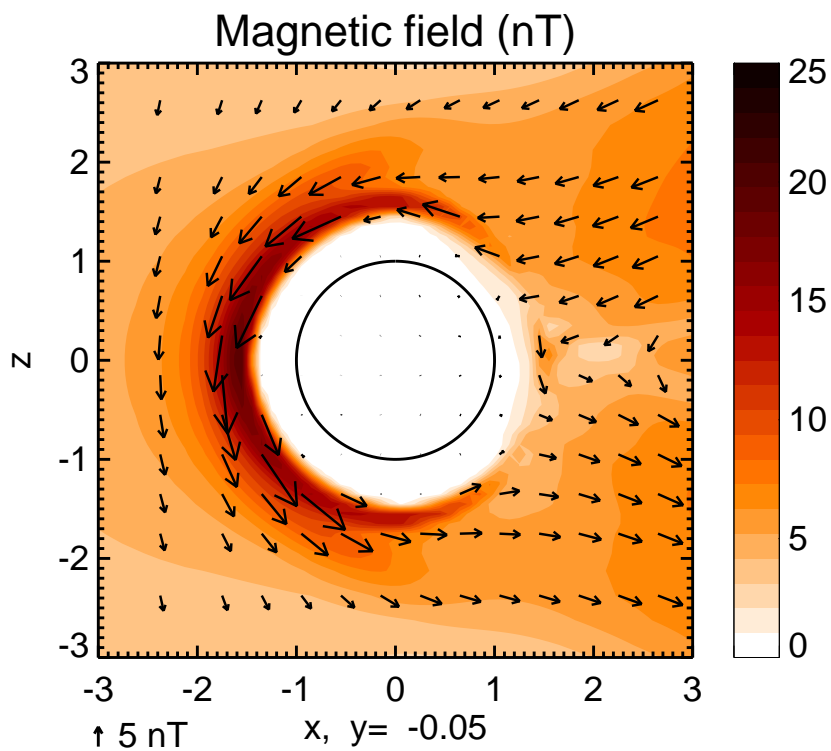


Figure 5.29: Magnetic field magnitude and vectors in the xz plane at T34 conditions.

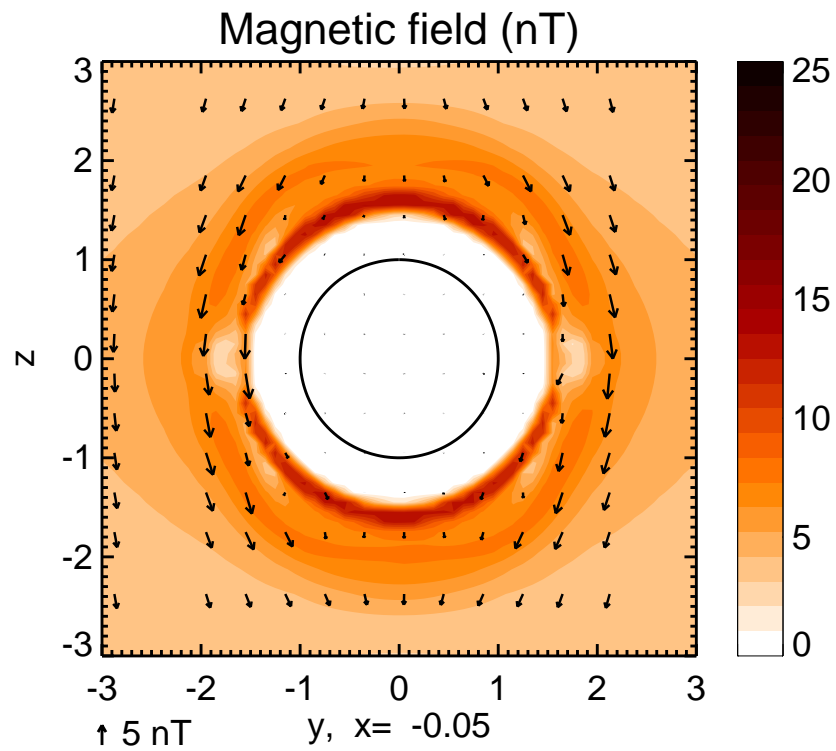


Figure 5.30: Magnetic field magnitude and vectors in the  $yz$  plane at T34 conditions.

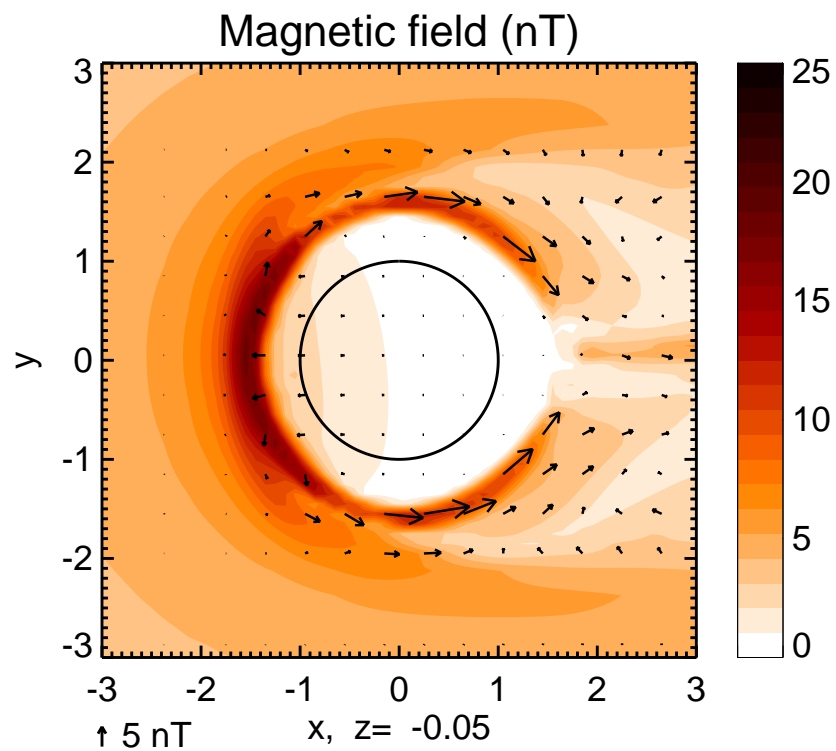


Figure 5.31: Magnetic field magnitude and vectors in the  $xy$  plane at T5 conditions.

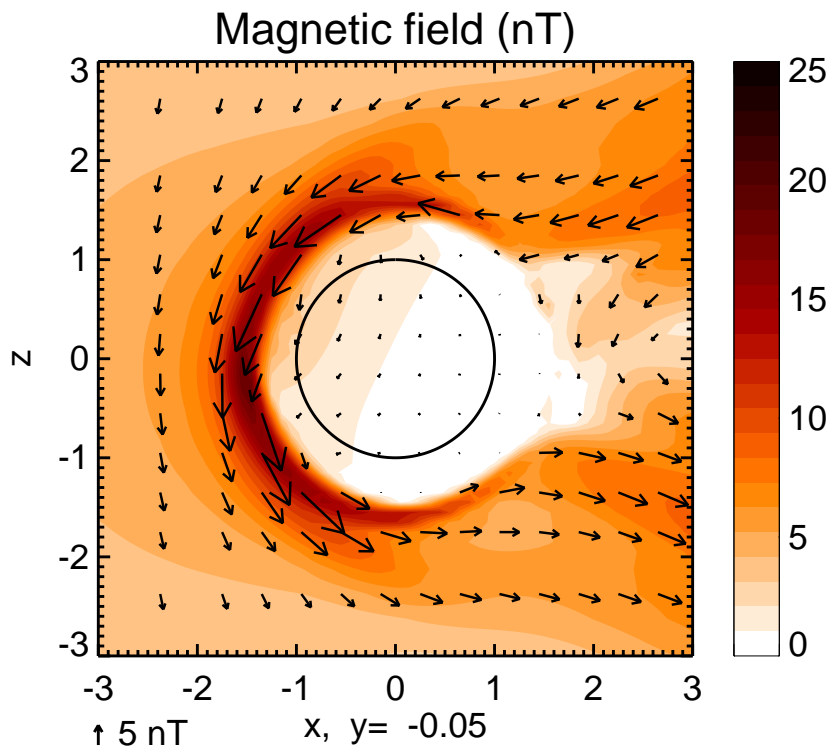


Figure 5.32: Magnetic field magnitude and vectors in the  $xz$  plane at T5 conditions.

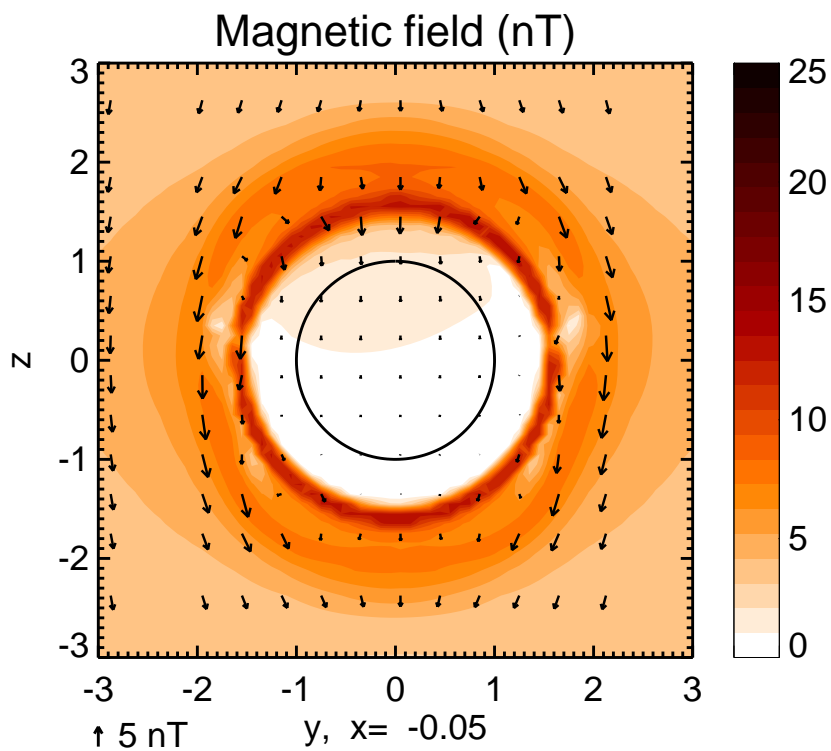
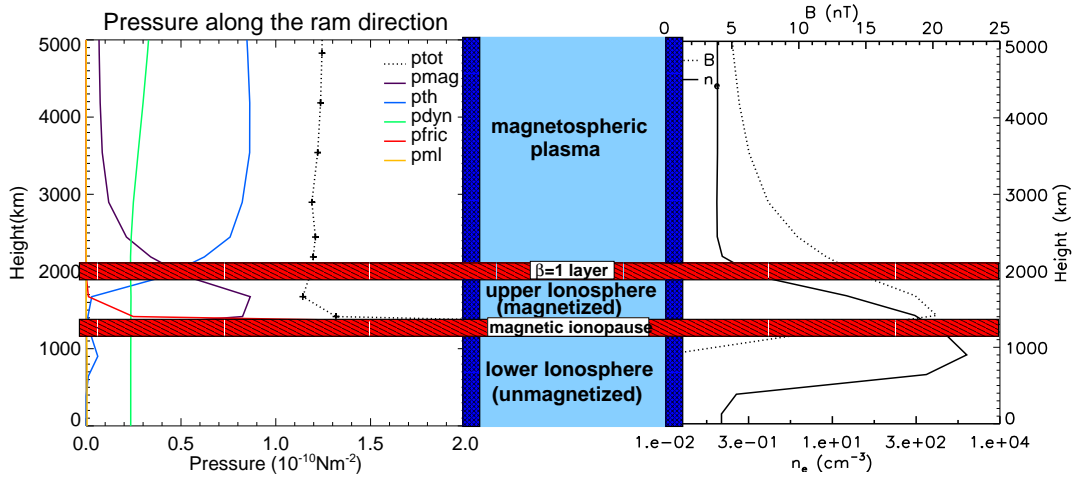


Figure 5.33: Magnetic field magnitude and vectors in the  $yz$  plane at T5 conditions.



**Figure 5.34:** Classification of the plasma along the ram direction into 3 regions: (1) magnetospheric plasma, (2) upper (magnetized) ionospheric plasma, and (3) lower (non or weakly) magnetized plasma (blue areas). In-between the regions are the  $\beta=1$ -layer and the magnetic ionopause (MIP). The criteria for the classification are the pressure profile (left plot) and the electron number density and magnetic field profile (right plot).

unmagnetized (or weakly magnetized). (4) Diffusion magnetic field differs in direction from the draped magnetic field.

### 5.2.5 Layers and plasma regions

At the end of Section 5.2.3, inspired by the examination of the ram pressure profiles we have argued that it is reasonable to divide the plasma along the ram direction into three regions: (1) magnetospheric plasma, (2) upper ionospheric plasma, and (3) lower ionospheric plasma. We have called the transition region between the magnetospheric and the upper ionospheric plasma  $\beta=1$ -layer due to the transition from high to low  $\beta$ -plasma. We have called the transition region between upper and lower ionospheric plasma magnetic ionopause (MIP) since it separates the magnetized upper from the non or weakly magnetized lower ionosphere. In this section the 3D shape of the layers is examined. Apart from that the altitude of the layers at TA, T5, and T34 conditions are compared. Doing so, dependencies on the angle to the upstream direction can be separated from Saturnian local time (SLT) dependencies. Additionally the magnetic barrier peak magnitude and altitude is examined which is located in-between the two layers.

Figure 5.34 is a plot of the pressure profile and the magnetic field magnitude and electron number density along the ram direction during T34 conditions. The plasma regions and the layers between them are marked in the plot. It shows that the criteria that have been used to define the plasma regions and layers that were derived from the pressure profiles (in Section 5.2.3) are still reasonable when the plasma density is taken into account. In the magnetospheric plasma the density is quite low. In the upper ionosphere between the  $\beta=1$ -layer and the MIP the density increases about four orders of magnitude. Below the MIP

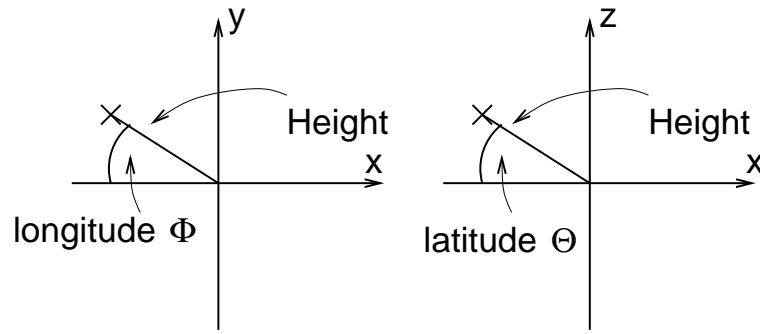


**Figure 5.35:** Definition of the longitude ( $\Phi$ ), the latitude ( $\Theta$ ), and the height in this Section.

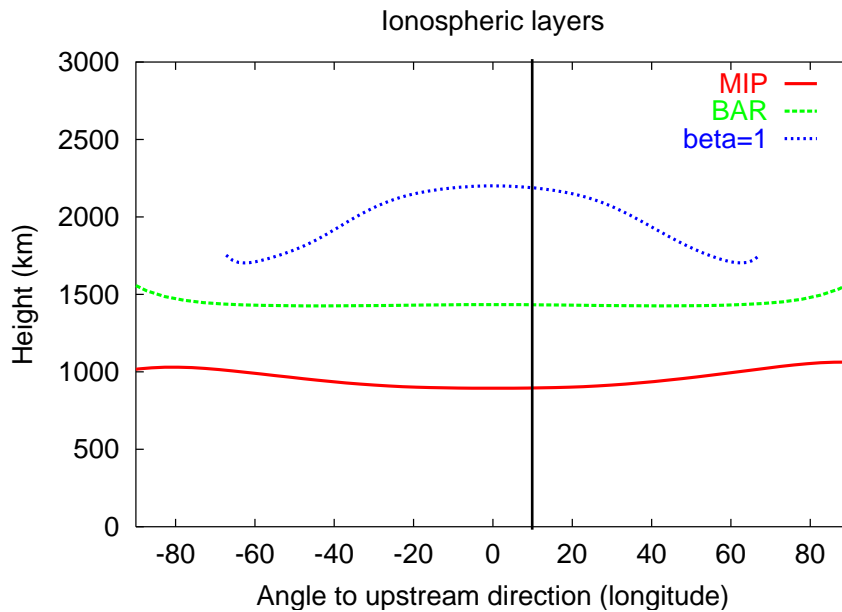


**Figure 5.36:** Altitude of magnetic ionopause (MIP), magnetic barrier peak (BAR), and  $\beta_1$ -layer as a function of the longitude angle ( $\phi$ ) for the T34 case. The solid line marks the solar zenith position and the dashed line the midnight position.

the ionosphere is dense and non or weakly magnetized. The upper ionosphere coincides with part of the magnetic barrier (or magnetic pile-up region). But the magnetic barrier reaches up to higher altitudes and it is important to distinguish between these two. The peak of the magnetic barrier is always in the upper ionosphere because per definition the upper ionosphere lies between the altitude with  $\beta = 1$  and the decrease of the magnetic field inside of the ionosphere. The altitude of the two layers and the magnetic barrier peak (BAR) is plotted as a function of the angle to the ram direction in the equatorial plane (longitude,  $\phi$ ) in Figure 5.36, 5.37, and 5.38 and as a function of the angle to the ram direction in the  $xz$ -plane (latitude,  $\theta$ ) in Figure 5.39, 5.40, and 5.41 for the three cases TA, T5, and T34.  $\phi = 90^\circ$  represents the Saturnian flank and  $\phi = -90^\circ$  the anti-Saturnian flank.  $\theta = 90^\circ$  represents the north pole and  $\theta = -90^\circ$  the south pole (see also Figure 5.35 for the definition of the angles). The mid-day angle i.e. the solar zenith position is marked with a black line and the midnight angle is marked by a dashed line. The altitude of the layers has been extracted

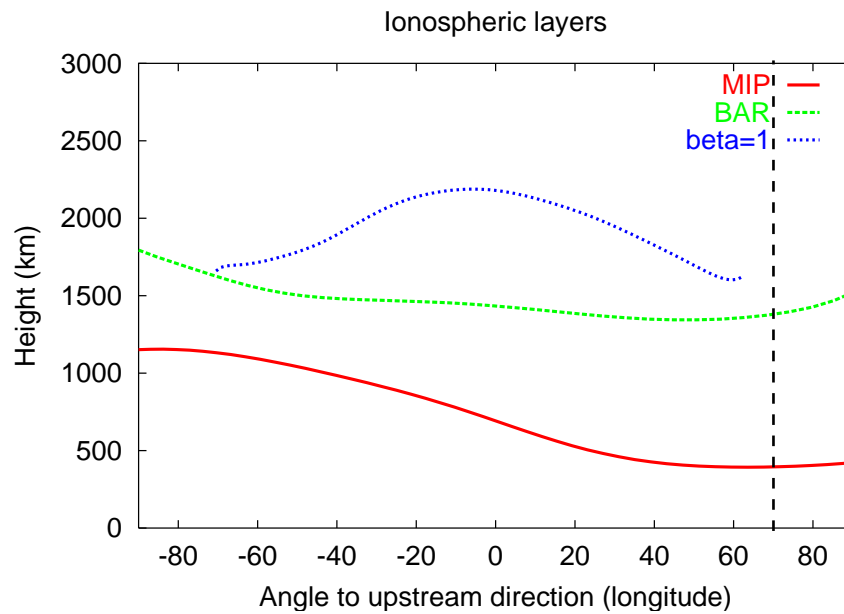


**Figure 5.37:** Altitude of magnetic ionopause (MIP), magnetic barrier peak (BAR), and  $\beta_1$ -layer as a function of the longitude angle ( $\phi$ ) for the TA case. The solid line marks the solar zenith position and the dashed line the midnight position.

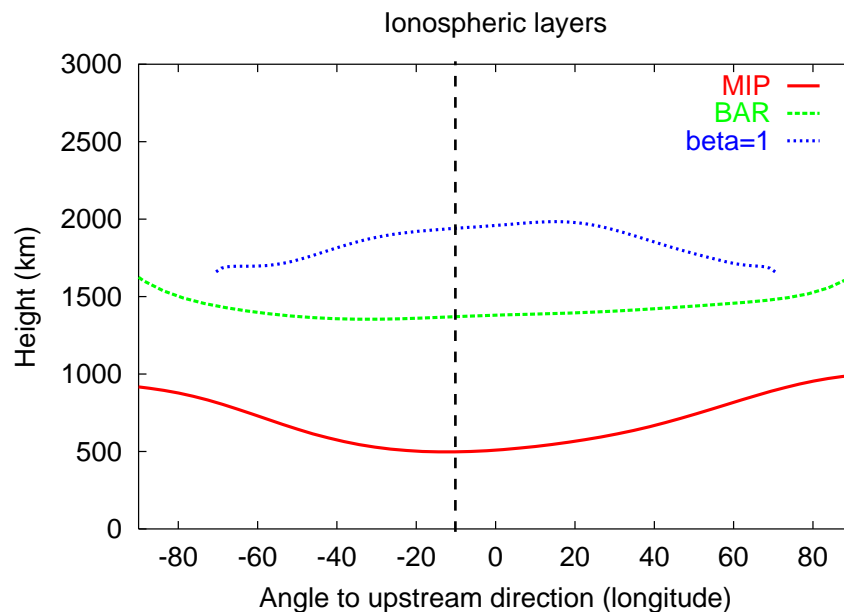


**Figure 5.38:** Altitude of magnetic ionopause (MIP), magnetic barrier peak (BAR), and  $\beta_1$ -layer as a function of the longitude angle ( $\phi$ ) for the T5 case. The solid line marks the solar zenith position and the dashed line the midnight position.

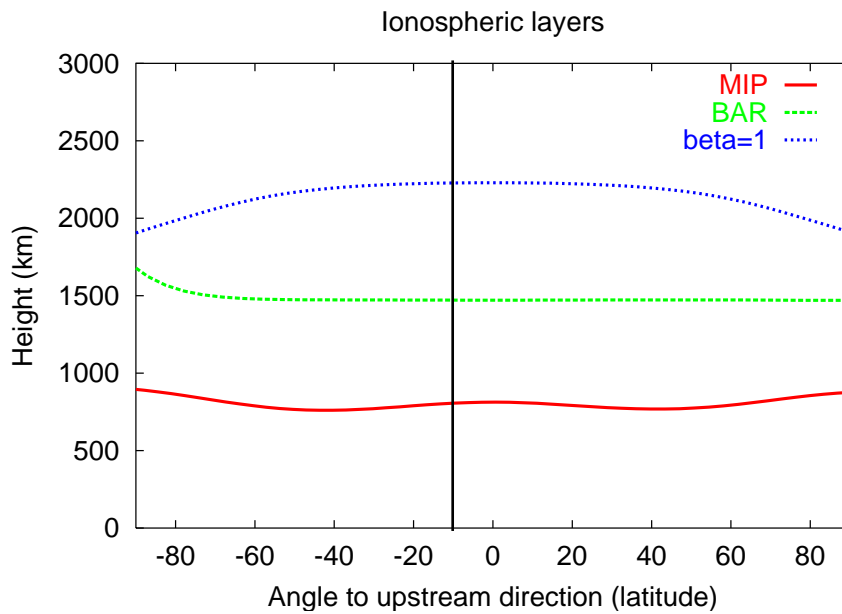


**Figure 5.39:** Altitude of magnetic ionopause (MIP), magnetic barrier peak (BAR), and  $\beta_1$ -layer as a function of the latitude angle ( $\theta$ ) for the T34 case. The solid line marks the solar zenith position and the dashed line the midnight position.

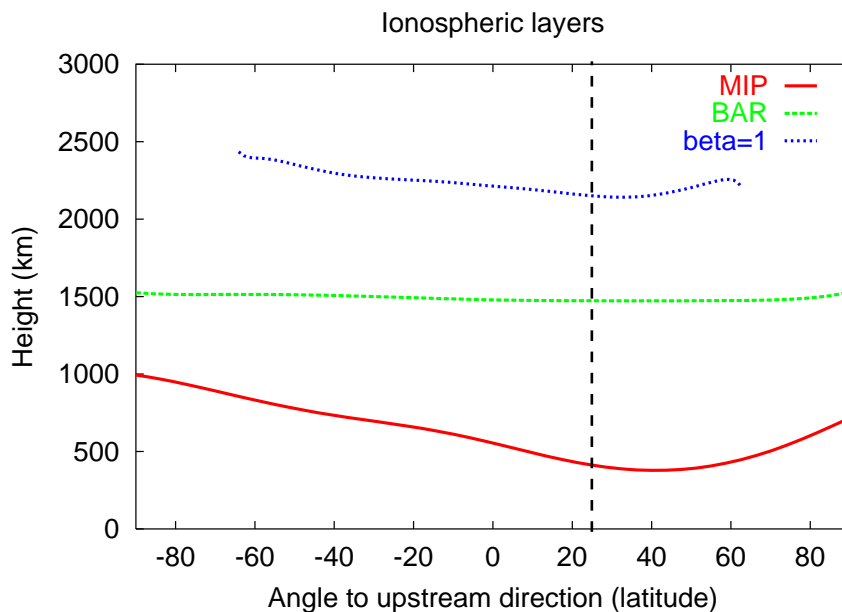


**Figure 5.40:** Altitude of magnetic ionopause (MIP), magnetic barrier peak (BAR), and  $\beta_1$ -layer as a function of the latitude angle ( $\theta$ ) for the TA case. The solid line marks the solar zenith position and the dashed line the midnight position.

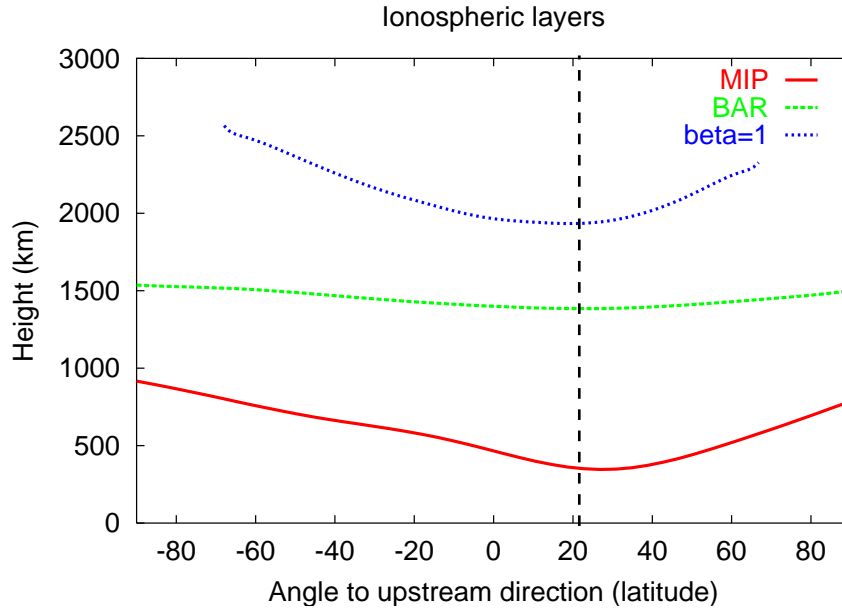


**Figure 5.41:** Altitude of magnetic ionopause (MIP), magnetic barrier peak (BAR), and  $\beta_1$ -layer as a function of the latitude angle ( $\theta$ ) for the T34 case. The solid line marks the solar zenith position and the dashed line the midnight position.

from the simulation results by applying the following criteria: The MIP is the location where the increase of magnetic field magnitude with radial distance from the center of Titan is maximum. For BAR and the  $\beta_1$ -layer the definitions are unambiguous. The functions plotted in Figure 5.36 to Figure 5.41 are smoothed in order to wash out the effects of the Cartesian grid. For angles larger than  $90^\circ$  the layers are poorly defined. We limit the region of the analysis to angles  $\leq 90^\circ$  i.e. to the upstream hemisphere.

The altitude of the MIP varies between 500 km and 1200 km. The minimum altitude is always near the midnight angle. Thus, the MIP altitude depends on the solar zenith angle and therefore on SLT. The dependence of the MIP on the angle to the ram direction, i.e. on the external plasma flow, can be obtained from Figure 5.36. From the decrease of altitude with solar zenith angle the altitude should decrease towards the flanks in the T34 case (upstream side = dayside). Instead it smoothly increases with  $\phi$  with a maximum altitude at  $\phi = 90^\circ$ . This indicates a weak dependence of the MIP altitude on the angle to the flow direction.

As a function of the angle towards the poles ( $\theta$ ) the MIP altitude is also minimum at the midnight angle (see Figure 5.39, 5.40, and 5.41). In the T34 case where the upstream side is identical with the dayside the variation of the altitude with  $\theta$  is quite low ( $\Delta h \approx 150$  km), less than the grid resolution.

The  $\beta_1$ -layer is higher at higher altitudes than the MIP. In the equatorial plane the altitude of the  $\beta_1$ -layer at T34 and TA conditions has a maximum at  $\phi = 0^\circ$  (see Figure 5.36, 5.37) indicating that the altitude depends on the plasma flow. In the T5 case the maximum is shifted by about  $20^\circ$  towards the Saturnian flank which is away from the midnight angle (see Figure 5.38). The peak altitude decrease from T34 (2200 km) over TA (2150 km) to T5 (2,000 km). The difference between peak and minimum altitude decreases from T34

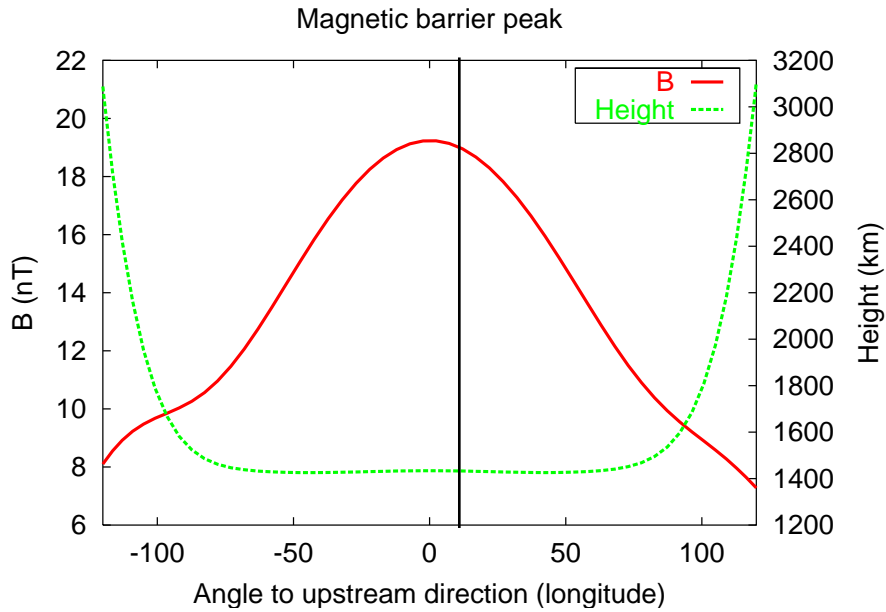


**Figure 5.42:** Altitude and magnitude of the magnetic barrier peak at T34 as a function of the longitude angle ( $\phi$ ) for the T34 case.

( $\Delta \approx 450$  km) over TA ( $\Delta \approx 300$  km) to T5 ( $\Delta \approx 200$  km).

As a function of  $\theta$  the altitude of the  $\beta_1$ -layer also decreases with increasing angle to the ram direction in the T34 case, but weaker than in the equatorial plane. The altitudes at TA (Figure 5.40) and T5 (Figure 5.41) have a minimum near at the midnight angle.

There are two competing effects that take influence on the altitude of the  $\beta_1$ -layer: the altitude increases with ionospheric density (minimum at midnight) and decreases as a function of the equatorial angle to the ram direction. Towards the poles it is independent of the angle to the ram direction ( $\theta$ ) but it is rather controlled by the ionosphere leading to a minimum near midnight and increasing altitude towards the dayside.

The BAR altitude shows neither a strong dependence on  $\phi$  nor on  $\theta$ . The BAR is at an altitude of  $h \leq 1500$  km. The total variation is about  $\Delta h = 100$  km which is below our grid resolution. But despite that we are able to extract information about the functional behavior from Figure 5.36 to Figure 5.41 the location of the minimum coincides always with the midnight angle. We can conclude that the BAR altitude is neither controlled by the plasma flow nor by the ionosphere but rather by the neutral atmosphere which is spherical symmetric in our model. The lower altitude around midnight may be due to magnetic diffusion which is maximum there.

In Figure 5.42 to Figure 5.47 the peak magnetic field magnitude is plotted as a function of  $\phi$  and  $\theta$  in addition to the peak altitude. Although the altitude is nearly constant the magnitude shows a strong dependence on the angle to the ram direction. The maximum is always at  $\phi = 0^\circ$  and  $\theta = 0^\circ$  and it decreases as the absolute value of the angles increases. The decrease towards the poles is lower than in the equatorial plane and appears to be linearly in the angle, i.e. the magnitude towards the poles is a linear function of the arc length of the magnetic field

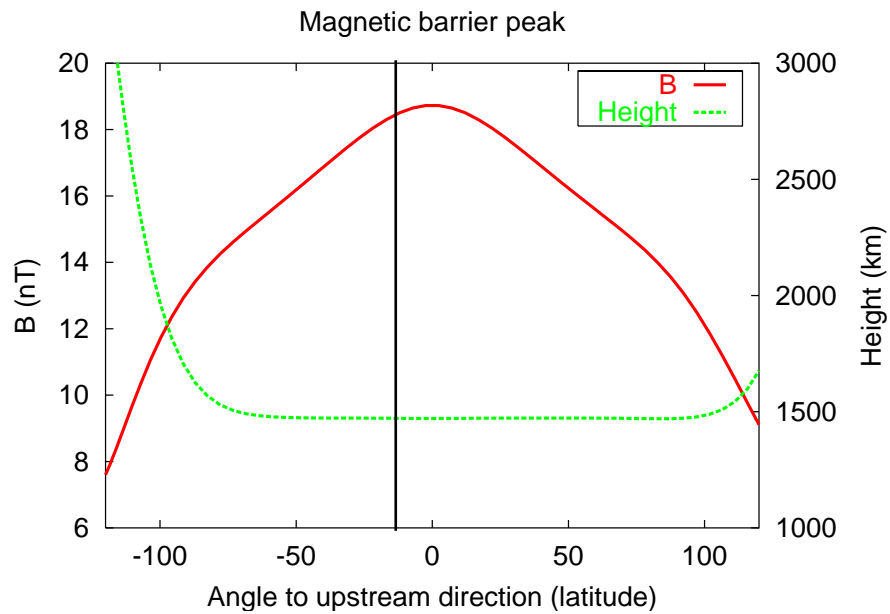


**Figure 5.43:** Altitude and magnitude of the magnetic barrier peak as a function of the latitude angle ( $\theta$ ) for the T34 case.

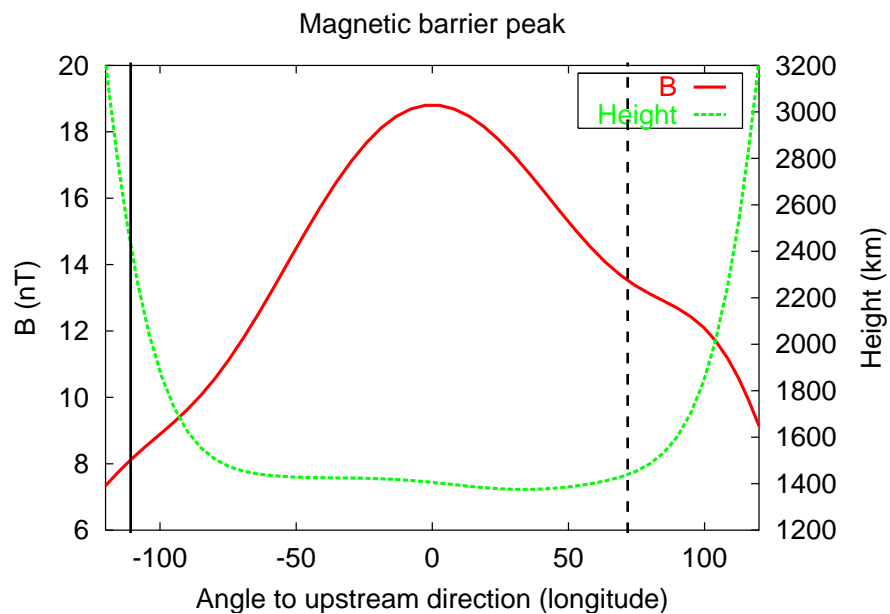


**Figure 5.44:** Altitude and magnitude of the magnetic barrier peak as a function of the longitude angle ( $\phi$ ) for the TA case.

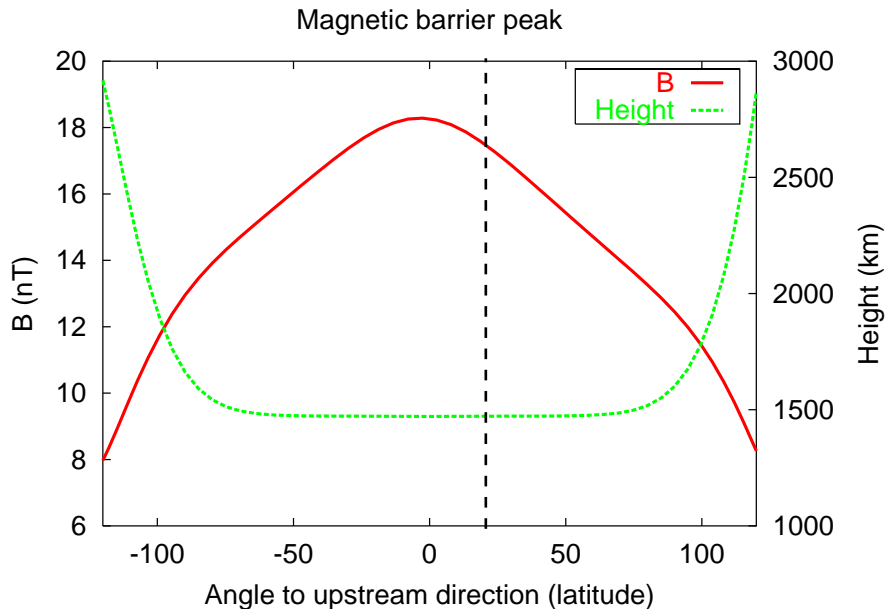


**Figure 5.45:** Altitude and magnitude of the magnetic barrier peak as a function of the latitude angle ( $\theta$ ) for the TA case.

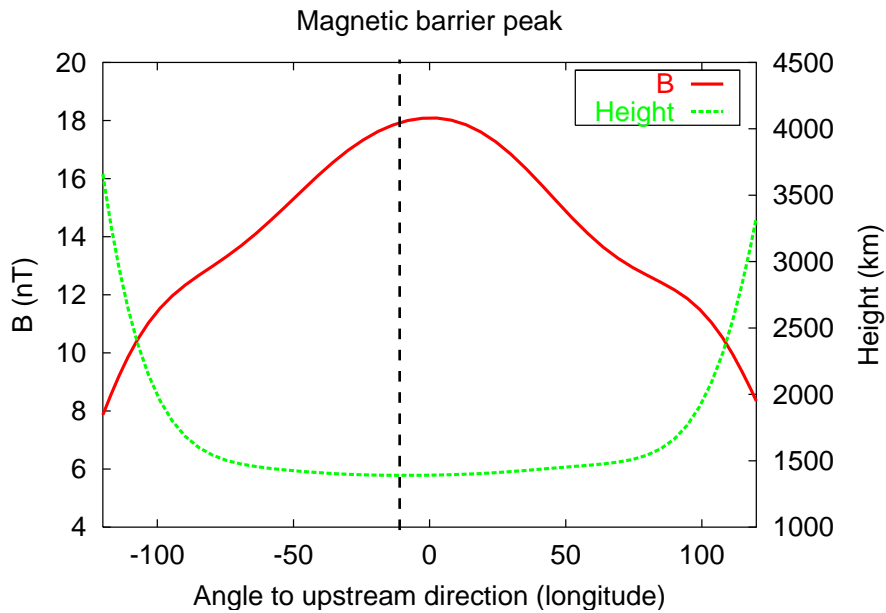


**Figure 5.46:** Altitude and magnitude of the magnetic barrier peak as a function of the longitude angle ( $\phi$ ) for the T5 case.

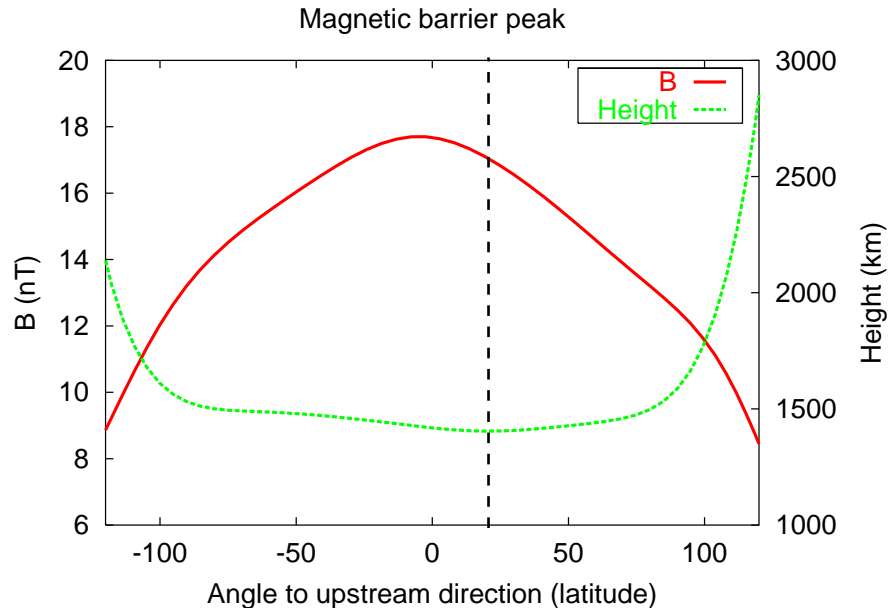


**Figure 5.47:** Altitude and magnitude of the magnetic barrier peak as a function of the latitude angle ( $\theta$ ) for the T5 case.

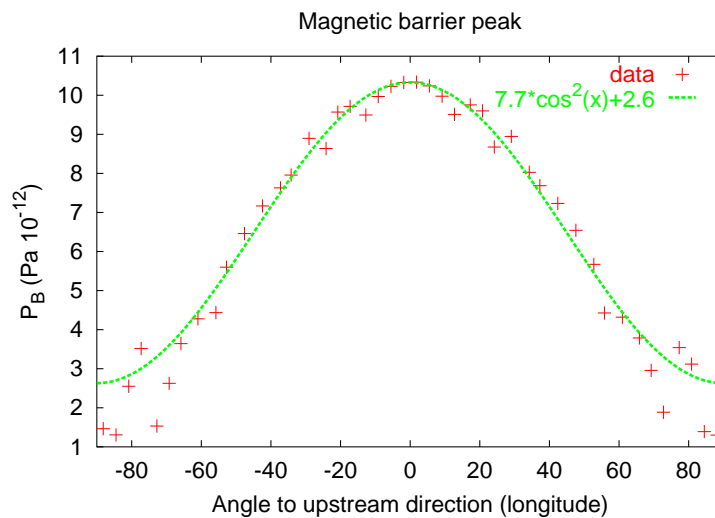


**Figure 5.48:** Magnetic pressure at the magnetic barrier peak in the equatorial plane as a function of the angle to the upstream direction. The crosses are the results from our T34 model and the line is a  $\cos^2 \phi$  function fitted to the data.

line.

The functional behavior of the magnetic pressure at the magnetic barrier peak in the equatorial plane can be fitted by the square of a cosine function (see Figure 5.48) which implies a proportionality of the magnitude to the radial component of the upstream velocity ( $\sim \cos(\phi)$ ). For the T34 case (see Figure 5.48) the fit agrees very well with the simulation result between  $-70^\circ < \phi < 65^\circ$ . For  $|\phi| > 70^\circ$  the solar zenith angle is large and the ionospheric peak density low and magnetic diffusion broadens the function. The behavior of the peak magnitude as

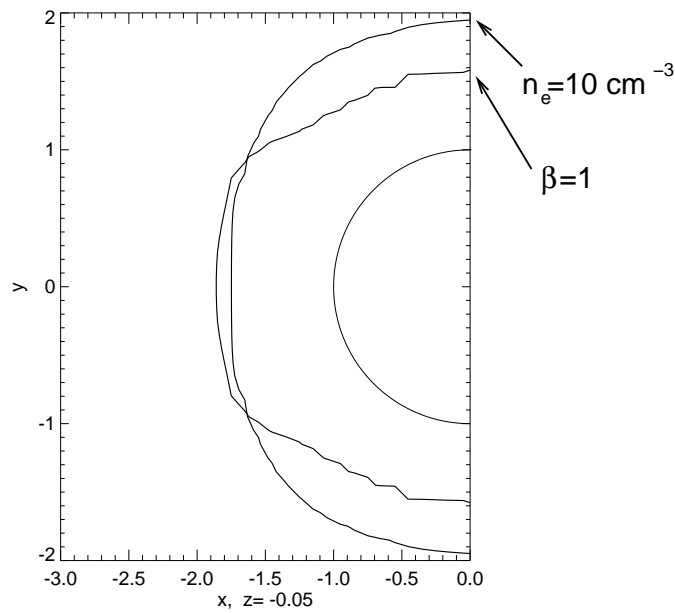


**Figure 5.49:** Location of  $\beta = 1$  and the contour line of  $n_e = 10 \text{ cm}^{-3}$  in the equatorial plane at T34.

a function of  $\phi$  for case TA (Figure 5.44) supports this interpretation: on the anti-Saturnian side ( $\phi < 0^\circ$ ), which corresponds to the dayside, the cosine function fits the data very well, while on the Saturnian (night) side the function is broadened. At T5 conditions the function is broader on both flanks (see Figure 5.46). The large scale fields observed in the ionosphere of Venus have also been shown to be proportional to the cosine of the ram angle to the ram direction [Russell *et al.*, 1982]. The peak magnitude decreases from T34 ( $B \approx 19.5 \text{ nT}$ ) over TA ( $B \approx 19 \text{ nT}$ ) to T5 ( $B \approx 18 \text{ nT}$ ). The decrease may be due to magnetic diffusion.

At the end of this section the physical processes that are responsible for the formation of the layers are combined with the information gained from the analysis of this section. The MIP is the position where the magnetic field from the upper ionosphere drops with decreasing altitude. At that position the unmagnetized lower ionosphere has to balance the pressure of the magnetized upper ionosphere. This happens with the support of the neutral gas. At positions where the ionospheric density is high, a low support of the neutral gas is sufficient which leads to the formation of the MIP at high altitudes. At locations where the ionospheric density is quite low like on the nightside, a larger support by the neutral gas is necessary and the MIP forms at lower altitudes. This is consistent with our analysis above.

For the creation of the  $\beta 1$ -layer the magnetic pressure has to increase with a simultaneous decreasing thermal pressure. In Section 5.4 we have shown that this is connected to the flow divergence parallel to the magnetic field or alternatively it can be caused by mass-loading or friction with the neutral gas. In Section 5.1 we have discussed the pressure profiles along the ram direction and we have shown that mass-loading does not play a crucial role at Titan but friction with the neutral gas does. Thus, there are two candidates for causing the pressure conversion.

In Figure 5.49 we have plotted the  $\beta 1$ -layer together with the  $10 \text{ cm}^{-3}$  electron density contour line. One can recognize that in the range of  $-50^\circ < \phi < 50^\circ$  the distance between the two lines is nearly constant ( $\sim 200 \text{ km}$ ). This indicates that the conductive ionosphere in that region determines the altitude of the  $\beta 1$ -layer and that pressure conversion is achieved by the "ideal" pile-up with diverging flow along  $\vec{B}$ . At the flanks, the altitude decouples from the electron density contour and decreases. By that the neutral gas influence increases. Then, the pile-up mechanism consists of a mixture of frictional and ideal pile-up. The altitude towards the poles is determined by the field aligned plasma flow.

The the magnetic barrier peak altitude shows a similar behavior as the altitude of the MIP but with a much weaker total variation. Therefore it is also controlled by the ionosphere and the neutral gas.

In the equatorial plane the magnitude of the magnetic barrier peak is proportional to  $\cos(\phi)$  indicating that the peak magnitude is controlled by the radial component of the flow. In the T34 case the best fit was obtained with the function

$$B_{BAR}(\phi) = \sqrt{B_{BAR,0}^2 + \Delta B_{BAR}^2 \cos^2(\phi)} \quad (5.9)$$

with  $B_{BAR,0} = 10.3 \text{ nT}$  and  $\Delta B_{BAR} = 17.5 \text{ nT}$ . The expression can be rewritten in a dimensionless form by taking the square and dividing through  $2\mu_0$  and dividing the equation by the total pressure of the incident plasma i.e.  $\rho_0 v_0^2 + B_0^2/(2\mu_0) + p_0$ :

$$\frac{P_{B,BAR}(\phi)}{\rho_0 v_0^2 + P_{B,0} + p} = 0.25 + 0.74 \cos^2(\phi). \quad (5.10)$$

That means that the magnetic pressure at the peak of the magnetic barrier in the equatorial plane is one fourth of the total pressure of the incident plasma plus a part which depends on  $\phi$ . This part is at maximum three fourth of the total pressure at  $\phi = 0^\circ$ . In this case the peak magnetic pressure in the barrier is nearly equal to the total incident plasma pressure and only a small fraction  $\sim 1\%$  of the total pressure is thermal pressure. For comparison: at Venus Pioneer Venus orbiter measurements have shown that the magnetic field at the barrier peak is  $B^2/(2\mu_0) = 0.85 \rho_{sw} u_{sw}^2 \cos^2 \chi$ , where  $sw$  means solar wind and  $\chi$  is the solar zenith angle *Russell et al.* [1982]. Thus at Venus about 85% of the incident solar wind pressure is transformed into magnetic pressure inside of the magnetic barrier. A difference between Venus and Titan is that at Venus there is a bow shock between the incident plasma and the magnetic barrier peak.

The angular dependence of the peak magnetic barrier magnitude towards the poles is different from that in the equatorial plane. Replacing  $\phi$  by  $\theta$  in Eq. 5.9 does not fit the simulation results. Apart from the region around the ram angle  $-20^\circ < \theta < 20^\circ$  the peak magnitude is a linear function of  $|\theta|$  and thereby of the arc length of the magnetic field lines. From our analysis we derived that the slope of the linear decrease with  $\theta$  is proportional to  $\cos(\phi)$ . Figure 5.66 shows that the magnetic field lines do not have  $y$  components in the upstream side even near the flanks. See also a schematic drawing of the magnetic field configuration in Figure 5.50. The altitude of the magnetic barrier peak is quite constant as we have just seen. Then, the field lines through the barrier peak on the upstream side are half-circles with a radius of  $R_0 \cos(\phi)$  when  $R_0$  is the distance of the barrier peak from the center of Titan at

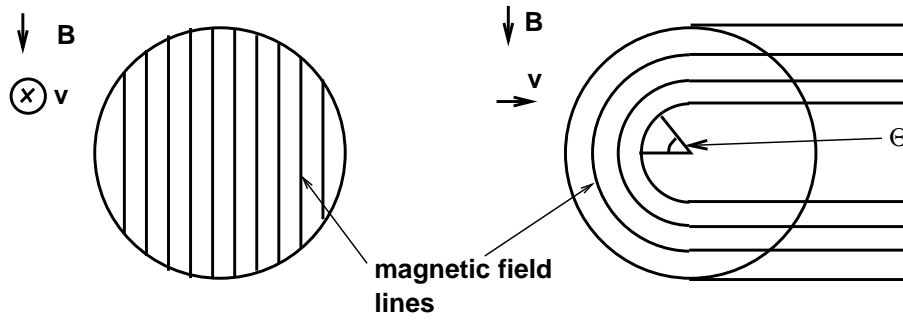


**Figure 5.50:** Schematic drawing of the magnetic field lines through the magnetic barrier peak in two projections. In the upstream hemisphere the field lines are half circles. Figure 5.66 displays the same field lines resulting from the simulation of T34.

the sub-flow point. The functional behavior of the magnetic barrier peak magnitude can be expressed as:

$$B_{BAR}(\phi, \theta) = \sqrt{B_{BAR,0}^2 + \Delta B_{BAR}^2 \cos^2(\phi)} - (K_{BAR,0} + K_{BAR,1} * \cos(\phi))|\theta|. \quad (5.11)$$

The parameters of the decrease have been calculated from the numerical results:  $K_{BAR,0} = -8.3 \times 10^{-2} \text{ nT}(\text{°})^{-1}$  and  $K_{BAR,1} = 1.5 \times 10^{-2} \text{ nT}(\text{°})^{-1}$ . Eq. (5.11) has to be read as follows: The magnitude of the barrier peak in the equatorial plane at an angle  $\phi$  is obtained by setting  $\theta = 0$  in Eq. (5.11). Along the field line that intersects the equatorial plane at that position the magnetic field magnitude decreases linearly with the arc length of the field line. The radius of the field line is proportional to  $\cos \phi$  and the arc length is then  $\sim \cos(\phi)\theta$ . Note, that our angles  $\phi$  and  $\theta$  are not the usual spherical angles.  $\phi$  is a cylindrical angle in the  $xy$ -plane and  $\theta$  is a cylindrical angle in the  $xz$ -plane. They can be transformed into spherical angles by applying  $\sin \phi = \sin \phi_{sph} \sin \theta_{sph}$  and  $\tan \theta = \tan \theta_{sph} / \cos \phi_{sph}$ . The expressions in Eq. (5.11) are more complicated functions of the angles in that case because spherical coordinates do not match the field line geometry.

To summarize the information we gained about the magnitude of the magnetic barrier peak: the peak magnitude decreases in the equatorial plane with  $\sim \cos \phi$ . For a given field line the magnitude is maximum where the field line intersects the equatorial plane. Along the field line the magnitude decreases linearly with the length of the path.

### 5.3 Collision frequencies and magnetic diffusion

In this section we want to examine some typical frequencies in the ionosphere as they turn out from our calculations and draw conclusions from the behavior of the frequencies as a function of altitude.

A typical frequency in a plasma is the gyro- or cyclotron frequency which is a measure for the gyration of a charged particle around a magnetic field line. This frequency is direct proportional to the magnetic field magnitude ( $f_{ci} = eB/2\pi m_i$ ). Because of the inverse proportionality to the particle mass the gyrofrequency of the electrons is about five orders of

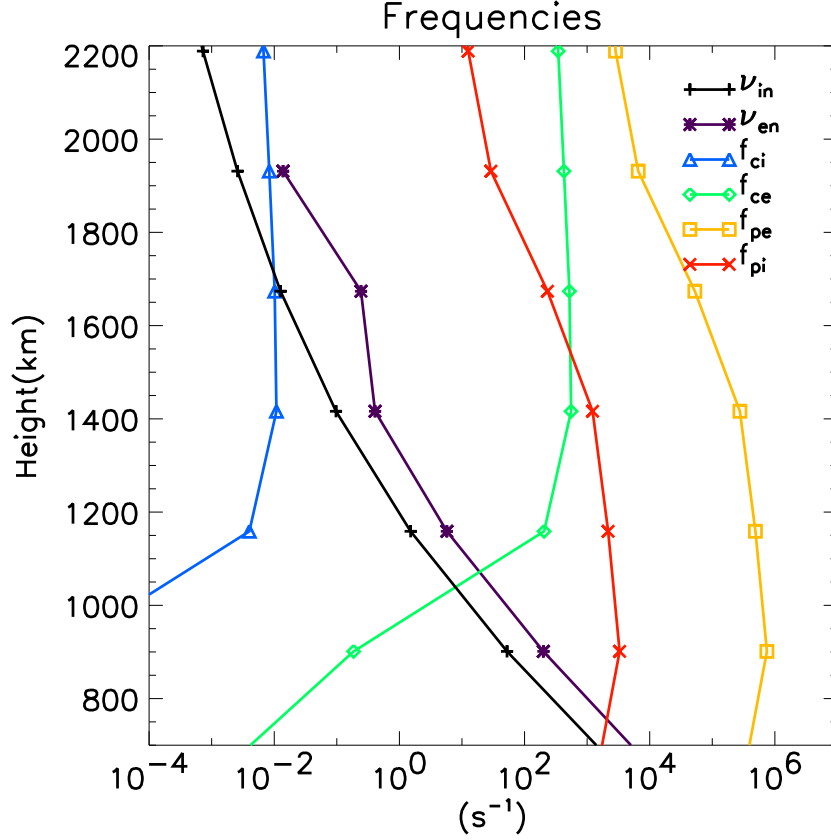


**Figure 5.51:** Gyrofrequencies and collision frequencies and plasma frequencies of ions ( $f_{ci}$ ,  $\nu_{in}$ ,  $f_{pi}$ ) and electrons ( $f_{ce}$ ,  $\nu_{en}$ ,  $f_{pe}$ ) in the dayside upstream ionosphere at T34 conditions. For the mass of the ion species we assumed 28 amu.

magnitude higher than that of the ions. In Figure 5.51 the gyrofrequencies are plotted in the dayside upstream ionosphere in the T34 case. The gyrofrequency of the ions ( $m_i = 28$  amu) in the incident plasma is of the order of  $10^{-3} s^{-1}$  and of the electrons  $10^2 s^{-1}$ . In the log-scale the increase of the frequencies in the magnetic pile-up region is barely noticeable. In the magnetic ionopause the frequencies sharply decrease due to the drop of magnetic field magnitude.

The absolute value of the gyrofrequency is not very meaningful. More significant is the relation of the gyrofrequencies to other frequencies. Since the plasma is embedded into a neutral gas the gyrofrequencies have to compete with the ion-neutral or electron-neutral collision frequencies. These frequencies are also plotted in Figure 5.51. They are more or less proportional to the neutral gas density (see Eq. (4.17)).

At an altitude of about 1700 km the collision frequency of the ions with the neutral gas is equal to the gyrofrequency. That means that below that altitude the gyration of the ions is significantly perturbed by the collisions with the neutral gas while the electrons due to the much higher gyrofrequency are relatively unaffected by the collisions. This implies that the magnetic field is frozen into the electron fluid rather than into the bulk plasma below that altitude which means further that the Hall term in the induction equation becomes important.

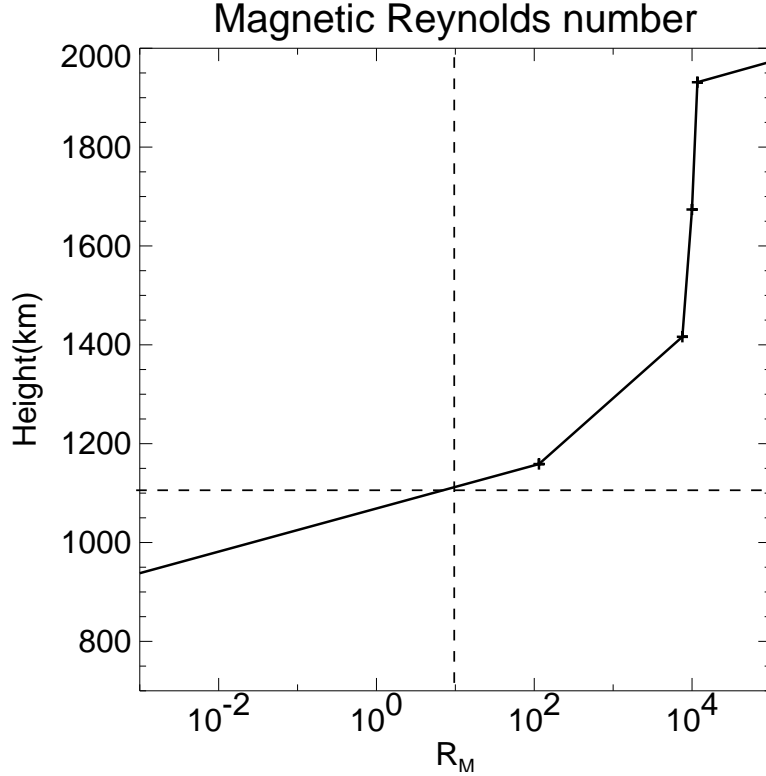


**Figure 5.52:** Magnetic Reynolds number in the dayside upstream ionosphere at T34 conditions.

Combining Hall term and convection term in the induction equation leads to

$$\frac{\partial \vec{B}}{\partial t} = \vec{\nabla} \times (\vec{v}_e \times \vec{B}). \quad (5.12)$$

In this model we have neglected the Hall term basically because of numerical reasons. We solve the induction equation given in Eq. 4.25. At this point we can estimate in which region the Hall term would alter the results.

At about 1100 km (in the T34 case, at T5 it is at  $\sim 900$  km) the electron gyrofrequency is equal to the electron-neutral collision frequency. Below this altitude the frozen-in condition completely loses its validity and the magnetic field transport is dominated by magnetic diffusion. The relation of the Hall term to the diffusion term in the induction equation is of the order of  $f_{ce}/\nu_{en}$  meaning that below 1100 km magnetic field is transported by magnetic diffusion. The magnetic Reynolds number  $R_M = Lv/D_B$  which is a measure for the relation between convection and diffusion term in the induction equation (Eq. 4.25) is equal to 1 at 1100 km and far below 1 below that altitude (Figure 5.52). The length scale  $L$  in the magnetic Reynolds number is the length scale of the magnetic field and has been calculated as  $L = |B/\frac{\partial B}{\partial x}|$ .

From the analyses of the gyrofrequencies and the collision frequencies in the ionosphere can be concluded that the Hall term could possibly alter the results presented here in the region between 1100 km and 1700 km. As Saur [2000] has shown, the Hall effect rotates the electric field towards the flow velocity of the incident plasma. The rotation angle can be up to  $90^\circ$ .

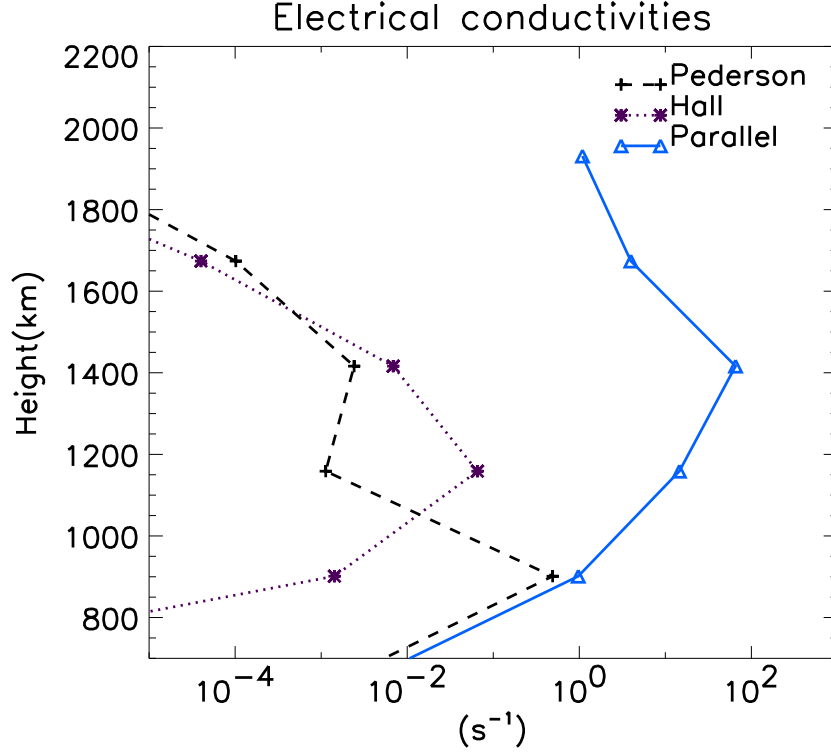


**Figure 5.53:** Electrical conductivities in the upstream ionosphere of T34.

As far as we know there is no Hall MHD model of the plasma interaction of a satellite with a streaming plasma. In the hybrid model of *Brecht et al.* [2000] the electric field rotation due to the Hall effect is visible (see Section 5.6) but one has to keep in mind that the model does not include ion-neutral collisions.

Another conclusion can be drawn from the relation of gyrofrequency to collision frequency. The relation of electronic heat conduction perpendicular to the magnetic field to heat conduction parallel to the magnetic field is proportional to  $1/(1 + f_{ce}^2/v_{en}^2)$  [*Banks and Kockarts, 1973b*] which means that perpendicular heat conduction is only effective if the electron-neutral collision frequency is of the order or higher than the electron gyrofrequency. In the flux tube model we assumed that heat conduction solely occurs parallel to the magnetic field. Figure 5.51 indicates that above 1100 km heat conduction is parallel to the magnetic field and below it is isotropic. The flux tubes in our model for the magnetospheric electrons do not reach altitudes below 1200 km (see Figure 5.17 and Figure 5.18). Thus, our assumption is justified.

The plasma frequency ( $f_{ps} = \sqrt{n_s e^2 / \epsilon_0 m_s}$ ) is also plotted in Figure 5.51. At the ionospheric peak it is about  $10^6 \text{ s}^{-1}$  for the electrons and  $\sim 10^3$  for the ions. Electromagnetic waves with a frequency lower than the electron plasma frequency cannot propagate in the plasma.

From the cyclotron and collision frequencies the electrical conductivities in Titan's ionosphere can be calculated. The Pedersen conductivity is given by [*Schunk and Nagy, 2000*]

$$\sigma_P = \frac{n_e e}{B} \left( \frac{\omega_{ci} \nu_{in}}{\nu_{in}^2 + \omega_{ci}^2} + \frac{\omega_{ce} \nu_{en}}{\nu_{en}^2 + \omega_{ce}^2} \right) \quad (5.13)$$

and the Hall conductivity is

$$\sigma_H = \frac{n_e e}{B} \left( \frac{\omega_{ci}^2}{v_{in}^2 + \omega_{ci}^2} + \frac{\omega_{ce}^2}{v_{en}^2 + \omega_{ce}^2} \right) \quad (5.14)$$

with  $\omega_{ci,e} = 2\pi f_{ci,e}$ . The resulting conductivities through the upstream ionosphere in the T34 case are displayed in Figure 5.53. Between about 1100 km and 1550 the Hall conductivity is larger than the Pedersen conductivity which is consistent with range of altitude where the Hall term is effective.

## 5.4 Magnetic pile-up

The pressure profiles along the upstream direction (see Figure 5.20) show that in the so-called magnetic pile-up region or magnetic barrier thermal pressure is transformed into magnetic pressure. This occurs at an altitude where the magnetic Reynolds number is much larger than 1 (see Figure 5.52) and where the cooling or heating terms due to the neutral gas are negligible in the pressure equation (Eq. 4.26). That means magnetic field and thermal pressure at least in the upper magnetic pile-up region are described by the ideal MHD equations (Eq. (4.6) and Eq. (4.7)).

In this Section we will discuss the *ideal* pile-up process and compare it with a second pile-up process that we call collisional pile-up.

The adiabatic pressure equation and the induction equation in ideal MHD can be written as [Baumjohann and Treumann, 1996]

$$\frac{d\vec{B}}{dt} = -\vec{B}\vec{\nabla} \cdot \vec{v} + \vec{B} \cdot \vec{\nabla}\vec{v} \quad (5.15)$$

and

$$\frac{dp}{dt} = -\gamma p \vec{\nabla} \cdot \vec{v} \quad (5.16)$$

where  $\frac{d}{dt} = \frac{\partial}{\partial t} + \vec{v} \cdot \vec{\nabla}$  is the derivative along a stream line. By multiplying Eq. (5.15) with  $\vec{B}/\mu_0$  we obtain an equation for the magnetic pressure

$$\frac{dB^2/(2\mu_0)}{dt} = -\frac{B^2}{\mu_0} \vec{\nabla} \cdot \vec{v} + \frac{\vec{B}}{\mu_0} \cdot (\vec{B} \cdot \vec{\nabla}\vec{v}). \quad (5.17)$$

Eq. (5.16) states that in ideal adiabatic MHD the thermal pressure along a stream line changes only if  $\vec{\nabla} \cdot \vec{v} \neq 0$ . The first term on the right hand side of Eq. (5.17) changes the magnetic pressure qualitatively in the same way as the thermal pressure. If along a stream line magnetic pressure increases while thermal pressure decreases, the second term on the right hand side of Eq. (5.17) must exceed the first, i.e.

$$|\hat{B}(\hat{B} \cdot \vec{\nabla})\vec{v}| > |\vec{\nabla} \cdot \vec{v}|. \quad (5.18)$$

Eq. (5.18) puts a constraint on the flow field. In other words, a magnetic pile-up with simultaneously decreasing thermal pressure occurs in ideal MHD if the flow fulfills Eq. (5.18) and if  $\vec{\nabla} \cdot \vec{v} > 0$  (according to Eq. (5.16)).

We want to demonstrate the consequences with the help of one example. In the 2D model of *Cravens et al.* [1998] of the plasma flow around Titan, the incident magnetic field is parallel to  $z$  and the incident flow velocity is  $v_{x,0}$ . The obstacle has a cylindrical geometry with the axis parallel to  $z$ . Because of the symmetry along  $z$  the resulting flow is  $\vec{v}(x,y) = (v_x(x,y), v_y(x,y), 0)$ , i.e. two dimensional. In that case only the  $z$  component of the magnetic field changes,  $\vec{B}(x,y) = (0, 0, B_z(x,y))$  and  $\frac{\partial}{\partial z} = 0$ . When we insert this into Eq. (5.18) we obtain

$$0 > |\vec{\nabla} \cdot \vec{v}| \quad (5.19)$$

which is only fulfilled if  $\vec{\nabla} \cdot \vec{v} = 0$ . In that case magnetic and thermal pressure are constant along a stream line and no ideal magnetic pile-up is possible at all.

But in the pressure profile along the ram direction displayed in *Cravens et al.* [1998] there is a pile-up region with enhanced magnetic pressure and reduced thermal pressure. They have included additional terms into the pressure equation and magnetic induction equation due to mass-loading and friction with the neutral gas which adds a magnetic diffusion term to the ideal induction equation. Magnetic diffusion cannot lead to a magnetic pile-up since it only transports magnetic field from a high field to a low field location. Hence, only the convection part in the induction equation can be responsible for the magnetic pile-up i.e. (from Eq. (5.17))  $\vec{\nabla} \cdot \vec{v} < 0$  (the second part in Eq. (5.17) is zero because of  $\frac{\partial}{\partial z} = 0$ ).

If  $\vec{\nabla} \cdot \vec{v} < 0$ , the thermal pressure in ideal MHD would increase as well. Thus, the decrease of the thermal pressure at the pile-up location in the *Cravens et al.* [1998] model can only be caused by the additional terms i.e. by the influence of the neutral gas.

From the considerations above, we can distinguish two different mechanisms that lead to magnetic pile-up while thermal pressure is reduced: the *ideal* pile-up and the *collisional* pile-up. A necessary condition for the ideal pile-up is that  $\vec{\nabla} \cdot \vec{v} > 0$  while in the collisional pile-up  $\vec{\nabla} \cdot \vec{v}$  can be negative.

This has consequences for the plasma density in the pile-up region. Because of

$$\frac{d\rho}{dt} = -\rho \vec{\nabla} \cdot \vec{v} \quad (5.20)$$

the plasma density in the ideal pile-up region is reduced. The result is consistent with the predicted plasma depletion in the pile-up region by *Zwan and Wolf* [1976].

The ideal pile-up mechanism is related to the plasma flow parallel to  $\vec{B}$ . Velocity components parallel to  $\vec{B}$  transport density and pressure but no magnetic field. An obstacle that causes part of the plasma to flow along  $\vec{B}$  leads to a situation where ideal pile-up can occur. In the 2D geometry in the *Cravens et al.* [1998] model plasma flow along  $\vec{B}$  is prohibited and therefore ideal pile-up is not possible.

At Titan both mechanisms for magnetic pile-up are present. Figure 5.54 shows the magnetic pressure, the thermal pressure, density, and  $\vec{\nabla} \cdot \vec{v}$  along the ram direction in the T5 case. Above about 1700 km magnetic pile-up is accompanied by a decrease of the plasma density, which indicates that there is no mass loading at that altitude, and  $\vec{\nabla} \cdot \vec{v} > 0$ . In that region pile-up is caused by the ideal mechanism. Between about 1550 km and 1400 km  $\vec{\nabla} \cdot \vec{v} < 0$  therefore ideal pile-up is not possible. Thus, magnetic pressure increases and thermal pressure decreases due

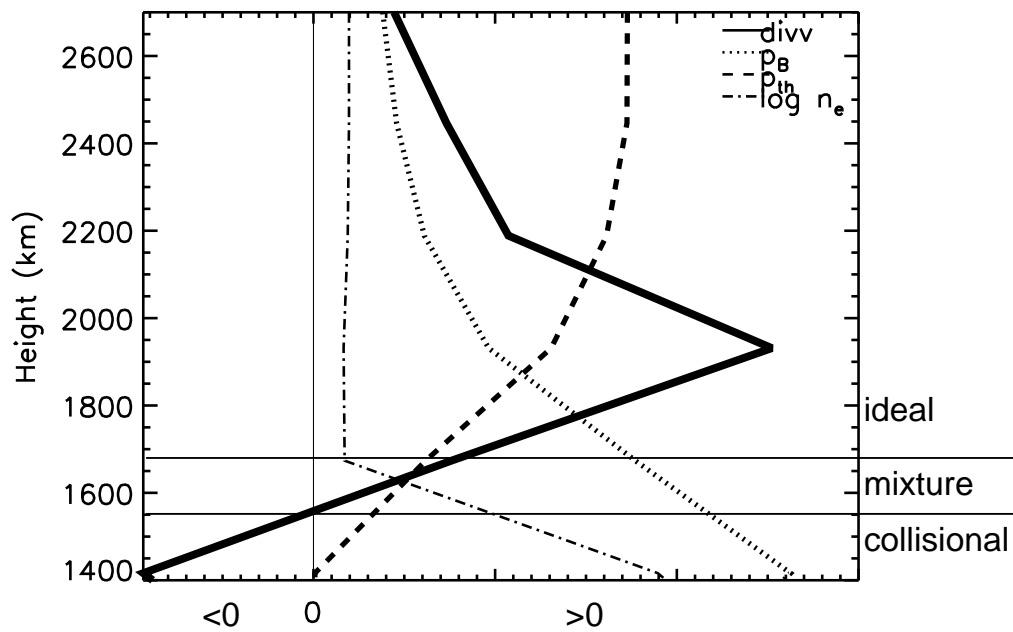


**Figure 5.54:** Different regions of magnetic pile-up. The x scale is different for every variable in order to combine them in one plot. Important is the change of sign of  $\vec{\nabla} \cdot \vec{v}$ . When  $\vec{\nabla} \cdot \vec{v} < 0$  ideal pile-up is not possible. Over the whole plotted range of altitude magnetic pressure increases while thermal pressure decreases with decreasing altitude. Above 1700 km is  $\vec{\nabla} \cdot \vec{v} > 0$  and plasma density decreases  $\rightarrow$  ideal magnetic pile-up. Below 1550 km is  $\vec{\nabla} \cdot \vec{v} < 0 \rightarrow$  collisional pile-up.

to the collisional mechanism. Between the two regions both processes occur.  $\vec{\nabla} \cdot \vec{v} > 0$  there but the plasma density increases because of mass-loading. The decrease of thermal pressure can be caused by both, cooling by ion-neutral collisions and  $\vec{\nabla} \cdot \vec{v} > 0$ .

In Figure 5.103 the magnetic field profile along the ram direction from *Cravens et al.* [1998] is plotted together with the profiles from our T34 and T5 model.

In summary the results of this Section are: (1) There are two different processes than can cause magnetic pile-up while keeping the sum of magnetic and thermal pressure constant: the *ideal* pile-up and the *collisional* pile-up. (2) If the plasma flow along the magnetic field is inhibited ideal pile-up is not possible. (3) At Titan the upper part of the pile-up is due to the ideal mechanism while in the lower part both mechanisms are active.

## 5.5 Global plasma interaction

### 5.5.1 Electric currents

Ampère's law ( $\vec{j} = \frac{1}{\mu_0} \vec{\nabla} \times \vec{B}$ ) connects all curvatures and tangential changes of the magnetic field to electric currents which fulfill  $\vec{\nabla} \cdot \vec{j} = 0$ . In this section the current system that is set up by the plasma interaction is discussed.

#### 5.5.1.1 Currents in the sub-Alfvénic case

Before we explain the currents at Titan, we briefly summarize the current system that is created by the interaction of a satellite with a sub-Alfvénic plasma occurring for example at Io.

The Alfvén wave current system at Io is described by *Neubauer* [1980]. In a non-linear theory he shows that the currents that correspond to the so-called Alfvén wings or Alfvén tubes can be divided into two parts: the *Alfvén current* ( $\vec{j}_{\parallel}$ ) that flows along the Alfvén characteristics

$$\vec{v}_A^{\pm} = \vec{v}_0 \pm \frac{\vec{B}_0}{\sqrt{\mu_0 \rho}} \quad (5.21)$$

and a current in the plane perpendicular to the characteristics, the *perpendicular current* ( $\vec{j}_{\perp}$ )<sup>2</sup>.  $\vec{j}_{\parallel}$  and  $\vec{j}_{\perp}$  have divergence zero separately!

In Figure 5.55 the Alfvén currents are shown schematically. On the Jupiter facing side of the wing there is a net current towards Io. In the vicinity of Io an ionospheric current connects the current on the Jupiter facing side with the current on the anti-Jupiter side (Figure 5.55b,c). On the anti-Jupiter side of the wing the net current flow is away from Io. In the theory of *Neubauer* [1980] the current circuit is closed at infinity. At the real Io they close in Jupiter's

<sup>2</sup>Note that the characteristic direction is not identical with the magnetic field direction in the tube. Throughout this Section *perpendicular* and *parallel* are meant with respect to the characteristic directions (Eq. (5.21)) and not with respect to the magnetic field.

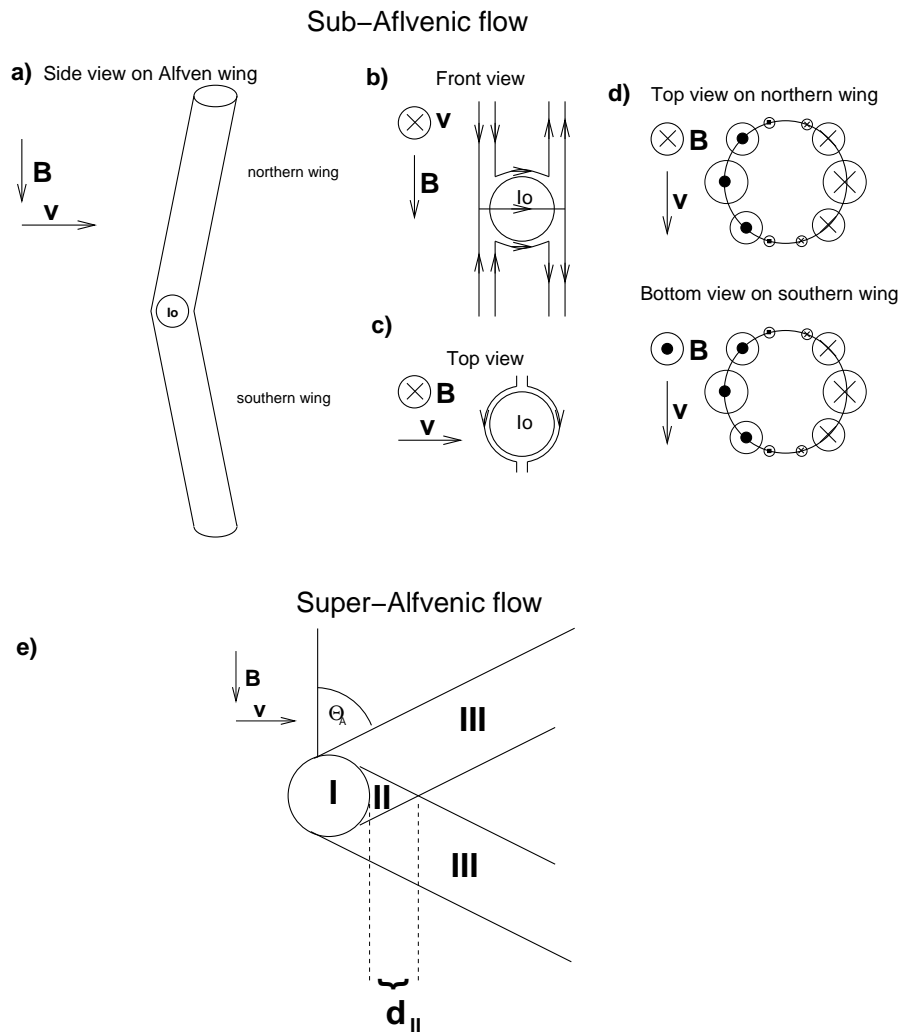


**Figure 5.55:** Schematic view of the Alfvén currents ( $\vec{j}_{\parallel}$ ) in the Alfvén wings at Io (a...d). Alfvén wings in the super-Alfvénic case like at Titan (f). I primary interaction region, II Alfvén tubes, and III nominal Alfvén tube intersection region.

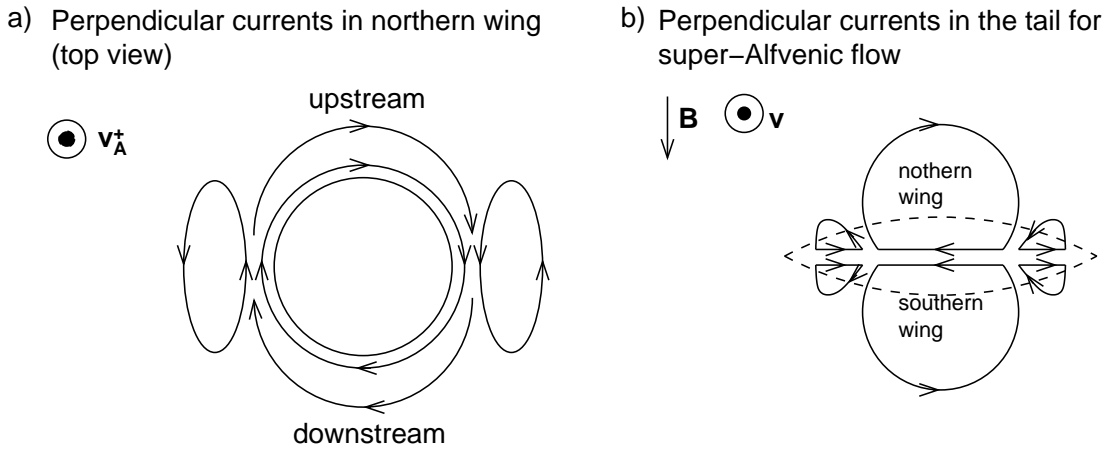


**Figure 5.56:** Schematic view of the perpendicular currents  $\vec{j}_\perp$  associated with the Alfvén wings [Neubauer, 1980] (a). Perpendicular currents in the nominal Alfvén intersection region at Titan (b).

ionosphere. Figure 5.55d shows the Alfvén currents on a cut through the Alfvén wing. In this sketch the currents perpendicular to the axis of the wing are not drawn.

The Alfvén currents flow along the characteristic directions while the perpendicular currents basically encircle the Alfvén tube in such a way that the plasma flow is deflected around the tube. The  $\vec{j} \times \vec{B}$  force slows the plasma upstream of the tube and accelerates it downstream. At the flanks of the tube part of the current circle is closed leading to two flank current circuits. The perpendicular currents are schematically drawn in Figure 5.56a.

### 5.5.1.2 The super-Alfvénic interaction

At Titan the incident plasma flow is super-Alfvénic and therefore the Alfvén angle (angle between Alfvén characteristic and incident magnetic field,  $\Theta_A = \arctan(M_A)$  when  $\vec{B}_0 \perp \vec{v}_0$ ) (with  $M_A$  the Alfvén Mach number) is about  $60^\circ$ , much greater than at Io (see Figure 5.55e). The angle between the two characteristic directions is also about  $60^\circ$  in that case.

We want to point out a difference between the sub-Alfvénic and the super-Alfvénic case with Figure 5.55e. The primary interaction region is a sphere (Titan plus atmosphere) which is marked as I. The radius of the sphere is determined by the requirement that outside of the sphere local perturbations caused by the obstacle are negligible. In other words, outside of the sphere the ideal MHD equations describe the plasma. Region I can be regarded as wave generator for MHD waves which propagate into the ideal surrounding plasma. For the plasma conditions at Titan (Alfvén velocity lower than sonic speed) Alfvén and slow mode wave propagate along the Alfvén characteristics marked by III in Figure 5.55e.

Apart from the primary interaction region (I) and the Alfvén tube region (III) there is a region marked by II in the tail of the obstacle. The plasma in this region is determined by the ideal MHD equations unlike the plasma in region I, but it does not belong to one of the two tubes and therefore the splitting of the currents in  $\vec{j}_\parallel$  and  $\vec{j}_\perp$  is not applicable. We call this region *nominal Alfvén tube intersection region* (or *nominal intersection region*).

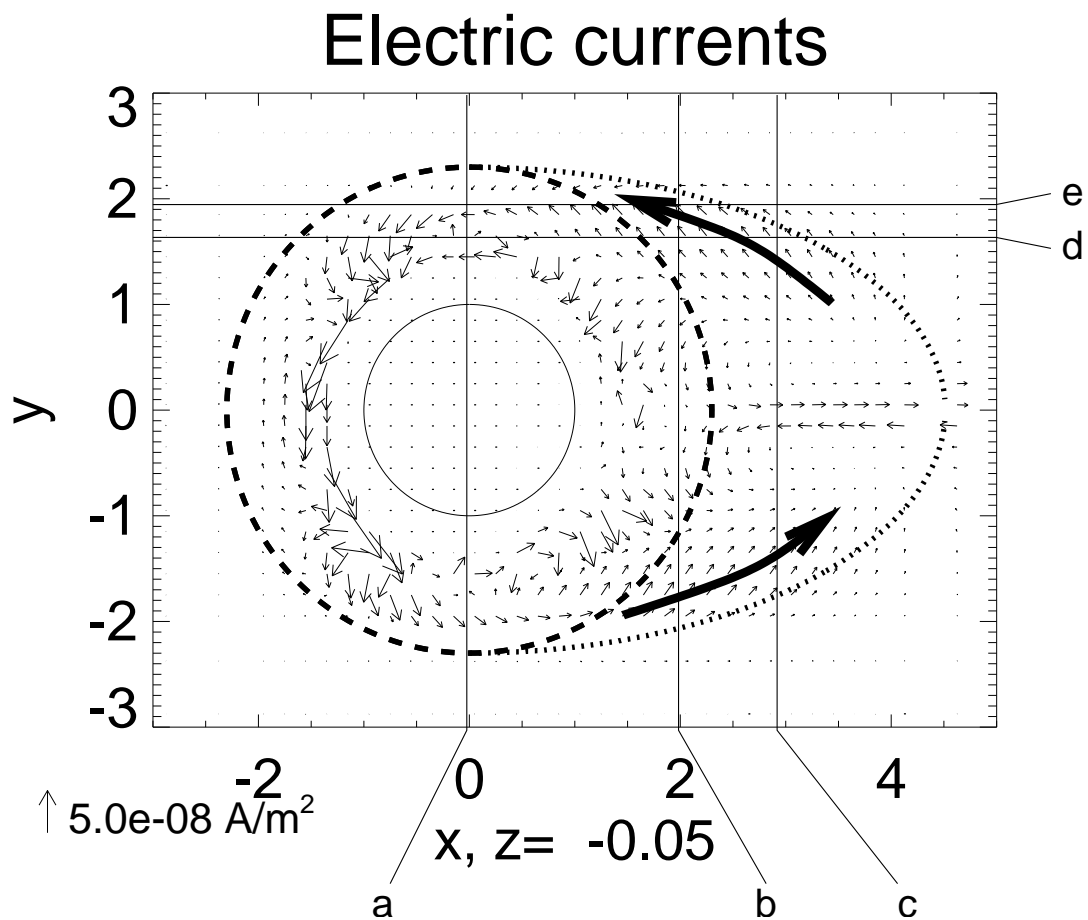


**Figure 5.57:** Electric currents in the equatorial plane in the T34 case. For the bold black arrows see explanation in the text. The vertical and horizontal lines mark the intersection of this plane with other displayed planes: a Figure 5.58, b Figure 5.64a, c Figure 5.64b, d Figure 5.65a, and e Figure 5.65b. The dashed circle marks the primary interaction region and the dotted line the nominal intersection region of the Alfvén tubes.

The extension of region II is given by  $d_{II} = R_{obs}(\frac{1}{\cos\Theta_A} - 1)$  with  $\Theta_A = \arctan(M_A)$ . In the sub-Alfvénic case  $d_{II}$  is small compared to the size of the obstacle. For an Alfvén angle of  $60^\circ$  we get  $d_{II} \approx 1R_{obs}$ . This is in the same order as the size of the primary interaction region. In the sub-Alfvénic case where  $M_A > 1$  this region is small compared to the obstacle size. We can calculate the extension of region II in the  $xy$ -plane as the intersection region of the nominal flux tubes. The border line is then given by  $y = \pm\sqrt{R_{obs}^2 - x^2 \cos^2 \Theta_A}$ .

Now, we define a criterion to determine the radius of the primary interaction region  $R_{obs}$ . In the stationary state the momentum equation (Eq. (4.24) can be written as:

$$\rho\vec{v} \cdot \vec{\nabla}\vec{v} = -\vec{\nabla}p + \vec{j} \times \vec{B} - v_{tot}\rho\vec{v} \quad (5.22)$$

where  $v_{tot} = \sum_{ns} \left( \frac{1}{\rho} P_{ns} + \frac{m_e}{m_i} v_{e,ns} + v_{i,ns} \right)$ . The last term in Eq. (4.24) has been dropped because it has turned out that it is negligible for the momentum balance. Taking the cross product of Eq. (5.22) with  $\vec{B}$  and dividing it by  $B^2$  we obtain an equation for the current perpendicular to  $\vec{B}$ . This current is the sum of the diamagnetic current

$$\vec{j}_{dia} = \frac{\vec{B} \times \vec{\nabla}p}{B^2}, \quad (5.23)$$

the inertial current

$$\vec{j}_{inert} = \frac{\vec{B} \times \rho\vec{v} \cdot \vec{\nabla}\vec{v}}{B^2}, \quad (5.24)$$

and the atmospheric current

$$\vec{j}_{atmo} = \frac{\vec{B} \times v\rho\vec{v}}{B^2}. \quad (5.25)$$

For the determination of  $R_{obs}$  we require the contribution of the atmospheric currents to the total current (perpendicular to  $\vec{B}$ ) to be less than 1% outside of the obstacle. From this analyses we obtain  $R_{obs} = 2.3R_T$ .

It is interesting to mention that the obtained radius, i.e. the obstacle size, is determined by the mass-loading part of the frequency  $\nu$  and not by the collisional part, although we have shown in Section 5.2.3 that for the pressure balance mass-loading only plays a minor role.

Figure 5.57 displays the currents in the equatorial plane. The dashed line marks the size of the primary interaction region ( $R_{obs}$ ) and the dotted line marks the border of the nominal intersection region of the Alfvén tubes. Region II of Figure 5.55e is located in Figure 5.57 between the dashed and the dotted line. Note that except for the tail currents at  $y = 0$  nearly all currents in the equatorial plane are inside of the combined regions I and II.

### 5.5.1.3 Currents in the Alfvén tube

The currents in one (northern or southern) Alfvén tube can be splitted into the Alfvén currents  $\vec{j}_{\parallel}$  that flow parallel to the Alfvén characteristic and the perpendicular currents  $\vec{j}_{\perp}$ . Figure 5.59 displays the Alfvén currents of the southern tube through the  $yz$  plane at  $x = 4.9R_T$  and  $x = 6.5R_T$ . They are calculated as

$$\vec{j}_{\parallel}^+ = \frac{\vec{j} \cdot \vec{v}_A^+}{v_A^{+2}} \vec{v}_A^+. \quad (5.26)$$

!t

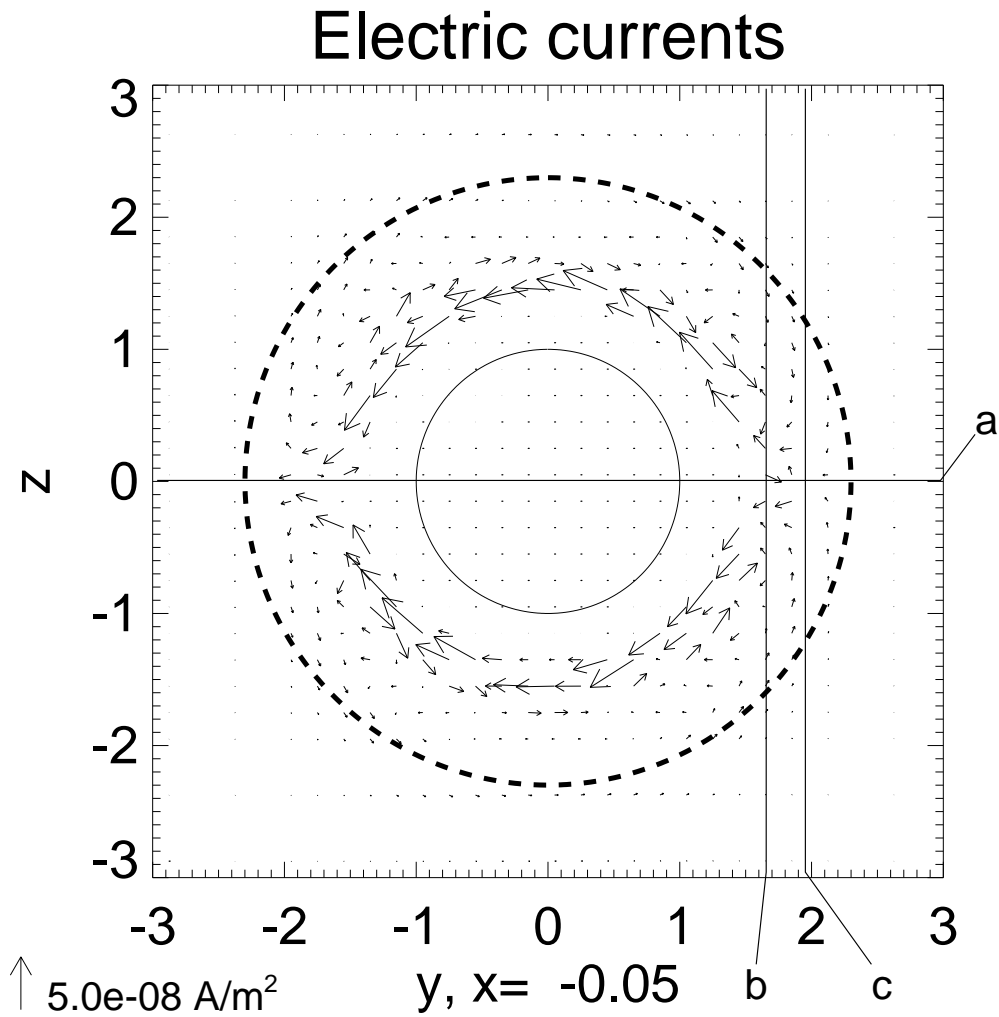
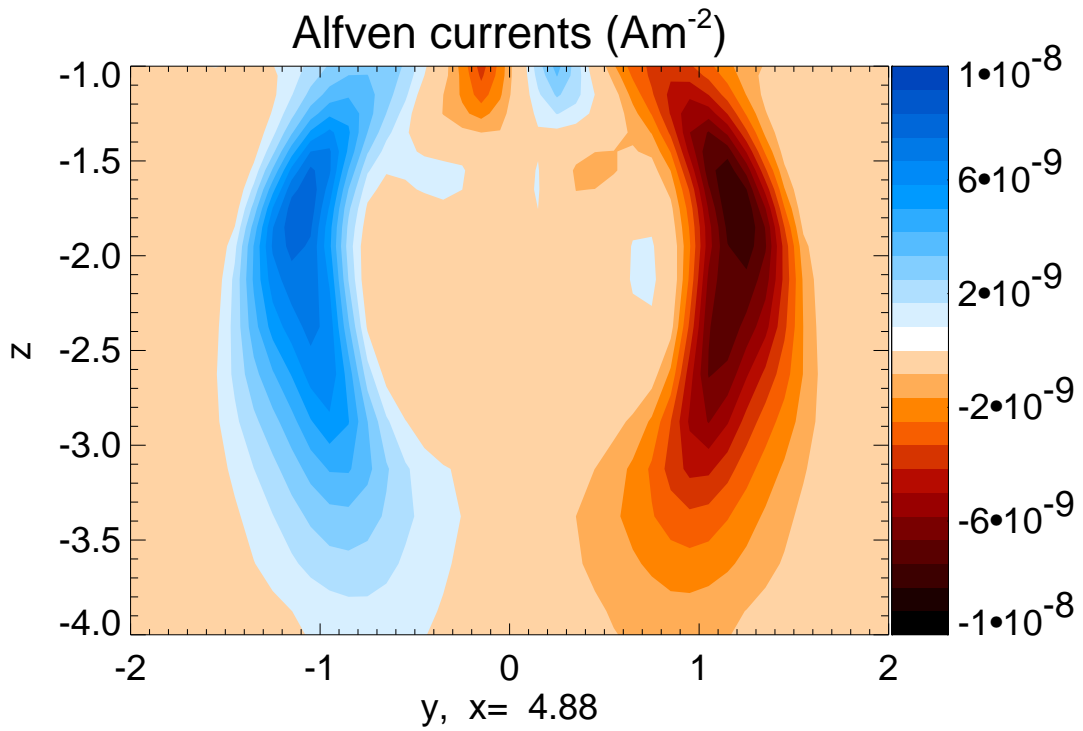
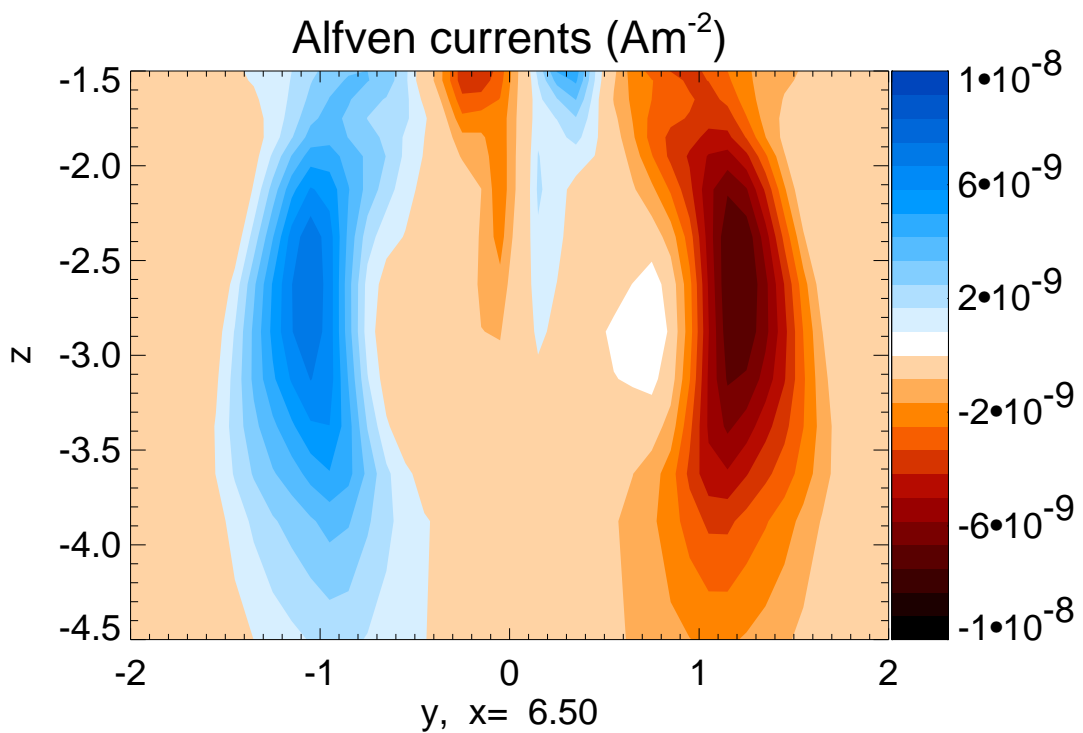


**Figure 5.58:** Electric current in the  $yz$ -plane at  $x = 0$ . The net currents flows from the Saturnian flank ( $y > 0$ ) over the poles to the anti-Saturnian flank. The vertical and horizontal lines mark the intersection of this plane with other displayed planes: *a* Figure 5.57, *b* Figure 5.65a, and *c* Figure 5.65b. The dashed circle marks the primary interaction region.

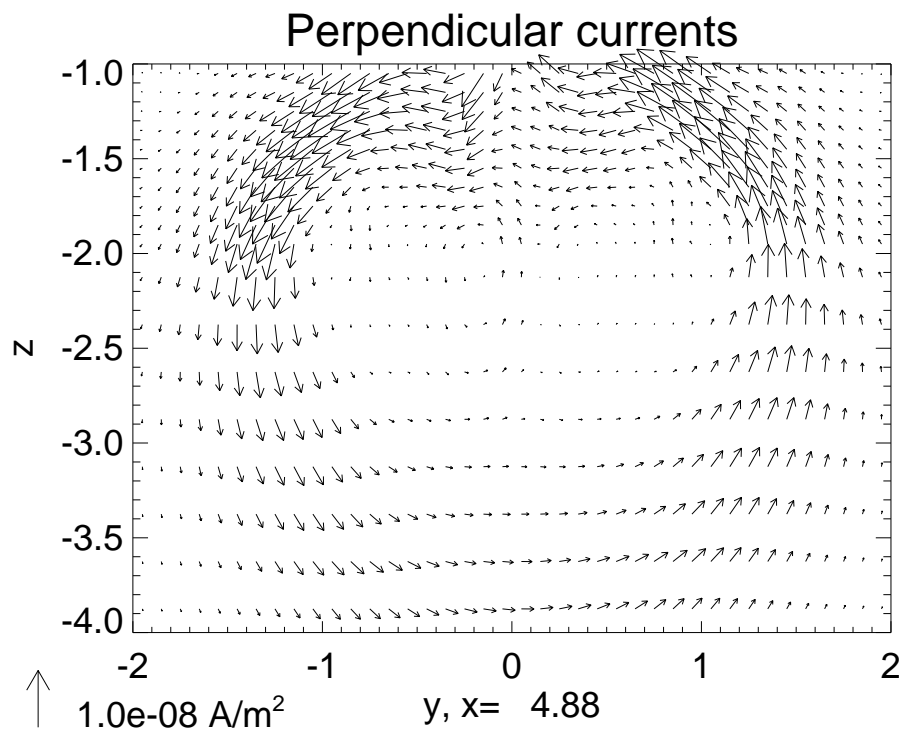


(a)

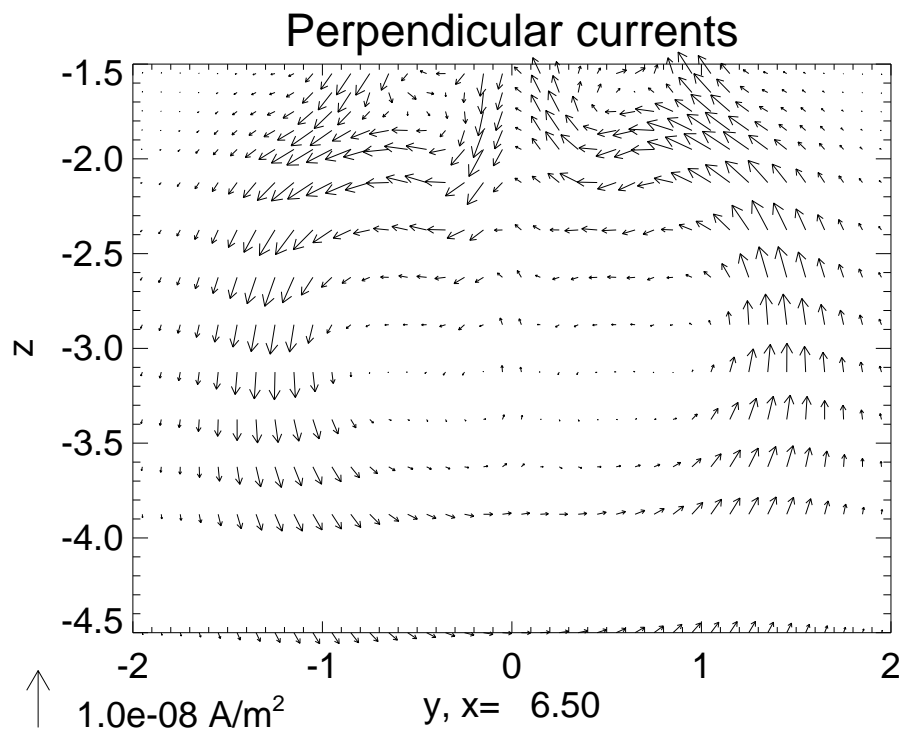


(b)

**Figure 5.59:** Alfvén currents in the southern Alfvén tube. The absolute value of the currents is plotted positive if the  $x$ -component is positive (blue color) and negative if the  $x$ -component is negative (red color). The currents at the Saturnian flank ( $y > 0$ ) flow towards Titan.



(a)



(b)

**Figure 5.60:** Perpendicular currents around the southern Alfvén tube projected on the yz-plane.

In Figure 5.59  $|\vec{j}_{\parallel}^+| \text{sign}(j_{\parallel,x}^+)$  is plotted, i.e. the absolute value of the Alfvén current is plotted if the current flows away from Titan and the negative of the absolute value if the current flows towards Titan. The Figure clearly shows that the Alfvén currents are concentrated on the flanks of the tube as in the sub-Alfvénic case, and as expected the current points towards Titan on the Saturnian flank (positive  $y$ ) and away from Titan on the anti-Saturnian flank.

The shape of the Alfvén current area and the magnitude is nearly unchanged from  $x = 4.9R_T$  to  $x = 6.5R_T$ . The translational invariance along the characteristic implies that  $\vec{\nabla} \cdot \vec{j}_{\parallel}^+ = 0$ . We have calculated  $\vec{\nabla} \cdot \vec{j}_{\parallel}^+$  directly from our simulation results and obtain  $\vec{\nabla} \cdot \vec{j}_{\parallel}^+ / |\vec{j}_{\parallel}^+| < 0.05R_T^{-1}$  which is within the numerical errors for the calculation of the divergence. Thus, we conclude that  $\vec{\nabla} \cdot \vec{j}_{\parallel} = 0$  is also fulfilled in the super-Alfvénic case and hence both currents fulfill divergence zero separately at least in the vicinity ( $r < 10R_T$ ) of Titan.

Figure 5.60 shows the perpendicular currents projected on the same planes as in Figure 5.59. They are given by

$$\vec{j}_{\perp}^+ = \vec{j} - \vec{j}_{\parallel}^+. \quad (5.27)$$

They basically encircle the Alfvén tube as in the sub-Alfvénic case.

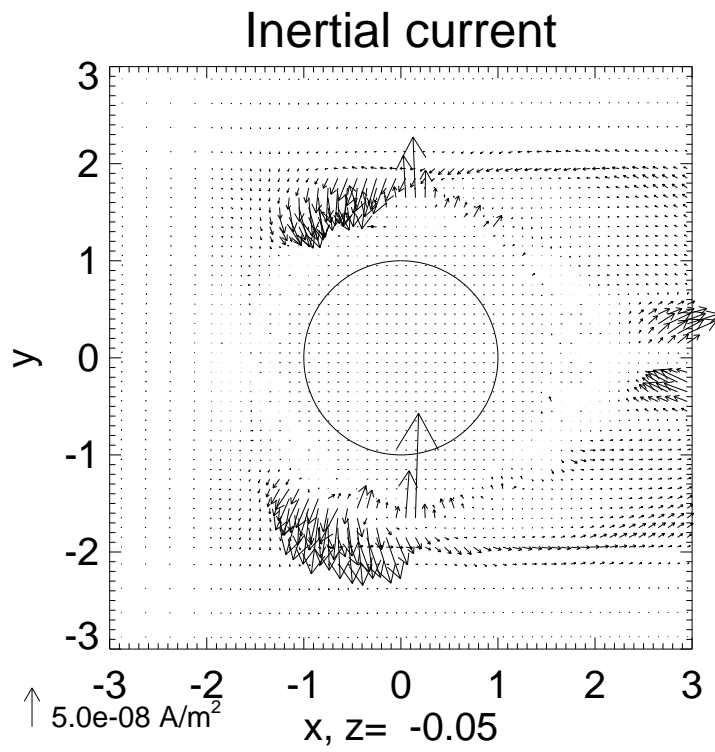
#### 5.5.1.4 Currents in the primary interaction region

The basic property of the primary interaction region from the viewpoint of the electric currents is that it enlarges the electric conductivity perpendicular to the magnetic field so that the Alfvén currents of the Saturnian flank and the Alfvén currents of the anti-Saturnian flank are connected by cross-field currents through the ionosphere of Titan. In order to interpret the currents in the primary interaction region it is reasonable to split them into its diamagnetic (Eq. (5.23)), inertial (Eq. (5.24)), and atmospheric parts (Eq. (5.25)). The different currents are displayed in the equatorial plane and in the  $yz$ -plane Figure 5.61, Figure 5.62, and Figure 5.63.

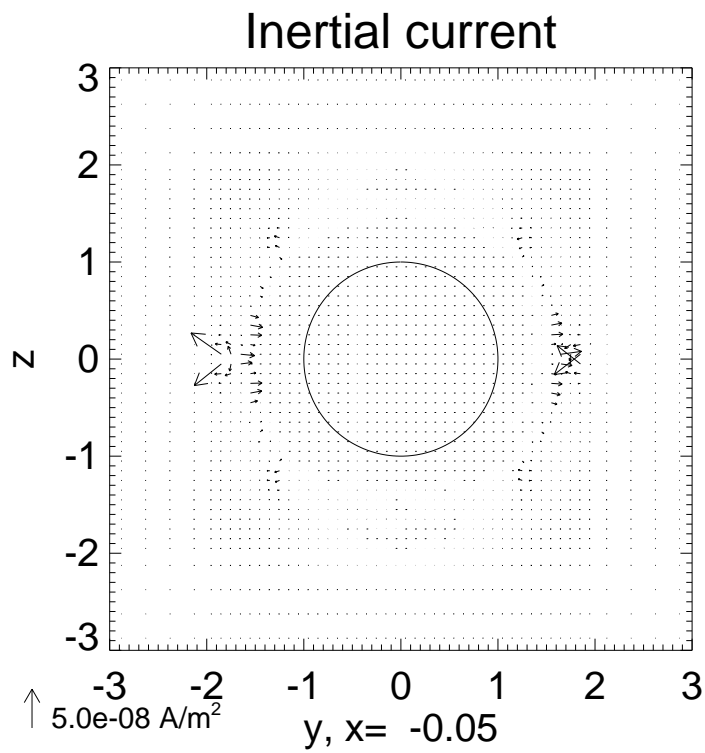
In the equatorial plane the diamagnetic current (Figure 5.62a) encircles the atmosphere in a clockwise direction. These currents correspond to the pile-up of magnetic field. They flow in the regions where thermal pressure decreases and magnetic pressure increases (compare with Figure 5.20). A thin diamagnetic current layer corresponds to a steep gradient of magnetic field magnitude in the pile-up region.

The calculation of the atmospheric currents from the results with Eq. (5.25) is quite inaccurate because the neutral density with steep gradients enters the calculation. In the momentum equation (Eq. (4.24)) the action of the collisional term is limited because it only acts decelerating but not accelerating on the plasma. Thus, the large absolute value of the current displayed in Figure 5.63a is a consequence of the calculation but is not real. However, we can draw some conclusions from the displayed atmospheric current.

The atmospheric current (Figure 5.63a) encircles Titan in an anti-clockwise direction at lower altitudes than the diamagnetic currents. The atmospheric currents shield the lower atmosphere from the external magnetic field and correspond to the magnetic ionopause (MIP, see Section 5.34). At the positions where the Alfvén currents enter and leave the atmosphere,

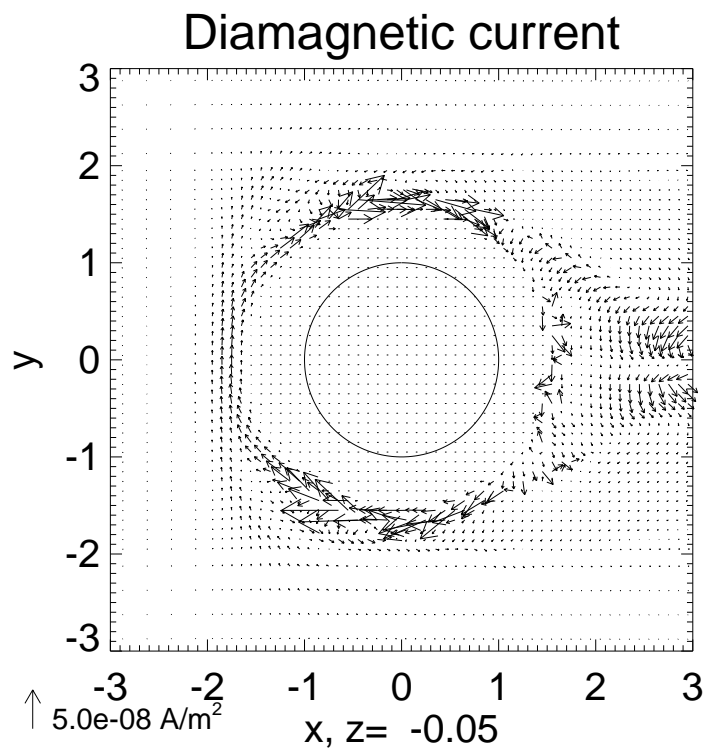


(a)

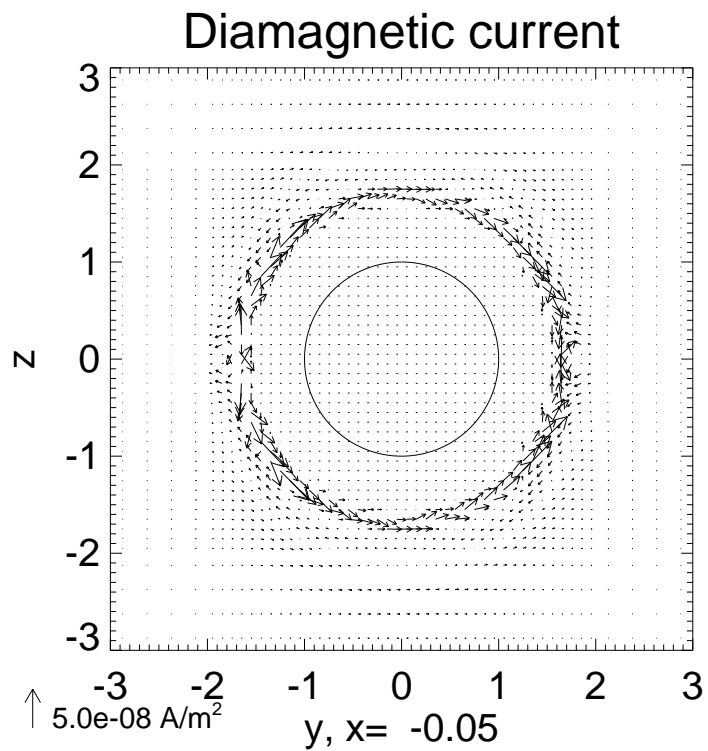


(b)

**Figure 5.61:** *Inertial currents in the  $xy$  and the  $yz$ -plane.*

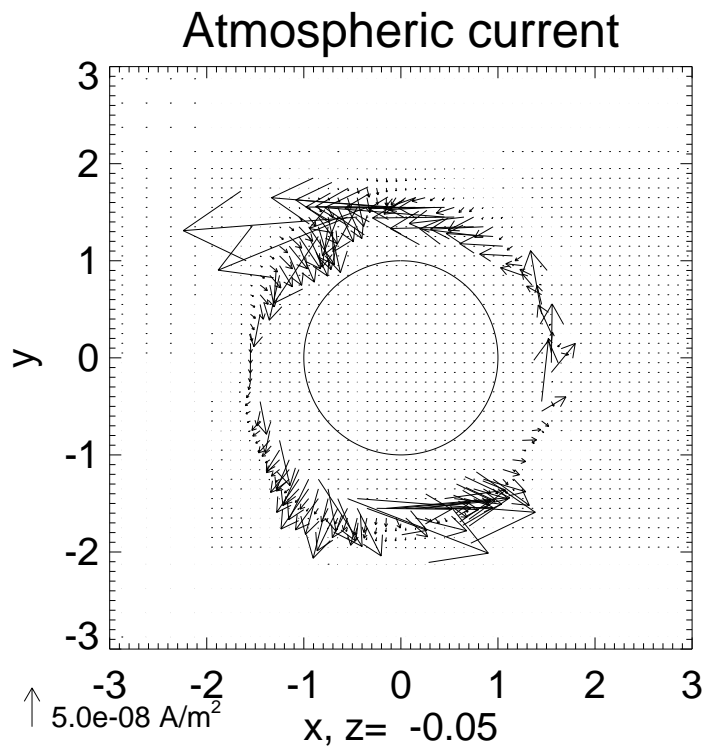


(a)

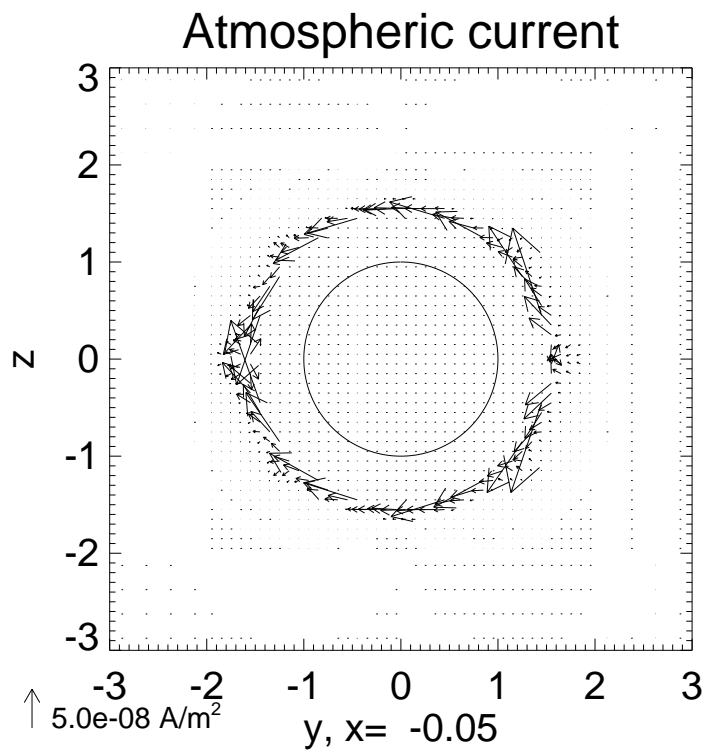


(b)

**Figure 5.62:** Diamagnetic currents in the  $xy$  and the  $yz$ -plane.



(a)



(b)

**Figure 5.63:** Atmospheric currents in the  $xy$  and the  $yz$ -plane.

the atmospheric currents are radially directed. The magnetic pile-up region is confined by the diamagnetic currents at the upper boundary and by atmospheric currents at the lower boundary.

The inertia currents (Figure 5.61a) above the ionosphere ( $r > 1.7R_T$ ) correspond to the regions of the main particle flux as a comparison with Figure 5.84 indicates. In this region the picked-up plasma is accelerated by the  $\vec{j} \times \vec{B}$ -force.

Inside of the upper magnetized ionosphere the inertial currents are oppositely directed (in  $y$  direction). Here the inertia of the magnetized ionospheric plasma prevents the plasma from being floated away by the bypassing magnetospheric plasma. That means that for example in Figure 5.61a at the point  $x = 0.$ ,  $y = -1.75R_T$  the shear flow is maximum: at  $y > -1.75R_T$  the ionospheric plasma and magnetic field is at rest, at  $y < -1.75R_T$  the magnetospheric plasma streams along.

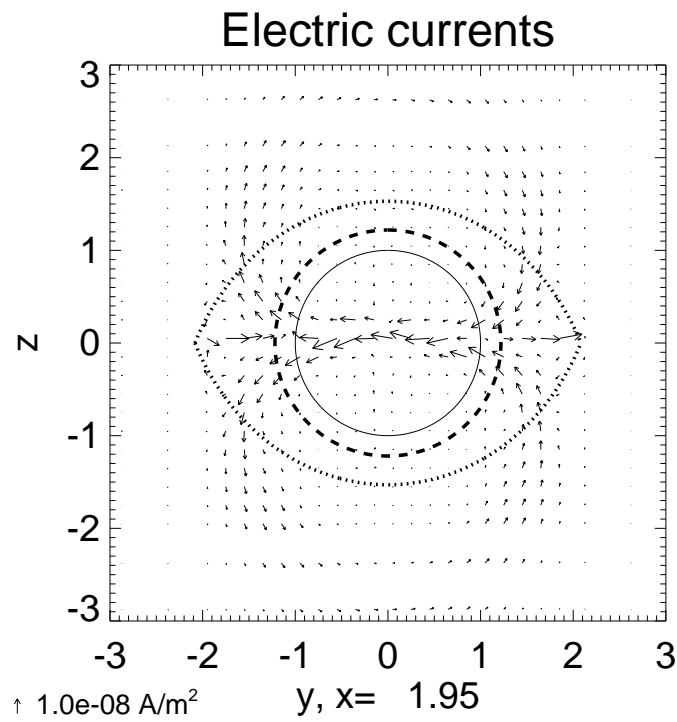
The decomposition of the currents over the poles shows that the diamagnetic current (Figure 5.62b) is at higher altitudes than the atmospheric current (Figure 5.63b) and flows from the anti-Saturnian to the Saturnian flank. Thus, again the diamagnetic current corresponds to the upper boundary of the magnetic pile-up region. The atmospheric current flows in opposite direction, from the Saturnian to the anti-Saturnian flank and is stronger than the diamagnetic current. Thus, the net current flow that connects the Alfvén current at the Saturnian flank with the Alfvén current at the anti-Saturnian flank is achieved by atmospheric currents. The inertia currents (Figure 5.61b) are again corresponding to the plasma pick-up regions (see Figure 5.86).

### 5.5.1.5 Currents in the nominal intersection region

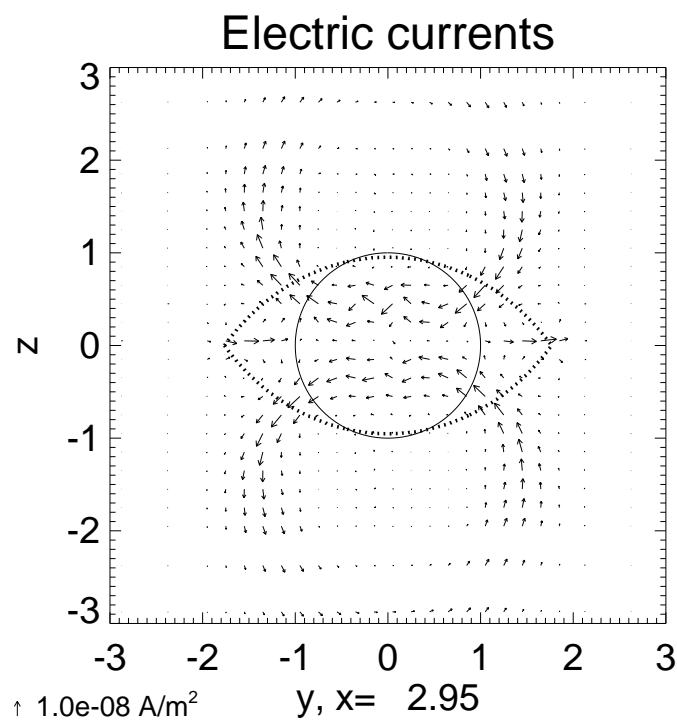
The equatorial currents in the nominal intersection region (see Figure 5.57) are determined by inertial currents created from the plasma pick-up at the flanks (see also Figure 5.84). The process is as follows: plasma pick-up slows down the flow and causes the magnetic field line to bend. The curvature of the magnetic field generates an electric current and the resulting  $\vec{j} \times \vec{B}$  force re-accelerates the plasma. Because the re-acceleration process is not terminated when the picked up plasma leaves the primary interaction region, the inertial currents continue in the nominal intersection region and cause the currents at the flank marked by bold black arrows in Figure 5.57.

The perpendicular currents that enter the nominal intersection region are simply continued as Figure 5.64b indicates. Two current layers (from the northern and southern tube) are noticeable. As they enter the primary interaction region the two current layers combine to one current layer in the equatorial plane (Figure 5.64a).

Apart from the main current ring the perpendicular current also consists of two flank current circuits (see Figure 5.56a). As they enter the nominal intersection region they combine in the equatorial plane and combine with the inertial currents (Figure 5.64). The resulting picture for the continuation of the perpendicular currents inside of the nominal intersection region is schematically shown in Figure 5.64b.



(a)



(b)

**Figure 5.64:** Electric currents in the  $yz$ -plane. The intersection of this plane with the equatorial plane is shown in Figure 5.57. The dashed circle marks the primary interaction region and the dotted line marks the nominal intersection region of the Alfvén tubes.

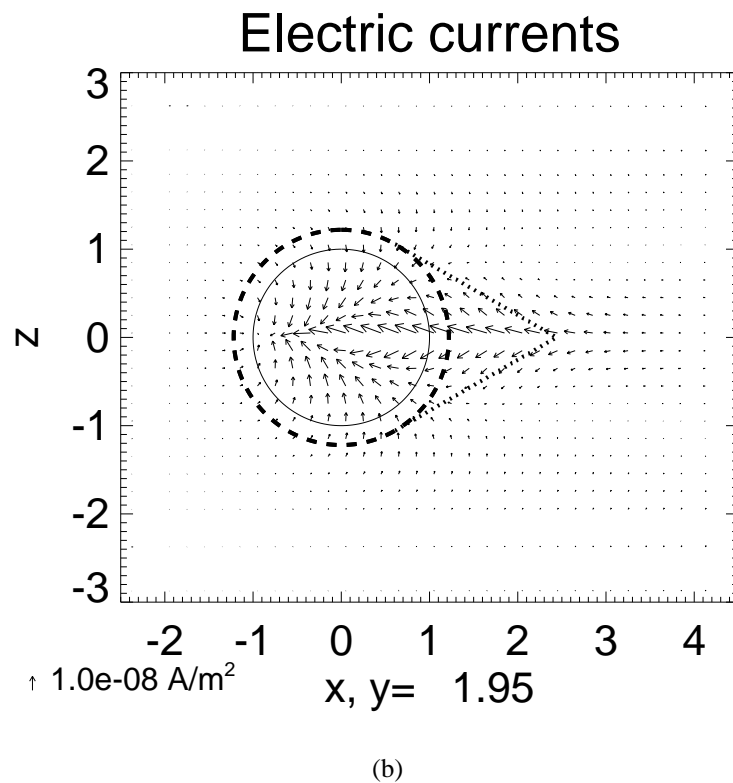
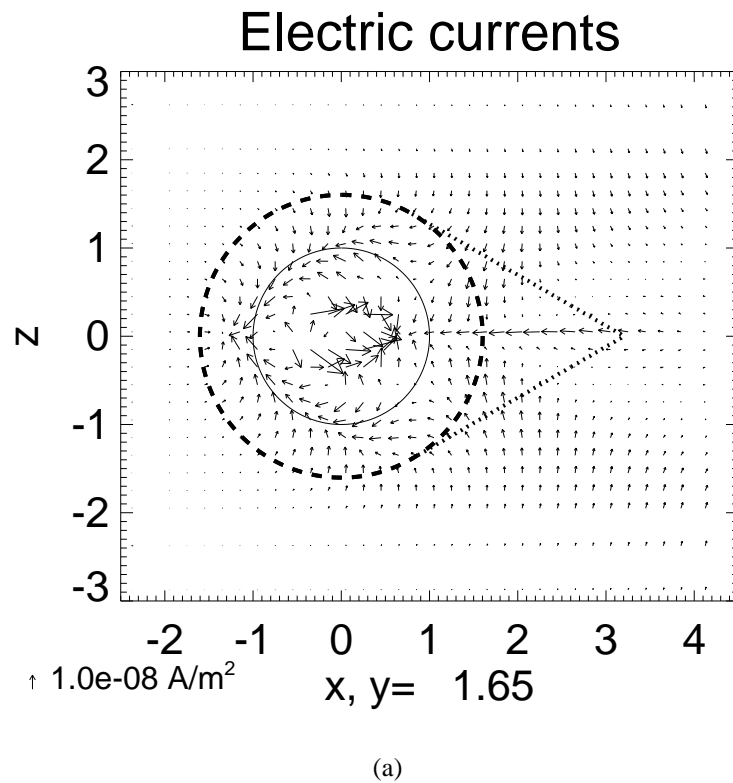


**Figure 5.65:** *Electric currents in the  $xz$ -plane. The intersection of this plane with the equatorial plane is shown in Figure 5.57. The dashed circle marks the primary interaction region and the dotted line marks the nominal intersection region of the Alfvén tubes.*

During the flyby through Titan's wake Voyager 1 has encountered a relatively thin current sheet near closest approach at a distance of  $2.7R_T$  [Ness *et al.*, 1982]. A thin current sheet exists in our results only inside of the interaction region (see Figure 5.57 and Figure 5.64a).

The Alfvén currents are also continued inside the nominal intersection region but we cannot isolate them from the total current since they do not flow along the characteristic direction anymore because the characteristic direction is not defined in that region. Figure 5.65 gives an impression of the currents at the flank.

### 5.5.1.6 Summary of current system

The splitting of the currents in the interaction region (I) into the different contributions from the momentum equation has shown that: (1) The connection of the Alfvén currents at the Saturnian flank with the Alfvén currents at the anti-Saturnian flank is accomplished by the atmospheric currents mainly through the ionosphere upstream and over the poles. (2) The atmospheric currents shield the lower atmosphere against the magnetic field. Thus, they correspond to the magnetic ionopause. (3) The diamagnetic currents flow at higher altitudes than the atmospheric and are in principal oppositely directed. They correspond to the upper boundary of the magnetic pile-up region. (4) Inertial currents appear where the plasma is decelerated by mass loading. The resulting  $\vec{j} \times \vec{B}$  force re-accelerates the plasma.

The equatorial currents in the nominal Alfvén tube intersection region consist of inertial currents that accompany the pick-up plasma sheet and the continuation of the currents from the two Alfvén tubes. The currents from the Alfvén tube are continued inside that region.

The results further indicate that the concept of Alfvén and perpendicular currents with divergence zero separately is also valid in the sub-Alfvénic tubes at least in the vicinity of the obstacle ( $r < 10R_T$ ).

### 5.5.1.7 Typical values for currents at Titan

At the end of the Section we give some typical values for the Titan electric current system derived from the results of T34. The maximum current density in the upstream ionosphere is  $\sim 90 \text{ nAm}^{-2}$  which is similar to the value of  $108 \text{ nAm}^{-2}$  obtained from the 1D model of Keller *et al.* [1994b]. The total Alfvén current through one Alfvén wing (upward or downward) is  $\sim 3 \times 10^4 \text{ A}$ . We have calculated the Alfvén current by integrating the current density through half of one tube at a distance of  $5R_T$ . The Alfvén and the perpendicular current densities are of the same order of magnitude at Titan.

A typical value for the Alfvén current at Io is  $\sim 5 \times 10^6 \text{ A}$  [Saur, 2000]. At Io the Alfvén current is related to the famous Io footprints [Connerney *et al.*, 1993; Clarke *et al.*, 1996; Prange *et al.*, 1996] in Jupiter's auroral atmosphere. At Titan the Alfvén currents that possibly could produce such a signature in Saturn's atmosphere are about two orders of magnitude lower than at Io.

## 5.5.2 Global plasma flow and magnetic field geometry

In the last section the current system that is set up by the interaction of the magnetized plasma with Titan has been described. The magnetization of the ionosphere has been discussed in Section 5.2.4. In this section the global magnetic field structure and the associated plasma flow resulting from the plasma interaction are discussed.

In Figure 5.66 magnetic field lines that cross the equatorial plane at an altitude of  $\sim 1400$  km through the upstream ionosphere are plotted for the T34 case. 1400 km is about the altitude of the magnetic barrier peak (see Figure 5.21a). The picture visualizes the draping of magnetic field lines around Titan's ionosphere. The altitude of a field line on the path from the north to the south pole is about constant. Note that the  $y$ -component of the magnetic field in the upstream ionosphere is about zero, i.e. in that region draping rotates the magnetic field solely in the  $xz$ -plane, the plane which is defined by the incident flow and magnetic field. The field lines along the Alfvén/slow mode tubes have no curvature. The angle to the incident undisturbed magnetic field is close to the angle of the Alfvén characteristics.

For altitudes above  $\sim 1100$  km the magnetic Reynolds number is much larger than 1 (see Figure 5.52) meaning that above that altitude the frozen-in magnetic field condition is fulfilled and transport of magnetic field is consistent with plasma transport. That does not mean that the magnetic field is completely determined by gasdynamics. It is rather a dependence in both directions: plasma transports magnetic field and magnetic field changes the plasma momentum through the  $\vec{j} \times \vec{B}$  force. We have seen in Section 5.2.3 that even in the case of an incident low- $\beta$  plasma there is a region where the plasma  $\beta$  is high and the dynamics is controlled by the magnetic field. *Zwan and Wolf [1976]* have shown that the insertion of magnetic field into a plasma, i.e. the change from a gasdynamic to a magnetogasdynamic formulation changes the solution of the flow even in the limit of weak magnetic field: the magnetogasdynamic solution of the interaction problem does not converge towards the solution of the gasdynamic flow. They have shown that in gas dynamics the plasma density increases along the ram direction in front of an obstacle while in magnetogasdynamics the density decreases in the so-called depletion layer which *Zwan and Wolf [1976]* explain as a "squeezing" of the magnetic flux tubes. However, above  $\sim 1100$  km the frozen-in condition is valid and explaining the magnetic field is part of explaining the flow and vice versa.

### 5.5.2.1 Upstream magnetic field and velocity profile

A good starting point for the discussion is to take a look at the linear waves in an ideal magnetohydrodynamic (MHD) plasma. The three wave modes that propagate in the plasma rest frame are the Alfvén wave and the slow and fast MHD wave (see e.g. *Stix [1962]*). In the linear case the Alfvén wave does not transport density, pressure, and magnetic field magnitude perturbations and the slow and fast mode are analogous to the sonic wave in hydrodynamics but with different properties due to the magnetic field. The phase velocities of the waves depend on the angle ( $\alpha$ ) between the direction of wave propagation and magnetic field and are given by

$$v_{ph,A} = v_A \cos \alpha \quad (5.28)$$

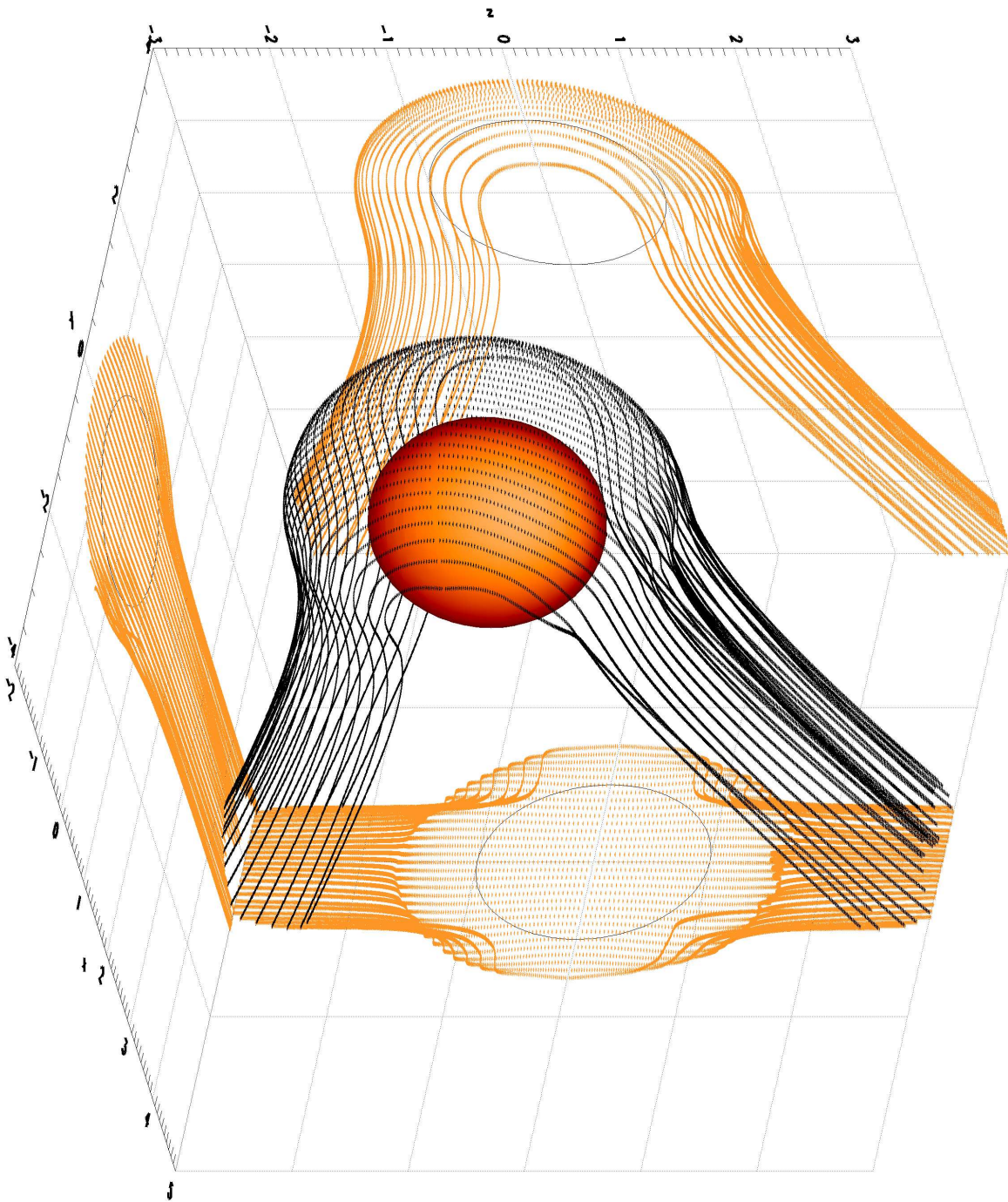


**Figure 5.66:** Draping of magnetic field lines around Titan. The field lines cross the upstream equatorial plane at an altitude of  $\sim 1400$  km.

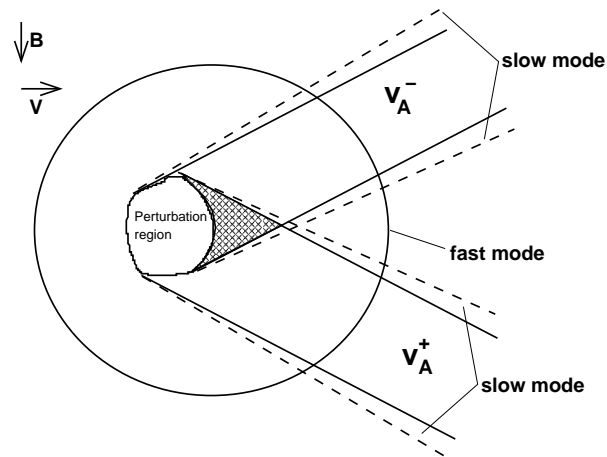


**Figure 5.67:** Ideal MHD waves for a sub-sonic super-Alfvénic flow.

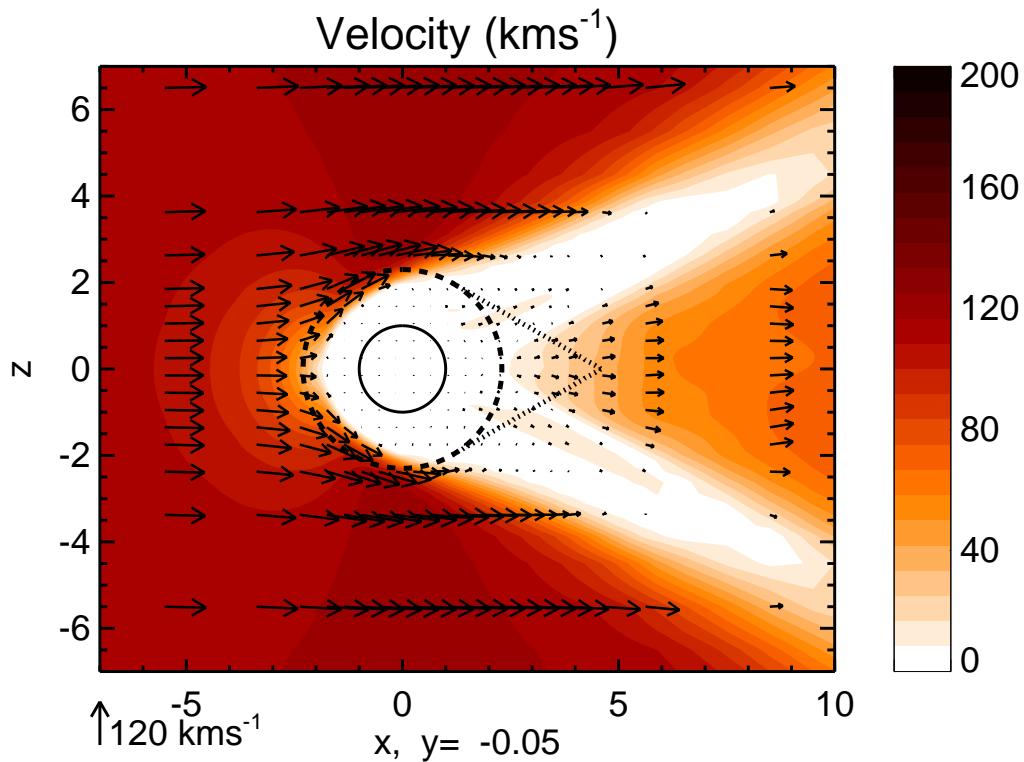


**Figure 5.68:** Absolute values and vectors of the plasma bulk velocity. The dashed circle marks the primary interaction region and the dotted line marks the nominal intersection region of the Alfvén tubes.

for the Alfvén wave (with  $v_A = B/\sqrt{\mu_0\rho}$  the Alfvén velocity) and

$$v_{f,s}^2 = \frac{1}{2} \left( (c_s^2 + v_A^2) \pm \sqrt{(c_s^2 + v_A^2)^2 - 4v_s^2 v_A^2 \cos^2 \alpha} \right) \quad (5.29)$$

for the fast (+ sign) and slow mode (− sign) where  $c_s = \sqrt{\gamma p/\rho}$  is the sonic speed.

If in a plasma the sonic speed is larger than the Alfvén speed, like it is the case for the plasma at Titan during the Voyager 1 encounter, Alfvén and slow mode propagate along the magnetic field with Alfvén velocity. While the group velocity of the Alfvén wave is exactly parallel to the magnetic field, the group velocity of the slow mode has small components perpendicular to  $\vec{B}$ . Taking into account the flow velocity, which was during the Voyager 1 encounter super-Alfvénic and sub-sonic, slow mode and Alfvén wave propagate along the Alfvén characteristics  $\vec{v}_A^\pm = \vec{v}_0 \pm \frac{\vec{B}_0}{\sqrt{\mu_0\rho}}$  (which holds true in the non-linear case [Neubauer, 1980]) and the fast mode propagates omni-directional but not isotropic. The three wave modes in the plane spanned by  $\vec{v}_0$  and  $\vec{B}_0$  are illustrated in Figure 5.67.

Energy conservation and the omni-directional propagation of the fast mode require that energy perturbation transported by this wave decreases  $\sim r^{-2}$  with distance to the source of the perturbation i.e. Titan. Thus, at a certain distance the fast mode has faded out and the only signatures in the plasma caused by the interaction with Titan are the Alfvén and the slow mode propagating in the direction of the Alfvén characteristics. Additionally, on stream lines that intersect the interaction region, convected features like picked-up plasma can be detected. The slow mode has a small spread angle towards the characteristic directions i.e. its cross sectional area increases with distance from Titan, and the amplitude decreases so that at huge distances only the Alfvén waves and convected structures are present.

The set of equations that is used in our model (Eq. (4.22), (4.24), (4.25), (4.26)) differs from the ideal MHD equations. The extra terms are due to the influence of the neutral atmosphere. The neutral gas density drops with radial distance (see Eq. 4.28, Eq. 4.29, and Figure 4.1). At a certain distance the neutral gas density is low enough that it effectively does not affect the plasma, and the equations reduce to the ideal MHD equations. Outside of a certain sphere the features in the plasma are compositions of MHD waves and the area inside of the sphere can be regarded as generator for the MHD waves.

In Section 5.5.1 we have determined the size of the wave generator region, i.e. of the real obstacle, by requiring the contribution of the atmospheric to the total current to be less than 1% outside of that region. An alternative criterion for the determination of the obstacle size is that the contribution of the frictional and mass-loading force is small compared to the other forces in the momentum equation (Eq. (4.24)). This leads to the same result and we obtain  $R_{obs} = 2.3R_T$  as radius for the obstacle. An examination of the neutral gas influence in the continuity equation (Eq. (4.22)), the magnetic induction equation (Eq. (4.25)), and the equation for the internal energy density (Eq. (4.26)) shows that obstacle size is really determined by the momentum equation.

In Section 5.5.1 we have divided the plasma into three regions: the interaction or wave generator region, the region of the Alfvén tubes, and the region where the nominal Alfvén tubes intersect each other (see Figure 5.55e).

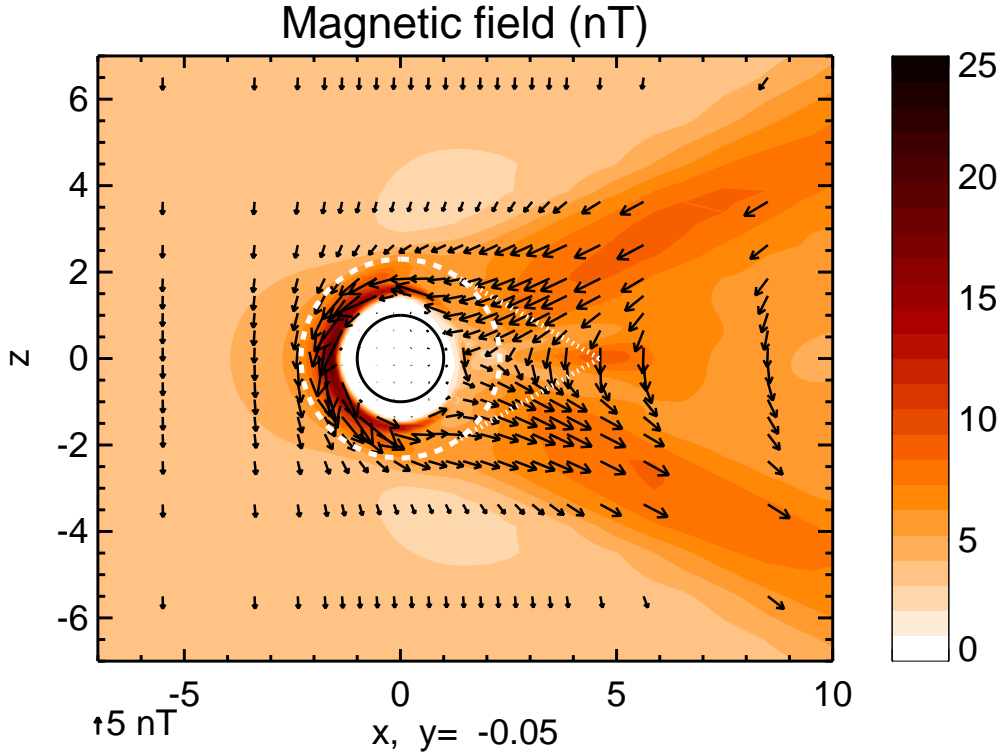


**Figure 5.69:** Magnetic field vectors and magnitude in the  $xz$ -plane. The dashed circle marks the primary interaction region and the dotted line marks the nominal intersection region of the Alfvén tubes.

In Figure 5.69 the magnetic field and in Figure 5.68 the velocity is displayed in the  $xz$ -plane.  $R_{obs}$  is displayed as a dashed circle. When we compare the results from our model with the theoretical wave pattern shown in Figure 5.67 we can clearly identify the two Alfvén/slow mode tubes. The magnetic field is nearly parallel to the characteristic directions in the tubes and the velocity is very low ( $\sim$  km/s) compared to the incident plasma velocity ( $\sim$  100 km/s) which indicates that the generated Alfvén waves are strong. Linear Alfvén waves do not change the magnetic field magnitude but non-linear can do. Thus the deviation of the magnetic field magnitude inside of the tubes from the incident magnetic field magnitude can be caused by both the Alfvén and the slow mode waves.

The fast mode propagates with  $v_{f,\perp} = \sqrt{c_s^2 + v_A^2}$  perpendicular and with  $v_{f,\parallel} = c_s$  parallel to the magnetic field (see Eq. (5.29)). The values at Titan during the Voyager 1 encounter were  $v_{f,\perp} = 220$  km/s and  $v_{f,\parallel} = 210$  km/s [Neubauer *et al.*, 1984]. Thus, the phase surface of the fast mode is approximately a sphere. The total wave energy on a phase surface is constant and therefore it decreases with distance to the generator with  $r^{-2}$ .

The wave energy is given by the square of the amplitude. When the wave generator is at  $x = 0$  the wave amplitude of the fast mode can be expressed as a function of  $x$  in a non-moving plasma by

$$A(x) = A_0 \frac{x_0}{x} \quad (5.30)$$

when the amplitude at  $x_0$  is  $A_0$ . If the plasma moves relative to the obstacle along the  $x$ -axis

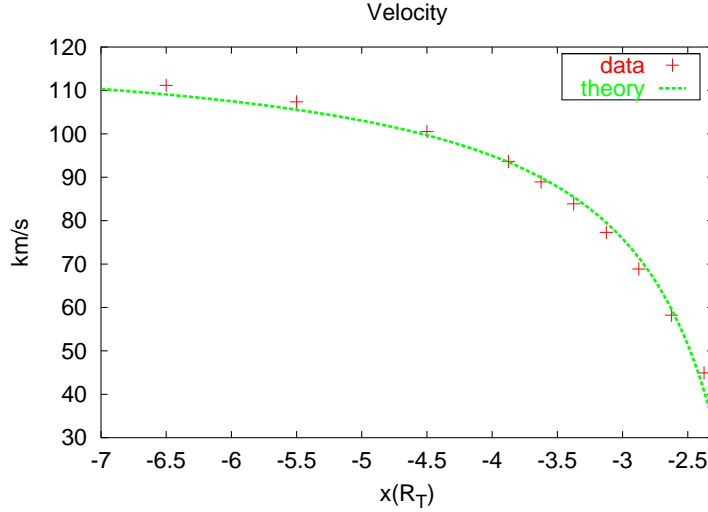


**Figure 5.70:** Velocity along the upstream direction from the model (crosses) and from the theoretical decay of the amplitude of the fast MHD amplitude (dotted line).

the functional behavior of the amplitude in the rest frame of the wave generator changes to

$$A(x) = A_0 \frac{x_0}{\frac{1}{1 \pm M_f}(x - x_0) + x_0} \quad (5.31)$$

where  $M_f$  is the fast magnetosonic Mach number. The  $\pm$  sign in Eq. 5.31 corresponds to the upstream and downstream propagation. Along the upstream direction the decay is steeper than in the static case and along the downstream direction it is more flat.

The fast mode does not perturb velocity and magnetic field components perpendicular to the plane defined by the incident magnetic field and the direction of wave propagation. Additionally, the magnetic field perturbation is perpendicular to the direction of wave propagation. Thus, for a wave propagating along the  $x$ -direction the fast mode perturbs  $v_x$  and  $B_z$ .

Now we want to compare the decay of the perturbation of  $v_x$  and  $B_z$  along the  $x$ -axis with the decay of the amplitude of the fast mode, i.e. we compare our data with the functions:

$$v'_x(x) = v'_{x,0} \frac{x_0}{\frac{1}{1 \pm M_f}(x - x_0) + x_0} \quad (5.32)$$

and

$$B'_z(x) = B'_{z,0} \frac{x_0}{\frac{1}{1 \pm M_f}(x - x_0) + x_0}. \quad (5.33)$$

In Figure 5.70  $v_x$  and in Figure 5.71  $-B_z$  from results of the T34 case are plotted along the upstream  $x$ -axis as crosses. The predictions from Eq. 5.32 and Eq. 5.33 plotted as dotted lines fit the results from the model quite well.

### 5.5.2.2 Magnetic field and velocity profile at the flanks

Analog to the decay of the fast mode along the  $x$ -axis we can calculate an expression for the decay along the  $y$ -axis. Thereafter, the decay perpendicular to the motional direction of the

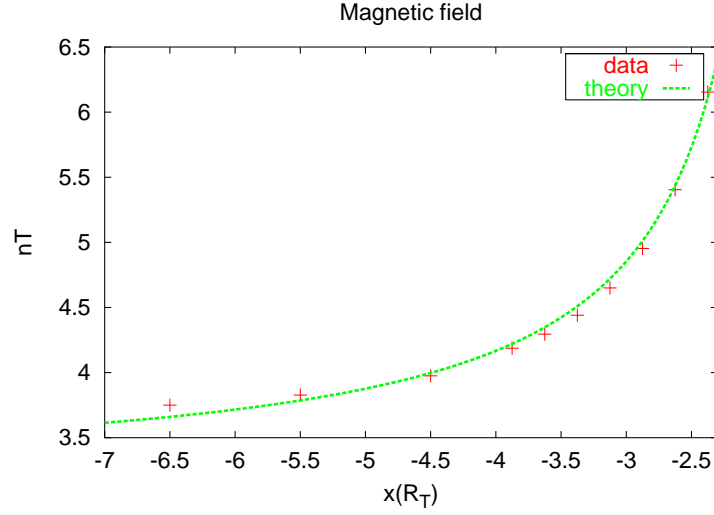


**Figure 5.71:**  $B_z$  along the upstream direction from the model (crosses) and from the theoretical decay of the amplitude of the fast MHD wave.

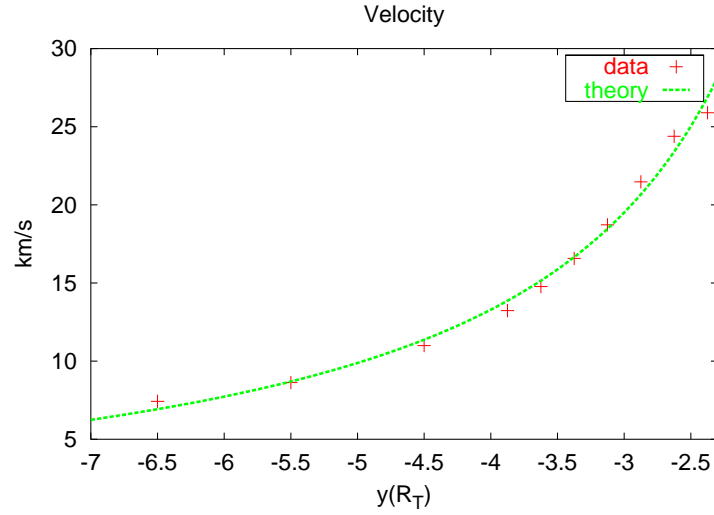


**Figure 5.72:** Velocity along the upstream direction from the model (crosses) and from the theoretical decay of the amplitude of the fast MHD amplitude (dotted line).

incident flow is given by

$$v'_y(y) = v'_{y,0} \frac{y_0}{\frac{1}{\sqrt{1-M_f^2}}(y - y_0) + y_0} \quad (5.34)$$

and

$$B'_z(y) = B'_{z,0} \frac{y_0}{\frac{1}{\sqrt{1-M_f^2}}(y - y_0) + y_0}. \quad (5.35)$$

Because of the direction of the fast mode in this case the perturbation affects all velocity components. Since they decay in the same manner we only regard the perturbation of the y-component. The comparison of the data from our model and the theoretical decay again is quite well although there are small deviations in the magnetic field.

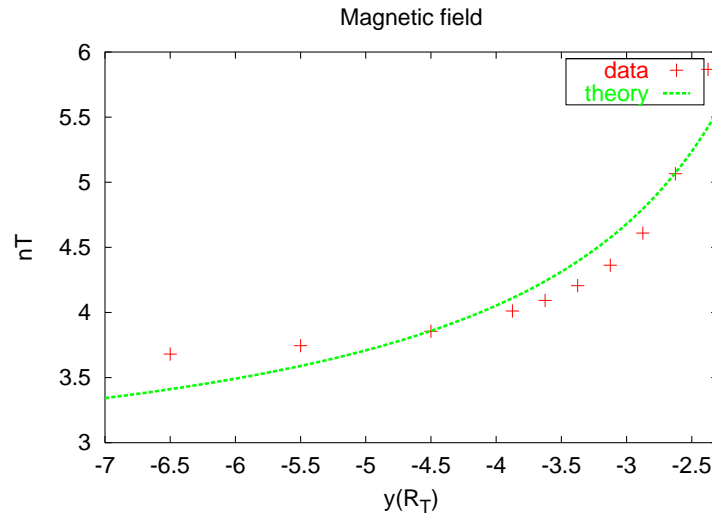


**Figure 5.73:**  $B_z$  along the upstream direction from the model (crosses) and from the theoretical decay of the amplitude of the fast MHD wave.

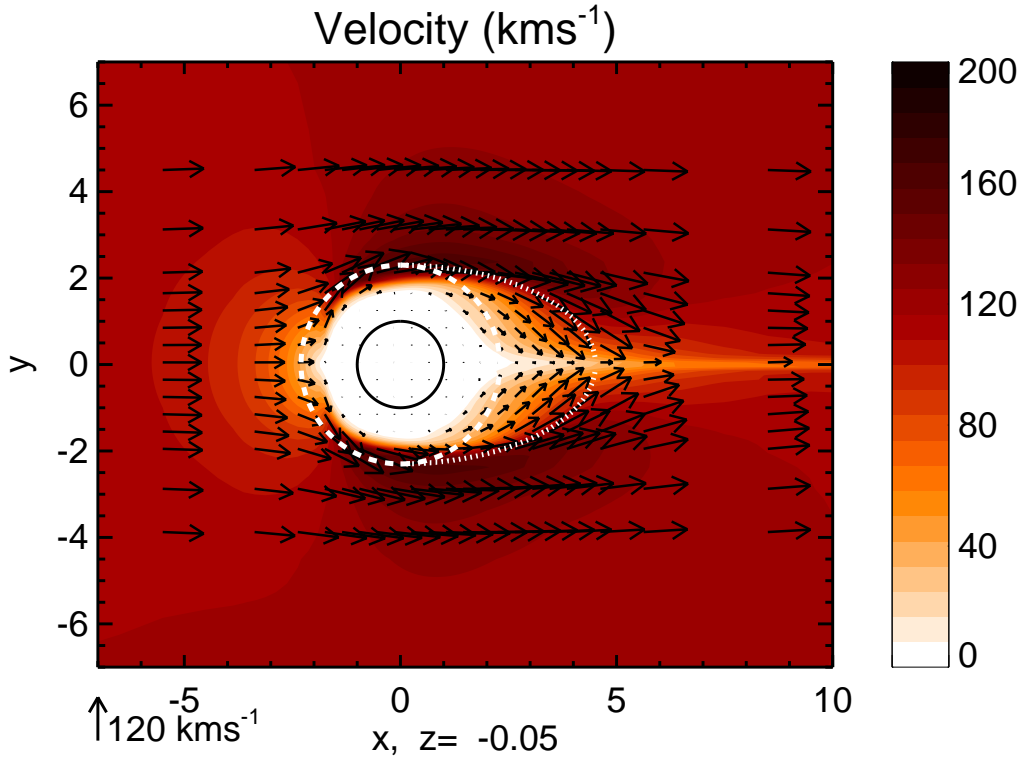
### 5.5.2.3 Plasma flow around the Alfvén tubes

The flow over the poles is disturbed by the Alfvén tubes. In Figure 5.76 the velocity around the northern Alfvén tube is plotted on three different planes parallel to the equatorial plane. Inside of the tubes the velocity is reduced to a few percent of the incident flow ( $v = 3\text{--}5$  km/s in the tube and 120 km/s in the incident plasma). Therefore, the major part of the plasma streams around the Alfvén tube. But on their way around the tube the plasma stream lines leave the displayed planes. As Figure 5.77 demonstrates, the flow around the Alfvén tubes is so that the flow velocity at the flanks of the tube is about perpendicular to the tube axis. Near the equatorial plane the flow from the northern and the southern wing converge in the tail behind the nominal intersection region ( $x \approx 4.5R_T$ ). Thus, the Alfvén tubes focus part of the flow in the tail. Behind the flux tube the plasma continues to stream in the same direction as the incident plasma (along  $x$ , see Figure 5.68).

### 5.5.2.4 Tail region

While Eq. 5.32 and Eq. 5.33 fit the behavior of the velocity and magnetic field disturbances along the upstream direction from our model, they do not fit the results along the tail. The tail is more complex than the upstream region. Perturbations from the interaction region due to mass loading and cooling enter the tail region. These perturbations are convected with the plasma. The tail region outside of the Alfvén/slow mode tubes that is directly connected with the interaction region along the plasma stream lines is determined by a mixture of fast mode and convected perturbations.

The propagation of the fast mode through the plasma that has different properties from the upstream plasma changes the decay of the wave amplitude. Qualitatively the decay must be the same (energy conservation) but the parameters in the functions (5.32) and (5.33) are different.



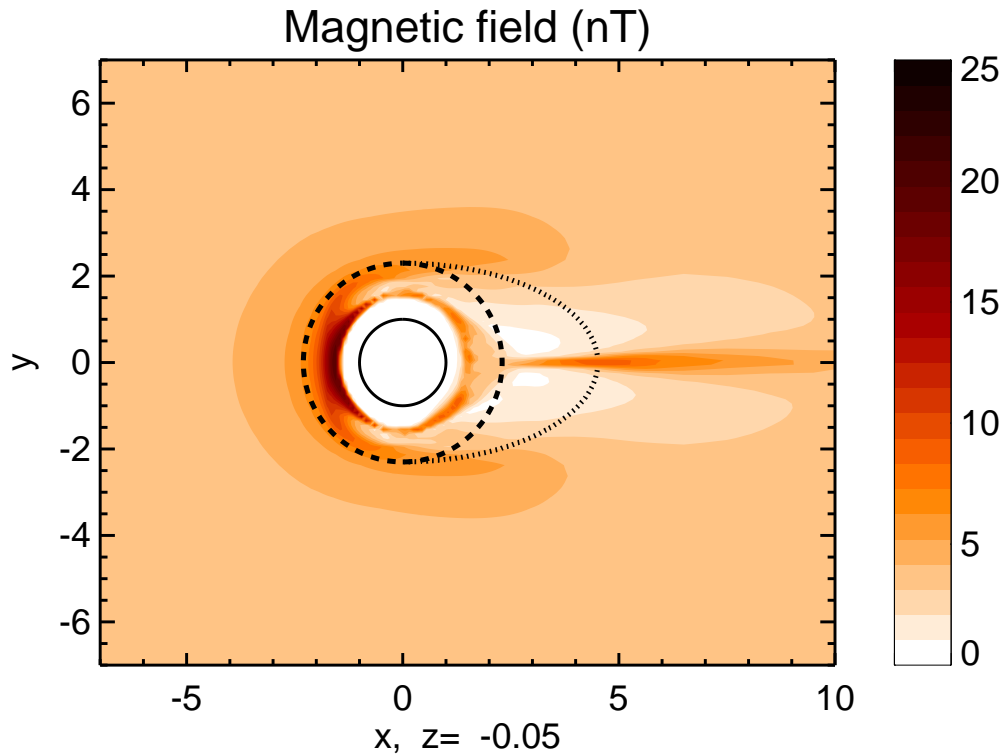
**Figure 5.74:** Plasma bulk velocity in the equatorial plane. The dashed circle marks the primary interaction region and the dotted line marks the nominal intersection region of the Alfvén tubes.

Figure 5.74 displays the plasma flow and Figure 5.75 the magnetic field magnitude in the equatorial plane. Figure 5.74 indicates that the main part of the plasma flow in the equatorial plane flows around the combined area of interaction region (dashed line) and nominal Alfvén tube intersection region (dotted line) and therefore converges at  $x \approx 4.5R_T$  (like the plasma that has been focused by the Alfvén tubes). The flow inside of that area is slowed down basically by mass-loading (see Section 5.5.3). At the position where the flow from both flanks from the tubes converges, the magnetic field is maximum.

The mechanism at the position of the flow convergence is similar to the mechanism that leads to magnetic pile-up in front of an obstacle: plasma flow changes its direction with respect to the magnetic field from perpendicular to parallel so that the magnetic pressure is increased while thermal pressure decreases. Figure 5.78 shows that indeed the thermal pressure is minimum at the maximum magnetic pressure. The pile-up mechanism is discussed in Section 5.4 and the evolution of pressure profile along the tail is demonstrated in Section 5.5.3. Figure 5.79 shows that at the position of the increased magnetic field the flow velocity has indeed components parallel to  $\vec{B}$  (magnetic field in the same plane is shown in Figure 5.82).

The magnetic field enhancement along the plane  $y = 0$  is accompanied by tail currents (see Figure 5.57). The resulting  $\vec{j} \times \vec{B}$ -force deviates the converging flow from the flanks tail-ward.

At the flanks of the region with enhanced magnetic field (towards and away from Saturn along  $y$ ), the magnetic field is reduced with respect to the field of the incident plasma. This is a consequence of the flow. In that region the stream lines divert and the frozen-in magnetic field decreases.



**Figure 5.75:** Magnetic field magnitude in the equatorial plane. The dashed circle marks the primary interaction region and the dotted line marks the nominal intersection region of the Alfvén tubes.

Magnetic field magnitude and orientation along the tail are shown on four different planes perpendicular to the incident plasma flow in Figure 5.80, Figure 5.81, Figure 5.82, and Figure 5.83. The left plot in the Figures displays the magnetic field magnitude while the right plot shows the three components of the magnetic field. The Figures demonstrate that the magnetic field component parallel to the incident flow direction ( $x$  in our coordinate system) is different from zero basically inside of the Alfvén tubes and in the nominal intersection region and nearly zero everywhere else in the tail.

The displayed plane in Figure 5.80 at  $x = 2R_T$  intersects the main interaction region. One can notice that the enhanced magnetic field in the tail around  $y = 0$  only appears outside of the main interaction region, i.e. at  $x > 2.3R_T$ .

### 5.5.2.5 Summary of plasma flow and magnetic field

At the end of this Section we want to summarize the main features of the plasma flow and the magnetic field around Titan as it appears in the results from our model. (1) The plasma environment of Titan can be divided into three regions: the main interaction region, the region of the Alfvén tubes, the nominal intersection region of the tubes (like in Section 5.5.1). (2) The magnetic field and velocity profile along the stagnation point stream line and along  $y$  can be described in terms of a standing fast mode. (3) The plasma flow around the Alfvén tubes is perpendicular to the tube axis which focuses the flow in the tail at the border of the nominal intersection region. (4) The convergence of the flow in the tail enhances the magnetic field

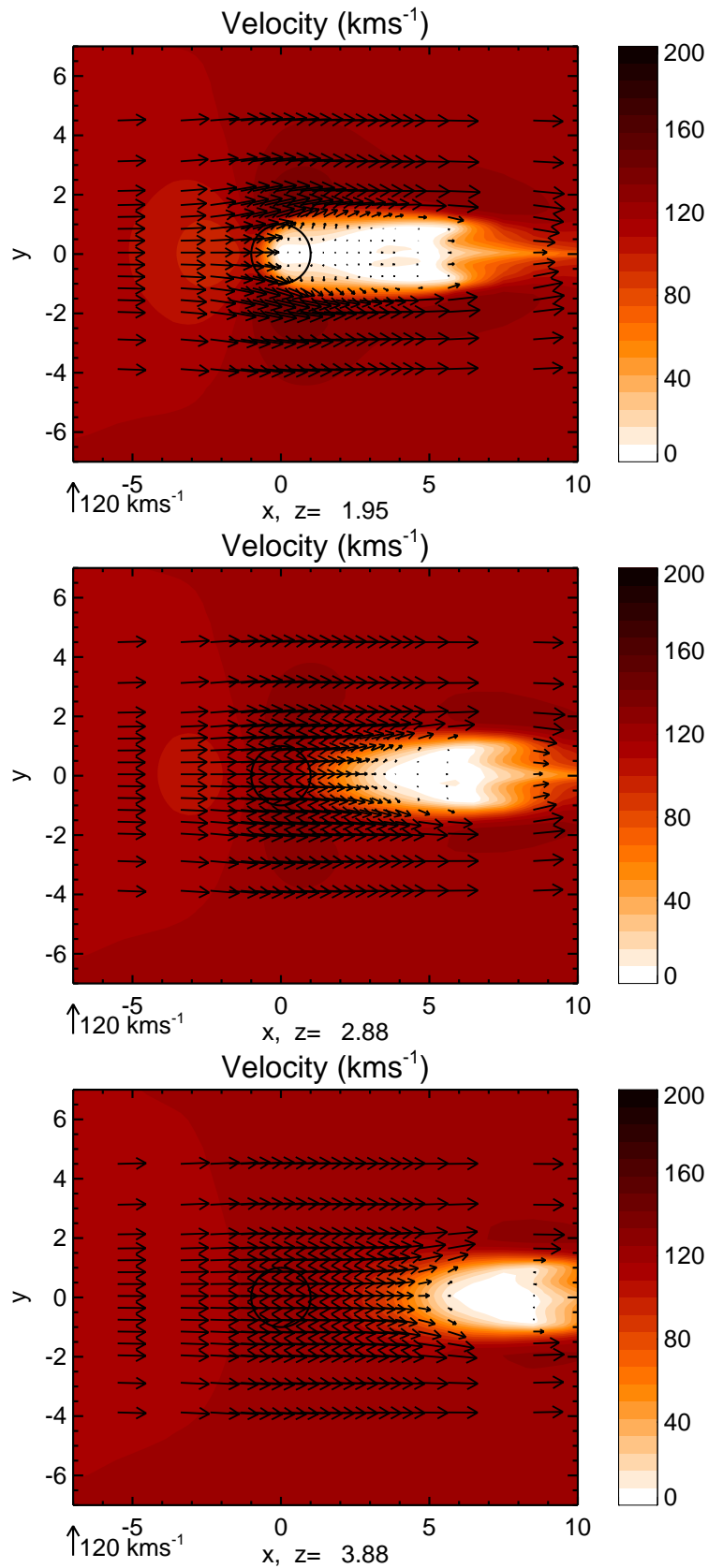


**Figure 5.76:** Velocity magnitude and vectors in the  $xy$ -plane at  $z = 1.95R_T$  (top),  $z = 2.88R_T$  (middle), and  $z = 3.88R_T$  (bottom). The flow is deflected around the Alfvén tube.

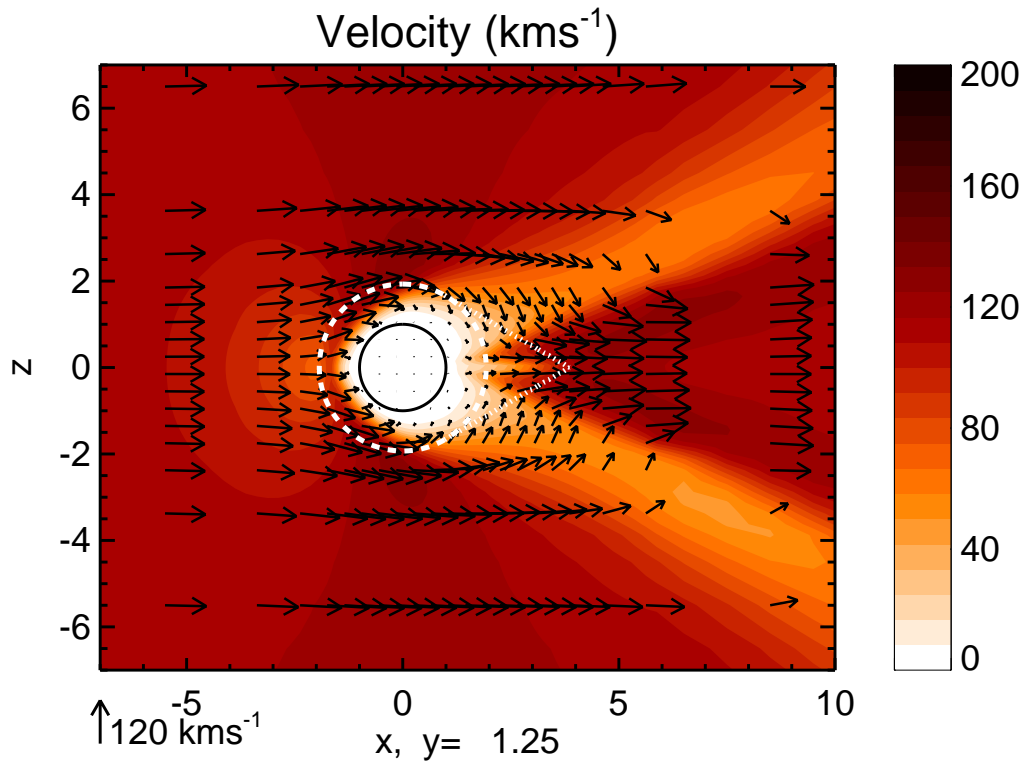


**Figure 5.77:** Flow velocity in the  $xz$ -plane at  $y = 1.25R_T$ . The dashed circle marks the primary interaction region and the dotted line marks the nominal intersection region of the Alfvén tubes.

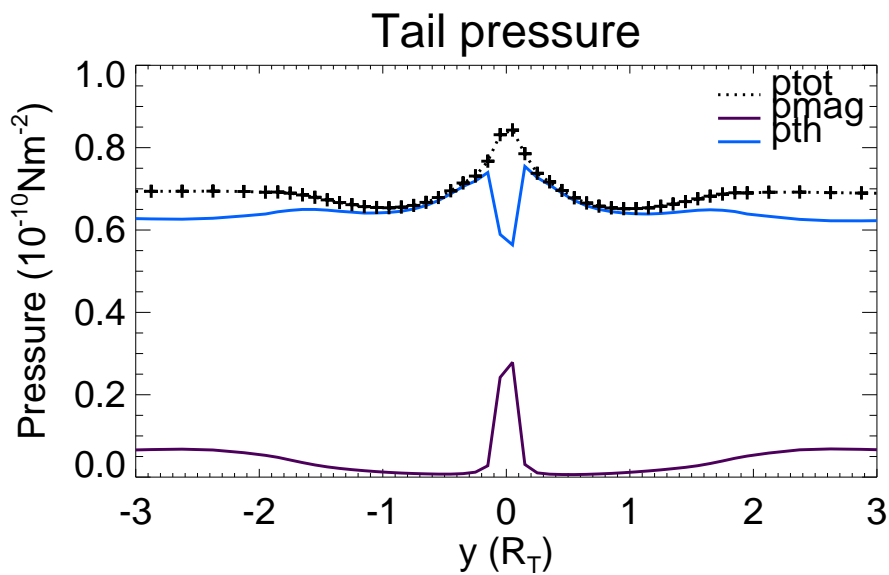


**Figure 5.78:** Magnetic pressure (dark blue line), thermal pressure (light blue line), and the sum of both (dotted line with crosses) along the  $y$ -axis at  $x = 4R_T$ .

behind the main interaction region at  $y = 0$  and decreases the thermal pressure at the same location. The mechanism is similar to the mechanism of magnetic pile-up in front of an obstacle. (5) The enhancement of the magnetic field in the central tail appears only behind the nominal intersection region, i.e. at  $x > 2.3R_T$ .

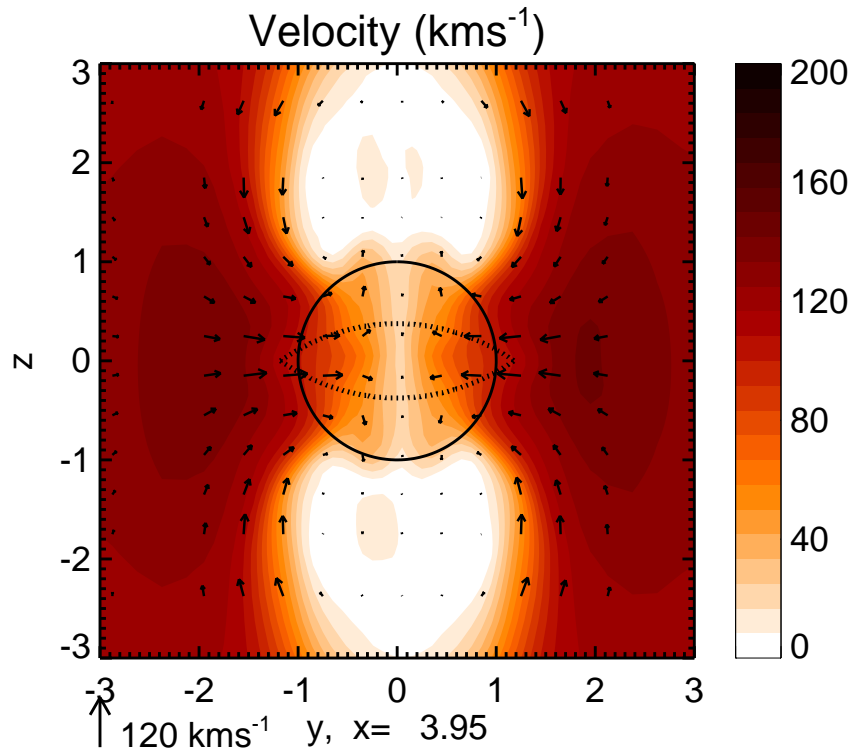


**Figure 5.79:** Absolute value of plasma bulk velocity and vectors projected on the  $yz$ -plane at  $x = 3.95R_T$ . The dotted line marks the nominal intersection region of the Alfvén tubes.

### 5.5.3 Plasma pick-up

One principal effect of the neutral atmosphere on the plasma is its interaction via pick-up (or mass-loading). An ionizing source (e.g. solar EUV, electrons) ionizes a neutral atom or molecule by creating an electron and an ion. If this process happens deep in the atmosphere it leads to the creation of an ionosphere. If it happens in a magnetized moving plasma like in the upper atmosphere, the newly created ion affects the plasma in several ways. The first effect that ionization has on the plasma is that the ion and electron number densities are changed by ionization (Eq. 4.22). Usually the neutral atom is very slow compared to the plasma bulk velocity (effectively  $v_n = 0$ ). The conservation of plasma momentum then leads to a reduction of the plasma bulk velocity caused by ion and electron production. When the rate of mass-loading is high enough it can decelerate the plasma and even bring it to rest [Wallis, 1973].

When an ion is created it moves relative to the magnetic field with a velocity of the local bulk plasma. The ion starts to gyrate around the magnetic field. Collisions with the other plasma particles broaden the velocity distribution of the newly created ions and they acquire a temperature that corresponds to the bulk flow velocity of the plasma relative to the neutral gas [Cravens, 1997]. Thus, ionization increases the thermal plasma pressure (Eq. 4.26).

At comets ion pick-up and mass-loading play a very important role for the solar wind interaction with the neutral coma. A detailed description of the pick-up process at comets can be found in Cravens [1997].

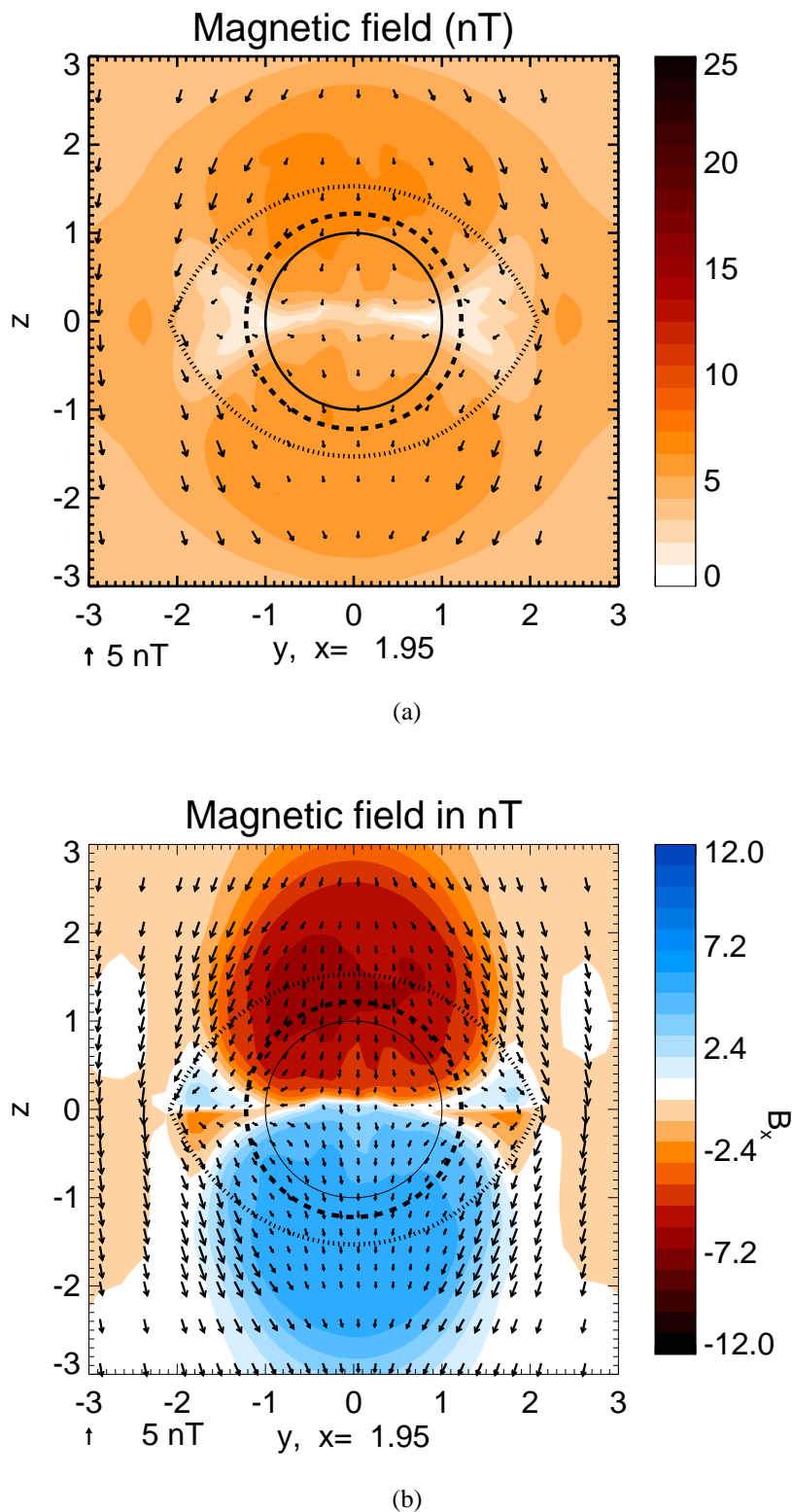


**Figure 5.80:** (a) Magnetic field magnitude in the  $yz$ -plane at  $x = 1.95R_T$ . (b) Components of the magnetic field in the same plane. The  $yz$ -components are displayed as vectors and the  $x$ -component is color coded, red: in  $-x$  direction, blue: in  $x$  direction. The dashed circle marks the primary interaction region and the dotted line marks the nominal intersection region of the Alfvén tubes.

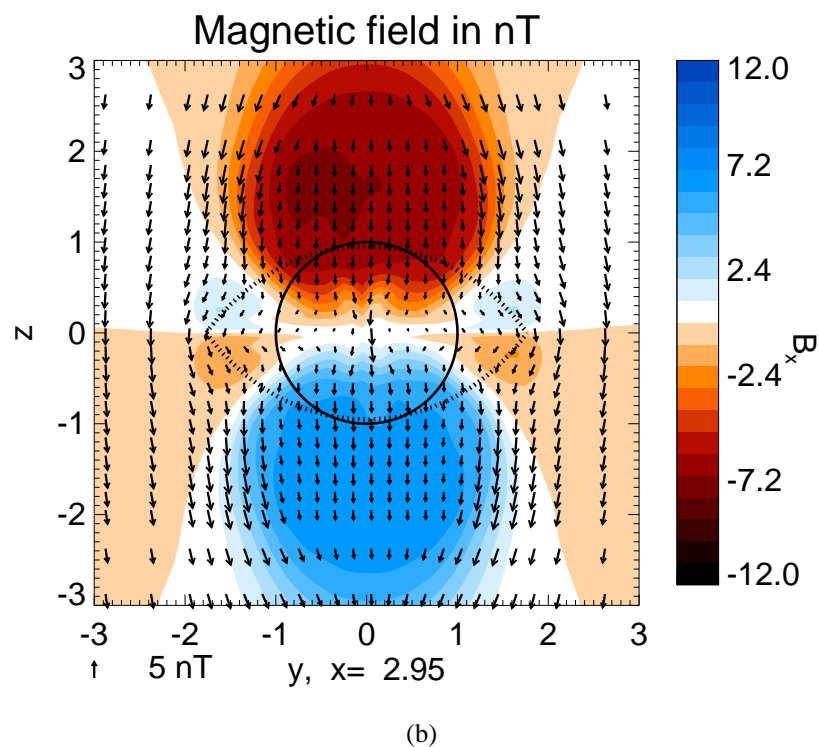
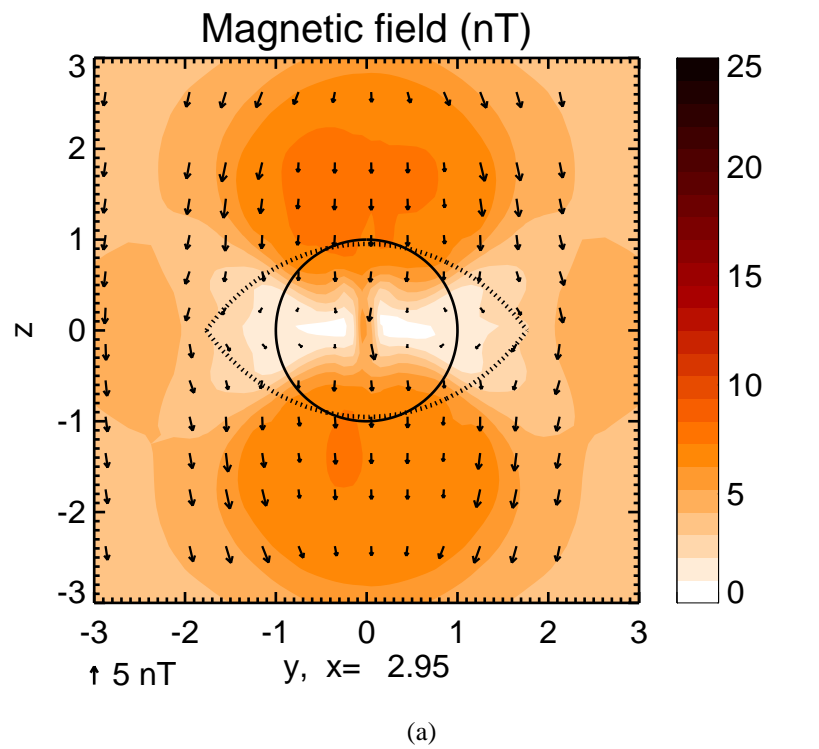


**Figure 5.81:** (a) Magnetic field magnitude in the  $yz$ -plane at  $x = 2.95R_T$ . (b) Components of the magnetic field in the same plane. The  $yz$ -components are displayed as vectors and the  $x$ -component is color coded, red: in  $-x$  direction, blue: in  $x$  direction. The dotted line marks the nominal intersection region of the Alfvén tubes.

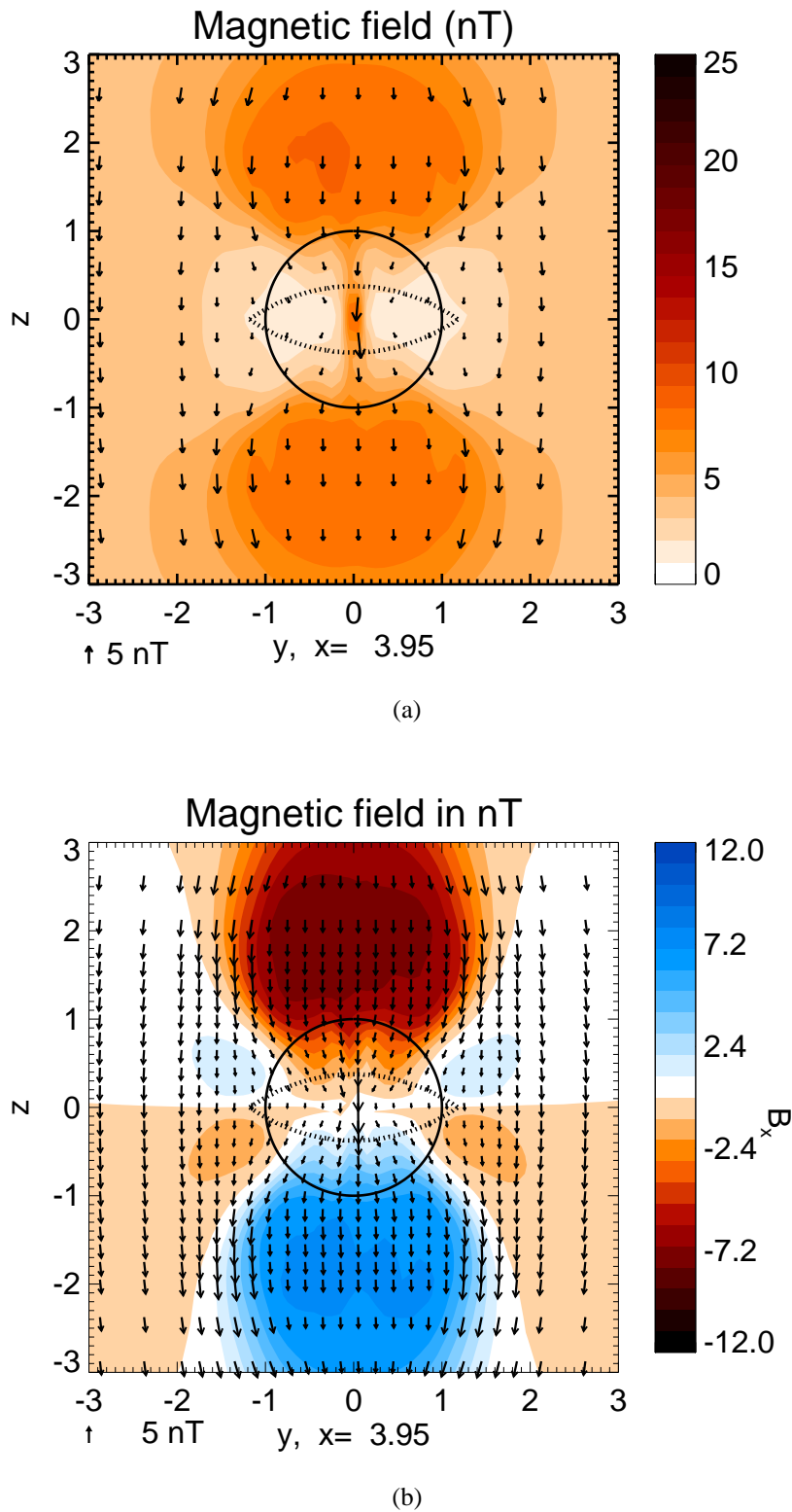


**Figure 5.82:** (a) Magnetic field magnitude in the  $yz$ -plane at  $x = 3.95R_T$ . (b) Components of the magnetic field in the same plane. The  $yz$ -components are displayed as vectors and the  $x$ -component is color coded, red: in  $-x$  direction, blue: in  $x$  direction. The dotted line marks the nominal intersection region of the Alfvén tubes.

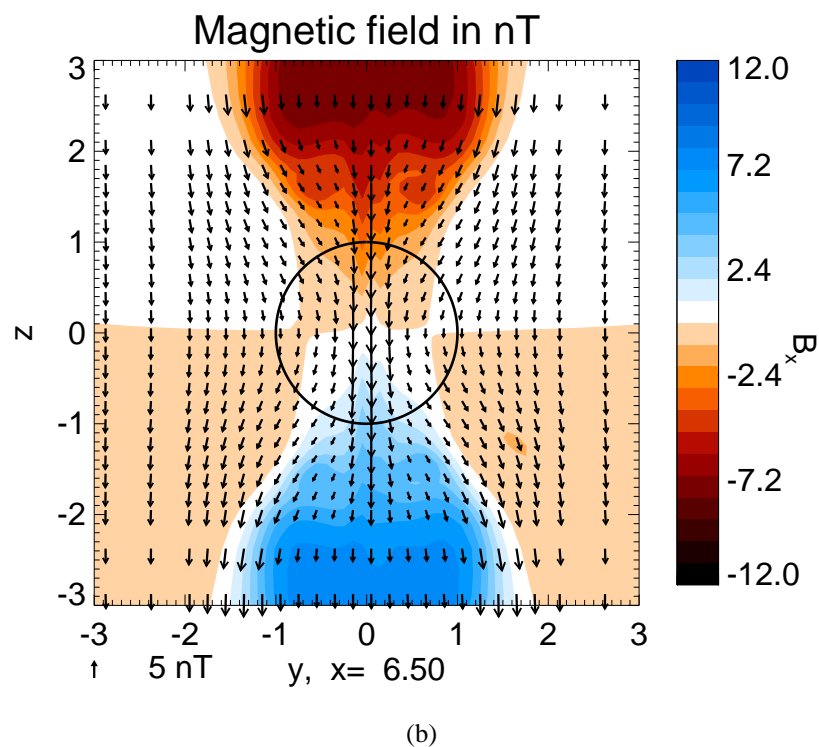
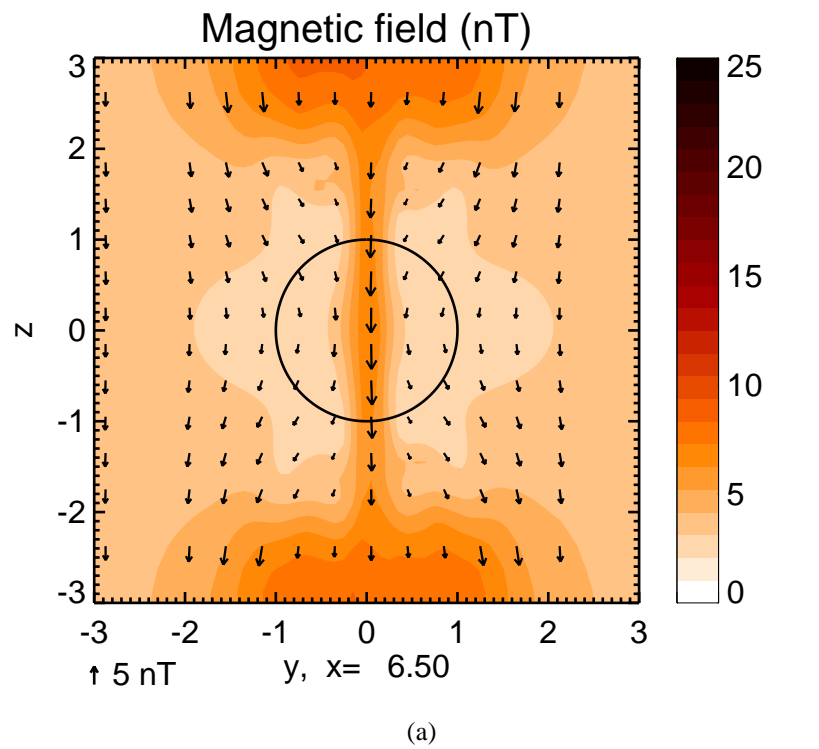


**Figure 5.83:** (a) Magnetic field magnitude in the  $yz$ -plane at  $x = 6.5R_T$ . (b) Components of the magnetic field in the same plane. The  $yz$ -components are displayed as vectors and the  $x$ -component is color coded, red: in  $-x$  direction, blue: in  $x$  direction. The dotted line marks the nominal intersection region of the Alfvén tubes.

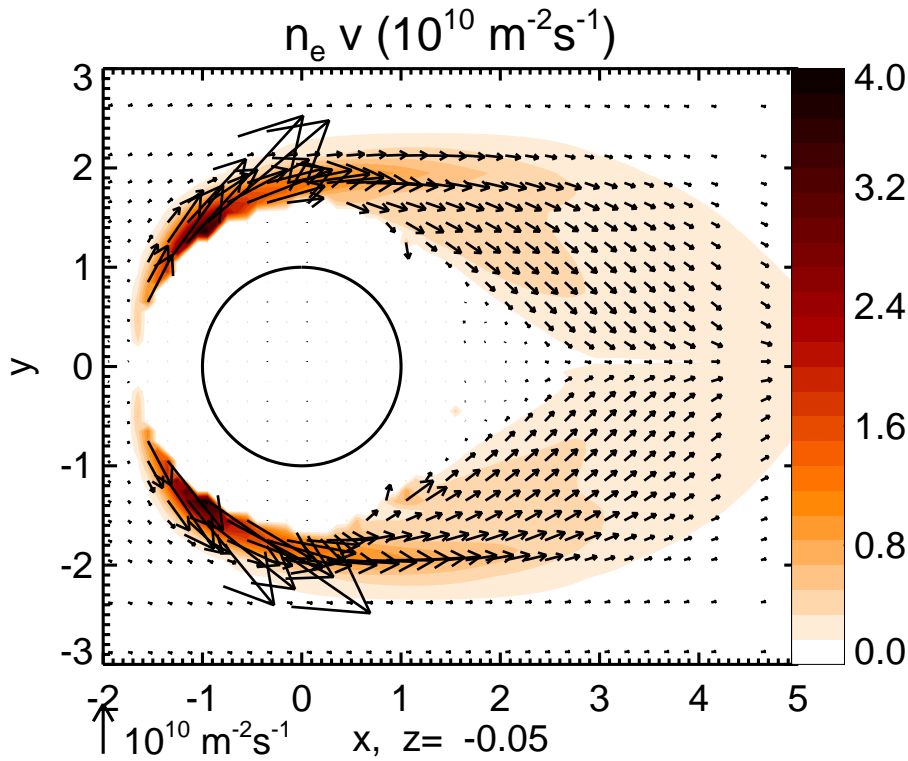


**Figure 5.84:** Plasma flux  $n_e \vec{v}$  in the  $xy$ -plane.

In Section 5.2.3 we have discussed the upstream pressure profile and we have shown that at Titan mass-loading is not essential for the global interaction. However, the pick-up of ions from the neutral atmosphere of Titan is on the one hand a steady source of plasma for the Saturnian magnetosphere and on the other hand a loss process for Titan's atmosphere. In this section we give the plasma loss rates that result from our model and discuss the plasma tail caused by pick-up. The ionization processes that have been taken into account in the model are discussed in Section 5.2.1.

In reality the finite gyro radius of the newly created ions plays an important role in the plasma pick-up process. In the Titan centered coordinate system the ions that are picked up start to gyrate and form cycloidal trajectories toward the electric field. The gyroradius depends on the local speed of the bulk plasma and on the local magnetic field magnitude. Typical plasma velocities at Titan are  $v \sim 10$  km/s and a typical magnetic field magnitude is  $B \approx 10$  nT leading to a gyroradius ( $r_g = \frac{mv_{\perp}}{eB}$ ) of 280 km for a newly created  $N^{2+}$  ion. Ions that are created on the Saturnian flank of Titan start the motion towards Titan, and as they enter the deeper atmosphere they cannot escape and are captured by the atmosphere [Bridge *et al.*, 1981]. On the anti-Saturnian flank the motion is away from Titan and the ion can move along with the magnetospheric plasma. We do not account for finite gyroradius effects in our fluid model. Thus, one has to keep in mind that finite radius effects alter the results that are presented here, e.g. the mass-loading is asymmetric and leads to an asymmetric tail even if the atmospheric conditions are symmetric. At Titan this effect has been studied by Ledvina *et al.* [2000] who examined ion trajectories in Titan's vicinity. Kopp and Ip [2001] included an asymmetric mass loading factor into a MHD simulation. Brecht *et al.* [2000] also obtain

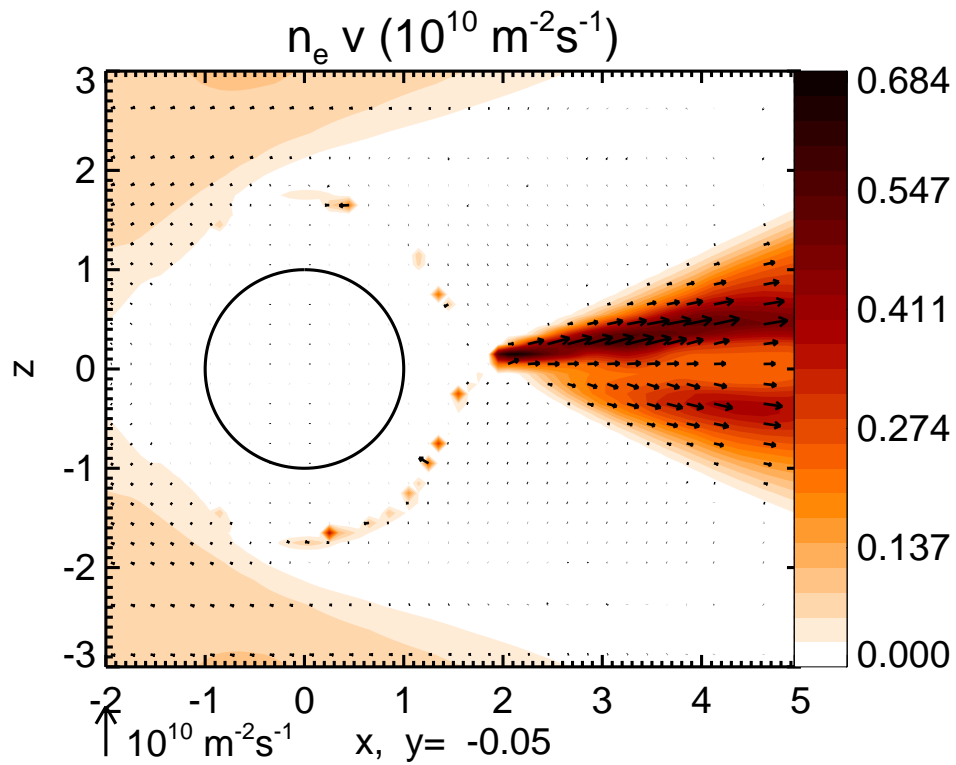


*Figure 5.85:* Plasma flux  $n_e \vec{v}$  in the  $xz$ -plane.

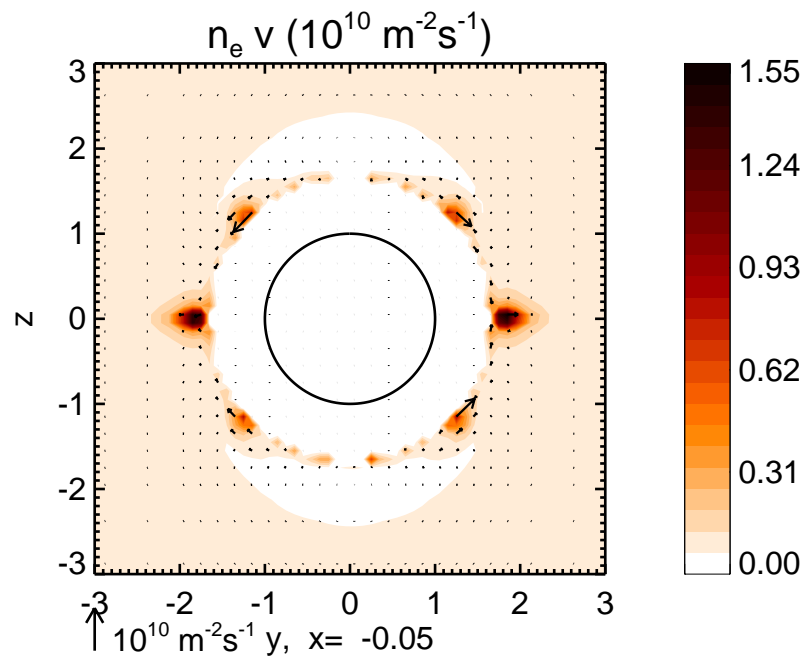


*Figure 5.86:* Plasma flux  $n_e \vec{v}$  in the  $yz$ -plane.

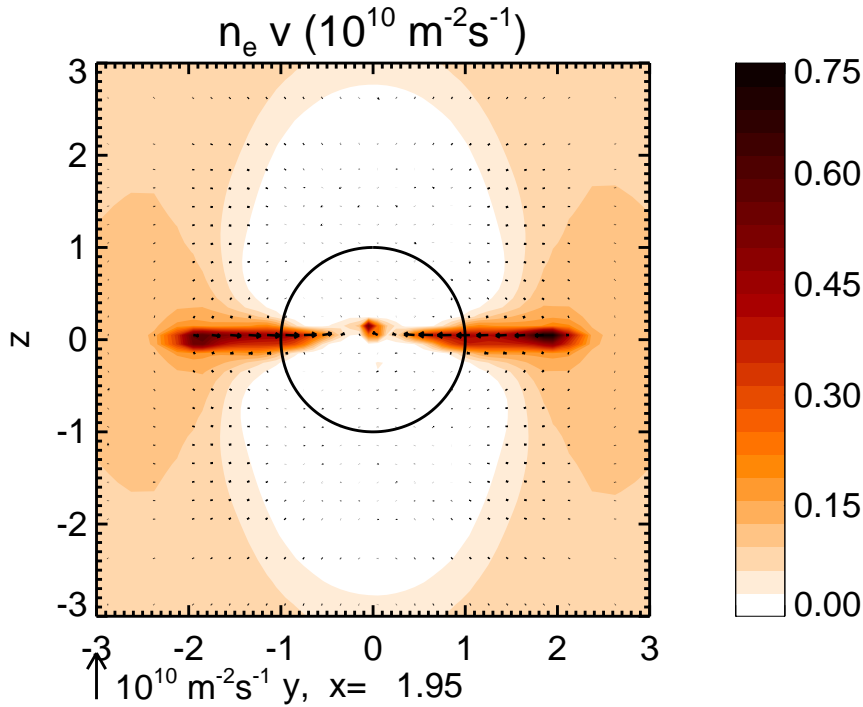


**Figure 5.87:** Plasma flux density in the tail in the  $yz$ -plane at  $T34$

an asymmetric wake a hybrid simulation.

However, from our results we obtain the order of magnitude of the loss rate. The local time dependency of the mass-loss rate can be examined by comparing the results for different local times. To visualize the plasma pick-up the number density flow  $n_e \vec{v}$  is plotted in the  $xy$ -plane (Figure 5.84), the  $xz$  plane (Figure 5.85), and the  $yz$ -plane (Figure 5.86). The plots show that most of the plasma is picked up at the flanks of the upstream atmosphere. There is nearly no pick-up over the poles. From the flow picture that has been discussed in Section 5.5.2 this is obvious because there is nearly no plasma flow over the poles because of the Alfvén tubes. At  $x \approx 2R_T$  the picked up plasma from the flanks enters the central wake.

From the four projections of  $n_e \vec{v}$  on the  $yz$ -plane in Figure 5.87 to Figure 5.90 the path of the pick-up plasma to the central wake is visible. At  $x = 2R_T$  the plasma is concentrated along the  $y$ -axis. The velocity components are directed tail-ward (see Figure 5.84) and towards  $y = 0$ . At about  $x = 2.3R_T$  the mass-loaded flux tubes that have passed Titan at the flanks at low altitude converge. As discussed in Section 5.5.2 at the convergence point the magnetic field is enhanced. The mass-loaded flux tubes that have passed Titan's flank atmosphere at higher altitudes converge further downstream along the  $x$ -axis.

The convergence of the flow not only enhances the magnetic field magnitude but it also combines the plasma picked-up at both flanks leading to a maximum of the plasma density around  $y = 0$ . The enhanced plasma density then expands along the magnetic field. The expansion is achieved by slow mode waves along the magnetic field lines. The expansion leads to the cross structure of the density flow in the tail (Figure 5.88).

Further downstream in the tail at  $x = 4R_T$  the extension of the enhanced density region along

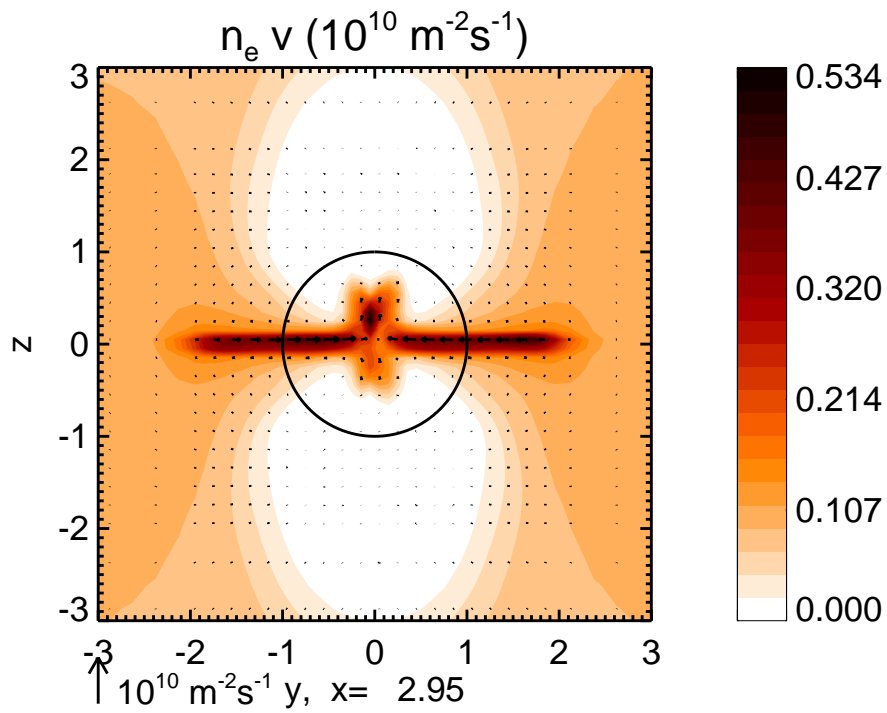


Figure 5.88: Plasma flux density in the tail in the  $yz$ -plane at  $T34$

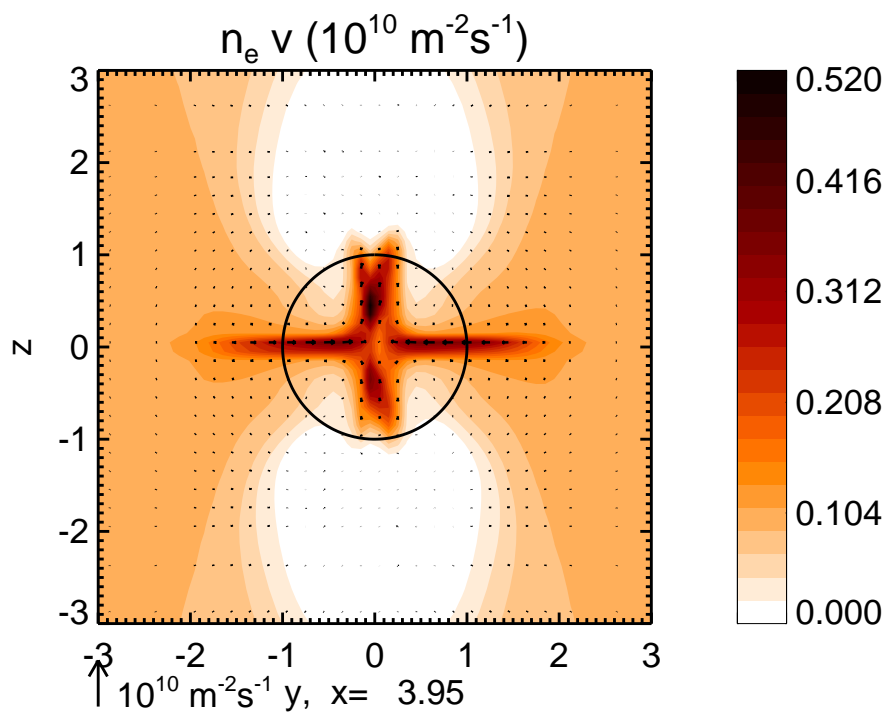
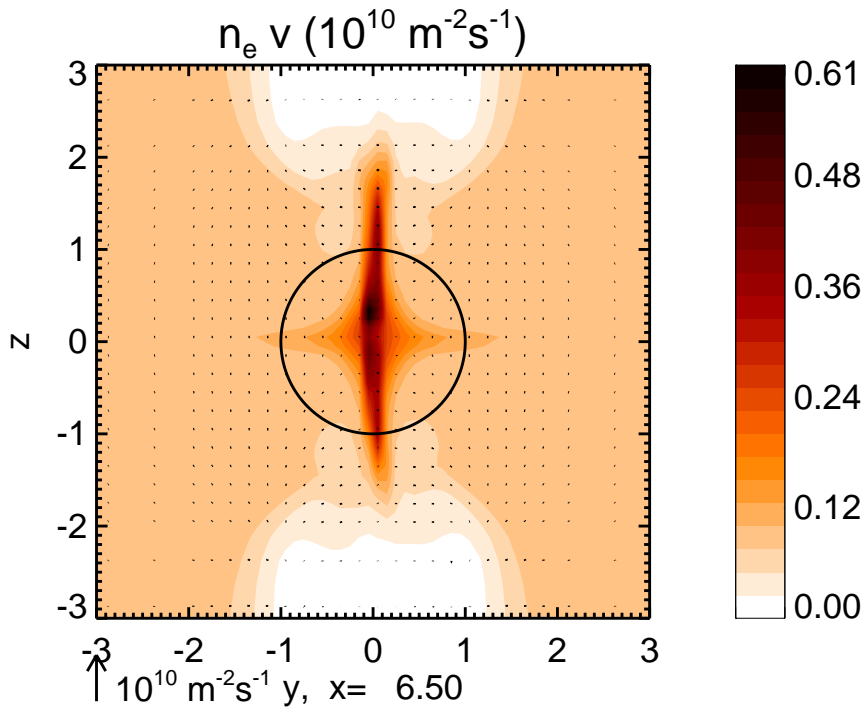


Figure 5.89: Plasma flux density in the tail in the  $yz$ -plane at  $T34$



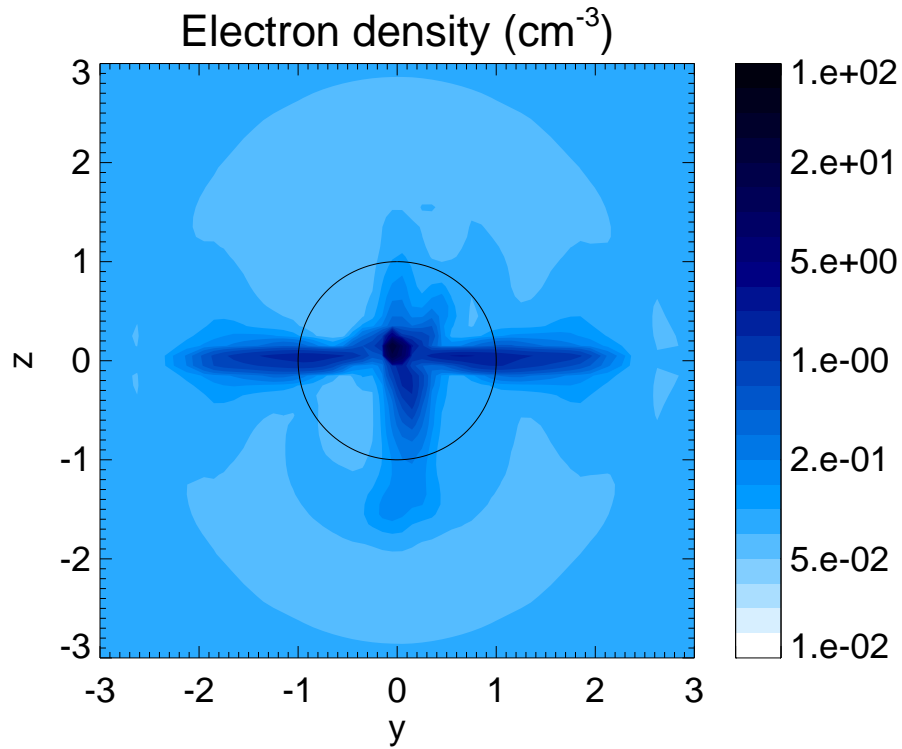
**Figure 5.90:** Plasma flux density in the tail in the  $yz$ -plane at  $T34$

the  $y$ -axis has decreased to about  $3R_T$  and the extension in  $z$ -direction has reached  $2R_T$  (Figure 5.89).

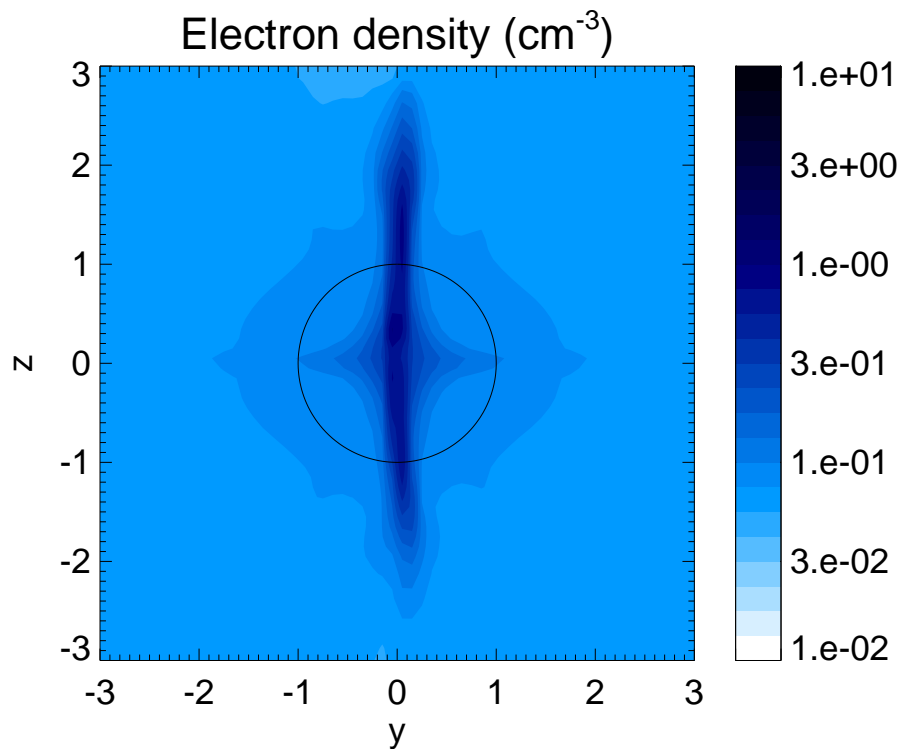
In the distant tail (at  $x = 6.5R_T$ ) the cross structure has nearly disappeared. The region with enhanced plasma flux density is distributed along the  $z$ -axis (Figure 5.90).

Figure 5.91 shows the electron density in the near and Figure 5.92 in the distant tail. The structure qualitatively maps the picture from the flow density: a cross-type density distribution near Titan develops along the tail into a density enhancement along the  $z$ -axis (when displayed on the  $yz$ -plane). The peak electron density in the tail is at  $x = 2R_T$   $10 \text{ cm}^{-3}$  and at  $x = 6.5R_T$   $1 \text{ cm}^{-3}$ . The ionospheric electron density at Titan in the three planes is shown in Figure 5.11, Figure 5.12, and Figure 5.13.

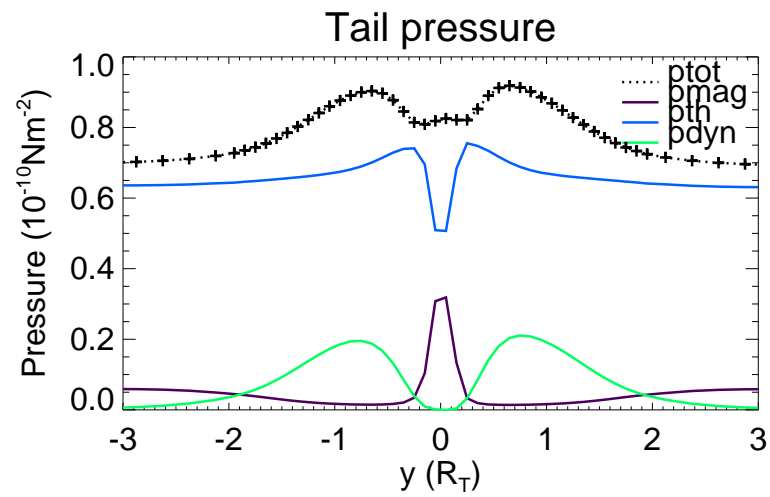
We will now explain the density distribution in the tail. The density in the near tail which is concentrated on the  $xy$ -plane (see Figure 5.91a) is simply a consequence of the locations where the plasma is picked up: the major part of the plasma is picked up on the upstream side and on the flanks in the equatorial plane. The plasma flow around the Alfvén tube is nearly perpendicular to the tube axis (characteristic direction) which focuses the plasma that has been picked up north or south of the equatorial plane to the equatorial plane in the tail (see Figure 5.77). The flow convergence along the tail at  $y = 0$  has been described in Section 5.5.2. One consequence of the flow convergence is the enhancement of the sum of magnetic and thermal pressure and the enhancement of the plasma density at  $y = 0$ . The acceleration of the plasma is caused by pressure gradients. In Figure 5.93 the thermal, magnetic, and dynamic pressure is plotted along the  $y$ -axis and along the  $z$ -axis at  $x = 5R_T$ . Along the  $y$ -axis the enhanced sum of thermal and magnetic pressure is over-compensated by the



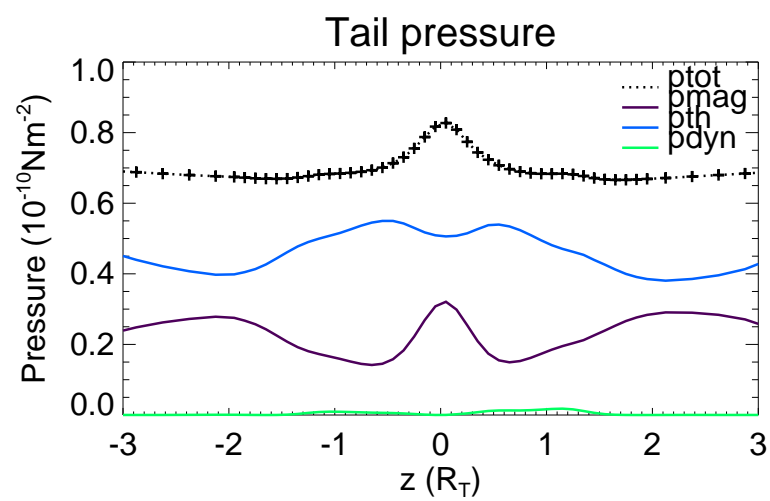
**Figure 5.91:** Electron number density in the tail at  $x = 2R_T$  in the T34 case



**Figure 5.92:** Electron number density in the tail at  $x = 7R_T$  in the T34 case



(a)



(b)

**Figure 5.93:** Magnetic ( $p_{mag}$ ), thermal ( $p_{th}$ ), dynamic ( $p_{dyn}$ ) pressure, and the sum of them ( $p_{tot}$ ) along the  $y$ -axis (a) and the  $z$ -axis (b) in the tail at  $x = 5R_T$ .

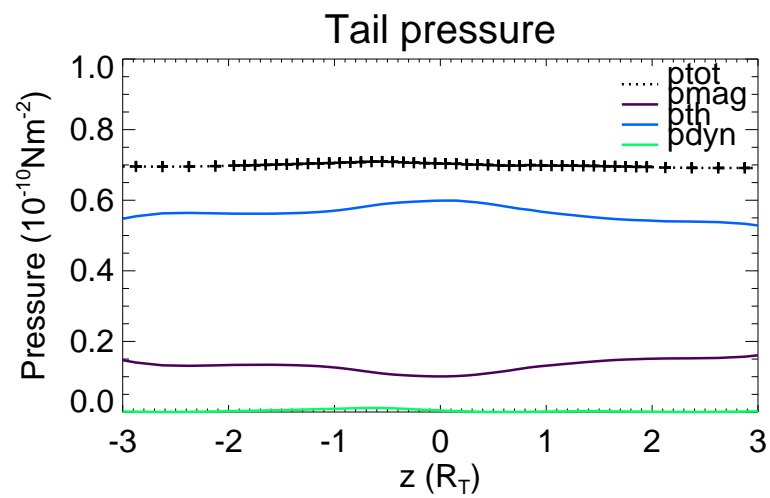
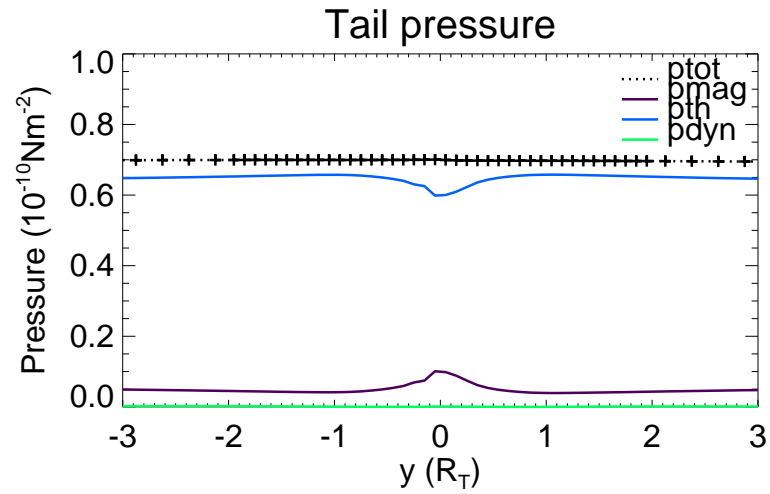


**Figure 5.94:** Magnetic ( $p_{mag}$ ), thermal ( $p_{th}$ ), dynamic ( $p_{dyn}$ ) pressure, and the sum of them ( $p_{tot}$ ) along the  $y$ -axis (a) and the  $z$ -axis (b) in the tail at  $x = 10R_T$ .

dynamic pressure such that there is a net acceleration of the plasma towards  $y = 0$  along the  $y$ -axis. Along the  $z$ -axis there is no flow towards  $z = 0$  and consequently no dynamic pressure. Then the enhanced sum of thermal and magnetic pressure accelerates the plasma away from  $z = 0$ . Thus, the non-isotropic character of the sum of thermal, magnetic, and dynamic pressure redistributes the plasma that was concentrated on the equatorial plane along the  $xz$ -plane.

As Figure 5.94 indicates, the pressure enhancement has decayed at  $x = 10R_T$ . Thus, the distribution of the tail plasma density in the  $yz$ -plane remains constant along the tail further downstream.

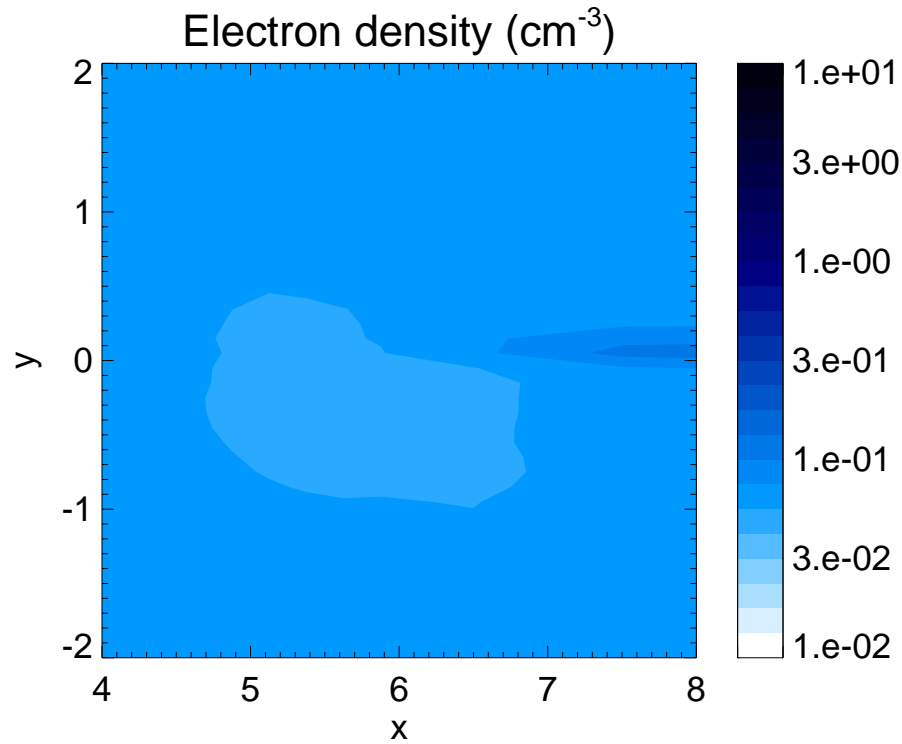
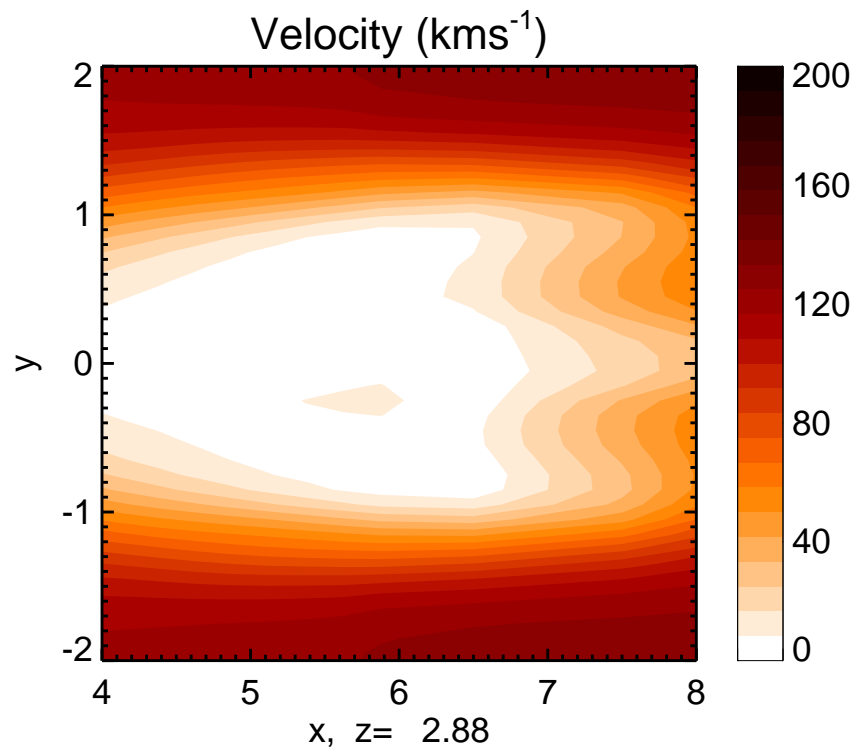
When we calculate the net mass flow through the surface of a box around Titan we can determine the total mass-loss rate. We obtain a value of  $\dot{m} \approx 30 \text{ gs}^{-1}$ . *Keller et al.* [1994b] estimate the plasma loss rate to be  $\dot{m} \approx 100 \text{ gs}^{-1}$  and *Eviatar et al.* [1982] obtain  $\dot{m} \approx 50 \text{ gs}^{-1}$ .

The comparison of the mass-loss rates for T34, TA, and T5 conditions shows that the total mass-loss rate is nearly the same for the three cases. That means the total mass-loss rate does not depend on SLT. But the transport of the picked up ions away from Titan is different for the three cases. When the dayside is the upstream side (T34) the pick-up takes place on field lines that move through the upper atmosphere. They are transported by the plasma flow around the Alfvén tubes to the tail of Titan. The field lines inside of the Alfvén tubes are not mass-loaded in this case. When Titan's nightside corresponds to the upstream side (T5 and partly TA) the field lines pass deeper into the atmosphere where they are mass-loaded by magnetospheric electron impact ionization. These field lines are inside of the Alfvén tubes and their transport to the tail is different from the transport of the field lines that move around the Alfvén tubes. Thus, in the T5 and TA cases the plasma density in the Alfvén tubes is enhanced while in the T34 case it is more or less equal to the background density. In Figure 5.95 and Figure 5.96 the absolute value of the plasma bulk velocity and the electron density is plotted in the  $xy$ -plane at  $z = 2.9R_T$ . Since inside of the Alfvén tube the plasma velocity is reduced, its location is given by the low velocity region in the velocity plots. In the T34 case the density inside of the tube is obviously unchanged while in the T5 case the density in the tube is enhanced by about an order of magnitude. This has consequences for the distribution of the plasma density in the tail.

The comparison of the tail densities at  $x = 7R_T$  at TA (Figure 5.97a) and at T5 (Figure 5.97b) conditions with the tail density at T34 conditions (Figure 5.92) shows some differences: (1) the extension of the enhanced density region along the  $z$  direction is larger in the T5 case. (2) The extension of the region along  $y$  at  $z = 0$  is smaller at T5. (3) In the TA case the extension along  $y$  at  $z = 0$  is asymmetric. There is no extension towards the nightside.

#### 5.5.4 Temperature of magnetospheric electrons

In the flux tube model that has been introduced in Section 4.4 the equation for the temperature of the magnetospheric electrons (ms-electrons) (Eq. 4.46) is solved. The major aim of the flux tube model consists in calculating the ionization rates from magnetospheric electron impact. The ionization rates depend on the temperature of the ms-electrons. Therefore, we

(a) T34,  $\rho$ (b) T34,  $v$ 

**Figure 5.95:** Electron number density (a) and absolute value of the flow velocity (b) in the  $xy$ -plane at  $z = 2.88R_T$  for case T34.

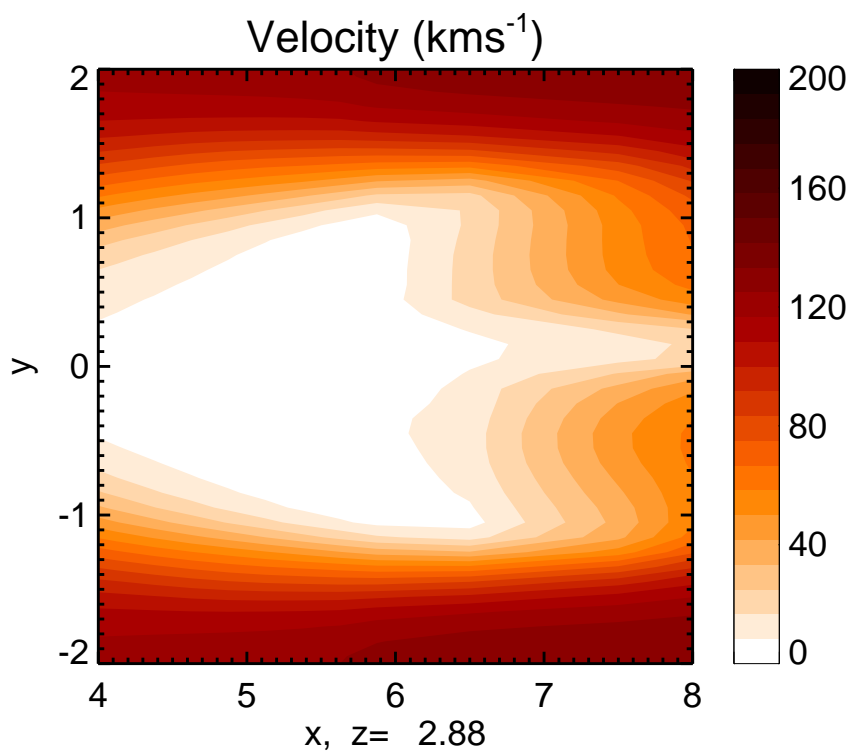
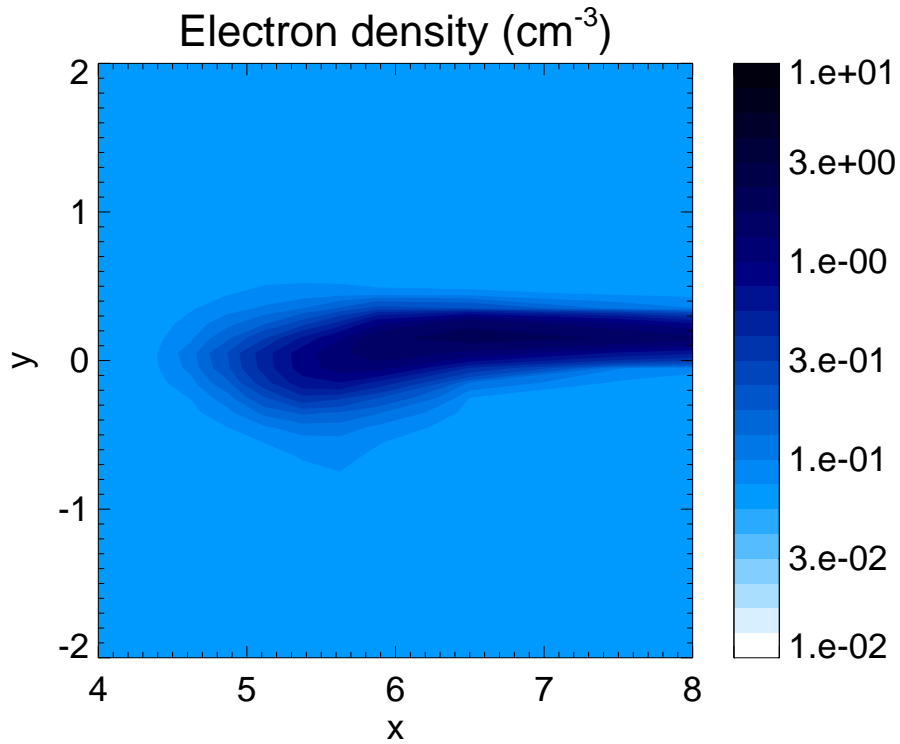
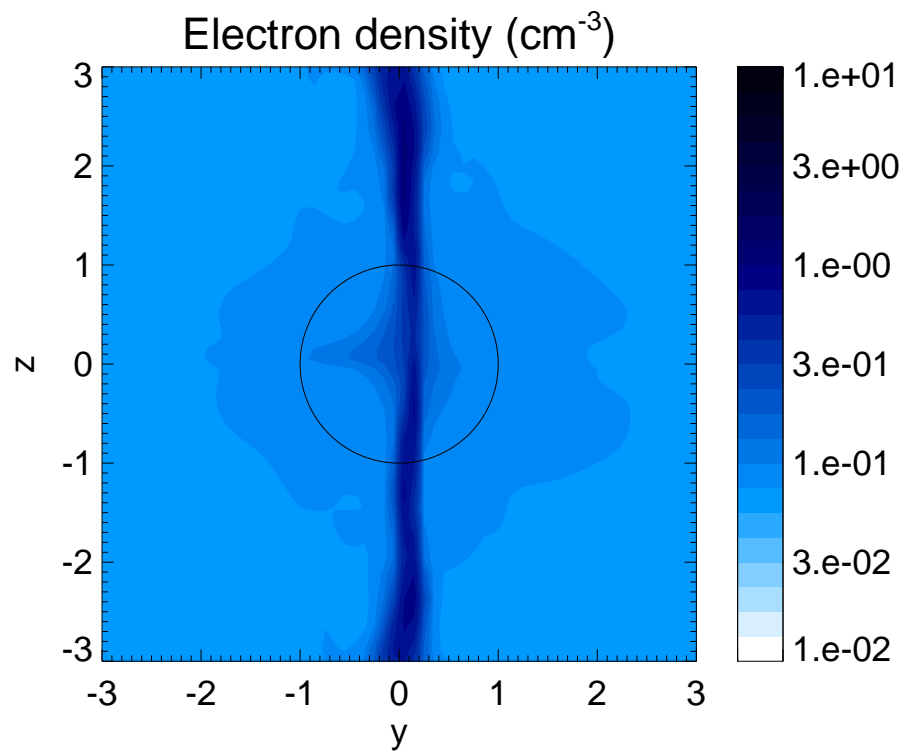
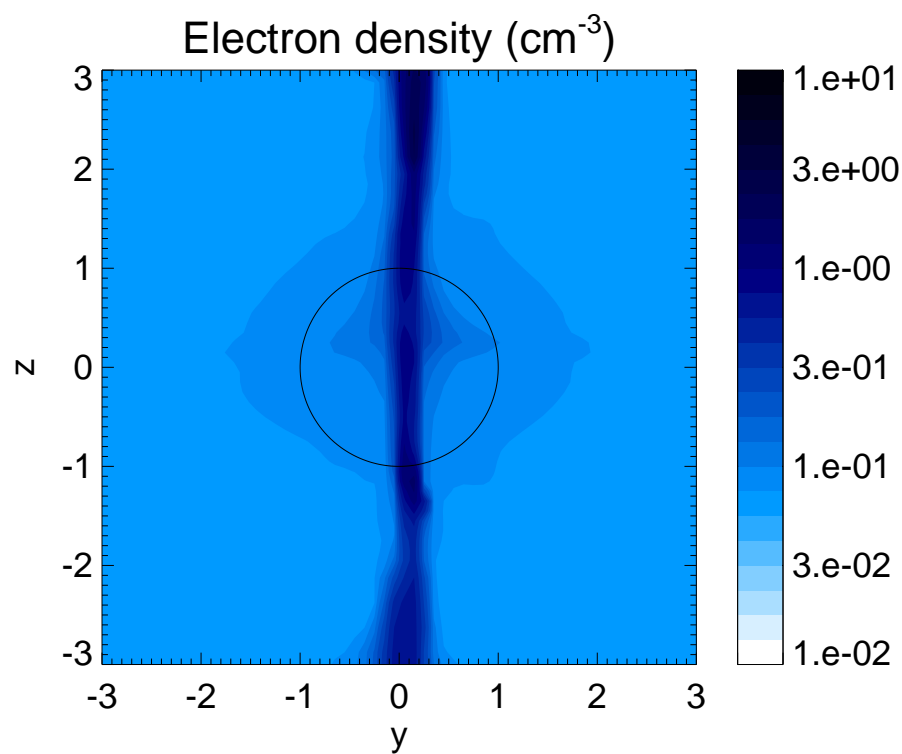


**Figure 5.96:** Electron number density (a) and absolute value of the flow velocity in the  $xy$ -plane at  $z = 2.88R_T$  for case T5.

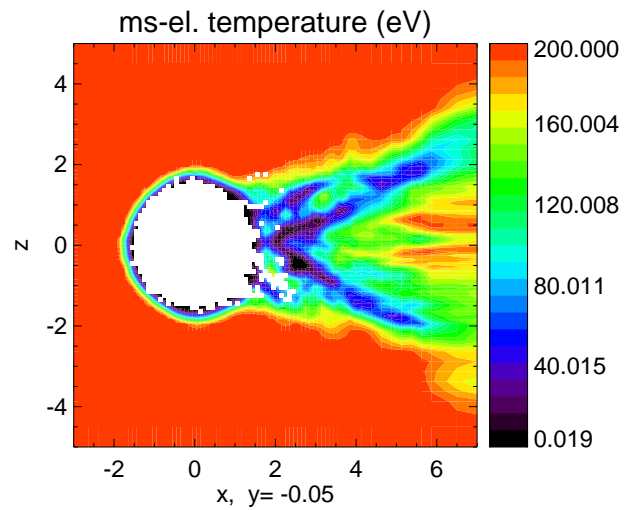


(a) TA

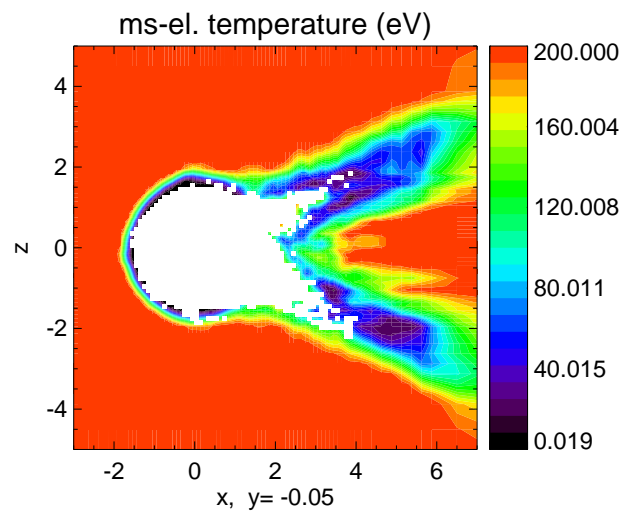


(b) T5

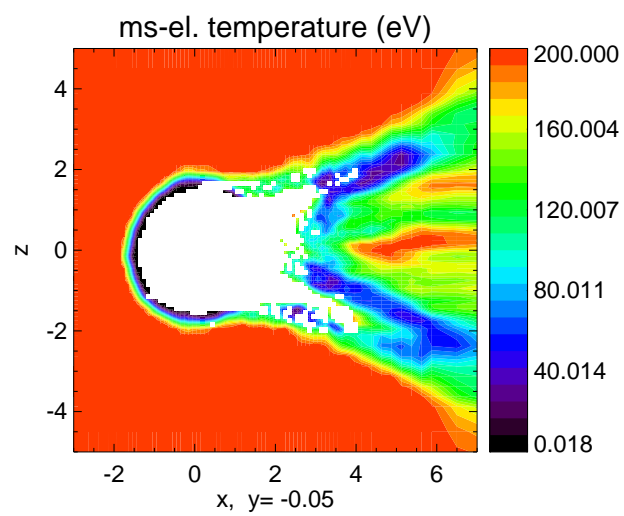
**Figure 5.97:** Electron number density in the tail at  $x = 7R_T$  at TA (a) and T5 (b).



(a) T34



(b) TA



(c) T5

**Figure 5.98:** Temperature of the magnetospheric electrons in the  $xz$ -plane. The temperatures are obtained from the flux tube model.

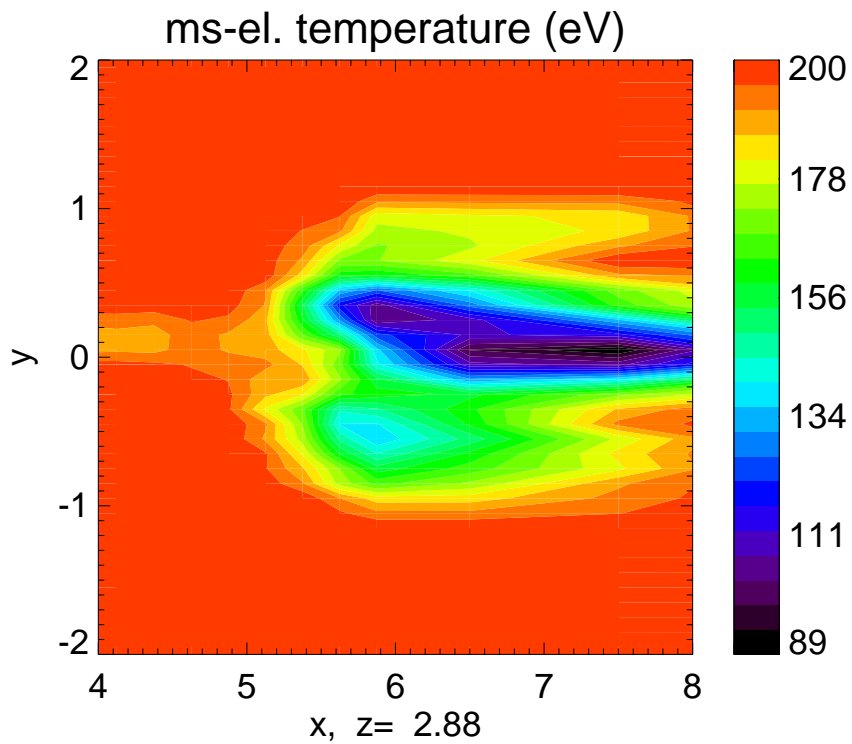
have to treat the ms-electrons as a separate species within the bulk plasma in order to obtain the ionization rates. Since the ms-electron temperature is an explicit variable in the flux tube model, the model not only provides us the production rates but also the ms-electron temperature. In this Section we want to discuss the 3D distribution of the temperature obtained from our model.

The flux tube model is calculated on a co-moving non-Cartesian grid. For the presentation of the temperature the data has been transferred into the Cartesian ZEUS coordinate system. The flux tube grid follows the stream lines. There are points in the ZEUS grid where none of the flux tube points have passed by during simulation time. In the following plots the regions corresponding to such points are left white.

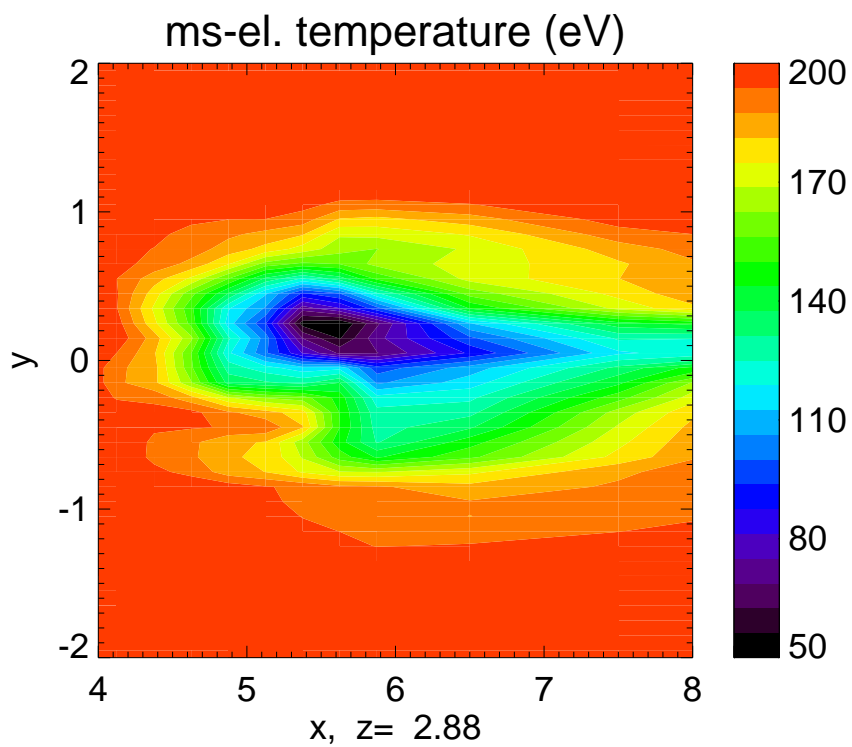
Figure 5.98 displays the temperature profile for T34 (a), TA (b), and T5 (c). Eq. 4.46 contains, apart from the local cooling effects, heat conduction which distributes energy along the flux tubes. This explains the tail structure in the temperature profile in Figure 5.98: points that are connected along the magnetic field lines with the neutral atmosphere are cooled. The field line geometry for T34 is plotted in Figure 5.66. The photo-ionosphere prevents magnetospheric flux tubes from entering deep into the atmosphere. Thus, basically those flux tubes are cooled that move through the nightside atmosphere. In the T34 case the downstream side is the night side and the cooled flux tubes are connected with the downstream side. The extension of the cooled region along  $z$  is narrow compared to the cooled region in the T5 and TA case. In Section 5.5.3 the pick-up process has been discussed. There has been demonstrated that the Alfvén wings are mass loaded only in the cases where the nightside corresponds to the flanks or to the upstream side which implies that if the interior of the Alfvén tubes is mass loaded it is due to impact ionization by ms-electrons. In the cases TA and T5 (Figure 5.98b,c) a larger part of the Alfvén tubes is cooled than in the T34 case. Figure 5.99 shows the ms-electron temperature in the  $xy$ -plane at  $z = 3R_T$  in the T34 and T5 case. In the T34 case the tail-ward part of the Alfvén tube is cooled while in the T5 case the cool part is more in the center of the Alfvén tube. The comparison of Figure 5.99 with Figure 5.95 and Figure 5.96 shows that the cooled area inside of the Alfvén tube in the T5 case corresponds to the mass loaded region.

Figure 5.101 shows the ms-electron temperature in the  $yz$ -plane at  $x = 2.5R_T$  i.e. on a cut through the tail. The cooled regions correspond to the field lines that are connected with the nightside of Titan. In the T34 case the nightside is the downstream side and consequently mainly the inner region in the projected plane is cooled. In the TA case where the nightside is on the upstream Saturnian flank the outer parts towards Saturn are cooler. Thus, the temperature distribution in the Alfvén wings maps the ionospheric properties and depends on the Saturnian local time.

The plotted planes in Figure 5.101 are close to the positions of the Voyager 1 encounter at Titan. Along the trajectory in the tail of Titan a bite-out of high energy electrons in the velocity distribution function has been observed (see Figure 5.100 from *Hartle et al.* [1982]). In our model the electron temperature in the near tail is reduced to about 1% of the background temperature. Thus, we suggest that inelastic collisions with the neutral gas can be responsible for the bite out of energetic electrons.



(a) T34



(b) T5

**Figure 5.99:** Magnetospheric electron temperature in the Alfvén tubes. For the determination of the position of the Alfvén tube see Figure 5.95 and Figure 5.96.

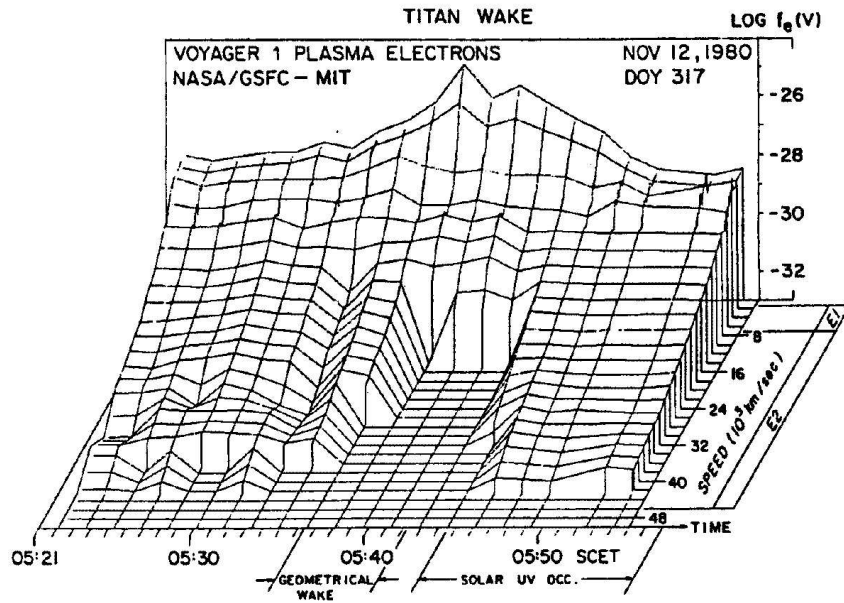
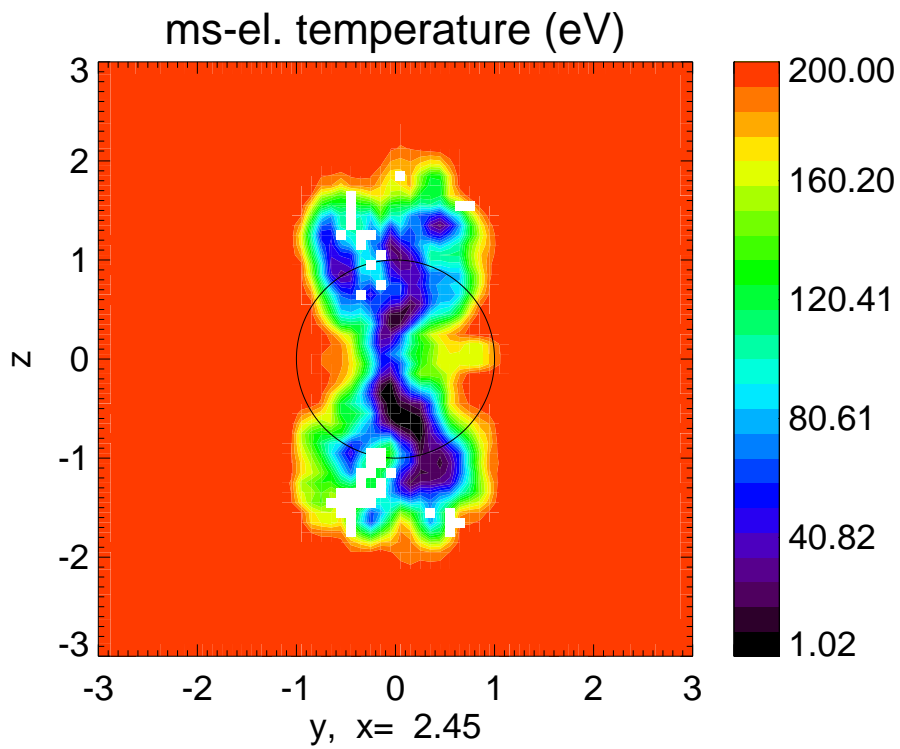


**Figure 5.100:** Electron distribution function  $f_e$  as a function of velocity along the Voyager 1 trajectory through Titan's wake (from Hartle *et al.* [1982]).

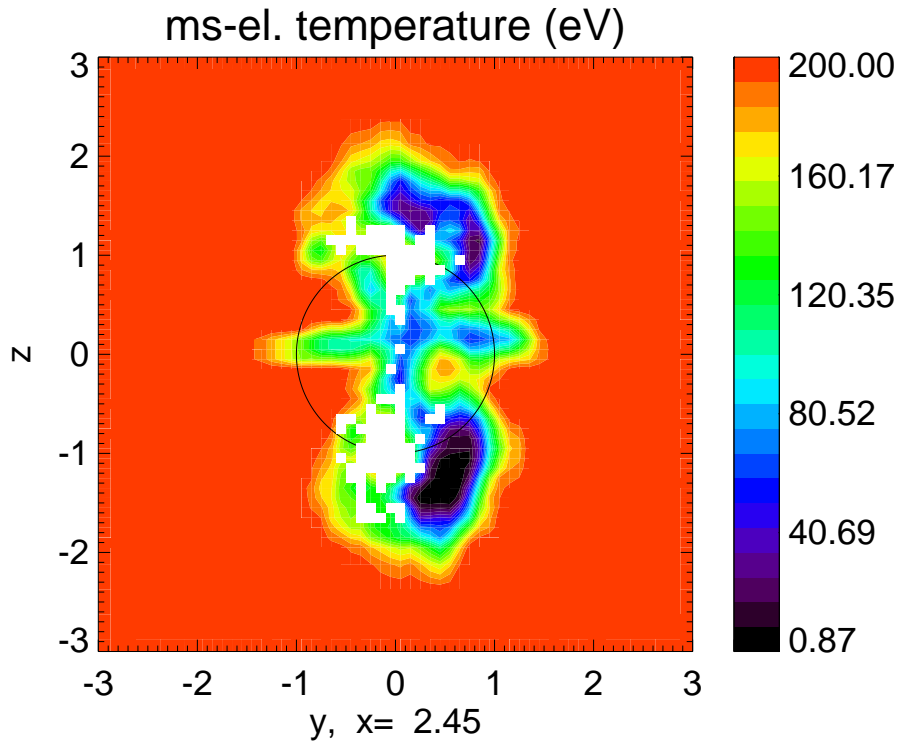
## 5.6 Comparison with other models

Several models concerning the plasma interaction of Titan have been developed. In this section we discuss these models and compare the results of our model with their results, if possible.

*Keller et al.* [1992] show in their model of the ionosphere for the first time that photoionization by the solar EUV radiation is the major source for the production of Titan's ionosphere. The model includes both photoionization and impact ionization by magnetospheric electrons. The impact ionization rates are taken from the two-stream electron model of *Gan et al.* [1992]. Apart from that, a lot of chemical reactions are calculated and they obtain a detailed ionospheric ion distribution. *Keller et al.* [1998] improved the model by including a more detailed hydrocarbon chemistry. The model does not include dynamical effects but the ionosphere from our ionospheric model can be compared with it. They calculated the profile for a solar zenith angle of  $60^\circ$  at solar maximum conditions appropriate for the time during the Voyager 1 encounter. The conditions during the Cassini mission are expected to be near solar minimum. Thus, there is a difference in the incident solar flux model between the *Keller et al.* [1992] model and our model. In our simulation of the conditions during flyby TA the solar zenith angle along the  $-z$ -axis is  $66.4^\circ$ . *Keller et al.* [1992] obtain a major production rate of  $17 \text{ cm}^{-3}\text{s}^{-1}$  at an altitude of 1050 km leading to a peak density of  $6150 \text{ cm}^{-3}$  at the same altitude. From our model we obtain a peak production rate of  $8 \text{ cm}^{-3}\text{s}^{-1}$  at an altitude of 900 km with a peak density of  $4255 \text{ cm}^{-3}$ . Apart from the lower values for ionization rate and density due to the solar minimum conditions, there is a good agreement between the ionosphere in our model and in the *Keller et al.* [1992] model (see Figure 5.102). Note that the difference in peak altitude ( $\sim 100 \text{ km}$ ) is below our grid resolution (275 km).



(a) T34



(b) TA

**Figure 5.101:** Magnetospheric electron temperature in the tail of Titan at  $x = 2.45R_T$ .

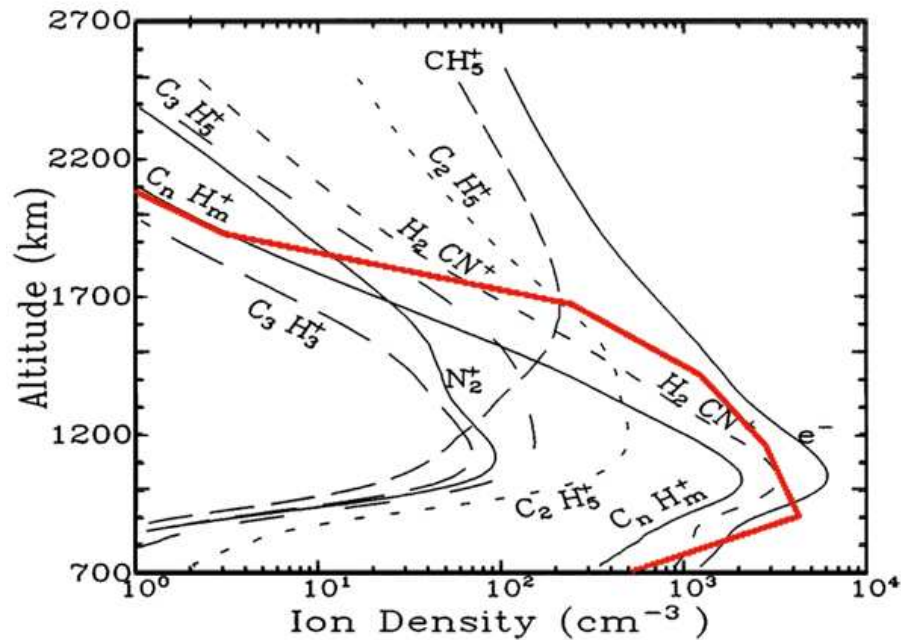


**Figure 5.102:** Comparison of the ionospheric electron density from our model (bold line) with the ion densities from the model of Keller *et al.* [1992].

In their model for the magnetospheric electrons *Gan et al.* [1992] use a two-stream method [*Gan and Cravens*, 1990] to calculate the energy distribution of the electron fluxes in both directions along a magnetic field lines. They are able to calculate very accurately the inelastic interaction of the electrons with the neutral atmosphere to obtain for example  $N_2$  airglow intensities or impact ionization rates. A limit of the model is that they adopt an artificial magnetic field line geometry and that the model has no time dependency.

The real interaction of a flux tube with Titan's atmosphere is a dynamical process. The path way of the flux tube through the atmosphere and the time the flux tube spends in the atmosphere are important parameters. In order to specify that argument we give two extreme examples: If the time a flux tube spends inside of the atmosphere is much lower than the travel time of the electrons along the field line, the electrons in the flux tube will not lose much of their energy. In the other extreme case the flux tube stagnates inside of the atmosphere. Then the electrons do not just move once through the atmosphere but many times until the total energy of the electrons in the incident flux tube is used up. Thus, the interaction of magnetospheric electrons with the neutral atmosphere depends on the plasma flow and the magnetic field line geometry.

*Gan et al.* [1993] included a time dependency into the *Gan et al.* [1992] model. They assumed a flow along the stagnation point stream line with a deceleration of the flow proportional to  $r^{-1}$ . The stagnation point stream line is a singular stream line on which the flux tube stagnates, and the total time the flux tube spends in the atmosphere is infinite. It is not possible to make predictions for the energy in a flux tube in the tail with this model. However, the model combines flux tube motion and energy absorption.

In our model we also combine flux tube motion and energy absorption. But the plasma

flow is three dimensional and is calculated within the model. Additionally, the magnetic field geometry is a result from our model and does not require additional assumptions. The energy absorption processes and the transport of energy along the field lines is less accurate than in *Gan et al.* [1992] because we always assume a Maxwellian distribution function (see Section 4.4). In our model we have put the emphasis on the combination of magnetic field, plasma flow, and magnetospheric electron fluxes, which all influence each other. However, a comparison of the results of the two models is interesting. *Gan et al.* [1992] obtain an upstream electron impact ionization rate from magnetospheric electrons of  $0.3 \text{ cm}^{-3}\text{s}^{-1}$  at an altitude of 1420 km. In the T5 case where the upstream side is equal to the nightside we obtain a production rate of  $0.07 \text{ cm}^{-3}\text{s}^{-1}$  at an altitude of 1670 km which is quite close to their results and therefore is a good validation of our model. On the upstream dayside the ion production from magnetospheric electron impact is negligible because the flux tubes are prevented from entering the atmosphere by the dense photo-ionosphere.

*Galand et al.* [1999] solve the stationary Boltzmann transport equation for the electron flux for two cases. In the first case Titan interacts directly with the solar wind (we do not treat this case). In the second case they assume radial magnetic field line geometry on the nightside. In that case they obtain peak production rates from magnetospheric electrons of  $1 - 5 \text{ cm}^{-3}\text{s}^{-1}$  at an altitude of 550-650 km. In our results a radial field line geometry appears only on the downstream nightside (T34). There we obtain a peak production rate of  $0.1 \text{ cm}^{-3}\text{s}^{-1}$  at an altitude of 1670 km. The difference is due to the history of the field lines in the tail. They have passed the dayside and flank regions of Titan where they already lose some of their energy until they enter the tail region while *Galand et al.* [1999] assume that the electrons on the radially directed field line have the energy of the incident flux tubes.

Basically our ionospheric model passes the comparison with the detailed ionospheric models described above with respect to peak electron density and altitude. Now, we want to compare our model with plasma interaction models.

The first model that described Titan's interaction with the Saturnian magnetospheric plasma was a 1D convection diffusion model by *Ip* [1990]. At that time electron impact ionization was assumed to be the main process for the production of the ionosphere. He included several ion species and chemical reactions in the model. The resulting ionosphere has a peak density of about  $5000 \text{ cm}^{-3}$  at an altitude of 1240 km which is above the altitude of later models including this model. *Ip* [1990] makes two important remarks that are confirmed by our results: He points out that ion-neutral friction plays a crucial role in stopping the ionospheric inflow above the exobase and that the magnetospheric plasma changes the ionospheric content above 2000 km.

The next model was the multi-species 1D MHD model of *Keller et al.* [1994b] for the ram plasma interaction in combination with a hydrodynamic model for the wake interaction [*Keller et al.*, 1994a]. The ionosphere in that model was taken from *Keller et al.* [1992]. The model has been reproduced with some extensions by *Mücke-Herzberg* [1998]. These models show a detailed ionospheric structure and allow the different species to have different velocities. As in the model of *Ip* [1990], the magnetic field drops to zero at about 1000 km altitude. We reproduce this feature that we call magnetic ionopause (MIP) with our 3D model.

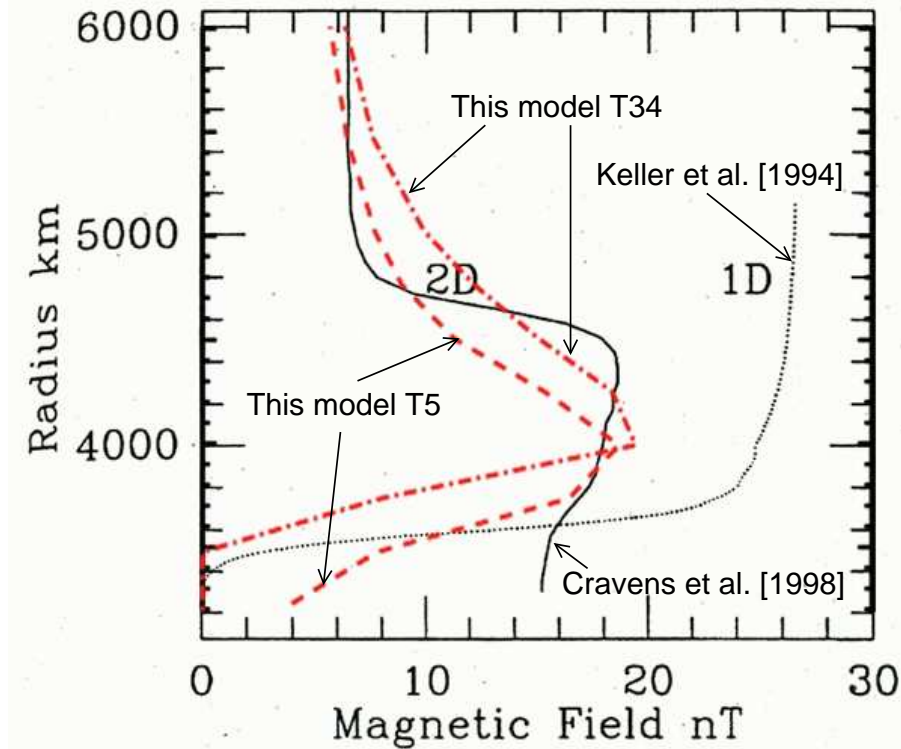


**Figure 5.103:** Magnetic field profiles along the ram direction from the 1D model Keller *et al.* [1994b], the 2D model of Cravens [1998], and our model at T5 and T34 conditions.

The above described 1D models have in common that the incident plasma velocities are of the order of  $\sim 10 \text{ ms}^{-1}$  which is four orders of magnitude lower than the velocity of the magnetospheric plasma at the position of Titan [Neubauer *et al.*, 1984], i.e. they do not describe the transition from the magnetospheric plasma to the ionospheric plasma. Keller *et al.* [1994b] point out that the fact that the ionospheric density profile from the photochemical model of Keller *et al.* [1992] is unchanged by the plasma interaction is artificial in their model. Thus, the statement of Ip [1990] that the density profile above 2,000 km is changed by the interaction remains true which is in accordance with our results.

The first model in more than one spatial dimension is the 2D MHD model of Cravens *et al.* [1998]. In the model three continuity equations are solved, for a light, a medium, and a heavy ion species. But the momentum equation is solved for the bulk velocity only. The smallest grid size in the model is 50 km which is quite high. The incident plasma velocity is assumed to be  $90 \text{ km s}^{-1}$ . Above the altitude of 2000 km the ionospheric density profile is clearly altered by the plasma flow. In Figure 5.103 the magnetic field profile along the upstream direction from the 2D model of Cravens *et al.* [1998] and the 1D model of Keller *et al.* [1994a] is plotted together with our results for the T5 and the T34 case. In contrast to the 1D model the 2D model does not produce a magnetic ionopause. See Section 5.4 for a discussion about the magnetic pile-up in the model of Cravens *et al.* [1998] and our model. The 1D model [Keller *et al.*, 1994a] does not produce magnetic pile-up because of the chosen incident plasma conditions (low- $\beta$ ).

The basic plasma interaction problem is a 3D problem: the flow is 3D, the magnetic field line

draping is 3D, and several processes are 3D effects (for example part of the magnetic pile-up (see Section 5.4)). 1D models have the advantage that they can treat processes very detailed but only along one certain direction. And the solutions are only right if in that direction 3D effects are negligible. Now we switch to the 3D models.

The first 3D model that has been published is the MHD model of *Ledvina and Cravens* [1998] which uses the same basic code that is used in our model: ZEUS 3D. In that model the solid Titan is modeled by a high density plasma region and the ideal MHD equations are solved with an included mass-loading rate in the continuity equation, since it is known [*Ip*, 1990; *Keller et al.*, 1992; *Cravens et al.*, 1998] that mass-loading is much less important than ion-neutral friction. A comparison of the results from our model with the results from *Ledvina and Cravens* [1998] demonstrates the great impact of the neutral atmosphere on the plasma interaction: magnetic field and high plasma velocities reach down to the upstream surface of the solid Titan in their model.

Another 3D MHD model is from *Kabin et al.* [1999]. They have a quite powerful numerical code with adaptive mesh refinement. Our global results agree with their results (Alfvén wings, magnetic barrier,...). But it is difficult to compare the results in more detail. For example it is not clear if they produce a magnetic ionopause or not. Apart from that we do not agree with their model equations.

*Brecht et al.* [2000] have published the first hybrid model for the plasma interaction of Titan. Electrons are treated as fluid and ions as particles. Thus, finite gyroradius effects and the function of the Hall term are not suppressed like in MHD models. Although they do not discuss the subject in the text we suspect that the Hall effect is clearly visible in their results. Following the theory of ion pick-up in the neutral atmosphere of Titan the ions picked up on the Saturnian side are accelerated towards Titan by the convective electric field and are captured by the dense atmosphere. The resulting pick-up ion flux in the tail should be larger on the anti-Saturnian than on the Saturnian side. The inclusion of asymmetric pick-up into a resistive MHD code [*Kopp and Ip*, 2001] fulfills this expectation. The results from the *Brecht et al.* [2000] model show the opposite. The pick-up and the tail flux are stronger on the Saturnian side. We suppose that this is caused by the Hall effect which rotates the electric field in the vicinity of Titan. The shift of the magnetic barrier location towards the anti-Saturnian flank which is visible in their results supports our suspicion. The hybrid code does not include ion-neutral friction which diminishes the Hall effect. Thus, the Hall effect visible in the results is overestimated.

*Nagy et al.* [2001] have included three continuity equations in their 3D MHD model for light, medium, and heavy ions, similar to *Cravens et al.* [1998]. But only one momentum equation is solved. They have included ion-neutral friction into the momentum equation but not into the magnetic induction equation and energy equation, which means that the equations are inconsistent. A comparison with their results is quite difficult because the displayed results in the paper are very global. However, it seems that in their model the magnetic barrier reaches down to the surface of Titan and there is no MIP in the ionosphere. Perhaps this is due to the missing magnetic diffusion in their code.

The latest model of Titan's interaction is a resistive MHD model from *Kopp and Ip* [2001]

where they included asymmetric mass-loading. Above we have discussed the difference of this model's results from the results of the hybrid model of *Brecht et al.* [2000] which we assume is caused by the missing Hall term. They compare the results with symmetric and asymmetric mass-loading. The comparison of our model with the model of *Kopp and Ip* [2001] shows obvious differences e.g. in the ionospheric magnetic field which is due to the fact that they have not included ion-neutral friction into their momentum equation. This is astonishing since one of the authors was the first to point out the importance of ion-neutral friction for the plasma flow around Titan.

In summary our ionospheric model agrees quite well with the model of *Keller et al.* [1992] at altitudes below 1700 km. Above, the ionospheric density profile is altered by the plasma flow. In contrast to all the other multi-dimensional models our model produces an magnetic ionopause layer. The influence of the neutral atmosphere on the plasma interaction of Titan is very important and most of the models neglect this effect or treat it in a too simple way.

The results from the hybrid model of *Brecht et al.* [2000] also neglect ion-neutral collisions. But therefore it demonstrates the possible action of the Hall effect at Titan.

## 5.7 The first close flyby of Cassini at Titan - TA

On 26 October 2004 the Cassini space craft has the first close flyby at Titan. The Saturnian local time (SLT) is 10.6, i.e. Titan is near the magnetopause of the Saturnian magnetosphere or - if the solar wind pressure is high - Titan is in the magnetosheath or solar wind. But, we hope that the most probable case occurs and Titan is in the magnetosphere surrounded by magnetospheric plasma. Then, our model is applicable. In this Section the plasma properties that we expect Cassini to measure along its trajectory from our model are presented and the structures are related to the physical picture of the interaction that has been drawn in the preceding chapters.

The trajectory of the TA flyby is visualized in three dimensions in Figure 5.2. Cassini approaches Titan from the anti-Saturnian flank and from the tail. The direction of motion is in principal towards Saturn with small northbound and upstream velocity components. The velocity vector at closest approach (CA) in the used coordinate system is given by  $(-1.3 \text{ km/s}, 5.7 \text{ km/s}, 1.3 \text{ km/s})$  with an absolute value of  $v = 6 \text{ km/s}$ . This determines the timescale for the flyby  $\tau_{flyby} = 2R_T/v \approx 15 \text{ min}$ . The closest approach altitude is 1200 km. At SLT=10.6 the Sun shines on the anti-Saturnian downstream hemisphere of Titan. The season at Titan is short after southern mid-summer i.e. the south pole is illuminated and the north pole is in darkness.

Figure 5.104 displays electron density, magnetic field magnitude, and absolute value of the plasma bulk velocity along the trajectory through the simulated data. The first signatures in magnetic field data appear about 25 min before CA. At that time there is a simultaneous increase of magnetic field and velocity. Figure 5.105 indicates the increase of magnetic field magnitude is basically an increase of the  $z$ -component without changing the direction of the magnetic field. The entrance of the spacecraft into the ionosphere occurs about 8 minutes be-

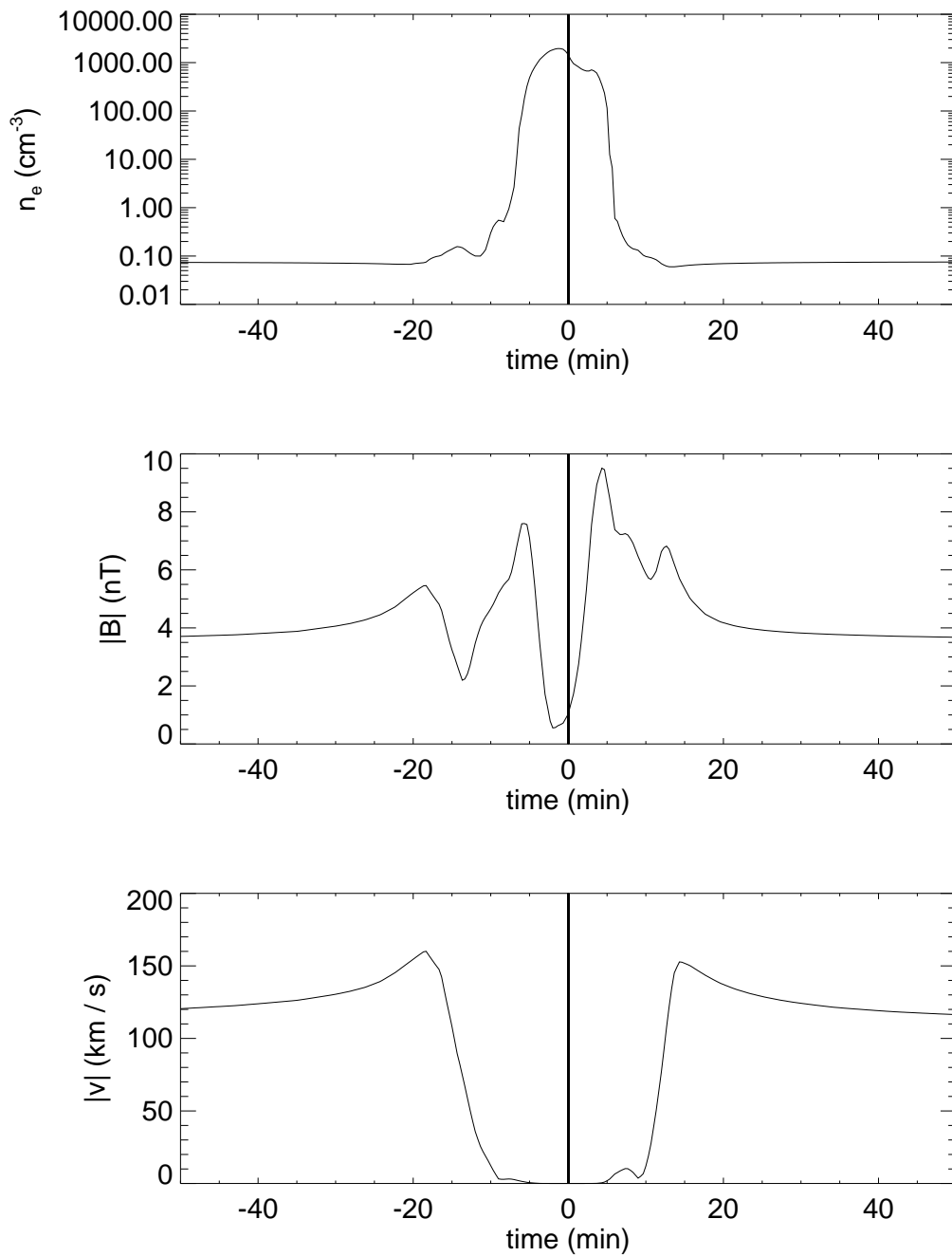


**Figure 5.104:** Electron density, magnetic field magnitude, and absolute value of velocity along the Cassini trajectory from the model for TA.

fore CA. Over a time period of  $\sim 3$  minutes the plasma density increases by about four orders of magnitude. The plasma bulk velocity is very low in that region ( $\sim km/s$ ). Cassini encounters a maximum ionospheric electron density shortly before CA of  $\sim 1900 cm^{-3}$ . About 8 minutes after CA Cassini leaves the ionosphere. In Figure 5.106 the electron density is plotted in the  $xy$ -plane at two different values for  $z$ . Additionally, the projection of the trajectory has been drawn. The asterisk on the trajectory marks the position where the trajectory crosses the displayed plane. Figure 5.106a shows the plane at  $z = 0.8$ . The trajectory crosses the plane at the position where it enters the ionosphere. In Figure 5.106b the trajectory crosses the plane at the exit point of the ionosphere. The plots show that Cassini transits the northern dusk atmosphere of Titan with the direction of flight pointing towards the nightside. Cassini moves from an ionosphere dominated by photoionization to an ionosphere dominated by electron impact ionization. On the one hand this explains why the maximum density is encountered before CA in our model. On the other hand the measured ionospheric electron density profile can tell us how the ionosphere changes from dayside to nightside.

The perturbation of the background electron density sets in about 10 minutes before the entrance into the ionosphere and continues until about 10 minutes after the exit time. These two periods will be very interesting since they provide some information about the pick-up process. The asymmetries in the pick-up will be observable comparing the ion data of the two periods. Apart from that, the time scale for the acceleration process of newly picked up ions can be estimated from the measured ion energies and velocity distributions.

Another interesting aspect is the magnetization of the ionosphere, especially with respect to a comparison of Titan and Venus. The magnetic field profile along the trajectory displays some interesting features (see Figure 5.105). The maxima in the absolute value of  $B_z$  at about 15 minutes before CA and 13 minutes after CA are due to a compression of the plasma at the flanks caused by the flow of the plasma around the obstacle. The maxima of  $B_z$  coincides exactly with the maxima in the plasma bulk velocity. 20 minutes before CA, plasma velocity and absolute value of  $B_z$  decrease simultaneously and 10 minutes after CA they simultaneously increase. These gradients mark the transition from the magnetospheric plasma into the "real" interaction region, i.e. the Alfvén/slow mode region. Inside the time interval from 15 minutes before to 10 minutes after CA the spacecraft will measure perturbations in the absolute value of the magnetic field as well as in all magnetic field components. In order to analyze the magnetic field profile in Figure 5.105 projections of the magnetic field magnitude and vectors on the  $yz$ -plane at different  $x$  positions together with the trajectory are shown in Figure 5.107, 5.108, 5.109, 5.110, and Figure 5.111. The positions where the trajectory crosses the displayed plane are marked by an asterisk. The asterisks have been labeled in order to identify the same locations in Figure 5.105.

At about 15 minutes before CA the magnetic field magnitude has a minimum which is about 50% of the background field. At the same position the magnetic field is rotated: although the space craft is clearly in the northern tube where the draped field lines point in  $-x$ -direction, the magnetic field has a positive  $x$ -component. The reason for the perturbation can be seen in Figure 5.107. The minimum and the positive  $x$ -component are at the position marked by the asterisk. At this point Cassini is quite close to the equatorial plane and crosses the flank current region that has been discussed in Section 5.5.1. Cassini should measure a tail-ward

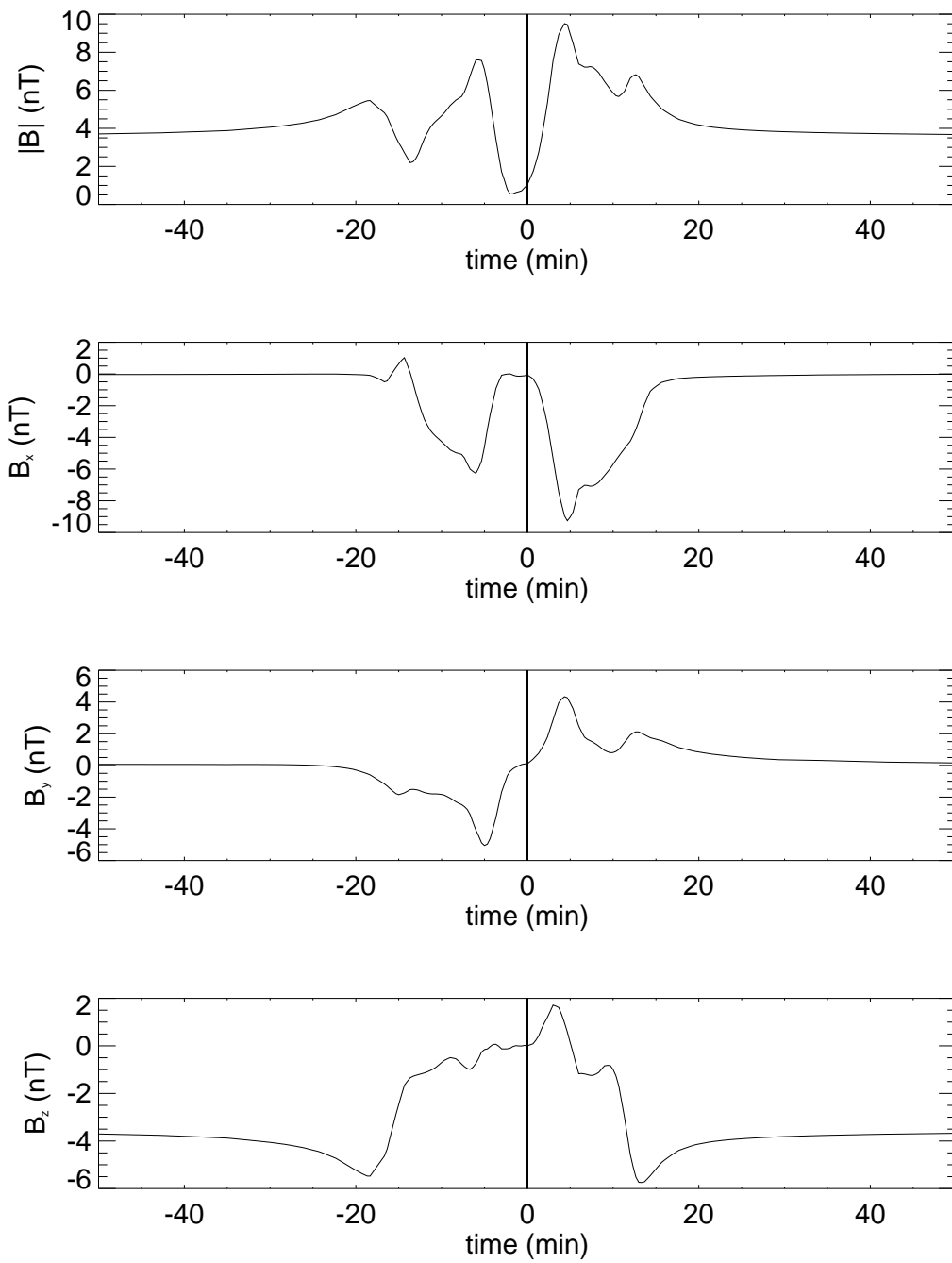
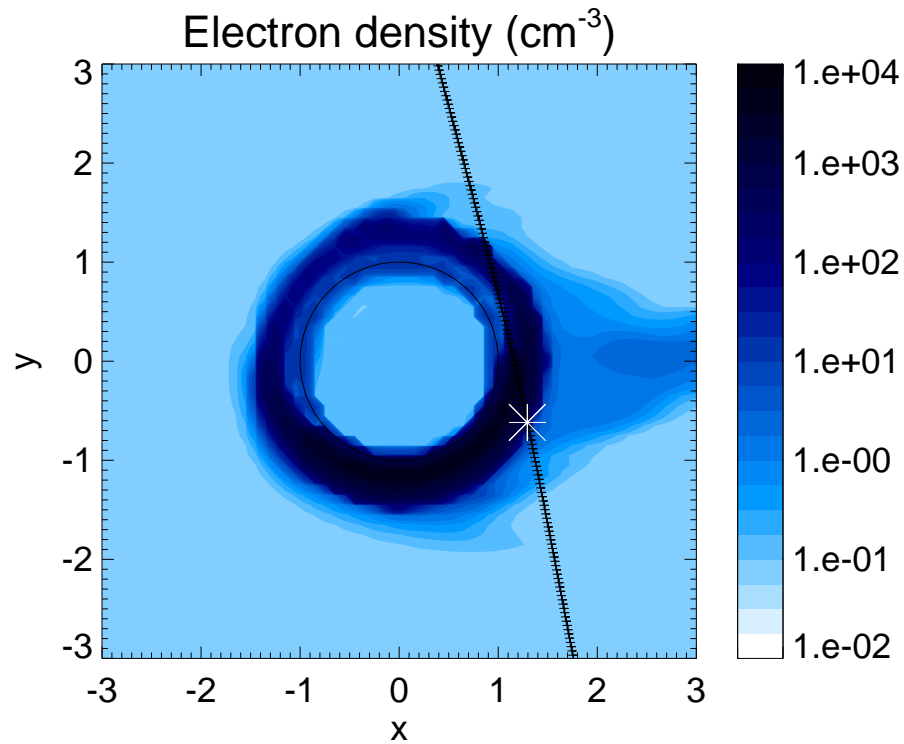
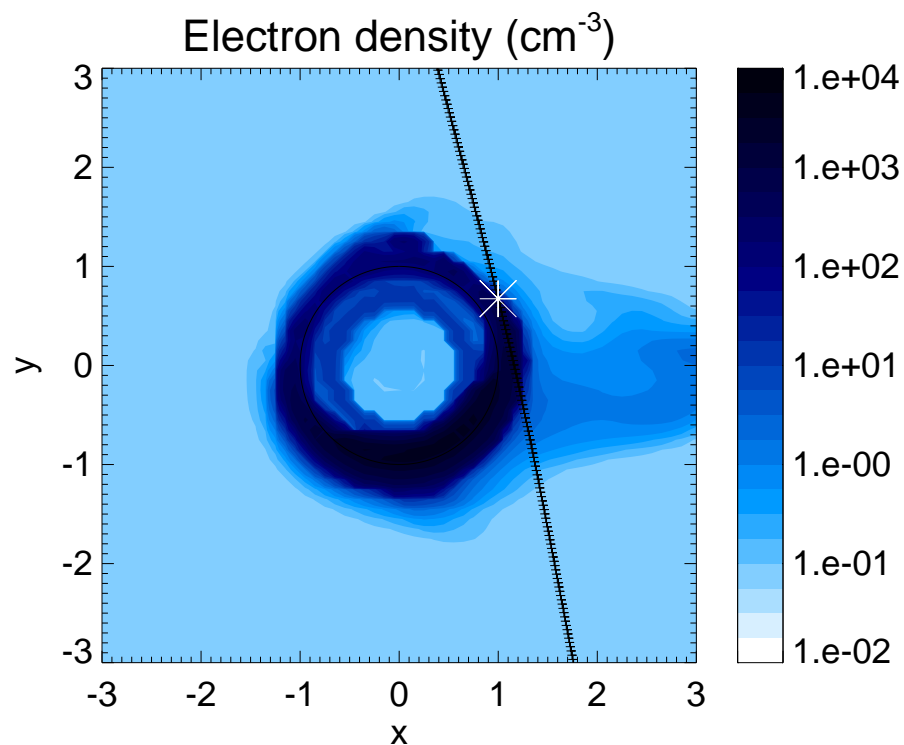


**Figure 5.105:** Magnetic field magnitude and the three magnetic field components along the Cassini trajectory from the model for TA.



(a)



(b)

**Figure 5.106:** Electron number density at  $z = 0.85R_T$  (a) and  $z = 1.05R_T$ . The Cassini trajectory at TA is drawn as a black line. At the asterisk the trajectory intersects the displayed plane.

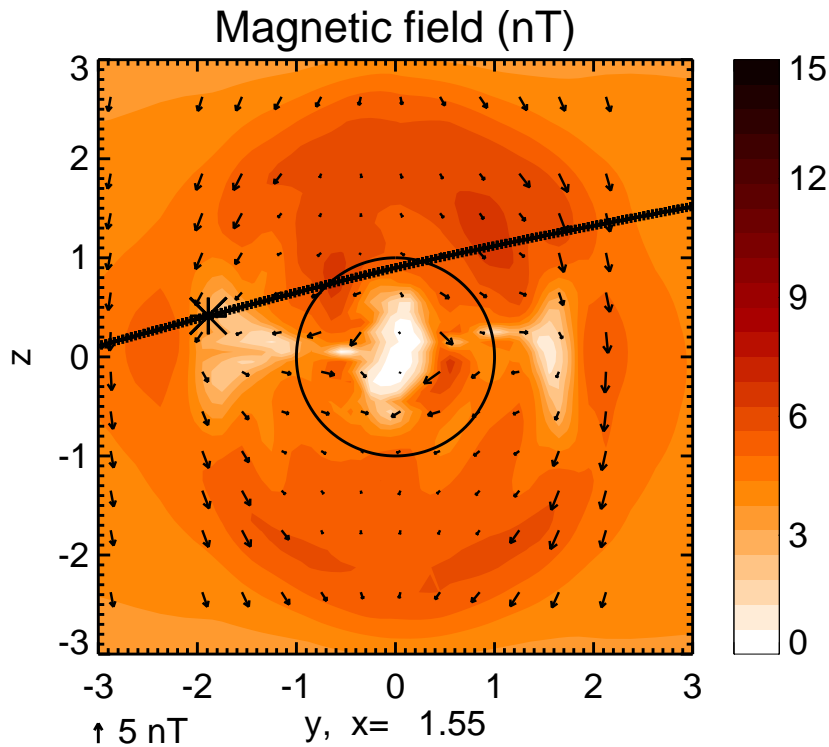


**Figure 5.107:** Magnetic field magnitude and vectors on the  $xz$  plane at  $x = 1.55R_T$ . The Cassini trajectory at TA is drawn as a black line. At the asterisk the trajectory intersects the displayed plane.

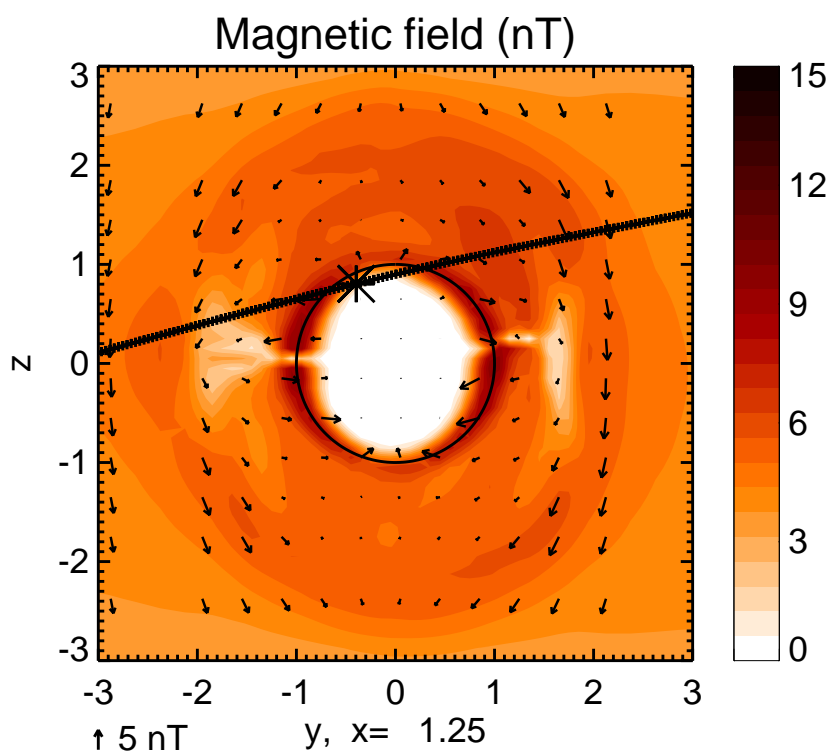


**Figure 5.108:** Magnetic field magnitude and vectors on the  $xz$  plane at  $x = 1.25R_T$ . The Cassini trajectory at TA is drawn as a black line. At the asterisk the trajectory intersects the displayed plane.

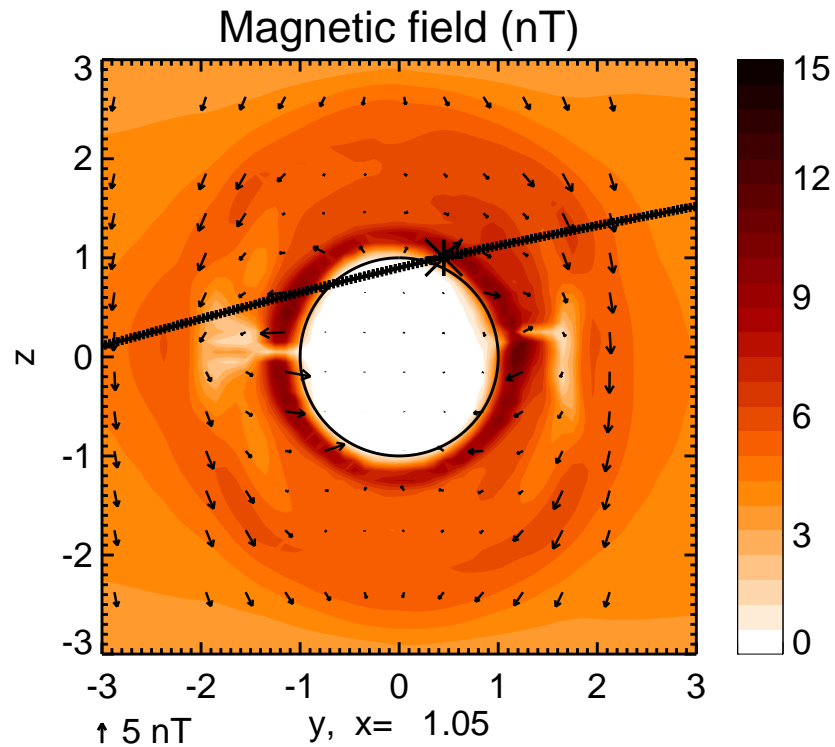


**Figure 5.109:** Magnetic field magnitude and vectors on the  $xz$  plane at  $x = 1.05R_T$ . The Cassini trajectory at TA is drawn as a black line. At the asterisk the trajectory intersects the displayed plane.

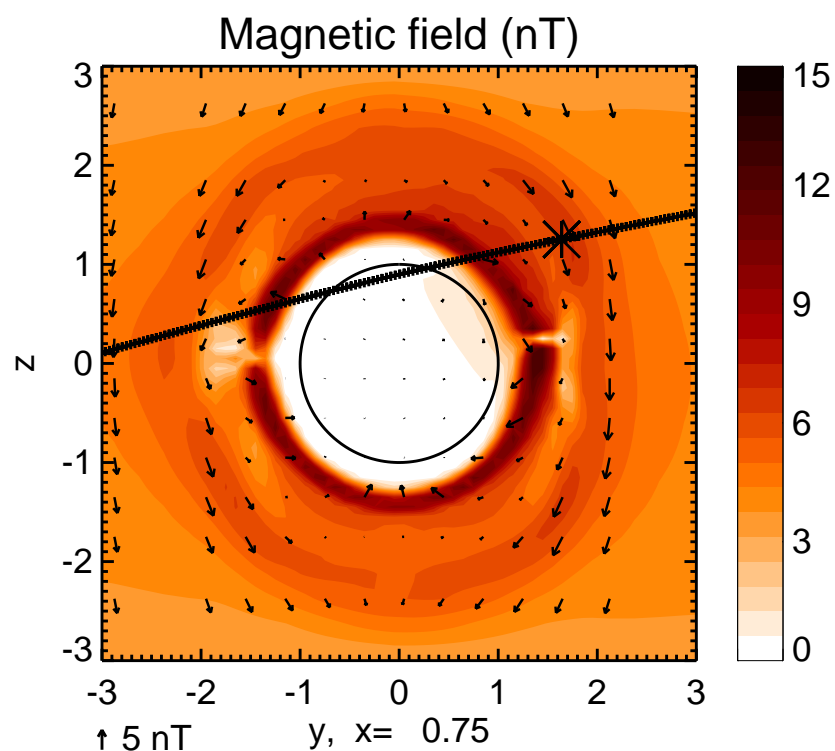


**Figure 5.110:** Magnetic field magnitude and vectors on the  $xz$  plane at  $x = 0.75R_T$ . The Cassini trajectory at TA is drawn as a black line. At the asterisk the trajectory intersects the displayed plane.

directed Alfvén current at that position.

Apart from the just described signature the basic shape of the magnetic field profile is quite symmetric around CA. When Cassini has left the current region it enters the draping region. As expected from the textbook draping picture for the northern tube, the magnetic field points in  $-x$  direction and has a negative  $y$ -component on the anti-Saturnian flank (i.e. inbound) and a positive  $y$ -component on the Saturnian flank (i.e. outbound). Inside of the draping region the magnetic field increases smoothly with decreasing distance to Titan's ionosphere. At about 7 minutes before CA the gradient in the magnetic field steepens and it increases from about the background magnitude to twice the background magnitude within one minute. This region corresponds to the pile-up region or magnetic barrier which even exists in the downstream atmosphere. Inside of the pile-up region the draping is different from outside: the magnetic field has a negative  $y$ -component in the pile-up region on the anti-Saturnian flank (i.e. inbound) and a positive  $y$ -component in the pile-up region on the Saturnian flank (i.e. outbound). In the outbound pile-up region the magnetic field even has a positive  $z$ -component. A comparison of the magnetic profile with the electron density profile in Figure 5.104 shows that the steep gradient at the upper boundary of the magnetic pile-up region coincides with the gradient of ionospheric electron density. At this point Cassini enters (or leaves) the ionosphere. Thus, the pile-up region is clearly inside of Titan's ionosphere.

At about 6 minutes before CA magnetic field magnitude decreases within two minutes to a low value. This corresponds to what we have called the magnetic ionopause (MIP). The inbound crossing of the MIP is marked by an asterisk in Figure 5.108 and Figure 5.111a and the outbound crossing in Figure 5.109 and Figure 5.111b.

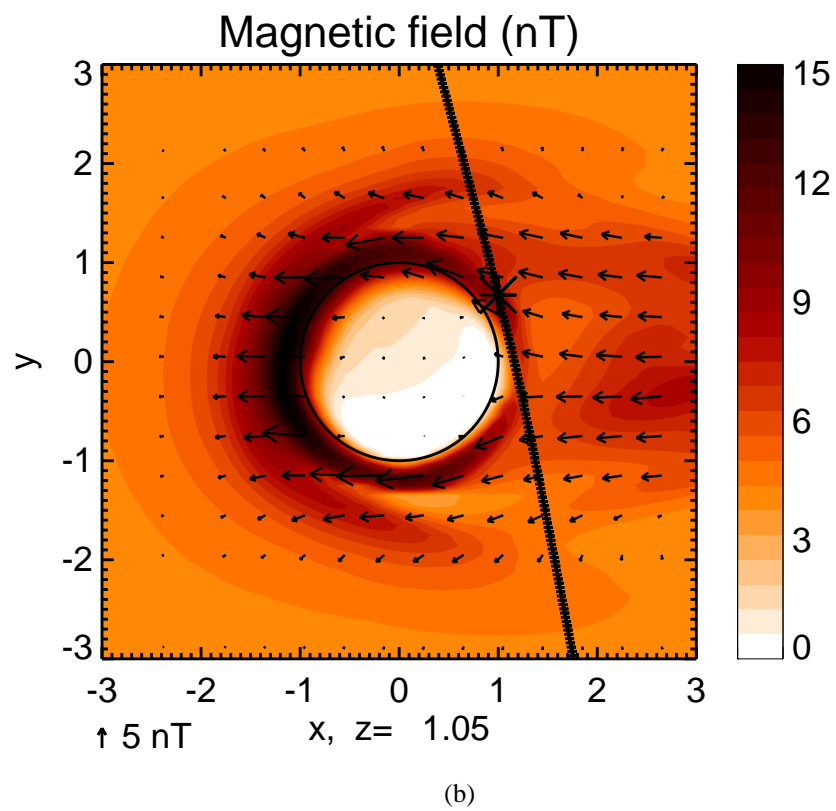
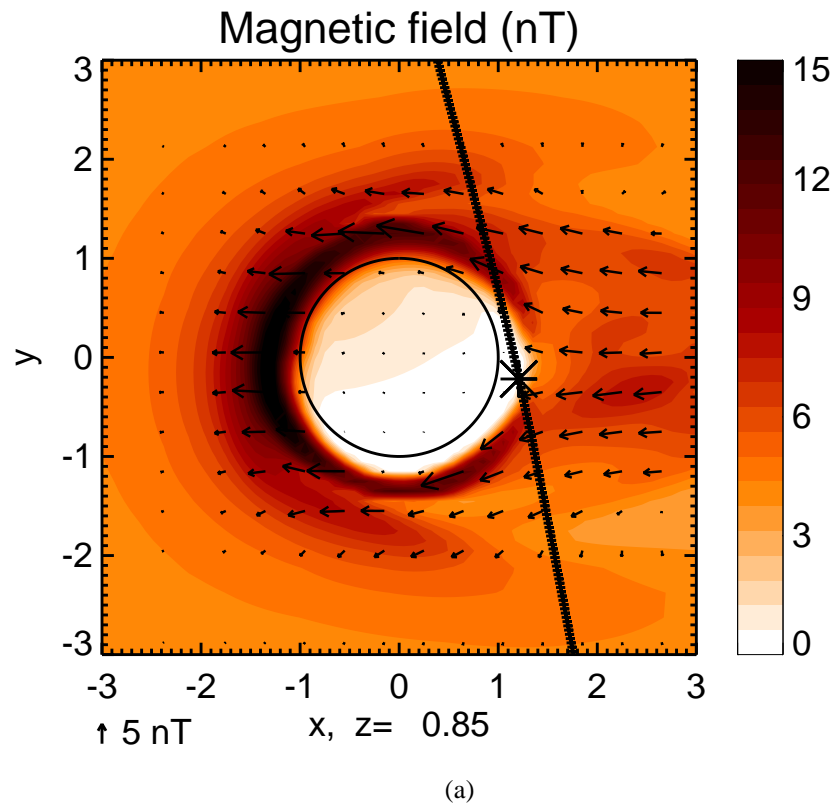


**Figure 5.111:** Magnetic field magnitude and vectors on the  $xy$  plane at different values for  $z$ . The Cassini trajectory at TA is drawn as a black line. At the asterisk the trajectory intersects the displayed plane.



---

## SUMMARY

---

We have developed a model for Titan's interaction with the Saturnian magnetospheric plasma. The ideal MHD model, ZEUS 3D [Stone and Norman, 1992a;b], has been extended in order to include the effect of the neutral atmosphere on the plasma. The neutral in the model atmosphere consists of two neutral species: methane and molecular nitrogen. The distribution is taken from the atmospheric model of Keller *et al.* [1992]; Yung *et al.* [1984]; Yung [1987]. The neutral gas affects the plasma via mass-loading or via collisions. The resulting processes are basically friction, magnetic diffusion, collisional cooling, and Joule heating.

The ionosphere in our model is produced from the neutral atmosphere by photoionization, ionization by photo electrons, and ionization by magnetospheric electrons. Although photoionization is known to be the major source for plasma production at Titan [Keller *et al.*, 1992], at least on the nightside where the solar radiation is absent magnetospheric electrons play the major role for the formation of an ionosphere.

Taking the incident solar EUV flux from the EUVAC model Richards *et al.* [1994], the 3D photoproduction rates are produced from the neutral atmosphere by integrating the flux through the atmosphere along the ray path. We also account effectively for the plasma production due to photoelectrons.

The impact ionization rates by magnetospheric electrons are calculated with the help of a newly developed flux tube model. The grid points in that model move with the plasma and thereby ensure that the electrons are coupled to the magnetic field lines. The temperature equation for the magnetospheric electrons is solved. We have included elastic and inelastic (like ionization) collisions with the neutral gas as well as heat conduction along the magnetic field lines.

Combining the three ionization processes the model produces a 3D ionosphere. An important parameter is the angle between upstream direction and Titan-Sun axis. The parameter can be

freely chosen in the model such that realistic ionospheric situations can be simulated.

The model has been applied to three cases according to situations Cassini will encounter during its flybys TA, T5, and T34. The results cover basically two fields, the ionosphere and the global plasma interaction.

On discrete lines (upstream dayside and upstream nightside) our model ionosphere agrees with the 1D models of *Keller et al.* [1992; 1994b]; *Gan et al.* [1992]. We have found that the upper ionosphere is magnetized while the lower ionosphere is weakly or non-magnetized. We call the layer that separates the two regions magnetic ionopause. The 1D models of *Ip* [1990]; *Keller et al.* [1994b]; *Mücke-Herzberg* [1998] also produce this feature but none of the higher dimensional models do [*Cravens et al.*, 1998; *Ledvina and Cravens*, 1998; *Kabin et al.*, 1999; *Brecht et al.*, 2000; *Nagy et al.*, 2001; *Kopp and Ip*, 2001]. The altitude of the magnetic ionopause strongly depends on Saturnian local time (SLT) and is high on the dayside ( $\sim 1200$  km) and low on the nightside ( $\sim 500$  km).

According to the pressure profile, the plasma in the upstream ionosphere can be divided into three regions. At high altitudes ( $>2500$  km at T34 and  $>2200$  km at T5 conditions) the plasma has a low density and is dominated by the thermal pressure. This is the region of the magnetospheric plasma. In the magnetic pile-up or magnetic barrier region the plasma is dominated by the magnetic pressure. We show that the upper magnetic pile-up is basically achieved by a divergence of the flow parallel to  $\vec{B}$  while in the lower pile-up region collisions play a role. Below the magnetic ionopause the plasma is dominated by collisions with the neutral gas.

From our results we derive an empirical expression for the magnetic field magnitude at the magnetic barrier peak. The magnetic pressure on the upstream point is 99% of the total pressure of the incident plasma. In the equatorial plane 74% decrease towards the flanks with  $\cos^2 \Phi$  while 25% are constant. Along a field line through the barrier peak, the magnetic field magnitude decreases linearly with the path along the field line away from the equatorial plane.

The global plasma interaction produces a southern and a northern Alfvén/slow mode tube. We have divided the plasma into a primary interaction region, which is defined by requiring that outside of this region the plasma is described by the ideal MHD equations, the Alfvén tubes, and the region where the nominal Alfvén tubes intersect each other. The last region has been called nominal intersection region.

We show that the upstream and flank velocity and magnetic field profile outside of the primary interaction region can be described by the decay of the fast mode amplitude. In the tail this is not possible because of the picked-up plasma.

We discuss the electric current system the interaction generates in the plasma. The currents in the primary interaction region are split into their contributions from diamagnetic, inertial, and atmospheric currents. The upper boundary of the magnetic barrier is accompanied by diamagnetic currents while in the lower boundary (in the magnetic ionopause) atmospheric currents shield the lower ionosphere from the external magnetic field.

The splitting of the currents that are associated with the Alfvén tube in currents that flow par-

allel to the characteristics and perpendicular currents indicates that, like in the sub-Alfvénic flow, they fulfill divergence zero separately. From our model we determine an Alfvén current of  $3 \times 10^4$  A through one half Alfvén tube two orders of magnitude less than at Io.

In the last chapter the results from our TA model are displayed along the Cassini trajectory. The flyby will be through the northern wake region. From our results we conclude that Cassini will enter the ionosphere and encounter electron densities above  $1000 \text{ cm}^{-3}$ . It will cross the magnetic ionopause twice (inbound and outbound). The MAG instrument on-board will measure a decrease (increase) of the magnetic field by more than a factor of three within two minutes.

Even if Cassini will not encounter our predicted plasma and magnetic field environment (and most probably it will not!) our model can be regarded as an instructive model for the basic understanding of the super-Alfvénic plasma interaction of a body with an extended neutral atmosphere.



---

## CALCULATIONS

---

### A.1 Decay of fast mode

When sonic and Alfvénic speed are approximately equal the phase surfaces of the fast mode can be approximated by spheres. The total energy density on a phase surface is constant. Therefore, the energy density of a propagating fast mode decays with  $r^{-2}$  and the amplitude which is the square root of the energy density decays with  $r^{-1}$ .

If the signal propagates into a moving plasma, the propagation velocity in the rest frame of the source depends on the direction of propagation (see Figure A.1).

Now, we want to calculate the amplitude of the fast mode in the rest frame of the source in upstream direction of the plasma and perpendicular to the plasma motion direction.

The propagation velocity of the fast mode is  $c_f$ , and the flow velocity is  $v$  (see velocity diagram in Figure A.1).

In the rest frame of the plasma the signal propagates omni-directional with  $c_f$ . Then, the distance of the signal to the source increases with time

$$r(t) = c_f t. \tag{A.1}$$

As the signal spreads the amplitude decreases with time as

$$A(t) = \frac{A_0 r_0}{c_f t + r_0} \tag{A.2}$$

where  $A_0$  is the amplitude at distance  $r_0$  from the source.

In the rest frame of the source the propagation velocity along a certain direction away from the source is constant  $v_r$ . Then, it takes a signal to propagate from position  $r_0$  to position  $r$

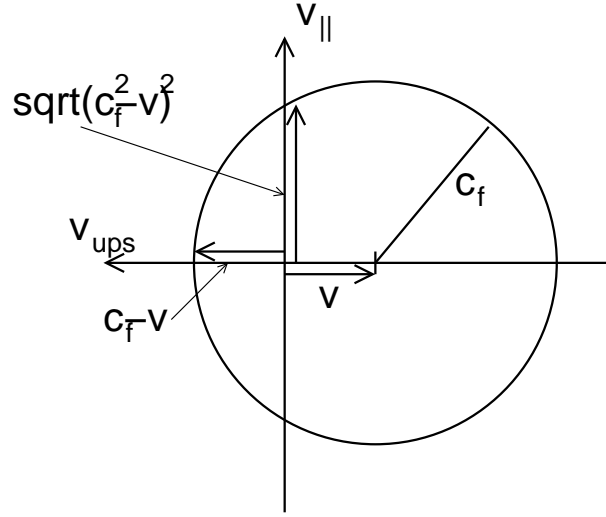


**Figure A.1:** Decay of the amplitude of a fast MHD wave in a plasma at rest (a) and a moving plasma (b).

along that direction

$$t(r) = \frac{r - r_0}{v_r}. \quad (\text{A.3})$$

According to Eq. A.2 the amplitude of the signal has decreased in that time and the amplitude at position  $r$  is given by

$$A(r) = A(t(r)) = \frac{A_0 r_0}{\frac{c_f}{v_r}(r - r_0) + r_0} \quad (\text{A.4})$$

The velocity in upstream direction is  $v_{ups} = c_f - v$ . Substituting this into Eq. (A.4) we obtain

$$A(y) = \frac{A_0 x_0}{\frac{1}{1 - M_f}(x - x_0) + x_0} \quad (\text{A.5})$$

with the fast Mach number  $M_f = v/c_f$ . The velocity parallel to the plasma flow is  $v_{||} = \sqrt{c_f^2 - v^2}$  which is together with Eq. (A.4)

$$A(y) = \frac{A_0 y_0}{\frac{1}{\sqrt{1 - M_f}}(y - y_0) + y_0}. \quad (\text{A.6})$$

## A.2 The thermal conductivity of supra-thermal electrons

In this Section we derive the expression for the thermal conductivity (Eq. (4.52)). The electron thermal conductivity for a partially ionized plasma is given by [Banks and Kockarts, 1973b]

$$\kappa = \frac{7.7 \times 10^5 T_e^{2.5}}{1 + 3.22 \times 10^4 T_e^2 / n_e \sum_n \bar{\sigma}_{en} n_n} \left[ \frac{\text{eV}}{\text{cm s K}} \right]. \quad (\text{A.7})$$

It depends on the temperature and density of the heat conducting electrons and the neutral gas density. Heat conduction from the magnetosphere into the ionosphere is achieved by the

supra-thermal magnetospheric electrons. When they enter the ionosphere where the cooler electron species is present, the influence of the thermal plasma on the thermal conductivity of the supra-thermal electrons has to be taken into account in Eq. (A.7). Treating the thermal plasma in analogy to the neutral gas leads to the following expression for the thermal conductivity

$$\kappa = \frac{7.7 \times 10^5 T_e^{2.5}}{1 + 3.22 \times 10^4 T_e^2 / n_e (\sum_n \bar{\sigma}_{en} n_n + \bar{\sigma}_{eeth} n_{eeth} + \bar{\sigma}_{eith} n_{eith})} \left[ \frac{\text{eV}}{\text{cm s K}} \right]. \quad (\text{A.8})$$

where  $\bar{\sigma}_{eeth}$ ,  $\bar{\sigma}_{eith}$  denote the Maxwell average elastic momentum transfer cross sections of supra-thermal (ms-) electrons with thermal electrons and thermal ions, and  $n_{eeth}$ ,  $n_{eith}$  are the appropriate densities.

The momentum transfer cross section for Coulomb interaction is given by [Schunk and Nagy, 2000]

$$Q_{st}(g_{st}) = 4\pi \left( \frac{e^2}{4\pi\epsilon_0\mu_{st}g_{st}^2} \right)^2 \ln \Lambda \quad (\text{A.9})$$

with  $g_{st} = |\vec{v}_s - \vec{v}_t|$  the velocity difference of particle  $s$  and  $t$ ,  $\mu_{st}$  the reduced mass, and  $\ln \Lambda$  the Coulomb logarithm ( $\Lambda = 9N_{\lambda_D}$ ). The Maxwellian average is calculated by integrating the cross section weighted with the distribution function

$$\bar{\sigma}_{st} = \frac{1}{c^6} \int_0^\infty dg_{st} g_{st}^5 Q_{st}(g_{st}) e^{-g^2/c^2} \quad (\text{A.10})$$

with  $c^2 = 2k(T_s/m_s + T_t/m_t)$ . Solving the integral leads to the result

$$\bar{\sigma}_{st} = 2\pi \left( \frac{e^2}{4\pi\epsilon_0\mu_{st}} \right)^2 \ln \Lambda \frac{1}{(2k(T_s/m_s + T_t/m_t))^2}. \quad (\text{A.11})$$

Inserting the appropriate masses and temperatures by assuming that the supra-thermal temperature is much larger than the thermal temperature and claiming quasi-neutrality for the plasma ( $n_{eith} = n_{eeth}$ ) we get as the final result for the average cross sections

$$\bar{\sigma}_{eeth} = 2\pi \left( \frac{e^2}{4\pi\epsilon_0} \right)^2 \ln \Lambda \frac{1}{(kT_e)^2} \quad (\text{A.12})$$

$$\bar{\sigma}_{eith} = \frac{1}{4} \bar{\sigma}_{eeth} \quad (\text{A.13})$$

$$n_{eith} \bar{\sigma}_{eith} + n_{eeth} \bar{\sigma}_{eeth} = \frac{5}{4} n_{eeth} \bar{\sigma}_{eeth}. \quad (\text{A.14})$$

Substituting this into Eq. (A.8) leads to the thermal conductivity for the supra-thermal electrons

$$\kappa = \frac{7.7 \times 10^5 T_e^{2.5}}{1 + 3.22 \times 10^4 T_e^2 / n_e (\sum_n \bar{\sigma}_{en} n_n + \frac{5}{4} \bar{\sigma}_{eeth} n_{eeth})} \left[ \frac{\text{eV}}{\text{cm s K}} \right]. \quad (\text{A.15})$$

For practical purposes it is useful to write the average cross sections as numerical expressions

$$\bar{\sigma}_{en} = (2.82 - 3.41 \times 10^{-4} T_e) T_e^{1/2} \times 10^{-17} [\text{cm}^2] \quad (\text{A.16})$$

$$\bar{\sigma}_{eeth} = 3.5 \times 10^{-5} \frac{\ln \Lambda}{T_e^2} [\text{cm}^2] \quad (\text{A.17})$$

(The expression for  $\bar{\sigma}_{en}$  for  $N_2$  is taken from *Banks and Kockarts [1973a]*.)

Now we have to show that the assumption that the supra-thermal electrons alone are responsible for the heat conduction is justified. This is the case when for the supra-thermal (magnetospheric) electrons the exchange of energy with the thermal electrons is negligible compared to heat conduction. Therefore, we have to show that the heat conduction for the supra-thermal electrons

$$HC = \frac{\partial}{\partial l} \kappa \frac{\partial T_e}{\partial l} \quad (\text{A.18})$$

is larger than the rate of heat exchange with the thermal electrons given by *Banks and Kockarts [1973b]*

$$HE = n_e n_{th} \tilde{\nu}_{eeth} k (T_e - T_{eth}). \quad (\text{A.19})$$

In the following, we estimate the orders of magnitude of  $HC$  (Eq. (A.18)) and  $HE$  (Eq. (A.19)). The neutral gas affects both, the supra-thermal and the thermal electrons. Where the neutral gas becomes effective in Eq. (A.15), it suppresses heat conduction. Therefore we neglect the neutral gas influence in the following considerations. Inserting Eq. (A.17) in Eq. (A.15), Eq. (A.18) reduces to ( $\ln \Lambda \sim 10$ , a value of 10 is appropriate for typical conditions in Titan's ionosphere)

$$HC = 5 \times 10^4 \frac{n_e}{n_{eth}} \frac{T_e^{7/2}}{L^2} \left[ \frac{\text{eV}}{\text{cm}^3 \text{s}} \right]. \quad (\text{A.20})$$

$n_e$ ,  $n_{eeth}$  are in  $\text{cm}^{-3}$  and  $T_e$  is in K.  $L$  is the scale for the heat conduction in cm. The momentum transfer collision rate  $\tilde{\nu}_{eeth}$  is given by [*Cravens, 1997*]

$$\tilde{\nu}_{eeth} = \frac{n_e e^4 \ln \Lambda}{16 \sqrt{2\pi} \epsilon_0^2 \sqrt{m_e} (kT_e)^{3/2}} \quad (\text{A.21})$$

Using this we can express the heat exchange term (Eq. (A.19)) as

$$HE = n_e n_{eth} 2.6 \times 10^{-3} \frac{1}{\sqrt{T_e}} \left[ \frac{\text{eV}}{\text{cm}^3 \text{s}} \right]. \quad (\text{A.22})$$

In order to fulfill the claimed situation that heat exchange is negligible there must be  $HE/HC \ll 1$  which introduces an upper bound for the scale of the heat conduction:

$$L \ll 4 \times 10^{-2} \frac{T_e^2}{n_{eth}} [\text{km}]. \quad (\text{A.23})$$

The lowest bound for the scale is reached at the ionospheric peak and at low temperatures. Taking a peak density of  $2000 \text{ cm}^{-3}$  and a temperature of 200 K the scale is bound to  $L \ll 0.8$  km. The very low bound for the scale implies that our assumptions are not valid in this case. Two remarks about that: First, the temperature of 200 K is only reached in regions where the neutral gas density is very high and the heat exchange with the neutral gas dominates the heat equation. Second, at a temperature of 200 K there is no temperature difference between the thermal and the supra-thermal electrons and therefore no heat exchange. This implies neither  $HC$  (Eq. (A.18)) nor  $HE$  (Eq. (A.19)) play a role and the supra-thermal electron temperature is determined by interaction with the neutral gas.

Taking the electron temperature in orders of  $\text{eV} \sim 1 \times 10^4$  K at a density of  $1000 \text{ cm}^{-3}$  leads to  $L \ll 4000 \text{ km} > R_T$ . This condition is satisfied because inside the atmosphere the scales are

determined by atmospheric scales which are an order of magnitude lower than a Titan radius. Outside of the atmosphere the thermal electron density decreases rapidly and temperature increases, both effects lead to a rapid increase of the upper bound of the scale. Thus, the assumption that heat is primarily transported by the magnetospheric electrons is justified.



---

## Bibliography

---

- Acuña, M. H. and N. F. Ness**, The magnetic field of Saturn: Pioneer 11 observations, *Science*, 207, 444–446, 1980.
- Alfvén, H.**, On the theory of comet tails, *Tellus*, IX, 92–97, 1957.
- Atreya, S. K.**, *Atmospheres and Ionospheres of the Outer Planets and their Satellites*, Springer, New York, 1986.
- Banks, P. M. and G. Kockarts**, *Aeronomy*, Vol. A, Academic Press, San Diego, Calif., 1973a.
- Banks, P. M. and G. Kockarts**, *Aeronomy*, Vol. B, Academic Press, San Diego, Calif., 1973b.
- Bauer, S. J.**, The upper atmosphere of Titan, in *The Atmospheres of Saturn and Titan*, ESA SP-241, 125–128, 1985.
- Bauer, S. J.**, Titan's ionosphere and atmospheric evolution, *Adv. Space Res.*, 7, (5), (5)65–(5)69, 1987.
- Baumjohann, W. and R. A. Treumann**, *Basic Space Plasma Physics*, Imperial College Press, London, 1996.
- Bertaux, J.-L. and G. Kockarts**, Distribution of molecular hydrogen in the atmosphere of Titan, *J. Geophys. Res.*, 88, (A11), 8716–8720, 1983.
- Biermann, L., B. Brosowski and H. U. Schmidt**, The interaction of the solar wind with a comet, *Sol. Physics*, 1, 254–283, 1967.
- Bird, M. K., R. Dutta-Roy, S. W. Asmar and T. A. Rebold**, Detection of Titan's ionosphere from Voyager 1 radio occultation observations, *Icarus*, 130, 426–436, 1997.

- Blanc, M., S. Bolton, J. Bradley, M. Burton, T. E. Cravens, I. Dandouras, M. K. Dougherty, M. C. Festou, J. Feynman, R. E. Johnson, T. G. Gombosi, W. S. Kurth, P. C. Liewer, B. H. Mauk, S. Maurice, D. Mitchell, F. M. Neubauer, J. D. Richardson, D. E. Shemansky, E. C. Sittler, B. T. Tsurutani, P. Zarka, L. W. Esposito, E. Grün, D. A. Gurnett, A. J. Kliore, S. M. Krimigis, D. Southwood, J. H. Waite and D. T. Young**, Magnetospheric and plasma science with Cassini-Huygens, *Space Sci. Rev.*, *104*, 253–346, 2002.
- Boyd, T. J. M. and J. J. Sanderson**, *Plasma Dynamics*, Barnes and Noble, New York, 1969.
- Brace, L. H. and A. J. Kliore**, The structure of the Venus ionosphere, *Space Sci. Rev.*, *55*, 81–163, 1991.
- Brace, L. H., R. C. Elphic, S. A. Curtis and C. T. Russel**, Wave structure in the Venus ionosphere downstream of the terminator, *Geophys. Res. Lett.*, *10*, 1116–1119, 1982.
- Brace, L. H., H. A. T. Jr, T. I. Gombosi, A. J. Kliore, W. C. Knudsen and A. F. Nagy**, The ionosphere of Venus: Observations and their interpretations, in *Venus*, edited by D. M. Hunten, L. Colin, T. M. Donahue, and V. I. Moroz, 779, Univ. of Ariz. Press, Tucson, 1983.
- Brecht, S. H., J. G. Luhmann and D. J. Larson**, Simulation of the saturnian magnetospheric interaction with Titan, *J. Geophys. Res.*, *105*, 13119, 2000.
- Bridge, H. S., J. W. Belcher, A. S. Lazarus, S. Olbert, J. D. Sullivan, F. Bagenal, P. R. Gazis, R. E. Hartle, K. W. Ogilvie, J. D. Scudder, E. C. Sittler, A. Eviatar, G. L. Siscoe, C. K. Goertz and V. M. Vasyliunas**, Plasma observations near Saturn - Initial results from Voyager 1, *Science*, *212*, 217–224, 1981.
- Broadfoot, A. L., B. R. Sandel, D. E. Shemansky, J. B. Holberg, G. R. Smith, D. F. Strobel, J. C. McConnell, S. Kumar, D. M. Hunten, S. K. Atreya, T. M. Donahue, H. W. Moos, J. L. Bertaux, J. E. Blamont, R. B. Pumphrey and S. Linick**, Extreme ultraviolet observations from Voyager 1 encounters with Saturn, *Science*, *212*, (4491), 206–211, 1981.
- Brown, M. E., A. H. Bouchez and C. A. Griffith**, Direct detection of variable tropospheric clouds near Titan's south pole, *Nature*, *420*, 795–797, 2002.
- Capone, L. A., R. C. Whitten, J. Dubach, S. S. Prasad and W. T. Huntress**, The lower ionosphere of Titan, *Icarus*, *28*, 367, 1976.
- Capone, L. A., J. Dubach, R. C. Whitten, S. S. Prasad and K. Santhanam**, Cosmic ray synthesis of organic molecules in Titan's atmosphere, *Icarus*, *44*, 72–84, 1980.
- Capone, L. A., S. S. Prasad, W. T. Huntress, R. C. Whitten, J. Dubach and K. Santhanam**, Formation of organic molecules on Titan, *Nature*, *293*, 45–46, 1981.
- Capone, L. A., J. Dubach, S. S. Prasad and R. C. Whitten**, Galactive cosmic rays and N<sub>2</sub> dissociation on Titan, *Icarus*, *55*, 73–82, 1983.

- Clarke, J. T. et al.**, Far-ultraviolet imaging of Jupiter's aurora and the Io "Footprint", *Science*, 274, (5286), 404–409, 1996.
- Comas Sola, J.**, Observations des satellites principaux de Jupiter et de Titan, *Astron. Nachr.*, 179:289, 1908.
- Connerney, J. E. P., R. Baron, T. Satoh and T. Owen**, Images of excited  $H_3^+$  at the foot of the Io flux tube in Jupiter's atmosphere, *Science*, 262, (5316), 1035–1038, 1993.
- Cravens, T. E.**, *Physics of Solar System Plasmas*, Cambridge Univ. Press, Cambridge, 1997.
- Cravens, T. E. and H. Shinagawa**, The ionopause current layer at Venus, *J. Geophys. Res.*, 96, (A7), 11119–11131, 1991.
- Cravens, T. E., H. Shinagawa and A. F. Nagy**, The evolution of large-scale magnetic fields in the ionosphere of Venus, *Geophys. Res. Lett.*, 11, (3), 267–270, 1984.
- Cravens, T. E., C. J. Lindgren and S. A. Ledvina**, A two-dimensional multifluid MHD model of Titan's plasma environment, *Planet. Space Sci.*, 46, 1193–1205, 1998.
- Eviatar, A. and J. D. Richardson**, Corotation of the Kronian magnetosphere, *J. Geophys. Res.*, 91, (A3), 3299–3303, 1986.
- Eviatar, A., G. L. Siscoe, J. D. Scudder, E. C. Sittler Jr. and J. D. Sullivan**, The plumes of Titan, *J. Geophys. Res.*, 87, (A10), 8091–8103, 1982.
- Fox, J. L.; Yelle, R. V.**, Hydrocarbon ions in the ionosphere of Titan, *Geophys. Res. Lett.*, 24, 2179, 1997.
- Friedson, A. J. and Y. L. Yung**, The thermosphere of Titan, *J. Geophys. Res.*, 89, 85–90, 1984.
- Galand, M., J. Lilensten, D. Toublanc and S. Maurice**, The ionosphere of Titan: ideal diurnal and nocturnal cases, *Icarus*, 140, 92, 1999.
- Gan, L. and T. E. Cravens**, Electron energetics in the inner coma of comet Halley, *J. Geophys. Res.*, 95, (A5), 6285–6303, 1990.
- Gan, L. and T. E. Cravens**, Electron impact cross-sections and cooling rates for methane, *Planet. Space Sci.*, 40, (11), 1535–1544, 1992.
- Gan, L., C. N. Keller and T. E. Cravens**, Electrons in the ionosphere of Titan, *J. Geophys. Res.*, 97, (A8), 12137–12151, 1992.
- Gan, L., T. E. Cravens and C. N. Keller**, A time-dependent model of suprathermal electrons at Titan, in *Plasma Environments of Non-Magnetic Planets*, edited by T. I. Gombosi, Vol. 4 of *COSPAR Colloquia*, 171–176, Pergamon Press, 1993.
- Giampieri, G. and M. K. Dougherty**, Rotation rate of Saturn's interior from magnetic field observations, *Geophys. Res. Lett.*, 31, CiteID L16701, 2004.

- Gibbard, S. et al.**, Titan: High-resolution speckle image from the Keck Telescope, *Icarus*, 139, 189–201, 1999.
- Gurnett, D. A., F. L. Scarf and W. S. Kurth**, The structure of Titan's wake from plasma wake observations., *J. Geophys. Res.*, 87, 1395–1403, 1982.
- Hanel, R., B. J. Conrad, F. M. Flasar, V. G. Kunde, W. Magcière, J. C. Pearl, J. A. Pirraslia, L. Horn, R. Koppany and C. Pornamperuma**, Infrared observations of the Saturnian system from Voyager 1, *Science*, 212, 192–200, 1981.
- Hartle, R. E., E. C. Sittler, K. W. Ogilvie, J. D. Scudder, A. J. Lazarus and S. K. Atreya**, Titan's ion exosphere observed from Voyager 1, *J. Geophys. Res.*, 87, (A3), 1383–1394, 1982.
- Hill, T. W.**, Inertial limit on corotation, *J. Geophys. Res.*, 84, (A11), 6554–6558, 1979.
- Huba, J. D.**, Hall Magnetohydrodynamics - A tutorial space plasma simulation , *Edited by J. Büchner, C. Dum, and M. Scholer, Lecture Notes in Physics*, 615, 166–192, 2003.
- Huebner, W. F.**, The photochemistry of comets, in *The Photochemistry of Atmospheres*, edited by J. S. Levine, Chapter 9 + Appendix I, 437–481, Academic Press, 1985.
- Hunten, D. M., M. G. Tomasko, F. M. Flasar, R. E. Samuelson, D. F. Strobel and D. J. Stevenson**, Titan, in *Saturn*, edited by T. Gehrels and M. S. Matthews, 671–759, Univ. of Ariz. Press, Tucson, 1984.
- Ip, W.-H.**, Titan's upper ionosphere, *Astrophys. J.*, 362, 354–363, 1990.
- Kabin, K., T. I. Gombosi, D. L. D. Zeeuw, K. G. Powell and P. L. Israelevich**, Interaction of the Saturnian magnetosphere with Titan: results of a three-dimensional MHD simulation, *J. Geophys. Res.*, 104, 2451, 1999.
- Keller, C. N.**, *One-dimensional multispecies magnetohydrodynamic models of the ionosphere of Titan and the inner coma of comet P/Halley*, Dissertation, University of Kansas, 1992.
- Keller, C. N., T. E. Cravens and L. Gan**, A model of the ionosphere of Titan, *J. Geophys. Res.*, 97, (A8), 12117–12135, 1992.
- Keller, C. N., T. E. Cravens and L. Gan**, One-dimensional multispecies hydrodynamic models of the wakeside ionosphere of Titan, *J. Geophys. Res.*, 99, (A4), 6527–6536, 1994a.
- Keller, C. N., T. E. Cravens and L. Gan**, One-dimensional multispecies magnetohydrodynamic models of the ramside ionosphere of Titan, *J. Geophys. Res.*, 99, (A4), 6511–6525, 1994b.
- Keller, C. N., A. V. G. and C. T. E.**, Model of Titan's ionosphere with detailed hydrocarbon ion chemistry, *Planet. Space Sci.*, 46, 1157–1174, 1998.
- Kim, Y.-K., K. K. Inikura, M. E. Rudd, M. A. Ali and P. M. Stone**, Electron-Impact ionization cross sections, 1997.

- Kivelson, M. G. and C. T. Russel**, The interaction of flowing plasmas with planetary ionospheres: A Titan-Venus comparison, *J. Geophys. Res.*, 88, 49, 1983.
- Kopp, A. and W.-H. Ip**, Asymmetric mass loading effect at Titan's ionosphere, *J. Geophys. Res.*, 106, 8323, 2001.
- Kuiper, G. P.**, A satellite with an atmosphere, *Astrophys. J.*, 100, 378–383, 1944.
- Lara, L. M., E. Lellouch, J. J. López-Moreno and R. Rodrigo**, Vertical distribution of Titan's atmospheric neutral constituents, *J. Geophys. Res.*, 101, (E10), 23261–23283, 1996.
- Ledvina, S. A. and T. E. Cravens**, A three-dimensional MHD model of plasma flow around Titan, *Planet. Space Sci.*, 46, 1175–1191, 1998.
- Ledvina, S. A., T. E. Cravens, A. Salman and K. Kecskemety**, Ion Trajectories in Saturn's Magnetosphere Near Titan, *Adv. Space Res.*, 26, 1691–1695, 2000.
- Lindal, G. F., G. E. Wood, H. B. Hotz, D. N. Sweetnam, V. R. Eshleman and G. L. Tyler**, The atmosphere of Titan: An analysis of the Voyager 1 radio occultation measurement, *Icarus*, 53, 348–363, 1983.
- Luhmann, J. G., R. C. Elphic, C. T. Russell, J. D. Mihalov and J. H. Wolfe**, Observations of large scale steady magnetic fields in the dayside Venus ionosphere, *J. Geophys. Res.*, 7, 917–920, 1980.
- Lunine, J. I., D. J. Stevenson and Y. L. Yung**, Ethane ocean on Titan, 2, *Science*, 222, 1229, 1983.
- Mahajan, K. K., H. G. Mayer and L. H. Brace**, On the lower altitude limit of the Venusian ionopause, *Geophys. Res. Lett.*, 16, 759–762, 1989.
- McNutt Jr., R. L. and J. D. Richardson**, Constraints on Titan's ionosphere, *Geophys. Res. Lett.*, 15, (7), 709–712, 1988.
- McNutt Jr., R. L., J. W. Belcher, J. D. Sullivan, F. Bagenal and H. S. Bridge**, Departure from rigid co-rotation of plasma in Jupiter's dayside magnetosphere, *Nature*, 280, (5725), 803, 1979.
- Molina-Cuberos, G. J., J. J. López-Moreno, R. Rodrigo and L. M. Lara**, Chemistry of the galactic cosmic ray induced ionosphere of Titan, *J. Geophys. Res.*, 104, 21997, 1999.
- Mücke-Herzberg, D.**, *Ein eindimensionales Multiionen-MHD-Modell der Ionosphärendynamik von Titan*, Dissertation, Institut für Geophysik und Meteorologie der Universität zu Köln, 1998.
- Müller-Wodarg, I. C. F., R. V. Yelle, M. Mendillo, L. A. Young and A. D. Aylward**, The thermosphere of Titan simulated by a global three-dimensional time-dependent model, *J. Geophys. Res.*, 105, 20, 833, 2000.

- Nagy, A. F., Y. Liu, K. C. Hansen, K. Kabin, T. I. Gambosi, M. R. Combi, D. L. D. Zeeuw, K. G. Powell and A. J. Klione**, The interaction between the magnetosphere of Saturn and Titan's ionosphere, *J. Geophys. Res.*, *106*, 6151, 2001.
- Ness, N. F., M. H. Acuña, K. W. Behannon and F. M. Neubauer**, The induced magnetosphere of Titan, *J. Geophys. Res.*, *87*, (A3), 1369–1381, 1982.
- Neubauer, F. M.**, Possible strengths of dynamo magnetic fields of the Galilean satellites and of Titan, *Geophys. Res. Lett.*, *5*, 905–908, 1978.
- Neubauer, F. M.**, Nonlinear standing alfvén wave current system at Io: Theory, *J. Geophys. Res.*, *85*, 1171–1178, 1980.
- Neubauer, F. M.**, Giotto magnetic field results on the magnetic field pile-up region and the cavity boundaries, in *Proc. 20th ESLAP Symposium on the Exploration of Halley's Comet, Heidelberg*, ESA SP-250, 35–41, 1986.
- Neubauer, F. M.**, The ionopause and boundary layers at comet Halley from Giotto magnetic field observations, *J. Geophys. Res.*, *93*, (A7), 7272–7281, 1988.
- Neubauer, F. M.**, Alfvén wings and electromagnetic induction in the interiors: Europa and Callisto, *J. Geophys. Res.*, *104*, (A12), 28671+, 1999.
- Neubauer, F. M., D. A. Gurnett, J. D. Scudder and R. E. Hartle**, Titan's magnetospheric interaction, in *Saturn*, edited by T. Gehrels and M. S. Matthews, 760–787, Univ. of Ariz. Press, Tucson, Arizona, 1984.
- Owen, T.**, The composition and origin of Titan's atmosphere, *Planet. Space Sci.*, *30*, 833–838, 1982.
- Prange, R., D. Rego, D. Southwood, P. Zarka, S. Miller and W. Ip**, Rapid energy dissipation and variability of the Io-Jupiter electrodynamic circuit, *Nature*, *379*, 323–325, 1996.
- Press, W. H.**, Numerical recipes in fortran, Cambridge University Press, Second Edition, 1992.
- Richards, P. G., J. A. Fennelly and D. G. Torr**, A solar EUV flux model for aeronomic calculations, *J. Geophys. Res.*, *99*, 8981, 1994.
- Richardson, J. D.**, Thermal plasma and neutral gas in Saturn's magnetosphere, *Rev. Geophys.*, *36*, 501, 1998.
- Roboz, A. and A. F. Nagy**, The energetics of Titan's atmosphere, *J. Geophys. Res.*, *99*, 2087, 1994.
- Roe, H. G., I. de Pater, B. A. Macintosh and C. P. McKay**, Titan's clouds from Gemini and Keck Adaptive optics imaging, *Astrophys. J.*, *581*, 1399, 2002.
- Russell, C. T. and M. M. Hoppe**, Upstream waves and particles, *Space Sci. Rev.*, *34*, 155–172, 1983.

- Russell, C. T., J. G. Luhmann and R. C. Elphic**, The properties of the low altitude magnetic belt in the Venus ionosphere, *Adv. Space Res.*, 2, 13–16, 1982.
- Saunders, M. A. and C. T. Russell**, Average Dimension and magnetic structure of the distant Venus Magnetotail, *J. Geophys. Res.*, 91, 5589–5604, 1986.
- Saur, J.**, *Plasma Interaction of Io and Europa with the Jovian Magnetosphere*, Dissertation, Institut für Geophysik und Meteorologie der Universität zu Köln, 2000.
- Schardt, A. W., K. W. Behannon, R. P. Lepping, J. F. Carbary, A. Eviatar and G. L. Siscoe**, The outer magnetosphere, in *Saturn*, edited by T. Gehrels and M. S. Matthews, 417–459, Univ. of Ariz. Press, 1984.
- Schatten, K. H. and W. D. Pesnell**, An early solar dynamo prediction: cycle 23 - cycle 22, *Geophys. Res. Lett.*, 20, (20), 2275–2278, 1993.
- Schmidt, H. U., R. Wegmann, W. F. Huebner and D. C. Boice**, Cometary gas and plasma flow with detailed chemistry, *Comp. Phys. Comm.*, 49, 17–59, 1988.
- Schunk, R. W. and A. F. Nagy**, *Ionospheres - Physics, Plasma Physics, and Chemistry*, Cambridge University Press, 2000.
- Shinagawa, H. and T. E. Cravens**, A one-dimensional multispecies magnetohydrodynamic model of the dayside ionosphere of Mars, *J. Geophys. Res.*, 94, 6506–6516, 1989.
- Siscoe, L. G.**, Magnetosphere of Saturn, in *The Saturn System*, edited by D. M. Hunten and D. Morrison, Vol. 2068 of *NASA Conf. Publ.*, 1978.
- Sittler Jr., E. C., K. W. Ogilvie and J. D. Scudder**, Survey of low-energy plasma electrons in Saturn's magnetosphere: Voyagers 1 and 2, *J. Geophys. Res.*, 88, (A11), 8847–8870, 1983.
- Smith, E. J., L. Davis, D. E. Jones, P. J. Coleman, D. S. Colburn, P. Dyal and C. P. Sonett**, Saturn's magnetic field and magnetosphere, 1980.
- Smith, G. R., D. F. Strobel, A. L. Broadfoot, B. R. Sandel, D. E. Shemansky and J. B. Holberg**, Titan's upper atmosphere - Composition and temperature from the EUV solar occultation results, *J. Geophys. Res.*, 87, (A3), 1351–1359, 1982.
- Smith, P. H., M. T. Lemmon, R. D. Lorenz, L. A. Sromovsky, J. J. Caldwell and M. D. Allison**, Titan's surface, revealed by HST imaging, *Icarus*, 119, 336–349, 1996.
- Stix, T. H.**, *The Theory of Plasma Waves*, McGraw Hill, New York, 1962.
- Stone, J. M. and M. L. Norman**, The hydrodynamic algorithms and tests, *Astron. Astrophys. Suppl. Ser.*, 80, 753, 1992a.
- Stone, J. M. and M. L. Norman**, The magnetohydrodynamic algorithms and tests, *Astron. Astrophys. Suppl. Ser.*, 80, 791, 1992b.

- Strobel, D. F.**, Photochemistry of Titan, in *The Photochemistry of Atmospheres*, edited by J. S. Levine, 425–431, Academic Press, 1985.
- Strobel, D. F. and D. E. Shemansky**, EUV emission from Titan's upper atmosphere: Voyager 1 encounter, *J. Geophys. Res.*, *87*, (A3), 1361–1368, 1982.
- Toublanc, D., J. P. Parisot, J. Brillet, D. Gautier, F. Raulin and C. P. McKay**, Photochemical modeling of Titan's atmosphere, *Icarus*, *113*, 2–26, 1995.
- Vaisberg, O. L., J. G. Luhmann and C. T. Russel**, Plasma observations of the solar wind interaction with Mars, *J. Geophys. Res.*, *95*, (B9), 741, 1990.
- von Zahn, U., S. Kumar, H. Niemann and R. Prinn**, Composition of the Venus atmosphere, *Venus (A83-37401 17-91)*. Tucson, AZ, University of Arizona Press, *81*, 299, 1983.
- Wallis, M. K.**, Weakly-shocked flows of the solar wind plasma through atmospheres of comets and planets, *Planet. Space Sci.*, *21*, 1647–1660, 1973.
- Wolf, D. A. and F. M. Neubauer**, Titan's highly variable plasma environment, *J. Geophys. Res.*, *87*, 881–885, 1982.
- Yelle, R. V., D. F. Strobel, E. Lellouch and D. Gautier**, Engineering models for Titan's atmosphere, *J. Geophys. Res.*, *ESA SP-1177*, 243–256, 1997.
- Yung, Y. L.**, An update of nitrile photochemistry on Titan, *Icarus*, *72*, 468, 1987.
- Yung, Y. L., M. Allen and J. P. Pinto**, Photochemistry of the atmosphere of Titan: comparison between model and observations, *Astron. Astrophys. Suppl. Ser.*, *465*, 465, 1984.
- Zwan, B. J. and R. A. Wolf**, Depletion of solar wind plasma near a planetary boundary, *J. Geophys. Res.*, *81*, 1636–1648, 1976.

# Acknowledgments

First of all I want to thank my advisor Prof. F. M. Neubauer for encouraging me during the whole period of this research. He always found a good balance between optimism and a critical view on the subject.

Prof. M. K. Dougherty I want to thank for being my co-supervisor. I really enjoyed our meetings at several conferences. I eagerly await the MAG data from the first Cassini flyby TA.

My thanks go to Prof. B. Tezkan for being my co-supervisor and helping me out in that issue.

For proof-reading I thank Jörg von Oertzen, Nico Schilling, Joachim Saur, Sven Jacobsen, and Tetsuya Tokano.

I really appreciated the scientific discussions with Nico Schilling and Joachim Saur. Some things only become clear when you talk about them.

Special thanks to my room mates Sven Jacobsen and Nico Schilling. They provided a good source of energy.

For system administration I thank Dr. A. Wennmacher, Sven Jacobsen, Nico Schilling, Rainer Bergers and Andreas Busse.

I obtained graphical and technical support from Stefan Hendrix and Steffen Rost, and Michael Commer helped me out with the Latex files.

I acknowledge the financial support by DLR and BMFT.

But my deepest thanks go to my lovely Fypsn.



Ich versichere, dass ich die von mir vorgelegte Dissertation selbständig angefertigt, die benutzten Quellen und Hilfsmittel vollständig angegeben und die Stellen der Arbeit - einschließlich Abbildungen und Tabellen -, die anderen Werken im Wortlaut oder dem Sinn nach entnommen sind, in jedem Einzelfall als Entlehnung kenntlich gemacht habe; dass diese Dissertation noch keiner anderen Fakultät oder Universität zur Prüfung vorgelegen hat; dass sie noch nicht veröffentlicht worden ist sowie, dass ich eine solche Veröffentlichung vor Abschluß des Promotionsverfahrens nicht vornehmen werde. Die Bestimmungen dieser Promotionsordnung sind mir bekannt. Die von mir vorgelegte Dissertation ist von Prof. F. M. Neubauer betreut worden.

Köln, September 2004

